

GENERIC WIRELESS SENSOR NETWORK FOR DYNAMIC MONITORING OF A NEW GENERATION OF BUILDING MATERIAL

Romwald Lihakanga

Submitted for the Degree of Doctor of Philosophy

Heriot-Watt University

School of Energy, Geo-Science, Infrastructure & Society and EPS, Heriot Watt
University, United Kingdom

Edinburgh-United Kingdom

December 2022

The copyright in this thesis is owned by the author. Any quotation from the thesis or use any of the information contained in it must acknowledge this thesis as the source of the quotation or information.

Abstract

Existing testing methods for building materials before deployment include a series of procedures as stipulated in British Standards, and most tests are performed in a controlled laboratory environment. Types of equipment used for measurements, data logging, and visualisation are commonly bulky, hard-wired, and consume a significant amount of power. Most of the off-the-shelf sensing nodes have been designed for a few specific applications and cannot be used for general purpose applications. This makes it difficult to modify or extend the sensing features when needed. This thesis takes the initiative of designing and implementing a low-powered, open-source, flexible, and small-sized Generic wireless sensor network (GWSN) that can continuously monitor the building materials and building environment, to address the limitations of the conventional measurement methods and the technological gap.

The designed system is comprised of two custom-made sensor nodes and a gateway, as well as purpose designed firmware for data collection and processing. For the proof of concept and experimental studies, several measurement strategies were designed, to demonstrate, evaluate, and validate the effectiveness of the system. The data was collected from selected case study areas in the School of Energy, Geoscience, Infrastructure and Society (EGIS) laboratories by measuring and monitoring building structures and indoor environment quality parameters using the designed GWSN. The measured data includes heat flux through the material, surface and air temperatures on both sides of the material/structure, moisture variation, ambient temperature, relative humidity, carbon dioxide, volatile organic compounds, particulate matter, and sound/acoustic levels.

The initial results show the potential of the designed system to become the new benchmark for tracking the variation of building materials with the environment and investigating the impact of variation of building materials on indoor environment quality. Based on the estimates of the thermal performance data, the sample used in the experiment had a typical U-value between 4.8 and 5.8 W/m²K and a thermal resistance value of 0.025 m²·K/W[1][2]. Thermal resistance values from the GWSN real-time measurement were between 0.025 and 0.03 m²K/W, with an average of 0.025 m²K/W, and thermal transmission values varied between 4.55 and 5.11 W/m²K. Based on the data obtained, the results are within the range of typical values[3].

For thermal comfort measurements, the results of humidity and temperature from GWSN were compared to values in the Kambic climatic chamber in the EGIS laboratory, and the accuracies were 99 % and 98 % respectively. For the IAQ measurements, the values of CO₂ and TVOCs were compared to the commercial off-the-shelf measuring system, and the accuracies were 98 %, and 97 %. Finally, the GWSN was tested for acoustic measurements in the range of 55 dB to 106 dB. The results were compared to class one Bruel & Kjaer SLM. The accuracy of GWSN was 97 %. The GWSN can be used for in-lab and in-situ applications, to measure and analyse the thermal physical properties of building materials/building structures (thermal transmittance, thermal conductivity, and thermal resistance). The system can also measure indoor air quality, thermal comfort, and airborne sound insulation of the building envelope. The key point here is to establish a direct link between how building materials vary with the environment and how this impacts indoor environment quality. Such a link is essential for long-term analysis of building materials, which cannot be achieved using current methods.

Regarding increasing the power efficient of the implemented GWSN as well as its performance and functionality, a new sensing platforms using backscatter technology have been introduced. The theory of modulation and spread spectrum technique used in backscattering has been explored. The trade-off between hardware complexity/power consumption and link performance has been investigated.

Theoretical analysis and simulation validation of the new sensing technique, using backscatter communication, has been performed. A novel multicarrier backscatter tag compatible with Wireless Fidelity has been implemented and an IEEE 802.11g OFDM preamble was synthesized by simulation. The tag consists of only two transistors with current consumption no larger than 0.2 μ A at voltage of less than 0.6 V.

Novel harmonic suppression approaches for frequency-shifted backscatter communication has been proposed and demonstrated. The proposed approaches independently manipulate mirror harmonics and higher order harmonics whereby; specified higher order harmonics can be removed by carefully designing the real-valued (continuous and discrete) reflection coefficients-based backscatter tags.

When successfully implemented, the backscatter system will reduce sensor node power consumption by shifting the power-consuming radio frequency carrier synthesis functions to carrier emitters.

Dedication

To my dad in Heaven, who passed away 14 years ago when I was about to receive my undergraduate degree.

To my mom in Heaven, who helped me throughout this PhD journey and always encouraged and prayed for me but didn't live to see me graduate and enjoy the fruits of my efforts.

Acknowledgments

I would like to express my gratitude to the Engineering and Physical Sciences Research Council for funding this research through EP/H009612/1 and the Carnegie Research Incentive through RIG008216.

To the leadership of Embassy of the Word of God, Edinburgh, for their constant prayers and support.

To my family and friends, who have been always there for me.

ACADEMIC REGISTRY

Research Thesis Submission

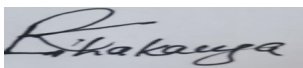
Name:	Romwald Lihakanga		
School:	EGIS		
Version: (<i>i.e. First, Resubmission, Final</i>)	Final	Degree Sought:	PhD

Declaration

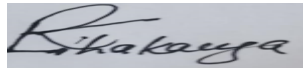
In accordance with the appropriate regulations I hereby submit my thesis and I declare that:

1. The thesis embodies the results of my own work and has been composed by myself
2. Where appropriate, I have made acknowledgement of the work of others
3. The thesis is the correct version for submission and is the same version as any electronic versions submitted*.
4. My thesis for the award referred to, deposited in the Heriot-Watt University Library, should be made available for loan or photocopying and be available via the Institutional Repository, subject to such conditions as the Librarian may require
5. I understand that as a student of the University I am required to abide by the Regulations of the University and to conform to its discipline.
6. I confirm that the thesis has been verified against plagiarism via an approved plagiarism detection application e.g. Turnitin.

* Please note that it is the responsibility of the candidate to ensure that the correct version of the thesis is submitted.

Signature of Candidate:		Date:	15/12/2022
-------------------------	--	-------	------------

Submission

Submitted By (<i>name in capitals</i>):	ROMWALD LIHAKANGA
Signature of Individual Submitting:	
Date Submitted:	15/12/2022

For Completion in the Student Service Centre (SSC)

Limited Access	Requested	Yes	No	Approved	Yes	No
E-thesis Submitted (mandatory for final theses)						
Received in the SSC by (<i>name in capitals</i>):				Date:		

Table of Contents

Abstract	ii
List of Publications	xxiv
Chapter One	1
Background and Motivation.....	1
1 Introduction.....	1
1.1 Background Information	1
1.2 Motivation	1
1.3 Objectives	3
1.4 Overview of the Proposed System: A GWSN for Real-Time Online Monitoring of New Generation of Building Materials	4
1.5 Demonstration structure	5
1.6 Research Methodology	5
1.7 Research Claims	7
1.8 Thesis Outline.....	8
Chapter Two.....	10
Literature Review	10
2 Introduction.....	10
2.1 Building Material Properties	10
2.1.1 Physical Properties	10
2.1.2 Mechanical Properties	11
2.1.3 Chemical Properties	11
2.1.4 Electrical Properties	11
2.1.5 Thermal Properties	11
2.2 The Effect of Building Material Properties on Indoor Environment Quality Variation	12
2.3 Building Monitoring.....	13
2.3.1 Introduction	13

2.3.2	Sensors in Building structure monitoring	13
2.3.2.1	Fibre Optic Sensors (FOSs)	14
2.3.2.2	Conclusion	16
2.3.2.3	Piezo Electric Sensors	16
2.3.2.4	Conclusion	17
2.3.2.5	Radio Frequency Identification (RFID) Sensors.....	17
2.3.2.6	MEMS sensors	20
2.3.3	Building Materials Thermal Performance Characterisation	22
2.3.4	Building Materials Hygrothermal Properties	26
2.3.5	Building Materials Electrical Resistivity Measurement Techniques	23
2.3.5.1	Wenner Technique (4-Point method).....	23
2.3.5.2	Two Point Electrode Method	25
2.3.5.3	Multi-Points Electrodes Method	26
2.3.6	Summary of Building Materials Electrical Resistivity Measurement Techniques	26
2.3.7	Indoor Thermal Comfort	27
2.3.8	Indoor Air Quality Monitoring.....	27
2.3.9	Acoustic/Sound Measurements.....	28
2.3.9.1	Airborne Sound Insulation Measurement	28
2.4	Internet of Things for Structural Monitoring.....	30
2.4.1	Introduction	30
2.4.2	Bluetooth Low Energy (BLE).....	30
2.4.3	Wi-Fi	31
2.4.4	LoRa.....	31
2.4.5	ZigBee Communication	32
2.4.5.1	XBee Configuration and Networking	33
2.4.5.2	ZigBee Network Topology	33
2.4.5.3	ZigBee Network Addressing and Data Transmission	34
2.4.5.4	Description of API Frame	35
2.5	Summary of the Chapter.....	35
	Chapter Three.....	37
	A Generic Wireless System Design and Instrumentation Strategies	37

3	Introduction.....	37
3.1	Electronics Hardware Design and Sensor Interface	37
3.1.1	Thermal Performance Characterisation.....	37
3.1.1.1	HFP01-05 Heat Flux Sensor	38
3.1.1.2	Temperature Sensors.....	39
3.1.1.3	Moisture and Temperature Measurements	40
3.1.2	Indoor Thermal Comfort	41
3.1.3	Indoor Air Quality Monitoring.....	41
3.1.3.1	TGS2602 Volatile Organic Compound Sensor.....	42
3.1.3.2	Cozir Ambient Carbon Dioxide Sensor	43
3.1.3.3	GP2Y1010AU0F Dust Sensor	43
3.1.4	Acoustic Measurement.....	44
3.1.5	S2C XBee Communication Module.....	45
3.1.5.1	XBee Modules Configuration.	46
3.1.6	Microcontroller Unit	47
3.1.7	Arduino Uno	48
3.1.8	Raspberry Pi	48
3.1.9	Power Supply	49
3.1.10	Sensor Nodes.....	49
3.1.11	Gateway Node.....	51
3.2	Software Architecture.....	51
3.2.1	Sensor Node	52
3.2.2	Gateway Node.....	54
3.2.3	Cloud Server	56
3.2.4	Power Saving Strategies.....	56
3.2.5	Sensor Calibration.....	57
3.3	Conclusion.....	57
	Chapter Four	58
	Design of the Experiments, Measurements, and Results Discussion	58
4	Introduction.....	58

4.1	Building Material Thermal Performance.....	58
4.1.1	Sensing System Calibration	58
4.1.2	Theoretical U-value calculation	60
4.1.3	Thermal Performance Measurement	62
4.1.3.1	Experimental Setup	63
4.1.4	Summary of Thermal Performance Measurements.....	68
4.1.5	Heat Loss in Real-Time	68
4.1.6	Indoor Thermal Comfort Measurement	69
4.1.7	Hygrothermal Properties of the Building Environment	70
4.1.8	Building Indoor Air Quality	71
4.1.8.1	Sensing System Calibration	71
4.1.9	TGS2602 Sensor Calibration	72
4.1.10	Summary of Indoor Air Quality Measurements.....	75
4.1.11	Building Material Acoustic Measurement	76
4.1.11.1	Acoustic Sensing System Calibration	76
4.1.12	Airborne Sound Insulation Measurement	80
4.1.13	Summary of Acoustic Measurement.....	81
4.2	Conclusion.....	81
	Chapter Five	83
	Universal Backscatter tag.....	83
5	Introduction.....	83
5.1	State of the Art Literature Backscatter Modulations	84
5.1.1	Amplitude Shift Keying (ASK)	84
5.1.2	Frequency Shift Keying (FSK)	85
5.1.3	Phase Shift Keying (PSK).....	86
5.1.4	Quadrature Amplitude Modulation (QAM)	87
5.1.5	Chirp Spread Spectrum (CSS) Modulation.....	88
5.1.6	Summary of SOTA Backscatter Modulation	89
5.2	IQ Backscatter Modulator	90

5.2.1	IQ Modulator Termination Impedances Analysis Using Phase Rotation	91
5.2.1.1	Chirp Spread Spectrum	92
5.2.1.2	Binary Phase Shift Keying (BPSK)	93
5.2.1.3	Quadrature Phase Shift Keying (QPSK)	94
5.2.1.4	Quadrature Amplitude Modulation	94
5.2.1.5	Frequency Shift Keying	95
5.2.2	Performance of Modulation Technique and Spread Spectrum used in Backscattering	95
5.2.2.1	Performance of Various Linear Digital Modulation Schemes Over AWGN Channel	96
5.2.2.2	Performance of M-PAM over AWGN Channel.....	97
5.2.2.3	Performance of M-PAM over Rayleigh Flat Fading Channel	98
5.2.2.4	Performance of M-PSK over Rayleigh Flat Fading Channel.....	99
5.2.2.5	Performance of M-PSK over AWGN Channel.....	100
5.2.2.6	Performance of M-FSK over AWGN Channel.....	101
5.2.2.7	Performance of M-QAM over Rayleigh Flat Fading Channel.....	102
5.2.2.8	Performance of M-QAM over AWGN Channel.....	103
5.2.3	Spread Spectrum Technology	103
5.2.4	Orthogonal Frequency-Division Multiplexing.....	104
5.2.4.1	OFDM Performance.....	104
5.2.4.2	Performance of MPSK-CP-OFDM and MQAM-CP-OFDM on AWGN Channel	105
5.2.4.3	Performance of MPSK-CP-OFDM and MQAM-CP-OFDM on Frequency Selective Rayleigh Channel	106
5.2.5	Direct Sequence Spread Spectrum	108
5.2.5.1	DSSS Performance Analysis.....	108
5.2.6	Chirp Spread Spectrum	109
5.2.6.1	CSS Performance with Different Spreading Factors (SF)	110
5.2.7	Summary	111
5.3	Conclusion.....	112
Chapter Six.....		113
Backscatter Systems Theoretical Analysis and Simulation Validation		113
6	Introduction.....	113
6.1	Multicarrier Backscatter Transmission	113
6.1.1	Introduction	113

6.1.2	Implementation of Multicarrier Backscatter	113
6.1.3	Summary of Multicarrier Backscatter Communication	115
6.2	Harmonic Suppression in Frequency Shifted Backscatter Communications	115
6.2.1	Mathematical Representation of Frequency Shifted Backscattering	116
6.2.2	Harmonic Suppression with Load Impedance of Complex Value.....	117
6.2.3	Mirror Harmonic Suppression with Orthogonal Loads	119
6.2.4	Summary of Harmonic Suppression in Frequency Shifted Backscatter Systems	120
6.3	Proposed Implementation of WiFi Backscatter Tags in the GWSN	120
6.4	Conclusion.....	121
Chapter Seven		122
Conclusion and Future Work		122
7	Introduction.....	122
7.1	Summary of the Research.....	122
7.2	Key Research Contributions.....	124
7.3	GWSN on Complex structures	126
7.4	Future Work	127
7.5	Research Conclusion	128
8	References.....	129
Appendix.....		144
Appendix 1: XBee S2C 3mW module Configurations		144
Appendix 2: Datasheet of a Generic Wireless sensor Network		150
Appendix 3: Packets formats		164
Appendix 4: Gateway Configuration		165
Appendix 5: Graphical User Interfaces.....		169
Appendix 6: Thermal Performance Measurement Matlab Scripts.....		172
Appendix 7: TGS 2602 Sensor calibration Code.....		173

Appendix 8: Linear Regression Model Output for Acoustic Sensing System Calibration	
.....	174

List of Figures

Figure 1.1. Diagram showing the architecture of the proposed system with the parameters to be measured, means of communication and access method.....	4
Figure 1.2. Diagram showing sensor mapping for selected measurements points with sensors installed on the surface and other sensors embedded within the structure (a) Plan view (b) Side view.	6
Figure 2.1. A picture of TRSYS01 heat flux measuring system with the carrying case of dimension 480 x 390 x 190 mm [77].	23
Figure 2.2. Measurement setup according to BS ISO 9869:2014 standard showing the location of temperature sensors and heat flux sensors on the MUT and physical connection of data logging equipment.	24
Figure 2.3. A picture of Infra-red thermography measurement methodology (a) Infra-red thermal camera (b)Image of the building under measurements showing thermal distribution on various part of the building [82].	25
Figure 2.4. Diagram demonstrating Wenner technique (4-Point electrode method) showing sensor position on the measured sample, wiring of the measuring equipment and current flow within the sample [97].	24
Figure 2.5. A diagram showing material resistivity measurement using the two-point method with sensor position and equipment interface [101].	25
Figure 2.6. Diagram of airborne sound insulation measurement setup with two SLM positioned on the opposite face of the MUT, acoustic source and computer for data processing [20].	29
Figure 2.7. Diagram of wireless technology performance showing how bandwidth varies with power consumption and distance [132].	32
Figure 2.8. A diagram of a simple star topology.....	34
Figure 2.9. Diagram of A basic API frame showing the position of data frame, length, delimiter and checksum.....	34
Figure 3.1. Thermal performance measurement (a) A picture of a heat flux sensor selected for the measurement of heat flux through the material (b) Surface temperature sensor used for measuring the temperature on the surface of the MUT.	37
Figure 3.2. Schematics showing a typical connection of ADC ADS1115 with microcontroller with pull-up resistors [135].	38
Figure 3.3. Schematics showing thermistor interface circuit to the GWSN [133].	39
Figure 3.4. A picture of HTM2500LF humidity and temperature sensor [133].	40

Figure 3.5. DHT22 Humidity and Temperature sensor [138].	41
Figure 3.6. A picture of sensors for indoor air quality measurements(a) COZIR Ambient CO2 sensor (b) GP2Y1010AU0F Dust sensor (c) TGS 2602 VOC sensor	42
Figure 3.7. Schematics of TGS2602 VOC sensor pinout setup and interface [141].	42
Figure 3.8. Diagram of Cozir Carbon dioxide sensor pin description [139].	43
Figure 3.9. Schematics of dust sensor pinout and interface [143].	44
Figure 3.10. A picture of GY-MAX4466 electret microphone as an acoustic sensor [144].	44
Figure 3.11. A picture of XBee ZigBee S2C module wired antenna – XB24CZ7WIT-004 [130].	45
Figure 3.12. Schematic of level shifter circuit use to converting voltage from 5 V to 3.3 V and 3.3 V to 5 V [150].	46
Figure 3.13. A diagram showing S2C Communication module interface with Atmel 328P [151].	46
Figure 3.14. A diagram showing network topology established by XBee modules with XCTU software.	47
Figure 3.15. A picture of Atmel 328P-PU microcontroller and pinout [153].	48
Figure 3.16. A picture of Arduino Uno development board [155].	48
Figure 3.17. A picture of Raspberry Pi model 3 B+ board [156].	49
Figure 3.18. A picture of manufactured system with dimensions (a) Sensor node (95 mm by 65 mm) (b) Gateway node (65 mm by 55 mm).	49
Figure 3.19. Sensor node 1. (a) Block diagram showing how various blocks are connected (b) Prototype showing the soldered components [3].	50
Figure 3.20. Sensor node 2. (a) Block diagram showing connection of various block (b) Prototype showing the soldered components [3].	50
Figure 3.21. A diagram of gateway node showing how slave gateway is interfaced with master gateway and display unit (a) Block diagram (b) Prototype [3].	51
Figure 3.22. Software Architecture showing how various software used in GWSN are connected from the sensor node to the remote device.	52
Figure 3.23. Flowchart of the main program of the sensor nodes of the GWSN showing how sensor data are collected, and how power consumed is reduced by operating transmitter in sleeping mode.	53
Figure 3.24. Flow chart showing program subroutines on the sensor nodes (a) Interrupt subroutine (b) Sensor read subroutine.	54

Figure 3.25. Program flowcharts (a) Slave server (b) Processing subroutine.....	55
Figure 3.26. Flowchart of the Master section of the Generic wireless sensor network showing how data is extracted and sent to the database for the storage.	56
Figure 4.1. A plot showing air temperature measurements comparison between reference measurement by standard device and measurements by GWSN.	59
Figure 4.2. A plot showing a surface temperature measurements comparison between reference measurement and measurement taken using GWSN.	59
Figure 4.3. A plot showing humidity measurements comparison between reference measurement and measurement taken using GWSN.	60
Figure 4.4. Diagram showing heat movement through the building material.	61
Figure 4.5. A diagram of a proposed measurement system architecture showing the position of the sensors, sensor nodes and flow of information from the sensor nodes, gateway node to the cloud [3].	62
Figure 4.6. A picture of measurement setup for thermal performance of building material with heat flux and temperature sensors located on the MUT [3].	64
Figure 4.7. A plot for overall thermal transmission parameters measurement data for 7 days.	65
Figure 4.8. A plot for thermal transmittance measurement data from Day 1 to Day 3. (W/(m ² K)).....	66
Figure 4.9. A plot for thermal transmittance measurement data between Day 2 and Day 4.....	66
Figure 4.10. A plot for thermal transmittance measurement data between Day 3 and Day 5.....	66
Figure 4.11. A plot for thermal transmittance measurement data between Day 4 and Day 6.....	67
Figure 4.12. A plot for thermal transmittance measurement data between Day 5 and Day 7.....	67
Figure 4.13. A plot for thermal resistance measurement data from Day 1 to Day 3. ...	67
Figure 4.14. A plot fort thermal conductivity measurement data from Day 1 to Day 3.	68
Figure 4.15. A plot showing a real-time temperature variations measurement data for external (surface and air) and internal (surface and air temperature) for 7 days.	69
Figure 4.16. A plot showing thermal comfort variation for 7 days.....	69

Figure 4.17. A diagram for moisture measurement setup showing location of sensors (with red line presenting inner layer of the material), sensor nodes and how data are communicated from the nodes to the cloud.	70
Figure 4.18. A plot showing humidity variations between indoor and outdoor for 7 days.	70
Figure 4.19. A plot showing CO ₂ measurements comparison between reference measurements and the measurements taken by GWSN.....	72
Figure 4.20. A plot showing sensitivity characteristics of TGS2602 for various organic compounds [141].....	73
Figure 4.21. A plot for VOC measurements comparison between the reference measurements and measurement taken using GWSN.....	75
Figure 4.22. Setup for laboratory calibration of the acoustic sensing system. Bruel & Kjaer Type 2250 SLM and acoustic sensor microphones were placed in two different points in the reverberation chamber. The acoustic sensing system was connected to the computer for data visualisation and power supply to the GWSN.....	76
Figure 4.23. A plot of a linear fit created from measured acoustic data for acoustic sensor calibration.....	77
Figure 4.24. Acoustic measurements and calibration at EGIS reverberant chamber. (a)The reverberant chamber entrance, (b) Sound source (Bruel & Kjaer Type 4224) used during measurements, (c) Sound source position during measurements, (d) GWSN and Standard SLM (Bruel & Kjaer Type 2250) position during measurements	78
Figure 4.25. A plot of sound level measurements comparison between Reference measurements and the measurements taken using GWSN.	79
Figure 4.26. A diagram for acoustic measurement showing the location of sensor (with red line presenting inner layer of the material), sensor nodes, sound sources and the flow data from the nodes to the cloud through the gateway.....	80
Figure 5.1. A diagram of communication systems (a) Conventional radio (b) Backscatter passive radio [166].	83
Figure 5.2. A schematics to illustrate a tag backscattering using OOK modulated signals with tag impedance Z_a an Z' and antenna impedance Z_a [165].	84
Figure 5.3. A smith chart plot showing design guidance on antenna termination impedance for ASK modulation with impedance allocation [165].....	85
Figure 5.4. A schematic for illustration of a tag backscattering using 2FSK modulated signals with tag impedance Z_1 and Z_2 and antenna impedance Z_a [165].	86

Figure 5.5. A Smith chart plot showing a design guidance on antenna termination impedance Z_I and Z_2 for 2FSK modulation [165].	86
Figure 5.6. A schematic for illustration of a tag backscattering using QPSK modulated signal with tag impedance Z_I , Z_2 , Z_3 and Z_4 and antenna impedance of Z_a [165].	87
Figure 5.7. A smith chart plot of an ideal choice of antenna termination impedance Z_I , Z_2 , Z_3 and Z_4 for the QPSK backscatter modulation [165].	87
Figure 5.8. A schematic for 16-QAM backscatter modulator [174].	88
Figure 5.9. A schematic for CSS (LoRa-PHY compatible) backscatter tag [176].	88
Figure 5.10. (a) A smith chart plot for the design guidance on antenna termination with the impedance accelerating/decelerating clockwise/anticlockwise of the unit circle (b) Spectrogram of backscattered signals [165].	89
Figure 5.11. IQ backscatter modulator (a) Circuit diagram (b) Implementation on [177].	90
Figure 5.12. A smith chart plot showing reflection coefficient observed at antenna port A when V_I and V_Q of two transistors (ATF-54143) on IQ backscatter tag are swept from 0 to 0.6 V [167].	91
Figure 5.13. A smith chart plot of IQ modulator reflection coefficients with constant envelope reflection circle fitted inside [165].	91
Figure 5.14. (a) A plot of a received LoRa packet spectrogram (measurement). (b) Spectrogram after LoRa decoding [177].	93
Figure 5.15. A smith chat plot of a 16-QAM backscatter modulation in IQ plane [165].	95
Figure 5.16. A Matlab plot showing the performance of various linear digital modulation schemes over AWGN channel [178].	97
Figure 5.17. A Matlab plot showing the performance of M-PAM over AWGN channel.	98
Figure 5.18. A Matlab plot showing the Performance of M-PAM over Rayleigh flat fading channel.	99
Figure 5.19. A Matlab plot showing the performance of M-PSK over Rayleigh flat fading channel.	100
Figure 5.20. A Matlab plot showing the performance of M-PSK over AWGN channel.	100
Figure 5.21. A Matlab plot showing the performance of M-FSK over AWGN channel.	101

Figure 5.22. A plot showing performance of M-QAM over Rayleigh flat fading channel.	102
Figure 5.23. A plot showing performance of M-QAM over AWGN channel.....	103
Figure 5.24. A Matlab plot showing the performance of CP-OFDM on AWGN channel (a) MPSK (b) MQAM.....	106
Figure 5.25. A diagram of OFDM transmitter and receiver model.	106
Figure 5.26. A Matlab plot showing the performance of CP-OFDM on frequency selective Rayleigh channel (a) MPSK (b) MQAM.	108
Figure 5.27. A Matlab plot for BER vs EbN0 plot for DSSS used with various phase modulation [180]......	109
Figure 5.28. A Matlab plot for LoRa BER Performance at different Spreading Factors (SF).....	110
Figure 6.1. A smith chart plot showing 320 preamble samples in IQ plane in the IEEE 802.11g. (Some samples are overlapped) [167]......	114
Figure 6.2. A smith chat plot for the scaled 320 samples to fit into the shaded area in Figure 5.12 [167]......	114
Figure 6.3. The diagram for the reflection coefficient Γ_{bs} in time when the switch is toggling between open and short at a frequency of $f_{bs} = 1/T_{bs}$. [23].	116
Figure 6.4. Proposed Implementation of Wi-Fi Backscatter on GWSN showing how the backscatter tag will replace the sensor node in GWSN and the flow of signal from the tag to the cloud.	121

List of Tables

Table 1.1. Building Structure Monitoring.....	3
Table 1.2. Indoor Environment Quality Monitoring.....	4
Table 2.1. Specifications of TRSYS01 Heat flux measurement System.	23
Table 2.2. Comparison of the novel GWSN system against the existing systems according to the proposed performance and operational metrics.....	22
Table 4.1. Climatic chamber operating ranges.....	58
Table 4.2. Summary of thermal performance measurement system response when compared to the reference or standard measurements.	60
Table 4.3. Summary of thermal transmittance measurement [3].	65
Table 4.4. Reference IAQ measuring system range and accuracy.....	71
Table 4.5. GWSN performance for CO ₂ measurements.....	72
Table 4.6. Logarithmic conversion model parameters are estimated from measurement data using the logarithmic estimation method.	74
Table 4.7. GWSN measurement performance on VOC measurements	75
Table 4.8. Linear regression model output from the measured acoustic data.....	79
Table 4.9. GWSN sound/acoustic level measurements response	80
Table 5.1. The Equations for the theoretical BER for various linear modulation [178].	96
Table 5.2. Simulation Parameters for OFDM.	105
Table 5.3. Simulation Parameters for DSSS	108
Table 5.4. Simulation parameters for CSS.....	110
Table 6.1. Normalised Power (Ap In dB) Of Backscatter Harmonics (Up To ± 5) For Different Numbers Of Discrete Impedances [23].	118
Table 7.1. Summary of the GWSN operating performance.....	124

List of Abbreviation and Acronyms

2FSK	Binary Frequency Shift Keying
A	Ampere
ADC	Analogue to Digital Converter
API	Application Programming Interface
API	Application Programming Interface
ASK	Amplitude Shift Keying
AVR	Advanced Virtual Reduced Instruction Set Computer
AWGN	Additive White Gaussian Noise
BER	Bit Error Rate
BLE	Bluetooth Low Energy
BPSK	Binary Phase Shift Keying
BS	British Standard
CMOS	Complementary Metal Oxide Semiconductor
CO ₂	Carbon Dioxide
COTS	Commercial Out of the Shelf
CSS	Chirp Spread Spectrum
DAC	Digital to Analogue Converter
dB	decibel
dBm	decibel-milliwatts
DC	Direct Current
DFT	Discrete Fourier Transform
DSPIC	Digital Signal Controllers
DSSS	Direct Sequence Spread Spectrum
EGIS	Energy, Geoscience, Infrastructure and Society
EMI	Electromagnetic interference
FHSS	Frequency Hopping Spread Spectrum
FOS	Fiber Optic Sensor
FSK	Frequency Shift Keying
GND	Ground
GWSN	Generic Wireless sensor Network
He	Outdoor Humidity
HFX	Heat Flux

Hi	Indoor humidity
IAQ	Indoor Air Quality
IQ	In-phase-Quadrature
IEEE	Institute of Electrical and Electronics Engineers.
IR	Infrared
ISO	International Standard Organization
K	Kelvin
LoRa	Long Range
LSB	Least Significant Bit
m	metres
MAC	Medium Access Control
MEMS	Micro Electromechanical systems
MOEMS	Micro Opto Electromechanical systems
MSB	Most Significant Bit
MUT	Material Under Test
NTC	Negative Temperature Coefficient
°C	Degree Centigrade
OFDM	Orthogonal Frequency Division Multiplexing
OOK	ON- OFF Keying
OTA	Over The Air Test
PAM	Pulse Amplitude Modulation
PAN	Personal Area Network
PHP	Hypertext Pre-processor
PM	Particulate Matter
PSK	Phase Shift Keying
PZT	Lead Zirconate Titanate
QAM	Quadrature Amplitude Modulation
QPSK	Quadrature Phase Shift Keying
RF	Radio Frequency
RFID	Radio Frequency Identification
RISC	Reduced Instruction Set Computer
R _T	Total Thermal Resistance
R-Value	Thermal Resistance
SF	Spreading Factor

SLM	Sound Level Meter
SNR	Signal to Noise Ratio
SOTA	State of The Art
SRI	Sound Reduction Index
Te	Exterior ambient Temperature
TH	Temperature and Humidity
Ti	Interior ambient temperature
Tse	Exterior surface Temperature
Tsi	Interior surface Temperature
UART	Universal Asynchronous Receiver Transmitter
U-value	Thermal transmittance
v	Volts
VCO	Voltage Controlled Oscillator
VOCs	Volatile Organic Compounds
WiFi	Wireless Fidelity
WPD	Wilkinson Power Divider
WSN	Wireless Sensor Network
Λ -Value	Thermal Conductance
ρ	Resistivity
Ω m	ohm-metres
Φ	Heat flux density

List of Publications

Abbasi, Q.H., Abbas, H.T., Alomainy, A., Imran, M.A., Ding, Y., Goussetis, G., Correia, R., Carvalho, N.B., **Lihakanga, R.** and Song, C. (2021). Signal Modulation Schemes in Backscatter Communications. In Backscattering and RF Sensing for Future Wireless Communication (eds Q.H. Abbasi, H.T. Abbas, A. Alomainy and M.A. Imran). <https://doi.org/10.1002/9781119695721.ch2>. (Chapter in a Book)

Y. Ding, **R. Lihakanga**, R. Correia, G. Goussetis and N. B. Carvalho, "Harmonic Suppression in Frequency Shifted Backscatter Communications," in IEEE Open Journal of the Communications Society, vol. 1, pp. 990-999, 2020, <https://doi:10.1109/OJCOMS.2020.3011520>. (Journal Article).

Y. Ding, G. Goussetis, R. Correia, **R. Lihakanga**, N. B. Carvalho and P. Petridis, "Enabling Multicarrier Backscattering Communications," 2020 IEEE MTT-S International Wireless Symposium (IWS), 2020, pp. 1-3, <https://doi:10.1109/IWS49314.2020.9360029> (Conference Paper)

Lihakanga, R.; Ding, Y.; Medero, G.M.; Chapman, S.; Goussetis, G. A High-Resolution Open Source Platform for Building Envelope Thermal Performance Assessment Using a Wireless Sensor Network. *Sensors* **2020**, 20, 1755. <https://doi.org/10.3390/s20061755> (Journal Article).

Chapter One

Background and Motivation

1 Introduction

This section presents the foundation of the research. It presents the background information and justification of the research, research aim, objectives, and research methods.

1.1 Background Information

Interest in real-time monitoring of the properties of building materials, as well as building structures, has increased in recent years. This is due to the need to observe and analyse the quality of building materials at each stage of their design and manufacturing. Also, by monitoring building structures and building characteristics, the impact of buildings on personal wellbeing can be assessed.

In this thesis, the development of a generic monitoring system to be used in a sample building (demonstration building) being built from a novel sustainable building material is elaborated. Demonstration building will help to show how the potential designed system is installed and operated. The project presents a unique opportunity to develop a novel monitoring platform to assist in the development of the next generation of building materials for the construction industry in Scotland and worldwide. Monitoring will focus on the current smart and fit (wellness) building to dynamically sense a variety of building characteristics, as well as develop a monitoring system that can be applied to further understand built environment interactions with people and assess the impact of a building on people's wellbeing.

1.2 Motivation

Currently, up to 85% of the bricks used in Scotland are imported from England or Europe, which is unsustainable in the long term. Recently, some research has focused on improving the brick to make it more environmentally friendly. The K-Briq, for instance, has been developed by Kenoteq as a more sustainable building brick that is unfired and made of 90% construction waste. The K-Briq looks like a normal brick, weighs the same, and behaves like clay brick, but offers better insulation properties. Invented by the

research group led by Professor Gabriela Medero at Heriot-Watt University, the K-Briq produces less than a tenth of the carbon emissions in its manufacture than regular brick[4][5][6].

Existing testing methods for building materials before deployment include a series of procedures as stipulated in BS, and most tests are performed in a controlled laboratory environment. The types of equipment that are used for measurements, data logging, and visualisation are commonly bulky, hard-wired, and consume a significant amount of power. Most of the commercial off-the-shelf (COTS) sensing nodes have been designed for a few specific applications and cannot be used for general purpose applications. This makes it difficult to modify or extend the sensing features when needed.

Numerous projects have been conducted to monitor the various building and environmental parameters. For example, thermal performance measurement has been used in different studies to predict energy consumption and analyse how building structures are affected by variations in temperature and humidity [7]–[11]. Temperature and humidity were measured in [12]–[14], as the inputs in predicting the level of human thermal comfort within the building. Different gases were measured in [15]–[18] to analyse indoor air quality.

To the best of the author's knowledge, there have been no projects implemented to monitor the property variation of building materials with the environment and the impact of this on indoor environment quality. The work presented in this thesis takes the initiative of building a generic wireless sensing network (GWSN) that can continuously monitor the building materials and building environment.

Therefore, the planned research will address the current challenges by developing a novel monitoring platform that will be used:

- a) To assess how building materials vary when interacting with the environment in real-time.
- b) To assess the impact of the building on the indoor environment.
- c) To design and characterise new low-power, low-cost sensing platforms.

This thesis elaborates on the design and implementation of a power-efficient wireless sensor network that will collect all sensing data from a demonstration building and enable remote monitoring and analysis.

1.3 Objectives

The project aims to develop a generic wireless sensing system that will assess how building materials interact with the environment and assess the impact of a building on indoor environment quality.

To achieve this, the following specific objectives were targeted:

- a) To study the state-of-the-art systems as benchmarks to understand the interactions between buildings, environment, and occupants' wellbeing.
- b) To design and implement a generic wireless sensing system that collects data from multiple sensors.
- c) To conduct laboratory experiments on measurements of building material properties and indoor environment quality.
- d) To develop an application platform for visualising, monitoring, and assessing the impact of the environment on buildings, and the impact of the building on indoor environment quality.
- e) Undertake the research on radio frequency backscattering technology to see how power consumption in the GWSN can be reduced using passive RF backscattering sensing mechanism.

The most significant parameters to be monitored in this project are summarised in Table 1.1 and 1.2.

Table 1.1. Building Structure Monitoring

Area of analysis	Related parameters
Thermal properties a) Thermal transmittance -U-value($\text{W}/\text{m}^2\text{K}$) b) Thermal resistance R-value ($\text{m}^2\text{K}/\text{W}$) c) Thermal conductance- Λ -value- ($\text{W}/(\text{m}^2\text{K})$)	Material related: a) Heat flux through the material (W/m^2) b) The surface temperature of both sides of the material under test (MUT) ($^{\circ}\text{C}$) c) Air temperature on both sides of the MUT ($^{\circ}\text{C}$).
Hygrothermal properties	Humidity/moisture buffering (%)

Table 1.2. Indoor Environment Quality Monitoring

Area of analysis	Related parameters
Human comfort (Indoor thermal comfort)	a) Ambient temperature (°C) b) Relative humidity (%)
Human health (Indoor air quality (IAQ))	a) Carbon dioxide (ppm) b) Volatile organic compound-VOCs (ppm) c) Particulate matter-PM 2.5 ($\mu\text{g}/\text{m}^3$)
Airborne sound insulation	Sound/Acoustic level (dB)

1.4 Overview of the Proposed System: A GWSN for Real-Time Online Monitoring of New Generation of Building Materials

To develop a GWSN system, various hardware, software, and interfaces have been designed. Figure 1.1 illustrates the overall system architecture and interfaces developed. The system is comprised of several wireless sensor nodes deployed in the building to measure various parameters, as shown in Tables 1.1 and 1.2. Each sensor node consists of sensors, signal conditioning circuits, microcontrollers, wireless communication modules, and a power supply unit.

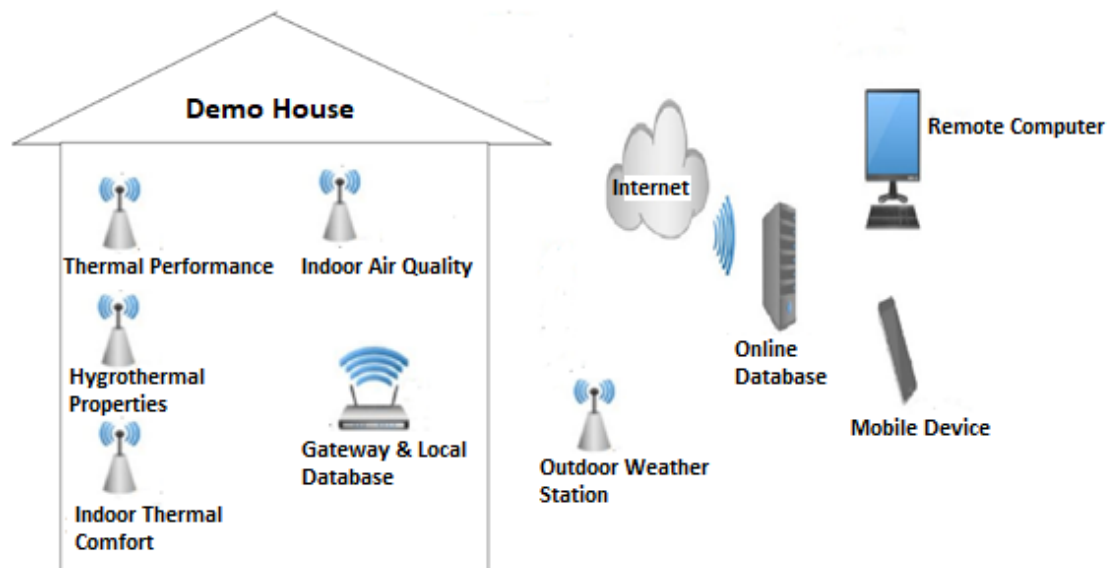


Figure 1.1. Diagram showing the architecture of the proposed system with the parameters to be measured, means of communication and access method.

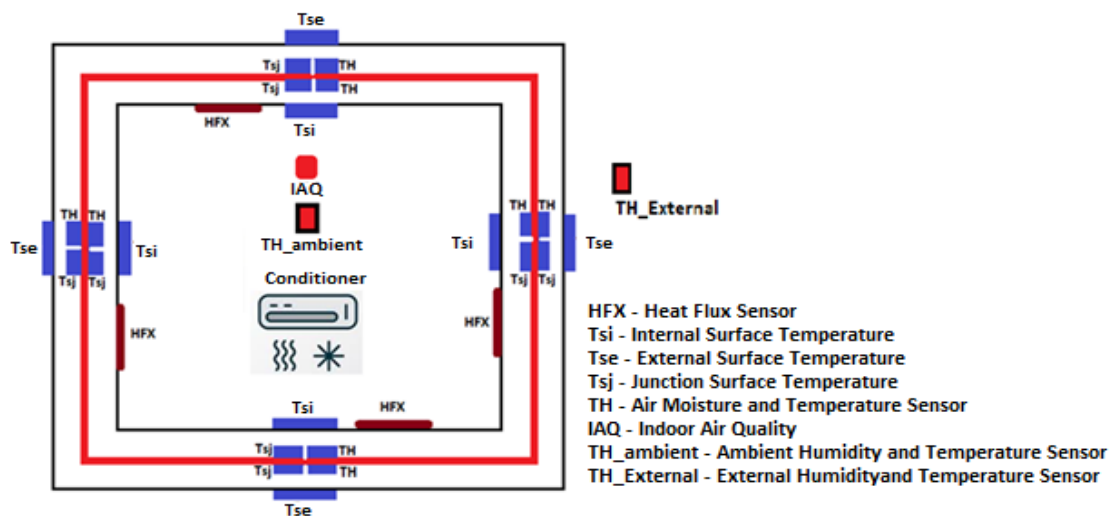
Sensor nodes send the collected sensing data to the gateway. The gateway is used as a coordinator by connecting all sensor nodes, pre-processing the data, and storing it. The gateway will then pass the information to the cloud server through the internet. The stored information and real-time information can be streamed in real-time or downloaded using computers or any other mobile device.

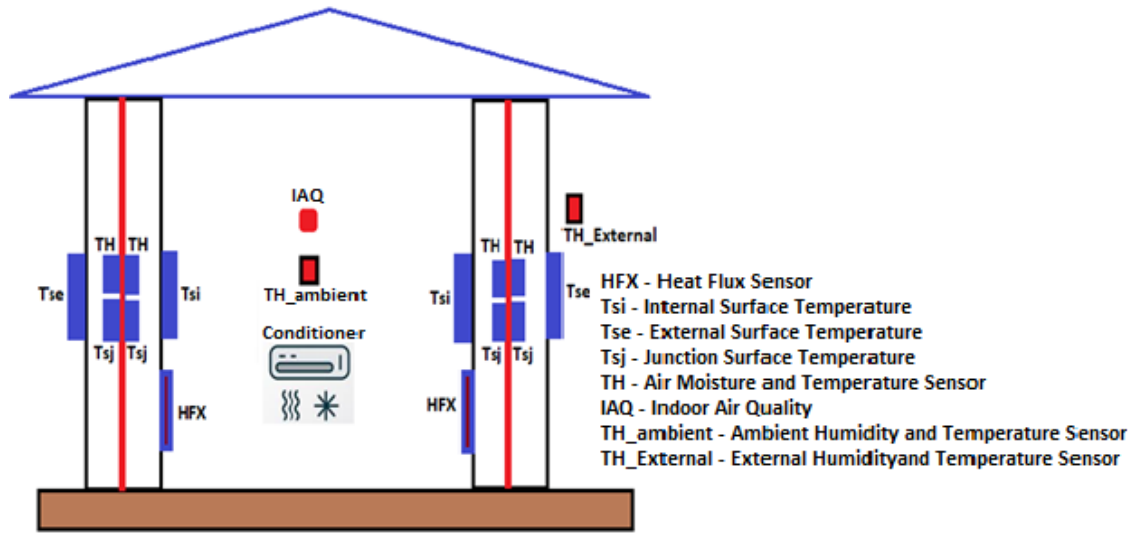
1.5 Demonstration structure

The initial plan of the research was to use the demo building structure that was to be built at Construction Scotland Innovation Centre (CSIC) as the case study for the research. The plan was to install the designed wireless platform and collect the data from the demo structure. So, for the proof of concept of designed system, data were supposed to be collected from the demo structure. But due the pandemic, the demo-structure construction was delayed. To handle the delays, the action was taken to build a smaller scale demo-structure in Figure 1.2 in the lab at EGIS. The system re-designed to accommodate the adjustment in measurements to make sure all necessary measurements are accommodated.

1.6 Research Methodology

The first part of the research focused on the design and implementation of the system to extract, process, store and visualise data from building materials and the building environment. The sensors and sensor mapping were selected based on the literature and requirements of the project. For the proof of concept and experimental studies, several measurement strategies were designed using sensor mapping (as shown in Figure 1.2(a) and Figure 1.2(b)), to demonstrate, evaluate and validate the effectiveness of the system.





(b)

Figure 1.2. Diagram showing sensor mapping for selected measurements points with sensors installed on the surface and other sensors embedded within the structure (a) Plan view (b) Side view.

A laboratory experiment on the thermal transmission of a building material was carried out for seven days. A glass window with known thermal transmission values was used for testing. In order to measure the outdoor temperatures and the temperature of the glass surface outside the window, one wireless node was placed outside the window. Another wireless node was placed inside to measure heat flow within the structure, air temperature, and surface temperature of the structure under test. The data was collected every five minutes for seven days. Thermal transmittance, thermal resistance, and thermal conductivity were calculated on three consecutive days to validate the designed system, as recommended in the British Standards[19]. The same setup was used for thermal comfort and hygrothermal measurements.

An acoustic measurement was carried out in the reverberant chamber. This removes the influence that positioning, or reverberation of the surface can have on sound pressure level readings. During the measurements, the GWSN and a standard sound level meter (SLM) were placed on one side of the reverberant, while the sound source was placed in the other corner of the reverberant room. The sound source was adjusted to produce different sound pressure levels. The sound level in decibels (dB) was recorded using a standard SLM, while the analogue to digital converted (ADC) values were recorded from the GWSN. The collected analogue data was used in a linear regression model to predict the level of acoustic in dB [20].

For IAQ the results from the carbon dioxide sensor and dust sensor were compared to a commercially available IAQ measurement system. For VOCs, the sensitivity characteristics curve of the TGS2602 sensor was used to estimate the values of various volatile organic compounds. After the characterisation using the logarithmic model, the measurements from the TGS2602 sensor were compared to those of a commercially available IAQ measurement system[21][22].

In the second part of the research, theoretical analysis and simulation validation of the new sensing technique (based on backscatter communication) was performed. A novel multicarrier backscatter tag compatible with WiFi was implemented, and novel harmonic suppression approaches for frequency-shifted backscatter communication were proposed and demonstrated. The applicability of these proposed harmonic suppression approaches was demonstrated by an exemplar backscatter network consisting of multiple nodes performing binary frequency-shifted keying (2FSK) modulated backscatter communications simultaneously[23].

1.7 Research Claims

Comprehensive research was covered and documented. The novel work includes:

For part one of the research:

- a) Design and implementation of a low-powered, open-source, flexible, and small-sized GWSN that can continuously monitor the building materials and building environment, to address the limitations of the conventional measurement methods and the technological gap stated in the previous studies. The GWSN can be used for in-lab and in-situ applications to measure and analyse the thermal physical properties of building materials/building structures. The system can also measure IAQ thermal comfort, and airborne sound insulation of the building envelope.
- b) Creation of:
 - New firmware to collect the data, process it and store it in the local database.
 - A novel logarithmic model that uses the sensitivity characteristics curve of TGS2602 to estimate the values of various VOCs.
 - A novel linear regression model that uses raw acoustic data to predict the acoustic dB levels.

One of the key contributions of part one of the research was the development of a generic wireless sensing system that solves the challenges of the existing measurement methods and allows the study of the change in building materials with the environment as well as the effect of change in building materials on the indoor environment quality.

For part two of the research:

- a) New sensing platforms using backscatter technology have been introduced. The theory of modulation and spread spectrum technique used in backscattering has been explored. The trade-off between hardware complexity/power consumption and link performance has been investigated.
- b) A novel multicarrier backscatter tag compatible with WiFi has been implemented. No dedicated reader is required. The existing WiFi infrastructure can be used directly as the receiver of the signal.
- c) A comprehensive study of the harmonics generated by a frequency-shifted backscatter communication system has been carried out, and a novel harmonic suppression approach is proposed and demonstrated.

1.8 Thesis Outline

The thesis begins with an introduction in **Chapter One** that gives the background of the thesis, sets out the benchmark for the research, and establishes the objectives of the study. The context of the research is further developed in the literature review (**Chapter Two**), which describes the state-of-the-art on the variation of building materials with the environment and the impact of variation of building materials on the indoor environment quality and defines the knowledge gap which this research seeks to fill.

Chapter Three describes the design and implementation of the custom sensor nodes and gateway of the wireless sensor network and firmware for data extraction, data processing, and data storage. It explains the different types of sensors selected for the application and the reasons for selecting them.

Chapter Four gives detailed information of the facilities, testing methods, and equipment that was used, explaining how and where the work was carried out, and the experiments which were carried out, essentially explaining what was done and why. It also presents and discusses the results of the measurements.

Chapter Five introduces new sensing platforms using backscatter technology. The theory of modulation and spread spectrum technique used in backscattering is explored. The trade-off between hardware complexity/power consumption and link performance is investigated.

In **Chapter Six**, a novel multicarrier backscatter tag compatible with WiFi is implemented. No dedicated tag reader is required for intercepting the incoming backscattered signal. The existing WiFi infrastructure is used directly as the receiver of the signal. A comprehensive study of the harmonics generated by a frequency-shifted backscatter communication system is carried out, and a novel harmonic suppression approach is proposed and demonstrated.

In **Chapter Seven**, conclusions from the results are discussed, the contributions presented, and recommendations for future work are made.

Chapter Two

Literature Review

2 Introduction

The chapter discusses background information on building materials measurements and how variations in building materials affect indoor environment quality. A description of the existing methods and types of equipment used for building material measurements, data logging, and visualisation is provided, as well as commercially available wireless technologies. The chapter concludes by defining the knowledge gap this research seeks to fill.

2.1 Building Material Properties

Building or construction materials are some of the most important requirements in the construction industry. There are several materials used for different purposes and construction tasks. For materials to be considered and used for certain construction tasks, they must be proved to have certain engineering properties. These properties will determine the quality and capacity of the material and will help determine the suitability of the material for certain construction work. The building materials are classified as per the following properties[24]:

- a) Physical properties,
- b) Mechanical properties,
- c) Chemical properties,
- d) Electrical properties,
- e) Thermal properties.

2.1.1 Physical Properties

The physical properties of building materials are those properties which determine the quality and condition of materials without considering the influence of external forces. The physical properties are classified as: porosity, bulky density, durability, density, fire resistance, water absorption, and water permeability[24].

2.1.2 Mechanical Properties

Mechanical properties of building materials are properties that determine how materials behave under the influence of external forces. They assist in assessing the behaviour of the materials and grading them accordingly. The properties are classified as: plasticity, fatigue, elasticity, hardness, strength, and brittleness[24].

2.1.3 Chemical Properties

Chemical properties of building materials reflect how the materials react to different chemicals. The properties can be classified as: chemical resistance and corrosion resistance[24].

2.1.4 Electrical Properties

The electrical properties of building materials are the properties that determine the ability of the materials to resist the flow of electricity through them[24].

2.1.5 Thermal Properties

Thermal properties of building materials are properties that determine the ability of the materials to resist/ allow or absorb heat flow through them. They can be classified as thermal conductivity, thermal resistivity, thermal capacity, and thermal transmittance. These properties will determine how quickly outdoor climate change can influence the indoor environment quality[24].

By understanding the thermal physical properties of materials, the following indoor environment quality parameters can be analysed:

- a) The effect of material thermal insulation on indoor climate variation.
- b) The effect of air temperature on indoor humidity.
- c) The effect of air temperature on air quality.
- d) The effect of humidity on air quality.

2.2 The Effect of Building Material Properties on Indoor Environment Quality Variation

Indoor environment quality refers to the interior environment conditions that relate directly to the health and wellbeing of the occupants[25][26]. Indoor environment quality can be classified by measuring thermal comfort (humidity, air temperature, radiation temperature), IAQ (carbon dioxide, VOCs and PM 2.5), light level, and acoustic levels[27][28]. The material used for the construction of the building envelope has an impact on how quickly changes in weather conditions are felt. As external weather changes, the indoor weather will also change[29]. Building material thermal insulation has a direct effect on the indoor environment weather. As the outdoor air temperature varies, the indoor air temperature will also vary. The time taken for the temperature change to be noticed depends on the quality and properties of the material used for construction.

When the outdoor humidity varies, the indoor humidity will also vary. The time taken for the changes to be felt depends on the quality and properties of the building materials used. By proper selection of building materials, the quality of the indoor environment can be controlled by regulating the influence of outdoor humidity and temperature on the indoor variations[29]. When air temperatures approach dew point, there is high relative humidity in the air. In response to an increase in air temperature, water molecules become more concentrated, decreasing relative humidity. Relative humidity increases as temperatures drop. Cold air moves more slowly than warm air and it has greater density than warm air. Air with low density caused by the cold traps pollution more easily than warm air[30]. Most bacteria and viruses that cause respiratory infections survive in high and low humidity. Dust mites, mould spores, and other allergens also survive in a high humidity environment. High humidity increases the levels of noxious gases such as ozone and formaldehyde[31][32].

The physical properties of the material determine the amount of sound which can be reflected and absorbed. As the sound/noise hits the surface of the building materials, a portion of sound will be reflected, and some will be absorbed. Acoustic or sound insulation is one of the important parameters when designing building materials. This is because of the importance of controlling and limiting the amount of noise, for the benefit and wellbeing of people in homes, offices, and schools. For the material experts to optimise building materials and structures, standard measurements such as impact sound

and airborne sound insulation have been established[19]. The sound reduction index (SRI) is a measure of the reduction in the intensity of sound when it passes through part of a building; in other words, the level of sound insulation provided.

2.3 Building Monitoring

2.3.1 Introduction

This section of the literature review introduces current and past research on the measurement and monitoring of building and environmental parameters. As per the scope of this research, the first part of this literature focuses on: thermal performance, hygrothermal performance, and indoor environment quality (IAQ and indoor thermal comfort) of the buildings.

As mentioned earlier, numerous research studies and projects have been implemented as the means of monitoring various building and environmental parameters as separate research.

Thermal performance measurement has been used in different studies to predict energy consumption and analyse how building structures are affected by variations in temperature and humidity [7]–[11]. Temperature and humidity were measured in [12]–[14], as the inputs in predicting the level of human thermal comfort within the building. Different gases were measured in [15]–[18], as the inputs in analysing IAQ.

2.3.2 Sensors in Building structure monitoring

To have a stable and reliable system for monitoring, inspection and damage detection of masonry structure a proper set of sensors has to be selected. For the proper selection of sensors, different properties and behaviours of materials and structure need to be analysed. By identifying how materials and building react in different types of defects and damage, appropriate sensor can be identified. For the sensor to operate in a specific application, the following parameters has be considered[33];

- a) Power consumption.
- b) Cost of the sensor.
- c) Installation restriction.
- d) Portability of the system.
- e) Spatial resolution.

- f) Speed and accuracy.
- g) Sensitivity.

Sensor such as fibre optic sensor, piezoelectric sensors, strain gauges, linear variable differential transformer, magnetostrictive sensors and self-diagnosing fibre reinforced structure composite has been proved to be capable of sensing various physical and chemical parameters that can be direct related the health of materials and structure[34]. Other sensing technologies are MEMS, RFID sensors, ground penetrating radar, imaging, laser, acoustic emission and imagery[33].

2.3.2.1 Fibre Optic Sensors (FOSs)

Fibre optic systems uses pulses of light to transmit information from one place to another. Fibre optic sensor uses fibre optic cable as sensing element. Sensors can be surface mounted on existing building or embedded within the new buildings. Pulses of light within fibre cable can be varied by different external parameters, so by comparing pulses before variation and pulses after variation, different physical and chemical parameters related to health of a structure can be analysed[34][33].

Different methods used in classifying fibre optic sensors. First method is by considering how light characteristics modified by parameter to be sensed. Characteristics are intensity, wavelength, phase, polarization etc. Second method is by considering sensor location. When sensing occur within the fibre, is classified as intrinsic sensor and when sensing is outside of the fibre, is classified as extrinsic sensor. Third method is by considering the sensing range of the sensor. Fabri-perot or long range fibre optic sensor (local), fibre Bragg grating (quasi distribution) and Brillouin-scattering based distributed fibre optic sensor (distributed sensor) are on this class of sensors[34].

Fibre optic sensor is used in structural health monitoring to measure strain (both static and dynamic), temperature, defects (corrosion, delamination and cracks) and chemical concentration (chloride concentration etc.). The information extracted is used to evaluate the health of civil structure.

To justify the practicality of fibre optic sensors, Newhook et al.[35], introduces sensor in civil structure. The system implemented to monitor the Hall Warf program. The system was subjected to a varying temperature of between -35 °C to +35 °C. After one year of monitoring, 10 out 17 sensors fail to operate. The observation show that failure was

because of manufacturing flaw on sensors, salt crystals and some dirty particles in sensor connections.

Fibre optic sensors installed in Stafford medical building of Vermont University. According to Fuhr et al.[36], sensor was embedded to measure stresses during construction, curing of concrete and sensing of internal cracks.

Brinoulli-based distributed fibre optic sensor used in measuring temperature distribution in a building structure. Temperature was changing up to 4°C per day[37].

Fibre optic sensors used in corrosion detection. Fuhr et al.[38], uses a colour from a corroding rebar to modulate the light in a fibre optic sensor. Spectra and wavelength variation was recorded and compared. The observation shows that fibre optic sensors can be used to detect corrosion.

Constantine et al.[39], uses fibre optic sensor in detecting concentration of chloride. Chemical reaction between optical chloride sensors made up of Ag_2CrO_4 and chloride produces a colour change from reddish brown to white AgCl . Light intensity changes recorded and used to determine the concentration of chlorine.

Some of the advantages of fibre optic sensors are:

- a) Compact and lightweight.
- b) Ease installation.
- c) Low installation and maintenance cost.
- d) Long-time monitoring capability.
- e) They are durable and corrosion free.
- f) Insensitive to external disturbance (EMI etc.).
- g) It is possible to divide system into point and distributed sensing.
- h) Good sensitivity and resolution

Despite of all these advantages, fibre optic sensors have the following disadvantages

- a) Signal decoding is required.
- b) Can break in large deformation.
- c) No communication after breakpoint.

2.3.2.2 Conclusion

Fibre optic sensors has proved to have the sensing capability in laboratory experiment as well as on site testing. FOS can measure strain, displacement, vibration, cracks, corrosion and chloride concentration. In addition, fibre optic sensor has proved to be applicable in harsh environments. The only limitation is their fragility in some applications and difficulty in coupling and decoding signals. Unless otherwise FOS is the best choice for structure health monitoring (SHM) applications.

2.3.2.3 Piezo Electric Sensors

Piezo electric sensor is an electroacoustic transducer used for conversion of pressure or mechanical stress in alternating electric force. It used to measure physical quantities such as force, pressure, stress etc. Piezo converts physical quantity into voltage. Piezo materials can be in different types, piezo electric ceramics, piezo electric polymers etc. In structural health monitoring, piezo electric sensors used as sensing mechanism-based measurement of elastic wave and impedance.

As a small deformation produced to a PZT patch attached to a structure driven by a fixed alternating electric field. Mechanical vibration near the sensor transferred to PZT. When crack or any other physical defect produces variation in mechanical dynamic response, the effect will influence variation in electrical impedance of the PZT. Therefore, damage can be indirectly detected and monitored by measuring the variation of electrical impedance of PZT[34].

Impedance-based structural health monitoring was carried out by Soh et al.[40], where by PZT patches attached in a prototype reinforced concrete. Eleven (11) PZT patches instrumented in selected points. During loading process, patches scanned to extract information on impedance variation. Observation reveals that, PZT patches was very sensitive when there was any damage close the respective patch.

In Lim et al.[41], other structural parameters like stiff, mass and damper identified using admittance signature measured. The method uses parameter identified to characterise the damage and the method successfully used in damage detection in truss, beams and concrete cubes.

In Song et al.[42], a waterproof PZT patches was embedded within the concrete specimen. A time history and location information were extracted from sensor-history damage index

and actuator-sensor damage index matrix. The method used to monitor strength in early concrete and impact on structure.

Zhao et al.[43], uses PZT in monitoring cracks in reinforced concrete beam. Different central frequency elastic waves extracted from damage index used to express the initiation and development of cracks in reinforced concrete.

Some of the advantages of piezo electric sensors are:

- a) Simple to use
- b) High frequency response.
- c) Available in different shapes and sizes.

Despite of all these advantages, piezo electric sensors have the following disadvantages

- a) Affected by humidity variation.
- b) Not suitable in static conditions.
- c) Affected by temperature variation.

2.3.2.4 Conclusion

Piezo sensor used in sensing disturbance close to the sensor vicinity is applicable in environment with known location of damage or defect. When using PZT, it becomes difficult to differentiate different type of damage since all effects produces changes in impedance. Expensive analysers needed to make PZT more efficient and reliable especially when deployed in large scale.

2.3.2.5 Radio Frequency Identification (RFID) Sensors

RFID is a technology that uses electromagnetic waves as means of identifying and tracking tags. RFID devices are classified as active or passive devices; Active RFID require power supply for its operation while passive RFID device do not require any power supply. RFID reader power passive tag during communication[44]. Due to its capability in sensing and communicating wirelessly using unique identity, RFID sensors has been developed and adopted in structural health monitoring[45][46]. In sensing application, RFID uses antenna as sensing mechanism. Whenever sensor experience changes in a physical parameter, its shape will vary accordingly causing shift in electromagnetic frequency resonance of the antenna[47].

For crack detection, Kalansuriya et al.[48], reported on development of an RFID tag antenna for sensing pervasive surface cracks. Sensor designed and tested. Laboratory results shows that, sensor was more accurate in detecting straight cracks but less accurate in angular cracks. Antenna sensor completely detuned to extent of losing communication with the RFID reader. Test performed only on limited samples.

Caizone et al.[49], designed a passive wireless RFID sensor for crack width measurement. The design tested in simulation and on laboratory experiment. The sensor was able to measure crack width successfully with minimum communication degradation. Sensing and measurement on the design depends on distance between tags and reader so the system supports fixed measurements only.

Adi et al.[50], presented a one chip-less RFID sensor for monitoring on a metallic objects. Different results recorded during simulations and laboratory experiment. The results shows that the system is usable but with limited tag readability and properties of materials was affecting the selectivity and reliability of the sensor. In addition, Chip RFID suffers from interference.

Asim et al.[51], reported on measuring humidity using RFID tag sensor. The system designed and tested in weather-controlled environment and accuracy of the tag compared to standard readings. The accuracy was ± 1 %, sensitivity was high and power consumption was low.

Emran et al.[52], presented a novel low cost chip-less RFID sensor. The designed sensor used to measure humidity while providing the identification of the location. Sensor validation experiment performed using Miller Nelson temperature and humidity controller. The results from recorded information show that, different levels of humidity produce different values of transmission coefficient. Sensor was highly sensitive. It is applicable in real time sensing and monitoring of humidity.

Yi et al.[53], developed passive RFID sensor to measure strain and crack of a structure. Folded patch dipole antenna was designed and simulated. During testing, antenna resonance frequency varies for each variation in strain. The information recorded and used to validate the response of the sensor. Experiment performed to determine the relationship between change dielectric constant and strain. The frequency was analysed and used to obtain levels of strain.

Geetha et al.[54], developed reusable passive RFID sensor for measuring strain. The design was tested on aluminium tensile specimen. The results show that the sensor deformation did not occur during tensile loading. Sensor reuse was possible, unlike other RFID sensors.

Occhiuzzi et al.[55], reported a design of passive UHF RFID sensor for strain monitoring with the objective of achieving desired resolution and dynamic range. Sensor was fabricated and tested the results shows that, tag deformed below the yield point and recover its original shape when applied stress was removed. Numerical and experimental analysis shows that the approach is valuable for future generation of passive RFID sensors.

Emidio et al.[56], proposed wireless technique for measuring strain. The approach utilises a traditional strain gauge and Wheatstone bridge. Sensing mechanism was switched ON and OFF by wireless signal. The calibration done by applying a controlled force up to 10 kN. The interrogation, linearity, sensitivity and accuracy were the same as of wired strain gauge.

Abdul et al,[57], presented on heat sensing mechanism using passive RFID tag sensor. In their approach, paraffin wax used as the heat sensing area. A narrowband tag detects physical change in substrate material. Change in properties of the substrate create a shifting in the operating frequency of the tag. The sensor was tested successfully. Since the process is irreversible, sensor can be used only once.

Jose et al.[58], presented on passive electromagnetic temperature sensor. Sensor response measured at different levels of temperature. Sensor output response agree with the simulation results. The integrity of the sensor was the same before and after heating and the difference between measured and expected value was 0.36 %.

Some advantages of RFID sensors include:

- a) Flexible and small size- embedded easily within the measured structure.
- b) Less expensive-can be fabricated using cheap materials available.
- c) Battery free- sensor can harvest power from nearby sources of electromagnetic waves.
- d) Multi-sensing- It can sense various physical, mechanical and chemical properties.
- e) Used for both sensing and communication.

- f) Ease multiplexing- sensors linked easily because each contains unique identity (UI).
- g) Embedded within materials which microwave penetrate.

Despite of all these advantages, RFID sensors possess the following disadvantage

- a) Limited range up to few metres.
- b) Limited storage since each memory require source of power to work.
- c) Require high power reader to for excitation.

Conclusion

Despite of having more advantages than disadvantages, more study in technology is required in order to bring idea into practice. New methodologies and implementation techniques are required for the system to be reliable and adaptable in in various applications. Solving existing challenges, RFID sensors will become a technical solution for the future structural health monitoring applications.

2.3.2.6 MEMS sensors

MEMS (Micro-Electro-Mechanical-Systems) is the technology that integrates mechanical elements, sensors, actuators and electronics within a single silicon chip. Functional elements within MEMS are miniaturised structure, sensors, actuators and Microelectronics. Micro-sensors gather environment information (mechanical, thermal, biological, or chemical) and pass to the microelectronics section. Microelectronics receives the signals from sensors, process and make the required decision. Micro-actuators used for external triggering when receives commands from microelectronics section. Due to their sensing capability and dimension, MEMS sensor was adopted in structural health monitoring in detecting and monitoring various damage and defects.[59][60][61].

Torfs et al.[62], presented a low power wireless sensing network to monitor a building and assess its damage after earthquake. MEMS strain sensor mounted at the base of the building to measure its settlement after earthquake. The readings collected periodically or as per demand from base station. MEMS accelerometers mounted on each floor to measure seismic response of the building during earthquake. Laboratory validation performed by creating a controllable earthquake in a laboratory environment. Sensitivity and linearity of MEMS sensor was recorded and analysed. The response was linear. Using

selected architecture, the implemented system offers long battery life and low cost in installation and maintenance.

Tan et al.[61], presented a low cost structural health monitoring using MEMS sensors. Accelerometers assembled with DSPIC microcontroller for processing. The primary results in simulations were analysed and used for testing the practicality of the system in real environment.

Ahmed et al.[63], proposed a MEMS sensors for monitoring force and pressure in structural health monitoring. Sensor designed and tested. Results obtained from preliminary measurement shows that, more investigation in bending effects of substrates as well as reliability of material used is required.

Caimmi et al.[64], adopted surface mounted MEMS accelerometers as sensing elements in structural health monitoring. Mechanical models of specimen built in order to find correlation between real crack length and acceleration output from MEMS sensors. Structural information from MEMS sensor was proportional to delamination size. More investigation proposed especially in deploying network of sensors over the sample or a structure, powering and on synchronization of the sensor output.

Azeem et al.[65], presented the design and simulation of MOEMS mechanical sensor in structural health monitoring. The sensor designed and simulated for validation. The strain in micron range sensed and recorded successfully. Using MEMS sensor together with photonic crystal sensing technology improves the sensitivity and stability of sensing mechanism.

Sindhuja et al.[66], introduces a wireless method of transmitting seismic harm. MEMS based sensor used as sensing mechanism for strain and acceleration. The system implemented and tested. The information collected from sensor used to analyse building conditions. The system and selected sensor prove to be a good choice for monitoring health of the selected structure.

MEMS accelerometers was also used by Buttarrazi et al.[67], Sabato et al.[68], Radaideh et al.[69], and Kruger et al.[59], in sensing and monitoring of health in bridges. Sensor performance in terms sensitivity and reliability reported to be high in all applications.

2.3.2.7 Advantages of MEMS sensors

- Compact in size.
- Less expensive.
- Easily integrated with other circuits.
- High performance (speed).
- Low power consumption.

Disadvantages of MEMS sensors

- Silicon is brittle material.
- Complex design process.

Conclusion

As MEMS sensors can be fabricated in compact size, robust and low power consumption packages, it allows easily installation in different structures. Using suitable methodologies of data gathering and analysis, installed MEMS sensors can continuously monitor the health of the building structure to extract its structural performance and predict its durability over time.

2.3.3 Building Materials Thermal Performance Characterisation

The thermal performance of building materials is one of the important factors to be considered when attempting to understand how building materials interact with people and the environment. Thermal performance measures how materials respond to external temperature in a daily or seasonal cycle. Thermal performance defines the optimal thermal comfort of the occupants, as well as determining the total energy consumption of heating and cooling systems [7], [70]–[72]. Thermal performance has been used in new and existing buildings in energy auditing, efficiency evaluation, and consumption rating [70][71][72]. Thermal performance can also be used to determine breathability and real-time heat loss of the building materials.

By evaluating thermal transmittance (U-value), thermal resistance, thermal conductivity, and diffusivity of building materials, you can determine the thermal performance of the building. According to BS ISO 9869-1:2014 [73], measurements can be performed in a laboratory using formulated standards and specified testing tools.

For in-situ measurements, the heat flow meter method[73] has been adopted for thermal performance characterisation because it is practical, simple, lightweight, and low cost[74]. Using the heat flow meter method, the parameters that can be measured are: thermal resistance (R) from surface to surface, thermal conductivity (λ) from surface to surface, total thermal resistance (R_T), and thermal resistance from environment to environment. Figure 2.1, is the TRSYS01 heat flux measuring system recommended by standard ISO 9869 for heat flux measurements. Some of the technical specifications for this measuring system is summarised in Table 2.1.

Table 2.1. Specifications of TRSYS01 Heat flux measurement System.

Measurand	Heat flux, temperature
Required data analysis	to be performed by the user according to ISO and ASTM standard practices
Rated operating temperature HFP01 and Temperature sensors	-30 to +70 °C range
Adapter rated power supply	110-220 VAC, 50 / 60 Hz
Connectivity	Personal computer via USB and RS232
Number of measurement locations	2 (Can be increased on request)
Data storage capacity	>30days
Measurement duration range	>days

Additionally, thermal transmittance and thermal resistance can be evaluated in-situ using infrared (IR) thermography[75] and calculation method [76]. Described below are some widely used methods of evaluating thermal performance using in situ measurements (which are the focus of this thesis) as well as the advantages and disadvantages of each [3].

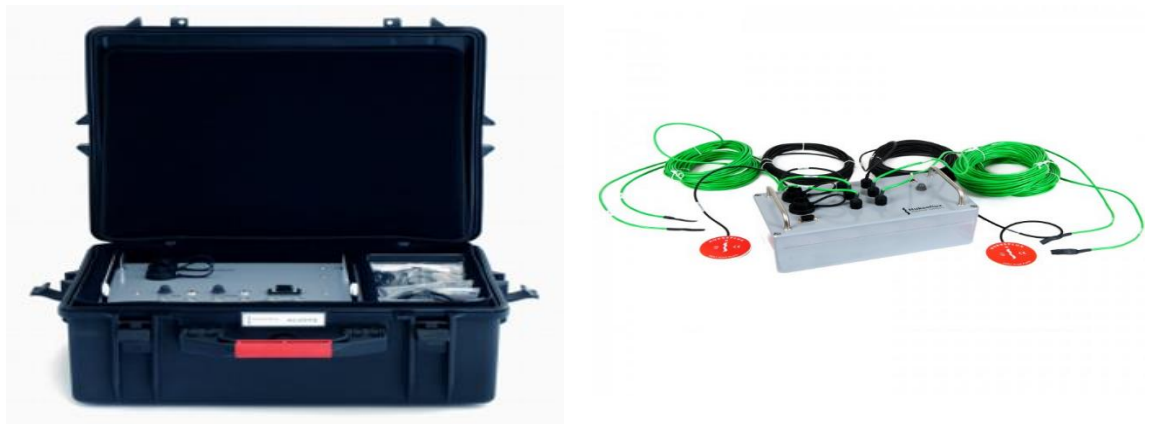


Figure 2.1. A picture of TRSYS01 heat flux measuring system with the carrying case of dimension 480 x 390 x 190 mm [77].

Figure 2.2 illustrates the heat flow method, as described in the standard ISO 9869[73], which has been utilized widely for measuring the thermal transmission properties of buildings that consist of homogeneous layers[3]. The properties that can be measured include:

- a) Thermal resistance and conductivity from surface to surface of both sides of the material.
- b) Thermal transmittance from environment to environment of both sides of the material.

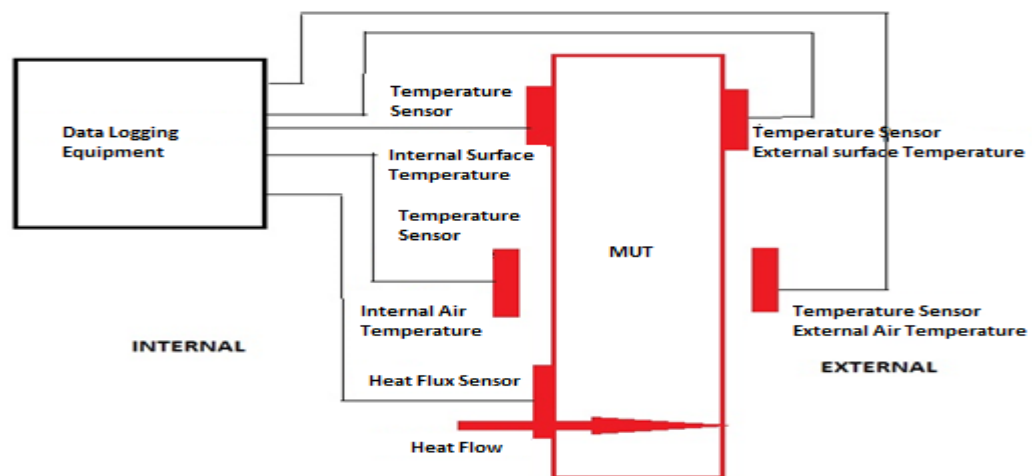


Figure 2.2. Measurement setup according to BS ISO 9869:2014 standard showing the location of temperature sensors and heat flux sensors on the MUT and physical connection of data logging equipment.

In order for this method to yield adequate thermal transmission estimations, the following factors (or assumptions) must be carefully examined[3][73]:

- a) It is important to maintain a constant heat transfer coefficient over the entire measurement area throughout the testing of the material under test.
- b) In contrast to the amount of heat passing through the materials, the heat stored in the materials is negligible.
- c) There is at least a 10°C difference between the temperature indoors and outdoors.
- d) Wind speed is less than 3m/s.
- e) Sunlight and moisture cannot directly reach the heat flow sensor.

Despite being able to meet the above requirements, the current measurement systems that utilize this method still pose the following limitations[3][78][79]:

- a) Since the collected data must be processed offline, the measurements are not continuous and not real-time. A measurement error cannot be detected and corrected during this process since there are no inconsistencies in measurement.
- b) Despite its size and power consumption, the equipment is heavy, hardwired, and bulky.

The calculation method, stipulated in ISO 6496 [76], specifies a method to calculate building material performances based on electrical analogy when the materials are assumed to be in steady-state conditions. With a given material's thickness and thermal conductivity, thermal transmittance can be approximated. These estimations, however, are not accurate due to the high uncertainty in material properties and the uncontrolled inconsistency between the lab and the field environment [3][76].

Non-destructive testing techniques such as infrared thermography are popular for building materials analysis. Thermal radiation is used to measure temperature. This produces images that display the detected IR energy of the target object. With the color-coded temperature distribution on the object, the material information and abnormalities on the object can be analysed. Measurement accuracy greatly depends on: the distance from the target object, the wind speed, atmospheric particles, and the ambient temperature[3][80][81]. Figure 2.3, shows the picture of the camera used in Infra-red thermography and sample of the image output from the camera.

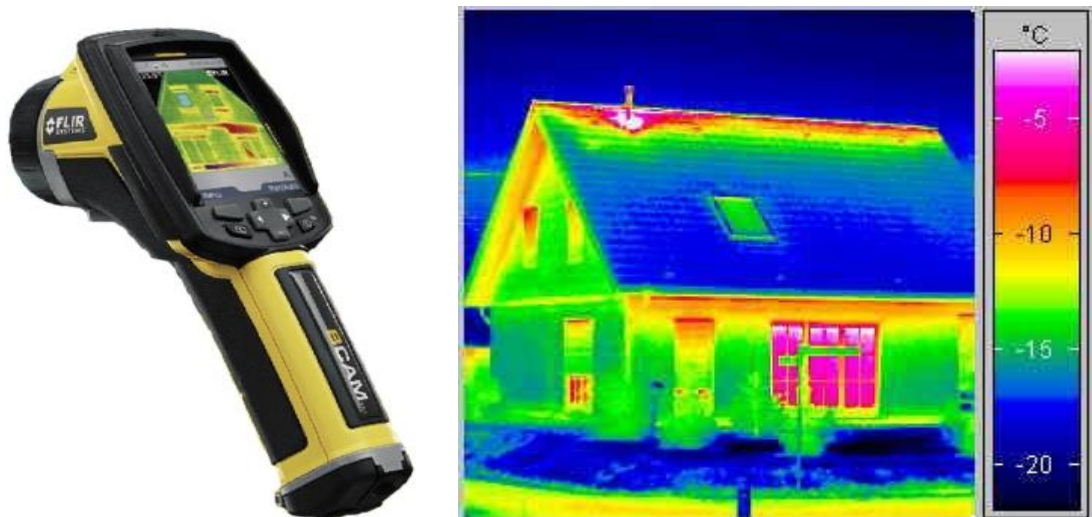


Figure 2.3. A picture of Infra-red thermography measurement methodology (a) Infra-red thermal camera (b)Image of the building under measurements showing thermal distribution on various part of the building [82].

Though the IR method achieves a tolerable level of accuracy, it still suffers from the following shortcomings:

- a) Image interpretation is usually challenging.
- b) Wind, solar radiation, and moisture need to be properly controlled to ensure that measurements are not impacted by external factors.
- c) Integration with other platforms is difficult.

Researchers have developed and used a three-temperature measurement methodology [78][79]. To evaluate the thermal performance of a material, three temperatures are measured (i.e., indoor surface temperature, indoor air temperature, and outdoor air temperature). This analysis is limited to the thermal transmittance measurement for energy efficiency evaluation only. Neither thermal conductivity nor thermal resistance have been measured using this method. Despite some promising results, the method is still at the research level and therefore cannot be used as a reference measurement. Prior to the adoption of this method, more research needs to be conducted to determine how thermal mass and homogeneity impact measurements[3].

Table 2.2, summarises the indications for dimensions, weight, power consumption and other features of the existing systems provided in the literature review and benchmark the novel generic wireless sensor system against the existing systems according to the proposed performance and operational metrics.

2.3.4 Building Materials Hygrothermal Properties

Moisture content and moisture movement are two of the important parameters for building materials. Moisture presence can influence chloride ions, mould growth, corrosion, frost damage, and degradation due to freeze and thaw cycles[83][84]. Most of the time, building material degradation occurs in the presence of water or moisture[85]. Without water, no chemical reaction will take place within the building material[86].

Initial water absorption can be used as an input in estimating material sensitivity to future deterioration[87]. Moisture formation can affect the performance of the building structure. Thermal energy loss can be reduced, and energy-saving can be achieved, if moisture is well controlled in building materials[88]. High moisture content can also create an uncomfortable indoor climate and can have a direct impact on the health of occupants[89].

Table 2.2. Comparison of the novel GWSN system against the existing systems according to the proposed performance and operational metrics.

System	TRSYS01 heat flux measuring system[77]	IR Thermography FLIR E5-Xt[90]	GWSN[3]	WiFi Backscatter[3]
Measurands	Heat flux, Surface Temperature, Air temperature	Thermal image	Heat flux, Surface temperature, Air temperature, Moisture, Humidity, VOC, PM2.5, Acoustic,	Heat flux, Surface temperature, Air temperature, Moisture, Humidity, VOC, PM2.5, Acoustic,
Connectivity	USB and RS-232	USB and WiFi	WiFi, BLE, USB	WiFi
Operating voltage	9.6 to 16 VDC	Battery is charged inside the camera	5 V	0.6 V
Number of measurement locations	2 locations	Random scanning	Unlimited	Unlimited
Required data analysis	To be performed by the user according to ISO and ASTM standard practices	Image captured must be interpreted by experts	Automated	Automated
Data storage capacity	>30 days	Depends on the memory card installed	Unlimited	Unlimited
Measurement duration	Days	When image is required	Unlimited	Unlimited
Dimension (with enclosure)	480 x 390 x 190 mm	244 × 95 × 140 mm	150 x 100 x 60 mm (with enclosure)	20 mm x 30 mm (Tag PCB)
Gross Weight	approx. 11 kg	Approx. 500 g (including battery)	Less than 1 Kg (sensor nodes, Gateway nodes, sensors)	Less than 50 g

Moisture can accumulate in the building material by condensation, capillary rise, rainwater infiltration, and water leakage (pipes and floods)[91][92], and migrate within the material through pores. Transport properties of the porous material cover zone determine its durability and performance[93].

Laboratory methods, tools, and procedures for measuring water absorption rates in building materials have been specified in BS EN 772-11[94]. For in-situ applications, various methods have been developed to make the assessment and evaluation of materials simple, non-destructive, less time-consuming, and cost-effective. Also, determination of the water transmission properties, hygroscopic sorption, and moisture adsorption/desorption of materials in response to humidity variation has been specified in BS EN 12571-2013[95] and BS EN 12572-2016[96].

Building materials resistivity measurement is a widely used approach for hygrothermal properties analysis. The testing procedures are considered to be simple and fast compared to other approaches. Several techniques have been developed for measuring the resistivity of building materials, especially concrete. In this section, surface measurements and bulk resistivity measurements are discussed.

2.3.5 Building Materials Electrical Resistivity Measurement Techniques

2.3.5.1 Wenner Technique (4-Point method)

One of the basic methods used for measuring porous material resistivity for in-situ applications is the Wenner technique, as shown in Figure 2.4. The technique was developed to be used in soil resistivity measurements, before being adopted for building materials evaluation.

In this technique, four equidistant electrodes are attached to the surface of the material to be evaluated. An electric current enters through the two outermost electrodes, and voltage variation is measured across the two inner electrodes. The resistivity for semi-infinite geometry can be determined by Equation (2.1):

$$Resistivity(\rho) = 2\pi a \frac{V}{I} \quad (2.1)$$

Whereby

ρ is resistivity in ohm-meter (Ωm),

a is the distance between the electrodes in metres (m).

V is the Potential difference in volts (v) and

I is the electric current in amperes (A).

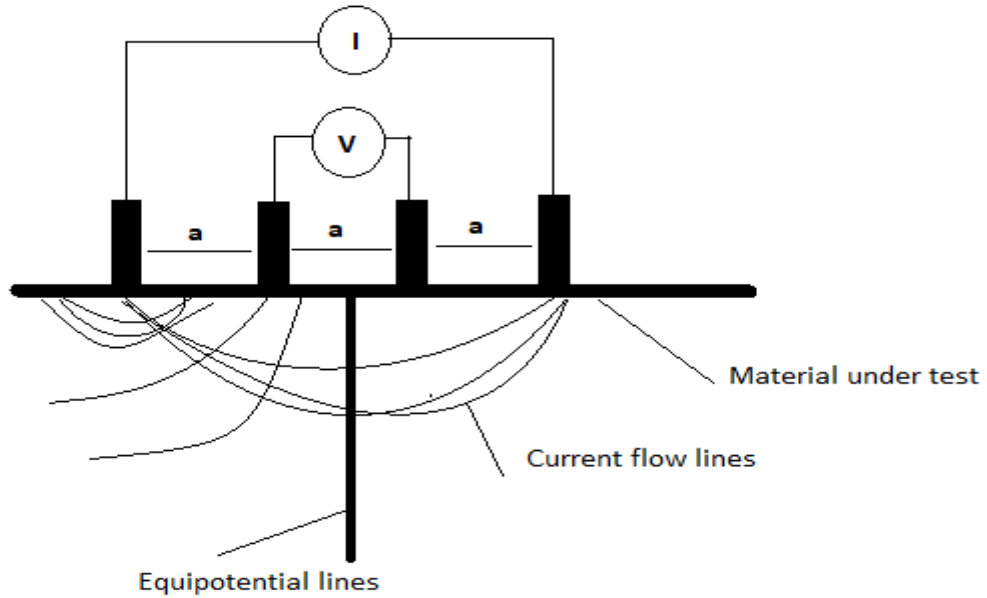


Figure 2.4. Diagram demonstrating Wenner technique (4-Point electrode method) showing sensor position on the measured sample, wiring of the measuring equipment and current flow within the sample [97].

The technique was adopted by Ramezaniapour et al.[98], in determining the relationship between concrete resistivity, water penetration, and rapid chloride penetration. According to the findings in[98], water penetration and chloride ion penetration are both directly correlated with electrical resistivity of concrete covers. Concrete permeability can be estimated based on this relationship.

Garzon et al.[99] used the four-point method for measuring concrete resistivity in the presence of reinforcing bars. The results showed that there was a modification in current distribution and potential drop.

McCarter et al.[93] came with the approach of embedding four electrodes within the concrete being measured. The results showed that, as resistivity increases, there was deviation because of boundary effects.

Lee et al.[100] studied the influence of environmental temperature and moisture on the resistance of conductive concrete. The measurement was performed using the four electrodes technique. The results showed that, at higher humidity and temperature, concrete showed little resistivity.

2.3.5.2 Two Point Electrode Method

Another method of measuring the electrical resistivity of porous materials (especially concrete) is by using the two electrodes method. In this method, as shown in Figure 2.5, a constant current is applied to the specimen, and voltage variation is measured. From the voltage variation resistivity can be determined.

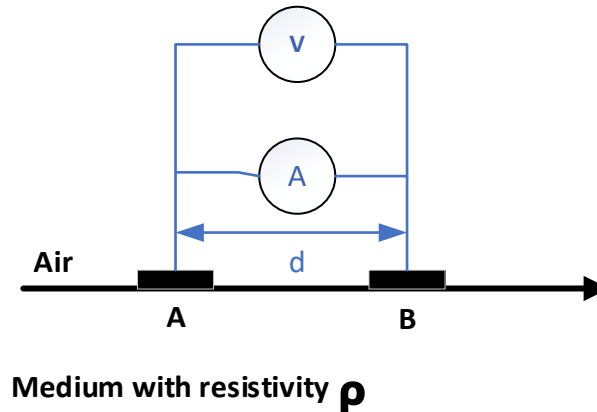


Figure 2.5. A diagram showing material resistivity measurement using the two-point method with sensor position and equipment interface [101].

Polder[102] used the 2-electrodes method in the characterisation of chloride transport in concrete, and the influence of drying and wetting. The results showed that the resistivity of concrete reflected its properties of resisting chloride penetration, corrosion initiation, and corrosion propagation.

McCarter et al.[93] used a configuration of 2-electrodes, and used them to evaluate the electrical resistance of saturated concrete. The results were compared to the 4-electrodes method. The results showed that 2-electrodes with a sponge system could give higher resistivity compared to the 4-electrodes method.

McCarter et al.[103] used a modified two points multi-electrodes array embedded within a concrete cover to monitor the distribution of electrical resistance. Remote monitoring was performed to provide real-time data of concrete exposed in an extreme environment. The relative resistive values obtained at each electrode were presented. Spatial and temporal changes of a cover zone were clearly described.

2.3.5.3 Multi-Points Electrodes Method

Plooy et al.[104] developed a multi-electrodes probe for resistivity measurements in concrete cover conditions. Concrete cover was investigated with the electrodes for the purpose of identifying chloride and chloride gradients. The probe was found useful under controlled laboratory conditions.

Duffor and Farina[105] developed an embeddable sensor for monitoring the state of a concrete structure. An open circuit potential sensor for rebar has been developed to measure corrosion current density, electrical resistivity, oxygen availability, chloride concentrations, and temperature within the structure. The sensor could determine the corrosion state of the existing concrete structure.

2.3.6 Summary of Building Materials Electrical Resistivity Measurement Techniques

From the discussion, it can be observed that the resistivity of the cover concrete depends upon:

- a) Conductivity and porousness of the solution (chloride concentration etc.).
- b) Temperature.
- c) Moisture content.
- d) Connectivity of the pores.
- e) Geometry.
- f) Frequency of supply voltage.

By measuring the resistivity of the porous material, the following parameters can be evaluated and estimated:

- a) Freeze and thaw resistance.
- b) Permeability of the material.
- c) Chloride penetration.
- d) Corrosion initiation and propagation (for concrete applications).
- e) Water absorption and moisture movement.

For accurate measurements when using electrode methods, the following have been recommended:

- a) Proper calibration of the sensor using an electrolyte with known resistivity.
- b) Sensors must be tested for their reproducibility and repeatability.

- c) To find a suitable method for compensating the variations influenced by surrounding temperature and humidity.
- d) A concrete geometry must be considered.
- e) A proper approach must be taken to avoid the influence of steel reinforcing bars.
- f) Avoiding measurements on wet surfaces.
- g) For surface measurement, make sure there is proper contact between electrodes and the surface of the material to be measured.
- h) It is recommended to use AC supply to avoid polarisation caused by DC supply.

Despite the benefits of this approach, the method is still bulky, intrusive, and power consuming. This hinders the method from being adopted in low power applications or being embedded in small structures like bricks. To be used in small structures like bricks, intensive research is required.

2.3.7 Indoor Thermal Comfort

The average person can spend up to 80-90% of their lifetime in an indoor environment[106][107]. This emphasises the need for a good and healthy indoor environment. Thermal comfort is the state of how a human being is satisfied by the surrounding environment[108][107]. Indoor thermal comfort is influenced by the environment (air temperature, mean radiant, relative air velocity, the vapour pressure in ambient air), activity level (metabolic action), and thermal resistance of clothing [108][109]. Since energy consumed in heating, ventilation, and air conditioning is about 40% of total energy, thermal comfort measurement is one of the important parameters to be considered in the building industry[110][111][112].

Measurement and evaluation methods have been specified in BS EN 7730[109]. The standard explains the level of environmental exposure suitable for a human being for quality living. Measuring instruments and tools for measuring physical quantities have been specified in BS EN 7726 [113].

Thermal comfort can be predicted by simply measuring the air temperature and humidity of the indoor environment.

2.3.8 Indoor Air Quality Monitoring

When assessing the impact of a building enclosure on human wellbeing, IAQ is one of the key parameters to consider. The indoor environment can determine the level of

occupancy comfort, health, and productivity [17][114][115]. IAQ information helps in identifying sources and levels of pollutants, and is used as inputs when designing and implementing suitable ventilation for a building [18]. The building and construction industry has become increasingly concerned about air quality as people spend more of their time in an indoor environment [116][117].

Criteria for evaluation of Indoor Environment Quality parameters have been specified by BS EN 15251 [118]. Threshold levels for various parameters have been specified in BS EN 13779 [119].

From the literature survey, it has been observed that sensor selection for various applications depends on the type of application, scope, and limitation of the study. Sensitivity, selectivity, size, low power consumption, low cost, and compatibility of the sensor with the existing platforms are the important factors when selecting sensors for IAQ. Using guidance specified in standards with the scope and limitation of the project to be implemented, VOCs, dust, and carbon dioxide have been selected for the study.

2.3.9 Acoustic/Sound Measurements

Acoustic (or sound) insulation is one of the important parameters when designing building materials. This is because of the importance of controlling and limiting the amount of noise for the benefit and wellbeing of people in homes, offices, and schools. For the material experts to optimise building materials and structures, standard measurements such as impact sound and airborne sound insulation have been established[19]. Impact noise is the noise that results from footsteps, while airborne noise is the sound transmitted through the air. For the scope of this thesis only airborne sound measurement is considered.

2.3.9.1 Airborne Sound Insulation Measurement

As per the British standard[19], on the transmitting side there is one sound level meter with a sound source, on the receiving side there is another sound level meter with a computer running analysis software. In Figure 2.6, the reference sound is generated in the transmitting room and received on the other side of the room by another sound level meter, before being sent to a computer for analysis.

The airborne sound insulation of facades can be determined using the same approach; the only difference is, for facades measurements, the source is positioned outside while the receiver is positioned inside the building under investigation[20].

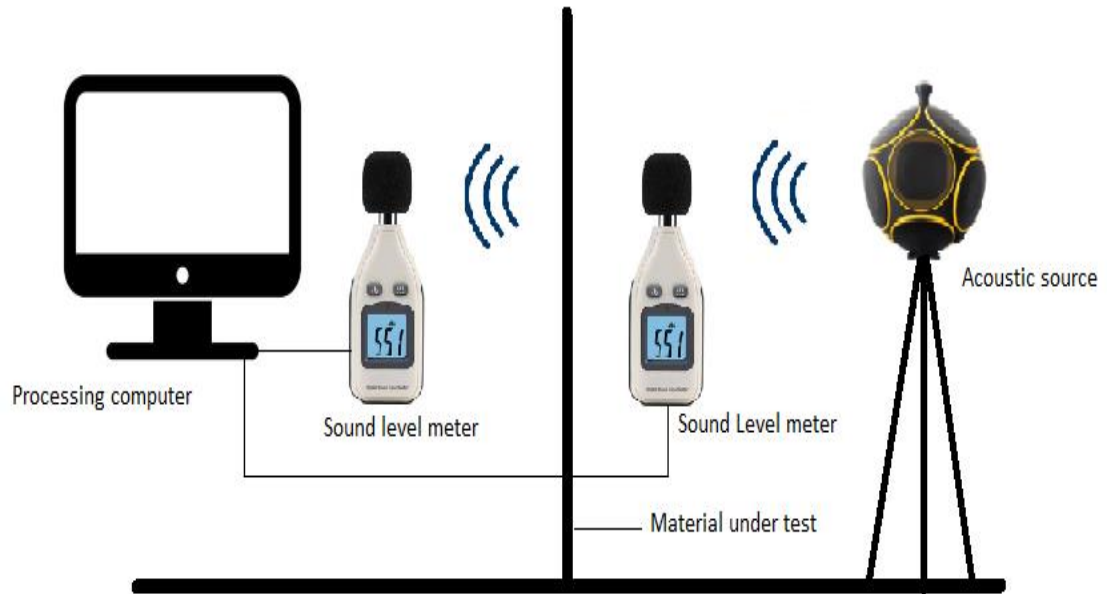


Figure 2.6. Diagram of airborne sound insulation measurement setup with two SLM positioned on the opposite face of the MUT, acoustic source and computer for data processing [20].

By comparing the difference in sound pressure levels between the source side and receiver side, the airborne sound insulation of a material or structure can be determined. As the ratio of incident sound power on the material to the sound power transmitted through the material or structure under test, the airborne sound insulation is presented as the sound reduction index R in dB [120]. The reduction index (R) is calculated by Equation (2.2).

$$R = 10 \log_{10} \frac{W_1}{W_t} \quad (2.2)$$

Whereby

W_1 = Sound power incident on the structure

W_t = Sound power transmitted through the material.

R = Sound reduction index, dB

2.4 Internet of Things for Structural Monitoring

2.4.1 Introduction

The monitoring of civil structures is critical in ensuring users' safety. The concept of installing sensors in masonry structures is not new in the field of structural engineering. Sensor systems have been installed to assess the performance of structures, particularly during seismic disturbances[121][122][123]. In some applications, sensor installation is done permanently, while in some applications sensors are installed temporarily. In most commercial monitoring systems, sensors are connected to the server using cables, which reduces the flexibility of the system[124]. This method of communication is expensive to install and maintain[121].

Due to fast development in the electronics industry, especially in the area of embedded systems, a low-cost monitoring system can be designed and implemented. The system can offer additional performance features, with high accuracy at a very low cost compared to the conventional method. Using microcontroller chips with added capability (such as analogue to digital conversion and compatibility with wireless radios), technology has produced wireless sensing systems[121][125][126].

In recent years, there has been massive internet of things (IoT) sensor node deployment, due to the increase in the number of applications that need to be connected. The applications vary from medical applications to agriculture, smart houses/building as well as smart cities[127][128]. As the demand for multisensory application increases, the internet of things has become a new platform for sensor deployment. This section will explore the existing commercial, low-power consumption, wireless systems with a long communication range (XBee, BLE, LoRa, WiFi, etc.). Finally, the new passive wireless sensor network will be proposed.

2.4.2 Bluetooth Low Energy (BLE)

Bluetooth is a wireless personal area network that operates at a 2.4 GHz free band. It uses the frequency hopping spread spectrum modulation technique to increase the resilience to adverse radio interference.

The technology uses low power compared to standard Bluetooth communication. BLE is commonly used for wireless medical devices and home automation, as well as on geo-fencing. Other benefits of using BLE are[129]:

- a) It can achieve low power consumption by keeping the radio off for a certain period and sending data at a low transfer rate.
- b) Low cost.
- c) It is compatible with most smartphones.

Despite all these benefits, BLE has the following disadvantages[129]:

- a) High power consumption compared to the range achieved.
- b) A limited number of slaves per master node.
- c) When sleep mode is activated, the node takes a significant amount of time to wake up, thus limiting power saving.
- d) Its master/slave architecture limits multi-hop operation.

2.4.3 Wi-Fi

Wi-Fi is a wireless technology based on the IEEE 802.11 family of standards. It utilises 2.4GHz or 5GHz. Depending upon the version, it can transmit data from a few megabits per second to several hundred megabits per second. Other advantages of Wi-Fi are[129]:

- a) Easy to install and deploy.
- b) High latency.
- c) High data transmission rate.

Despite all these advantages, Wi-Fi has the following disadvantages[129]:

- a) High power consumption.
- b) Limited range.
- c) It is not well suited to an indoor environment with concrete and metal obstructions.
- d) Difficult to estimate throughput.

2.4.4 LoRa

LoRa (Long Range) is a wide-area wireless protocol that requires low power. It uses Chirp spread spectrum technology as its basis for spreading spectrum modulation. In Europe, 915 MHz is used for free, along with 433 MHz and 868 MHz in Australia and North America, while 923 MHz is used in Asia. LoRa can offer the following[129]:

- a) Long-range up to 15km.
- b) Reduced power consumption.

- c) Reduced form factor.
- d) Low cost.
- e) High network capacity.

Despite all these benefits, LoRa has the following disadvantages[129]:

- a) Limited duty cycle.
- b) Low data rate.
- c) It is not ideal for real-time applications with low latency requirements.

2.4.5 ZigBee Communication

ZigBee is a free band, short-distance communication that operates in 868MHz, 915MHz, and 2.4GHz ISM bands [130]. Other features of ZigBee are[131]:

- a) Low cost.
- b) Low power consumption (6.3 mW (+8 dBm), boost mode 3.1 mW (+5 dBm), normal mode channel 26 max power is +3 dBm).
- c) Easy to install and maintain.
- d) Compact design.

The general performance of the wireless technologies is summarised in Figure 2.7.

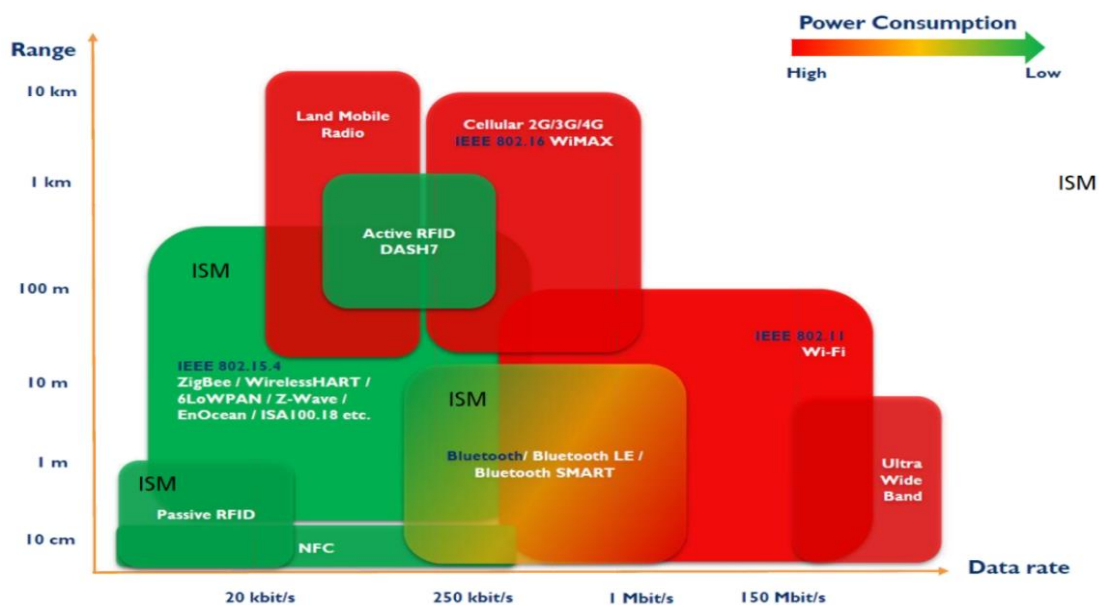


Figure 2.7. Diagram of wireless technology performance showing how bandwidth varies with power consumption and distance [132].

From Figure 2.7, as bandwidth is increased, the power consumption is also increased. As power is increased the coverage distance is also increased. Passive RFID has low power consumption but has limited coverage distance as well as data rate. WiFi has good coverage, good data rate but consume significant amount of power that make it not suitable for battery powered applications. Considering the coverage distance, data rate, and power consumption. ZigBee technology is the preferred choice for structural monitoring applications.

2.4.5.1 XBee Configuration and Networking

A ZigBee network must consist of one Coordinator device (a Gateway), with one or more Routers or End devices (Sensor nodes). A Coordinator device is responsible for starting a network, handling addresses, defining the network, and securing it. Each network must contain one device to work as a Coordinator. A Router is a full-featured node responsible for routing, sending, or receiving information. It supports communication between devices that are too far apart to establish communication. A single network can contain more than one Router.

End devices are the radios that can only send and receive information on a network; they cannot be used for routing purposes. End devices always need a Coordinator or Router device to establish a network. Multiple end devices are permitted in a single network[131][129].

2.4.5.2 ZigBee Network Topology

To establish communication between devices, Coordinators, Routers, and End devices must be connected logically to each other. The layout can range from a simple pair of devices to a star network, or to a complicated mesh network. Based on the nature of the project, star topology has been adopted.

In star topology (Figure 2.8), a coordinator device is at the centre of the network. All Routers or End devices have to pass messages directly to the coordinator. The Coordinator device will be a Gateway to other networks[129].

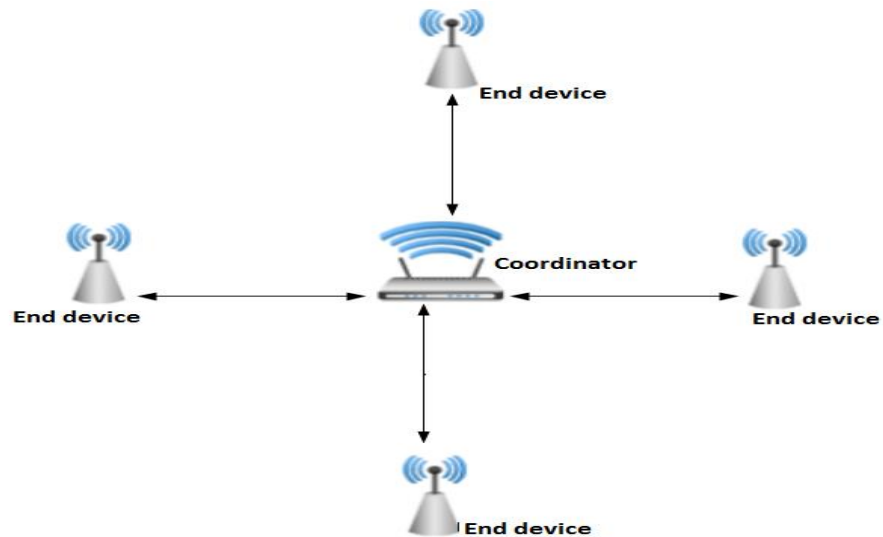


Figure 2.8. A diagram of a simple star topology.

2.4.5.3 ZigBee Network Addressing and Data Transmission

XBee modules use 64-bit and 16-bit addresses for communication. The 64-bit address is uniquely provided to each device during manufacturing. It can be used as a media access control (MAC address) for the device. The 16-bit address is provided to the device when the device is connected to the network.

XBee devices can be configured to operate in AT mode (Transparent) or API mode (Application programming interface). For this project, the API mode will be used. AT mode is effective when communication is between pairs of devices

API mode uses structured frames in communicating data from one point to another. The format of the frame has to be uniform throughout the network. Generally, an API frame (see Figure 2.9) contains start delimiter, frame length, frame type, frame data, and checksum.

Start delimiter	Length		Frame data								Checksum	
			API identifier	Identifier-specific Data								
1	2	3		4	5	6	7	8	9	...	n	n+1
0x7E	MSB	LSB	cmdID	cmdData								Single byte

Figure 2.9. Diagram of A basic API frame showing the position of data frame, length, delimiter and checksum.

2.4.5.4 Description of API Frame

- a) Start Delimiter shows the start of the frame. Any incoming data before the start delimiter is discarded.
- b) The frame type is a one-byte command representing the frame type.
- c) Frame data is the actual data/command to be sent.
- d) The checksum is one-byte data calculated by adding all bytes (excluding start delimiter and frame length). If the checksum is not correct, the data will be discarded.

2.5 Summary of the Chapter

This chapter has presented a review of how building material varies when interacting with the environment, and the impact of material variation on indoor environment quality. It has also presented existing testing methods for building materials and off-the-shelf wireless technologies. Through the review, several points have been discerned:

- a) The review has shown the fundamental relationship between building materials' thermal physical properties and indoor environment quality, as well as the effect of building material properties on sound insulation.
- b) The review has shown that existing building material measurements before deployment include a series of procedures as stipulated in British Standards, and most tests are performed in a controlled laboratory environment. Types of equipment used for measurements, data logging, and visualisation are commonly bulky, hard-wired, and consume a significant amount of power.
- c) Most of the sensor networks in the literature have been designed for specific applications and cannot be used for general purpose applications. This makes it difficult to modify or extend the sensing features when needed.
- d) From the review, it is obvious that there is a need for a well-defined and structured method to link the study on the variation of building materials with the environment and the impact of variation of building materials on indoor environment quality.
- e) The review has shown the need for a low-powered, open-source, flexible, and small-sized GWSN that can continuously monitor the building materials and building environment, to address the limitations of the conventional measurement methods and the technological gap stated in the previous studies.

f) COTs wireless technologies have been presented. Their advantages, disadvantages, and limitations have also been explored in detail. Based on the scope and limitation of the project, ZigBee technology has been selected as the means of communication in the reference measurement design. As all of the discussed technologies still consume a significant amount of power, the section has also suggested the novel design of a passive wireless sensing mechanism as the next stage of the research.

In conclusion, a GWSN for dynamic monitoring of a new generation of building material seems to be a potential solution in addressing the shortcomings of existing measurement methods and linking the study of building material variations and indoor environment quality. In the next chapter, the design of A Generic Wireless System specifically for this research is explained in detail.

Chapter Three

A Generic Wireless System Design and Instrumentation Strategies

3 Introduction

To implement the GWSN, two Generic sensor nodes and one Gateway node have been designed and implemented specifically for the task. The nodes have been designed to make sure all the sensors required to measure the proposed parameters are accommodated. For data collection and processing, custom firmware has been designed specifically for the task.

3.1 Electronics Hardware Design and Sensor Interface

This section explores all the hardware electronics used in designing the sensing system: from Sensor nodes with Sensor's interface to the Gateway.

3.1.1 Thermal Performance Characterisation

The sensor HFP01-05 in Figure 3.1(a) from Hukseflux with the sensitivity of $62.2 \times 10^{-6} \text{ V/(W/m}^2\text{)}$, recommended in the BS Standard [73], was chosen for heat flow measurement and is initially calibrated by the manufacturer. For surface temperature measurements, the sensors selected were NTC thermistor model B57703M0103A019 from EPCOS (Figure 3.1(b)) that are highly resistant to water and moisture. HTM2500LF [133] in Figure 3.4 has been chosen to measure air temperature on both sides of the structure under test. This sensor is stable, highly sensitive, and is not affected by water immersion[3].



Figure 3.1. Thermal performance measurement (a) A picture of a heat flux sensor selected for the measurement of heat flux through the material (b) Surface temperature sensor used for measuring the temperature on the surface of the MUT.

3.1.1.1 HFP01-05 Heat Flux Sensor

The HFP01 heat flux sensor is the recommended sensor by the British standard for measuring heat flux through walls and building envelopes. The thermal resistance of the sensor has been kept small by the use of a ceramic plastic composite body. Other features of HFP01 are[134]:

- a) Robust and stable.
- b) Suitable for long-term use.
- c) Passive, i.e. no power is required.
- d) High sensitivity.

The output of the heat flux sensor is a voltage from a few microvolts to millivolts. Each HFP01 comes with an individual calibration value of sensitivity. The sensitivity for the heat flux used on this measurement is $62.22\mu\text{V}/(\text{W}/\text{m}^2)$. The value of heat flux Φ can be calculated by Equation (3.1)[134].

$$\Phi = \frac{V}{S} \quad (3.1)$$

Whereby

Φ is heat flux in W/m^2

V is the voltage output in Volts

S is the sensitivity of HFP01 in $\text{V}/(\text{W}/\text{m}^2)$ (provided on the certificate)

For a good spatial average, each measurement is recommended to have at least two heat flux sensors.

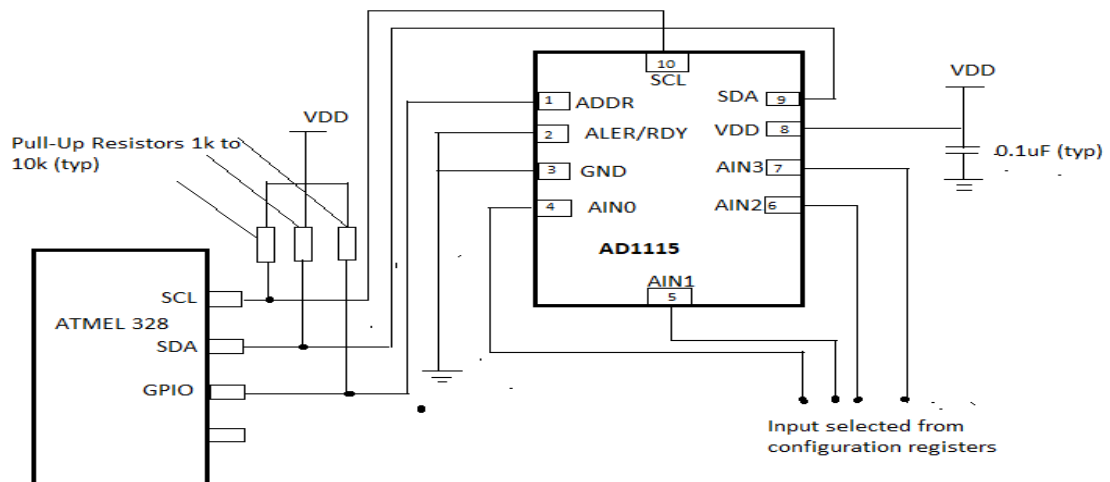


Figure 3.2. Schematics showing a typical connection of ADC ADS1115 with microcontroller with pull-up resistors [135].

The Atmel 328 has a built-in ADC of 10-bits. To obtain a good resolution on the measured signal, a resolution of at least 16-bits (preferably 24-bits) is required. To achieve this, an external ADC is needed to interface the sensor with a microcontroller. The selected 16-bits ADC is ADS1115 from Texas Instruments. The typical connection of ADS1115 with Atmel is shown in Figure 3.2. Some of the features that make it suitable for the project are[136]:

- a) Low current consumption (150 μ A in continuous conversion mode).
- b) Wide range of supply voltage (2.0V to 5.5V).
- c) Ultra-small footprint.
- d) Simple to interface with the Atmel328 microcontroller.

3.1.1.2 Temperature Sensors

B57020M2 and B57703M0103A019 are negative temperature coefficient (NTC) thermistors for the measurement of surface and material temperature[137]. The simplest and cheapest method of measuring temperature using a thermistor is by using a 10k Ohm resistor and an NTC Thermal Resistor divider circuit, connected to an analogue pin on a sensor node. The circuit of the interface is shown in Figure 3.3. The idea is to pull ground (GND) through the variable thermal resistor with the 5V pull-up through another 10k (standard) resistor. The effect is that the analogue pin will swing through the range of the thermal resistor from 5V to GND.

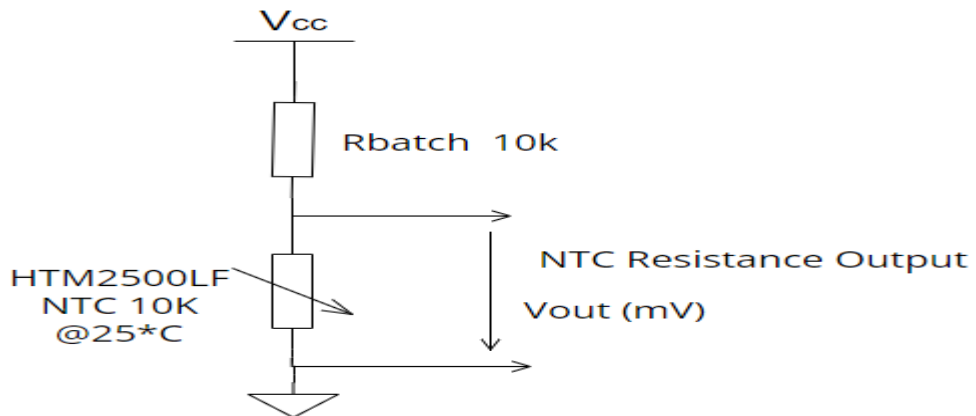


Figure 3.3. Schematics showing thermistor interface circuit to the GWSN [133].

The value of R_{batch} is chosen to be equal to NTC @25°C to get $V_{out} = V_{cc}/2$ @25°C in Equation (3.2)[133].

$$V_{out}(mV) = \frac{V_{cc}(mV) * NTC(\Omega)}{R_{batch} + NTC(\Omega)} \quad (3.2)$$

Whereby:

V_{out} is the output voltage in mV

V_{cc} is the supply voltage in mV

R_{batch} is an external resistor in Ω

NTC is resistance in Ω at temperature T in K

The value of temperature can be determined by Equation (3.3)[133].

$$T = \frac{1}{a + b * \ln(R) + c * \ln(R) * \ln(R) * \ln(R)} \quad (3.3)$$

Whereby:

T is the temperature in K

R is NTC resistance at temperature T in K

a , b and c are constant values (given by manufacturer)

3.1.1.3 Moisture and Temperature Measurements

The HTM2500LF humidity/moisture and temperature sensor [133] (Figure 3.4) has been chosen for the application. Accuracy, sensitivity, and ability to work in wet/harsh environments are some of the factors considered when selecting a sensor. Some of the features of the sensor are:

- a) High reliability and long-term stability.
- b) Not affected by water immersion.
- c) Suitable for 3 to 10Vdc supply.
- d) Fast response time.
- e) High resistance to chemicals.



Figure 3.4. A picture of HTM2500LF humidity and temperature sensor [133].

For humidity measurements, the analogue output pin of Humidity is connected directly to the analogue pin of the Atmel 328P microcontroller. From the datasheet, relative humidity (RH in %) is determined by Equation (3.4)[133].

$$RH = 0.0375 * V_{out} - 37.7 \quad (3.4)$$

Whereby.

RH is the relative humidity in %

V_{out} is the output voltage in mV

Temperature measurement is achieved using the voltage divider circuit in Figure 3.3 and Equation (3.3).

3.1.2 Indoor Thermal Comfort

For this project, the DHT22 sensor[138] (as shown in Figure 3.5) has been selected to be used for measuring indoor air humidity and air temperature.



Figure 3.5. DHT22 Humidity and Temperature sensor [138].

The DHT22 temperature and humidity sensor consists of a thermistor and humidity sensor in one package. It also contains a built-in low-power microprocessor for the conversion of sensor output from analogue to digital. The sensor output is given in serial format. The measurement can be delivered every 0.5 seconds[138].

To interface the DHT22 sensor, one pin will go to 5V. The 2nd pin, through which data flows, needs some operational voltage. The data pin can be connected to any digital pin of Atmel328. DHT22 uses a 1-Wire bus protocol.

3.1.3 Indoor Air Quality Monitoring.

Based on the type of application, scope, and limitation of the project, sensitivity, size, cost, power consumption, and compatibility have been considered as the main factors in choosing sensors. The COZIR Ambient CO2 sensor in Figure 3.6(a)[139] has been

chosen to measure for carbon dioxide; the Sharp Photoelectric dust Sensor in Figure 3.6(b)[140] for PM2.5; and the TGS2602 sensor in Figure 3.6(c)[141] for VOCs).

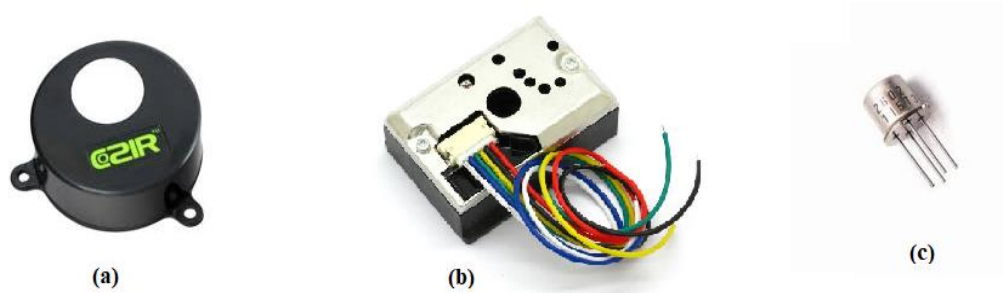


Figure 3.6. A picture of sensors for indoor air quality measurements(a) COZIR Ambient CO2 sensor (b) GP2Y1010AU0F Dust sensor (c) TGS 2602 VOC sensor

3.1.3.1 TGS2602 Volatile Organic Compound Sensor

TGS2602 is a thick film metal oxide semiconductor printed gas sensor. It is highly sensitive to air contaminants and low concentrations of odorous gases such as ammonia and H₂S generated from waste materials. Other features of TGS2602 are[141]:

- a) Low power consumption.
- b) Long life.
- c) Small size.

To interface with the Atmel328 microcontroller, the output pin of the sensor is directly connected to an analogue pin of the GWSN. Other connections are as shown in Figure 3.7.

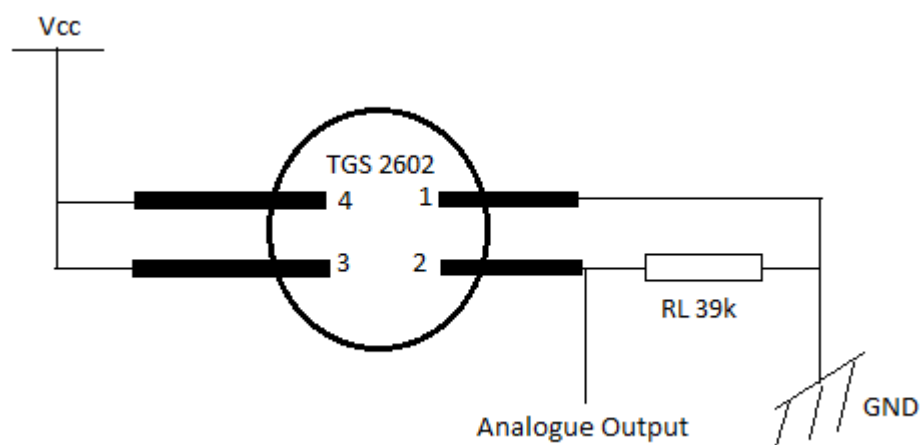


Figure 3.7. Schematics of TGS2602 VOC sensor pinout setup and interface [141].

3.1.3.2 Cozir Ambient Carbon Dioxide Sensor

Cozir ambient is a low-power sensor suitable for measuring a low level of CO₂. It can also sense temperature and humidity. Other features of Cozir A sensor are[139];

- a) Self-calibrating.
- b) Solid state - no moving parts, no heated filament.
- c) Vibration and shock resistant.
- d) 15 years plus lifetime.
- e) Low power consumption (3.5mW).

Pin description and interface are shown in Figure 3.8.

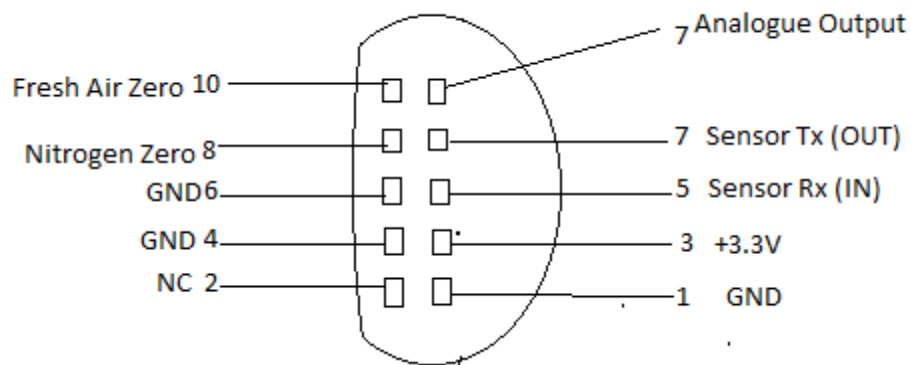


Figure 3.8. Diagram of Cozir Carbon dioxide sensor pin description [139].

3.1.3.3 GP2Y1010AU0F Dust Sensor

GP2Y1010AU is an optical dust sensor designed to sense dust particles by analysing the amount of light reflected by dust. The sensor is effective in detecting very fine particles of dust[142].

To work with the microcontroller in the GWSN, the output pin of the sensor is connected to any analogue pins of the GWSN. A resistor of 150 Ω and a capacitor of 220uF are connected externally for biasing the internal light-emitting diode of the sensor, as in Figure 3.9.

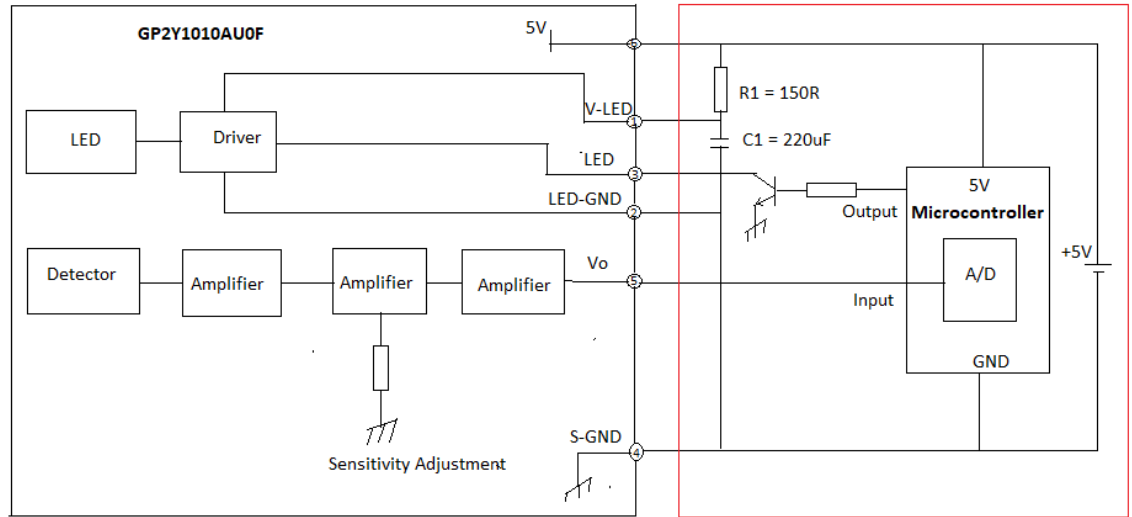


Figure 3.9. Schematics of dust sensor pinout and interface [143].

3.1.4 Acoustic Measurement

Based on the type of application, scope, and limitation of the project, sensitivity, size, cost, and power consumption have been considered in selecting a sensor for the design in this thesis. For this project, the GY-MAX4466 electret microphone[144]] in Figure 3.10, is proposed to be used for measuring sound.



Figure 3.10. A picture of GY-MAX4466 electret microphone as an acoustic sensor [144].

The module comprises microphones and an amplifier circuit. The microphone is an electret type CMA-4544PF-W[145]. The microphone is omnidirectional, with a frequency response between 20 Hz to 20 kHz. The voltage from the microphone passes through the amplifier circuit before being applied to the microcontroller. The amplifier is MAX4466[146]: a micro-power operational amplifier optimised to be used as a

microphone amplifier. The setup provides the ideal combination of an optimised gain-bandwidth product vs supply current and low voltage operation in an ultra-small package.

The noise on the measured data is removed by averaging on the node. This is achieved by adding together several measurements and calculating their average. By increasing the number of measurement points to be averaged, more noise is removed. The averaging method is simple to implement and does not occupy much space on the microcontroller.

3.1.5 S2C XBee Communication Module

Based on cost, size, power consumption, and performance, ZigBee technology has been chosen as the wireless communication technology for the reference design[147]. XBee S2C module[130] (as shown in Figure 3.11), operating at 2.4GHz, has been selected and used as a communication module between sensor nodes and Gateway.



Figure 3.11. A picture of XBee ZigBee S2C module wired antenna – XB24CZ7WIT-004 [130].

XBee S2C is an RF module designed for wireless communication or data exchange and it works on ZigBee mesh communication protocols that sit on top of IEEE 802.15.4 PHY. The module provides wireless connectivity to end-point devices in any ZigBee mesh networks, including devices from other vendors[148][131].

Since XBee uses 3.3V, and Atmel328P-PU uses 5V, the interface circuit in Figure 3.12 is used to convert 3.3V to 5V and vice versa and is inserted between UART data pins. The typical connection of Atmel 328P in the GWSN with the XBee module is shown in Figure 3.13. The Transistor 2N7002 from NXP Semiconductors[149] is used to achieve the switching.

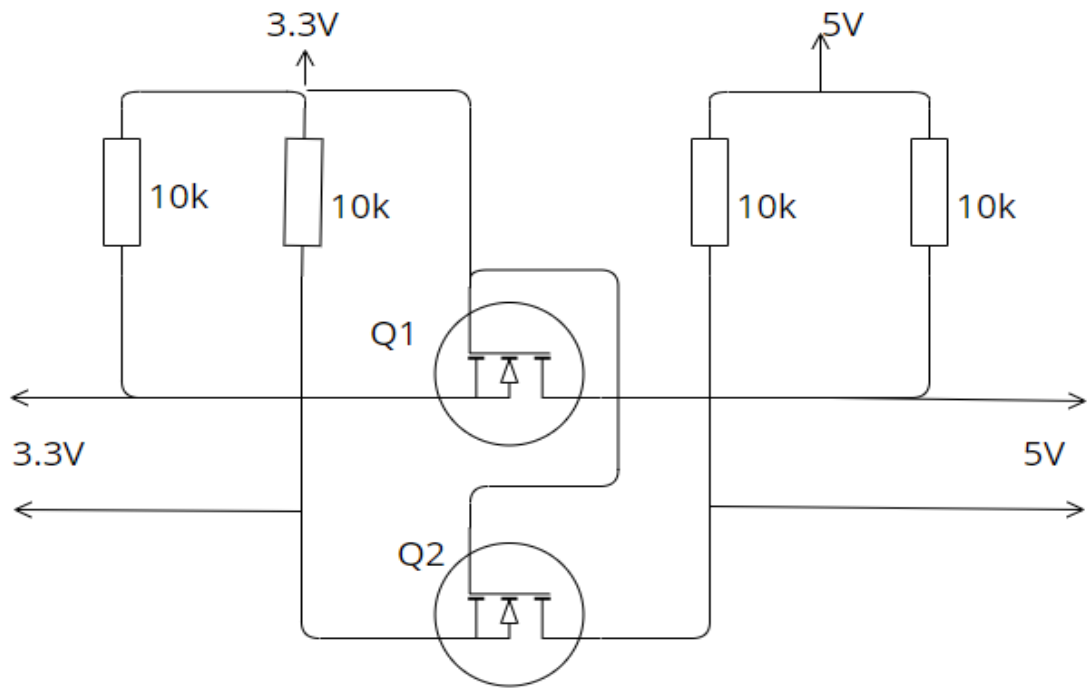


Figure 3.12. Schematic of level shifter circuit use to converting voltage from 5 V to 3.3 V and 3.3 V to 5 V [150].

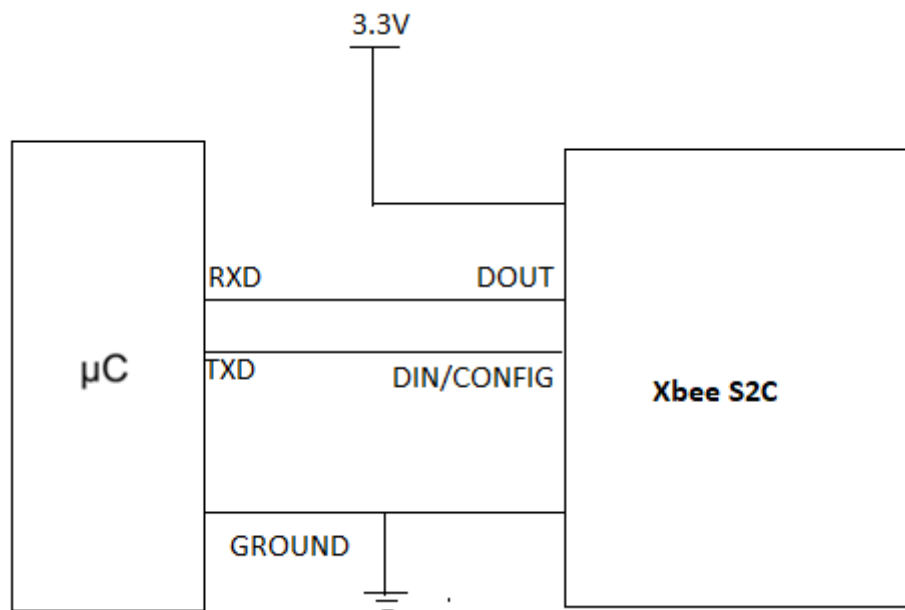


Figure 3.13. A diagram showing S2C Communication module interface with Atmel 328P [151].

3.1.5.1 XBee Modules Configuration.

Proper configuration is required for the XBee module to communicate. XCTU software from Digi International was used to configure one XBee radio as Coordinator and two

other radios as End devices. The PAN ID & Baud Rate should be the same for both Radios. Only one Coordinator is permitted for each network. A step-by-step configuration of the XBee Gateway and end nodes modules is detailed explained in Appendix 1.

The number of routers and devices depends on the requirements of the network. After the configuration, the devices are scanned to see the connectivity, as in Figure 3.14.

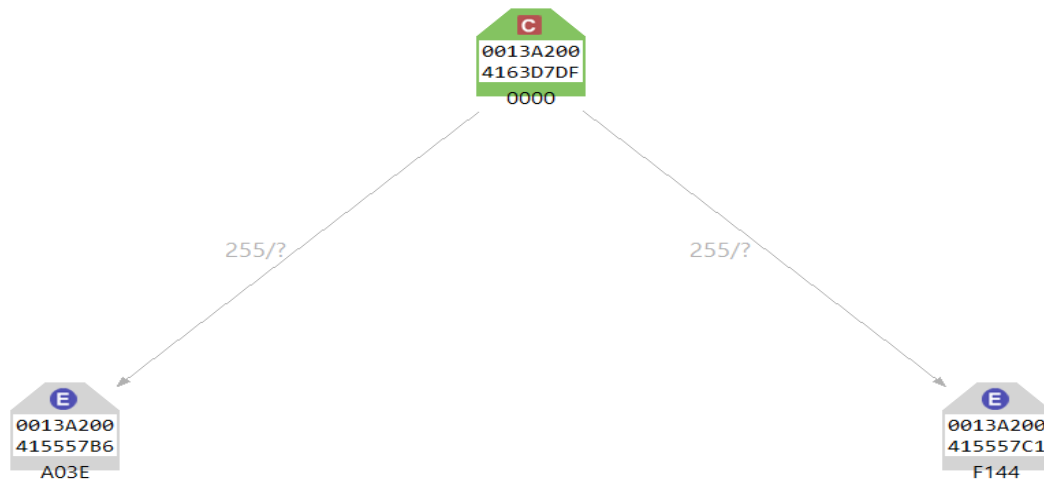


Figure 3.14. A diagram showing network topology established by XBee modules with XCTU software.

From Figure 3.14 at different points one node will be searching for another node on the same network and connect, when the network is not established between nodes, the status will indicate question mark sign (?) as indicated.

3.1.6 Microcontroller Unit

The Atmel 328P-PU microcontroller in Figure 3.15 has been used to achieve custom open-source single-board sensor nodes. It is a low-power, 8-bit microcontroller based on the AVR RISC architecture. The board has 14 digital pins and 6 analogue pins for connecting sensors and other components. The operating voltage is 1.8V to 5.5V[152].

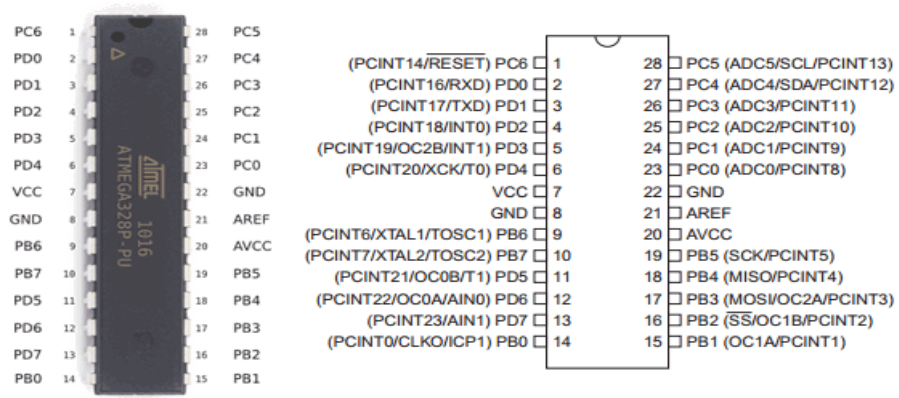


Figure 3.15. A picture of Atmel 328P-PU microcontroller and pinout [153].

3.1.7 Arduino Uno

To utilise the enriched Arduino software open-source libraries, the Arduino Uno development board in Figure 3.16 was selected. Uno allows simple and flexible serial communication between the S2C XBee communication module and Raspberry Pi.

Arduino Uno is one of the open-source microcontroller boards based on the Microchip ATmega328P-PU microcontroller. The board contains several digital and analogue input/output pins for different applications[154]. A custom shield was designed for the purpose of interfacing with the S2C XBee communication module.

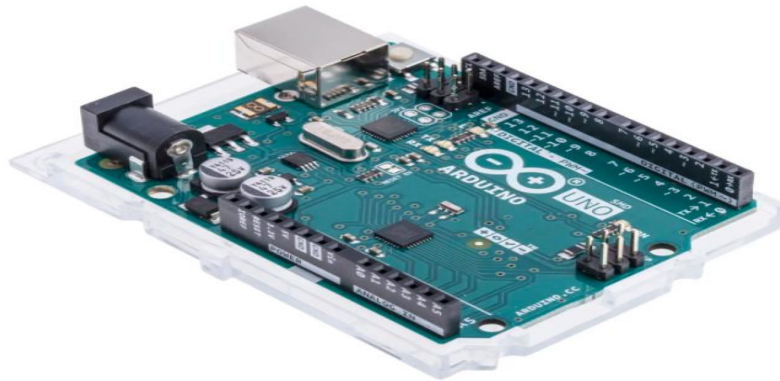


Figure 3.16. A picture of Arduino Uno development board [155].

3.1.8 Raspberry Pi

The Raspberry Pi is a low-cost, credit-card-sized single-board computer. Model 3 B+ (in Figure 3.17) is a 64-bit quad-core processor operating at 1.4GHz, with dual-band (2.4GHz and 5GHz) wireless LAN, Bluetooth 4.2/BLE, and faster Ethernet. It operates in an open-source environment with Raspbian as its main supported operating system,

accommodating several other open-source software[156]. The platform is configured to accommodate web server and database in one unit.



Figure 3.17. A picture of Raspberry Pi model 3 B+ board [156].

3.1.9 Power Supply

The power supply for the node can be a battery or DC adaptor supplying 9V to 12V. Power for 3.3V circuits was achieved by the use of the LD1117S33CTR low dropout regulator from STMicroelectronics[157], whilst the NCV7805BD2TR4G linear Voltage regulator from ON Semiconductor[158] was used to achieve a stable 5V. The Gateway node is powered directly by the DC adaptor.

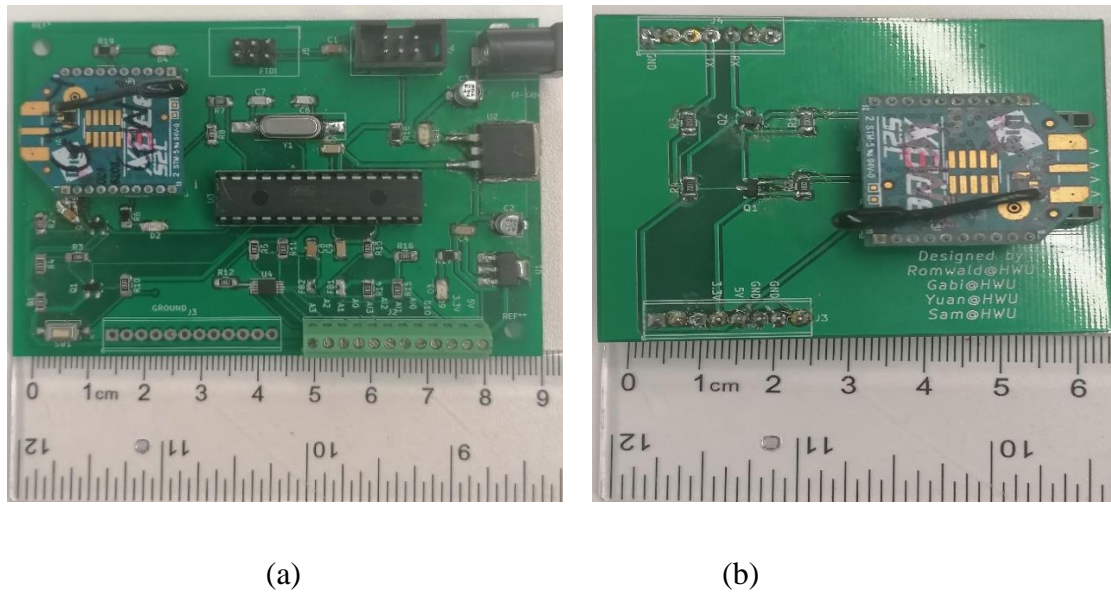


Figure 3.18. A picture of manufactured system with dimensions (a) Sensor node (95 mm by 65 mm) (b) Gateway node (65 mm by 55 mm).

3.1.10 Sensor Nodes

The designed system is comprised of two custom-made sensor nodes and a gateway. Dimensions of the sensor nodes is 95 mm by 65 mm, while gateway dimension is 65 mm by 55 mm. Figure 3.18 shows the manufactured system with dimensions.

A bespoke design (in Figure 3.19 for the first sensor node is based on the IEEE 802.15.4/ZigBee Standard based on the S2C XBee wireless communication module and a high-resolution ADS1115 16-bit ADC[159], an Atmeg328P-PU microcontroller [152], and a power supply unit[3][131]. The node can measure temperature, heat flux, humidity, and moisture.

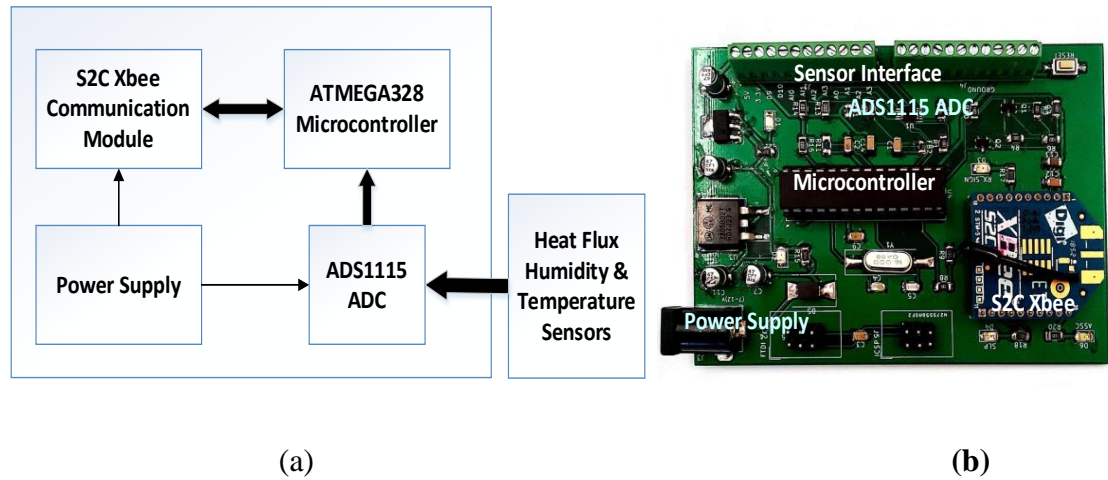


Figure 3.19. Sensor node 1. (a) Block diagram showing how various blocks are connected (b) Prototype showing the soldered components [3].

As with the first sensor node (in Figure 3.20), the second sensor node is also a custom design for low-power applications, comprising a power supply unit, an Atmeg328P-PU board, and an S2C XBee module based on IEEE 802.15.4/ZigBee technology[3]. The node also contains a built-in interface for the CO2 sensor, VOC sensor and dust sensor, temperature sensors, and humidity (moisture) sensors.

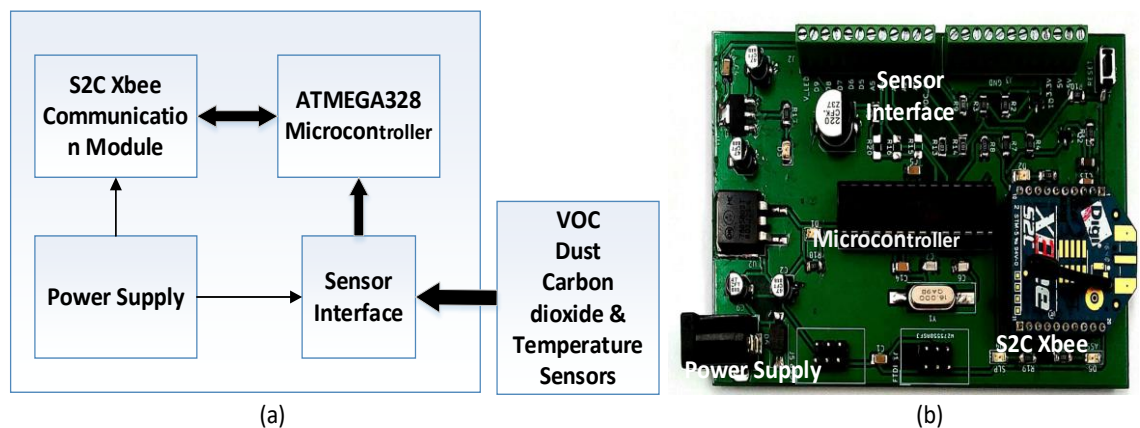


Figure 3.20. Sensor node 2. (a) Block diagram showing connection of various block (b) Prototype showing the soldered components [3].

3.1.11 Gateway Node

For data collection and data storage, a gateway or coordinator node has been designed. The gateway setup in Figure 3.21 consists of an S2C XBee module, an Arduino board, and Raspberry Pi 3B+. The complete datasheet of the designed GWSN is presented in Appendix 2. The datasheet shows detailed description of GWSN subsystems, Physical Dimensions, their technical specifications as well as how system is interfaced.

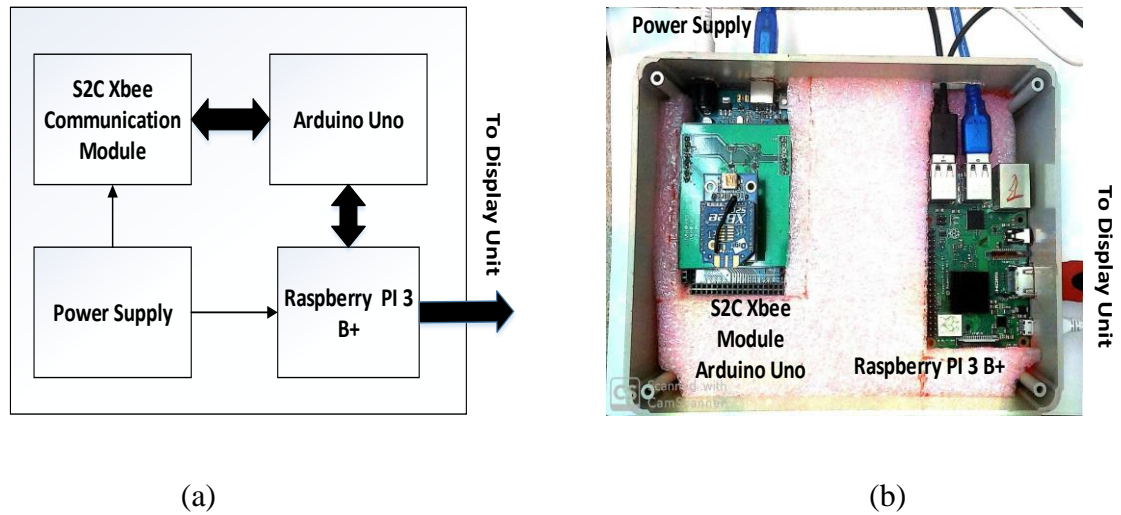


Figure 3.21.A diagram of gateway node showing how slave gateway is interfaced with master gateway and display unit (a) Block diagram (b) Prototype [3].

3.2 Software Architecture

This subsection explores all the software required to make the system operate to meet the intended objectives. The architecture of the entire design in Figure 3.22 has been kept simple and flexible to allow easy maintenance, adjustment, and allow portability. The distribution of the firmware starts from the sensor nodes where data is collected, pre-processed, and formatted, ready to be transmitted as a packet. The firmware on the sensor node has been developed using Arduino scripts to make the firmware flexible, portable, and open source.

The Gateway receives the raw sensor data from the sensor nodes, processes it, and stores it within the inbuilt database. To allow remote access to the data, Gateway has the access to forward the data to the cloud.

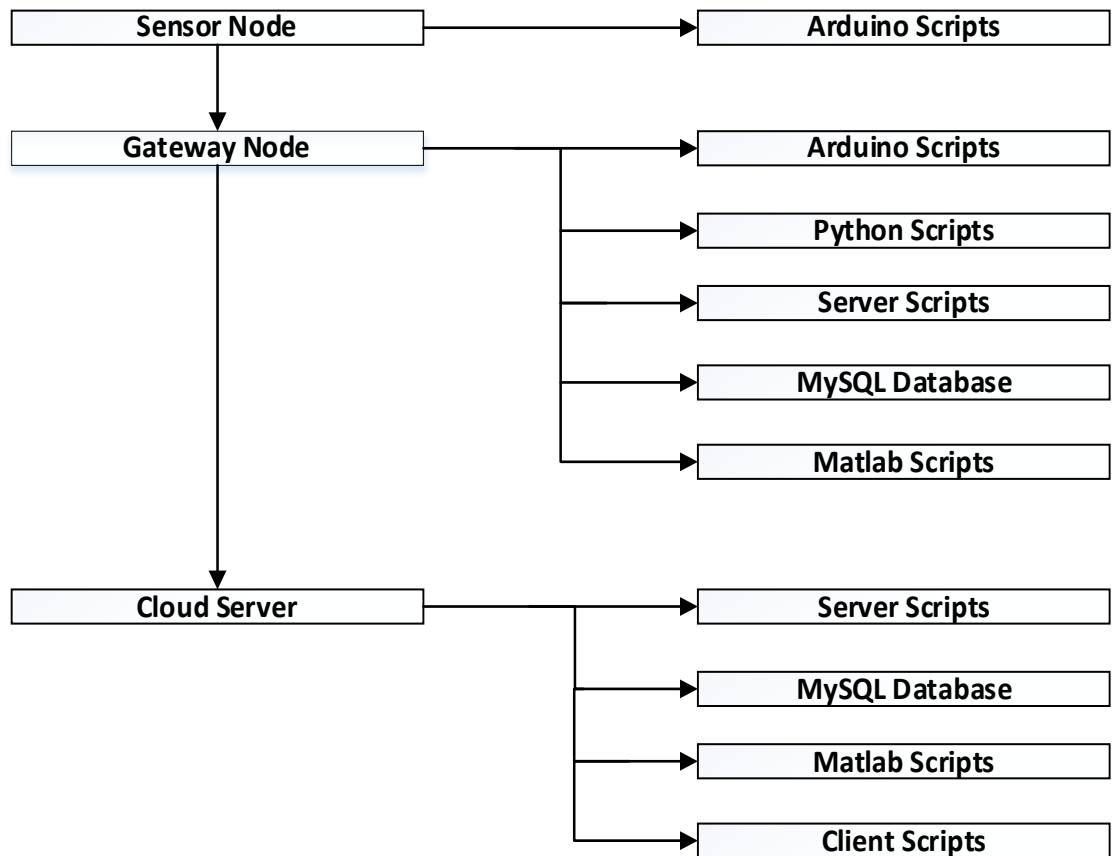


Figure 3.22. Software Architecture showing how various software used in GWSN are connected from the sensor node to the remote device.

Arduino scripts have been used for data extraction and processing, while Python has been used for data formatting and to prepare the data before forwarding it to the database. Matlab script is included for data analysis and manual graphics generation. MySQL database has been used for data storage. The same setup and configuration used on the Gateway can be on the cloud server for data extraction, processing, and storage.

3.2.1 Sensor Node

Arduino scripts written in C++ have been used on the sensor nodes to interface sensors, pre-processing, interface communication module, and forward data to the gateway. When sensor nodes are switched ON, the Arduino script is initialised within the hardware. As Arduino scripts execute sequentially, each task will be executed one by one in chronological order, as shown on the flowchart in Figure 3.23. An interrupt service routine is enabled to control switching ON and OFF the transmitter to allow the transmitter to operate in the sleeping mode as a power-saving strategy. The sleeping time or Wake-up can be easily adjusted based on measurement requirements. The interrupt

service routine in Figure 3.24(a) is declared out of the main program to reduce the complexity of the program, making it reusable and portable.

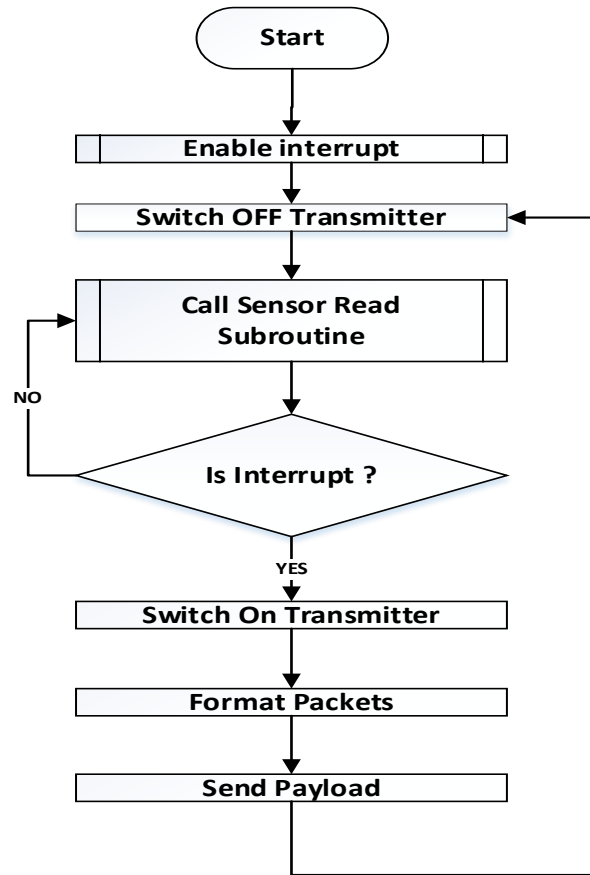


Figure 3.23. Flowchart of the main program of the sensor nodes of the GWSN showing how sensor data are collected, and how power consumed is reduced by operating transmitter in sleeping mode.

To extract sensor information, the Sensor Read subroutine of Figure 3.24(b) is executed. This allows sensor raw data to be extracted, pre-formatted, and returned to the main program. Then, the proper packet is formed, before sending it on air through serial communication.

For each execution, Interrupt is enabled, the sensor information is extracted, packets are formatted, and the payload is sent on air when the transmitter is switched on by the control of the interrupt signal.

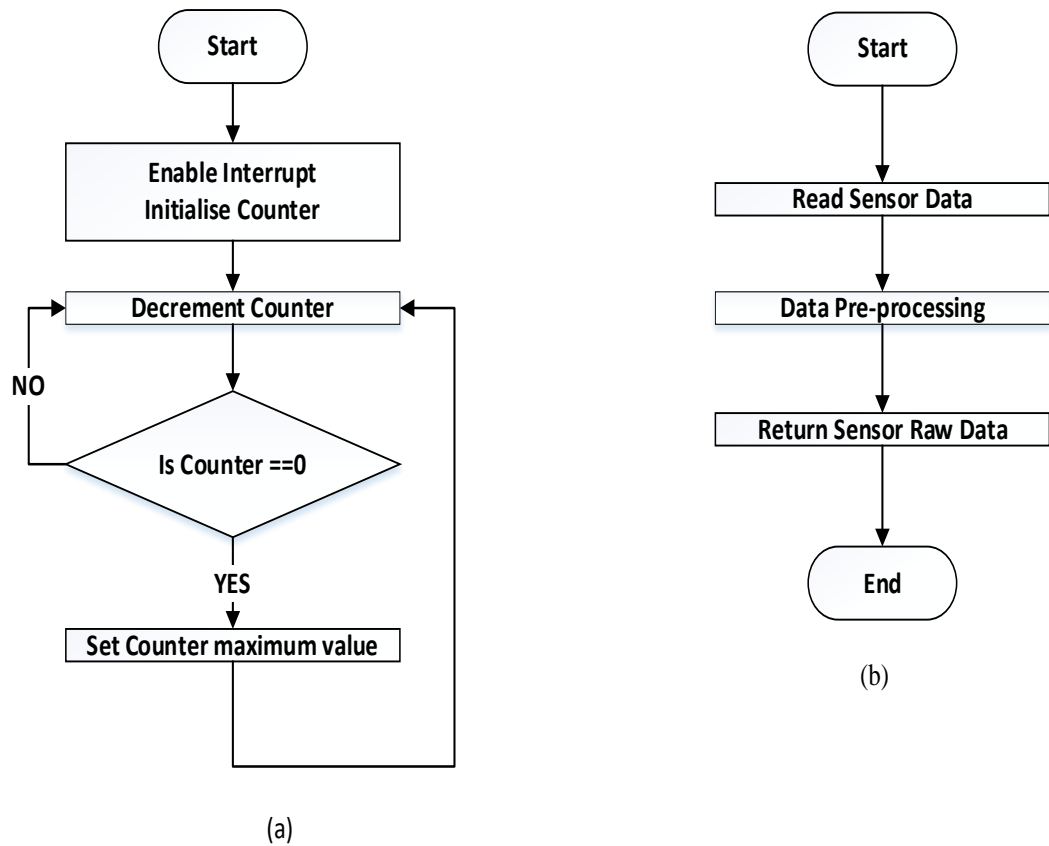


Figure 3.24. Flow chart showing program subroutines on the sensor nodes (a) Interrupt subroutine (b) Sensor read subroutine.

3.2.2 Gateway Node

To make the data processing flexible and ensure data integrity, the Gateway node is divided into Slave and Master sections. Python scripts, together with Arduino scripts, are used in the Slave section to interface the communication module, intercept data from sensor nodes, process, and forward to the Master section.

The scripts are in Figure 3.25(a), waits for the serial data to be available, then it checks to see if the data packet is complete. When packet integrity is confirmed, the MAC address of the node is extracted, to identify which node has sent the information.

Using the MAC information, the correct processing function will be called and executed. The flowchart of the processing subroutine is shown in Figure 3.25(b). Then the processed data is formatted again and given an identification to show the clear number of the sensor node. The format of packets to show how sensors are mapped within the firmware corresponding to their physical locations is shown in Appendix 3.

The formatted information is then forwarded to the Master section of the Gateway, which contains the local server hosting PHP scripts. Then the PHP scripts insert the received data into the MySQL table, as shown in Figure 3.26. Step by step configuration of the gateway and installation of various software packages is presented in Appendix 4.

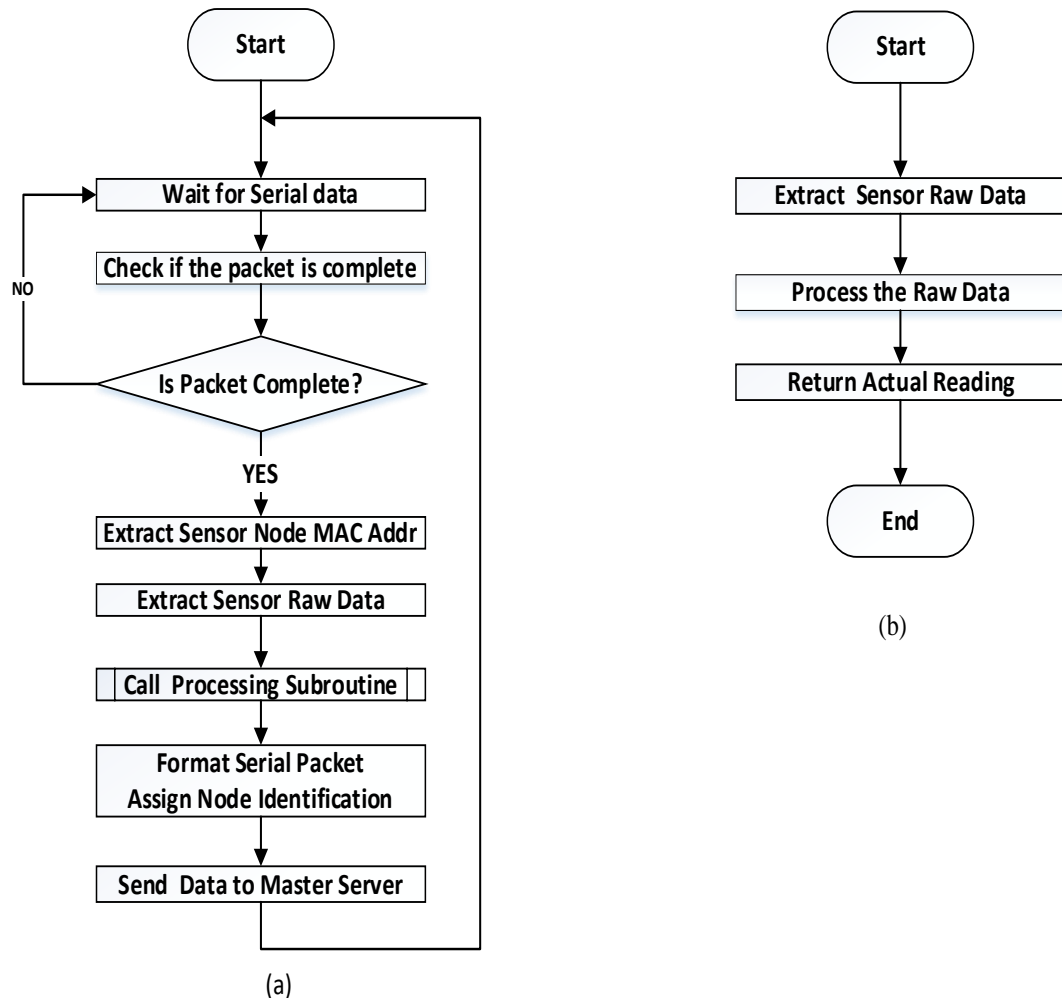


Figure 3.25. Program flowcharts (a) Slave server (b) Processing subroutine.

For administration of MySQL database on the web, phpMyAdmin is installed and configured. This is free software written in PHP to support most MySQL operations such as managing databases, columns, indexes, and user permission. All these operations can be performed through the user interface in Appendix 5. Step by step execution of the firmware is explained in Figure 3.26.

Also, through user application, users can access the web application within the local area network, or from any remote terminal on the internet, to access the system and perform remote configuration and management of deployed sensor nodes.

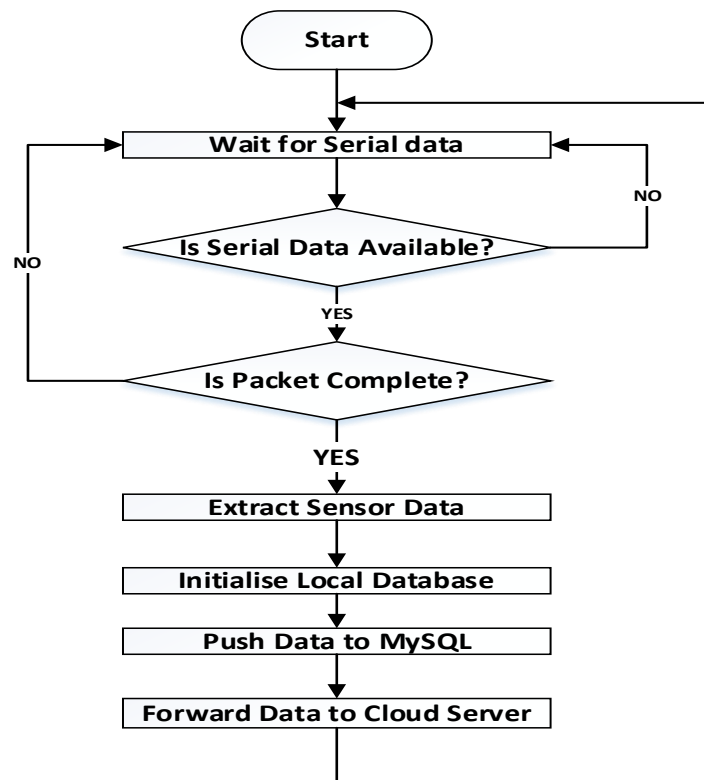


Figure 3.26. Flowchart of the Master section of the Generic wireless sensor network showing how data is extracted and sent to the database for the storage.

3.2.3 Cloud Server

As with the local server, the server script receives the sensor data from the gateway and forward/ inserts it into the MySQL database for storage. Matlab script is added on the client-side to perform the complex mathematical analysis, while JavaScript is added to display timely content updates and animated graphics. Finally, a web application is added so that the user (through the user interface) can access the system remotely for configuration and management.

3.2.4 Power Saving Strategies

Custom sensor nodes have been designed to achieve low power consumption by not including unnecessary components in the design. To further reduce the power consumption, interrupt service routines have been utilised on the microcontroller to allow the system to measure user-defined intervals. This allows the power-consuming modules like communication modules to go into sleep mode for a significant amount of time: to save power and lengthen battery life.

3.2.5 Sensor Calibration

Sensor calibration used to improve and maintain the performance and functionality of the system. For this design different sensors were initially calibrated differently; Heat flux sensor was initially calibrated by manufacturer and then validated in the laboratory before being used in the design. Manufacturer recommends recalibration at least once a year. CO2 sensors used has self-calibrating feature but can be validated in the lab before used in the measurements.

Temperature and humidity sensors were calibrated by the experiment conducted in the Kambic KK-190 CHLT climate chamber at Energy, Geoscience, Infrastructure and Society (EGIS). Acoustic sensor was calibrated by comparing with the standard sound level meter in Reverberation chamber in EGIS, while VOC sensor was calibrated in the lab by comparing its measurement with the reference measurements. When the measured value is equal to reference value, the system is said to be highly accurate with low errors. The accuracy of the system is calculated from Equation (3.5)

$$Accuracy = 100\% - Error Rate \quad (3.5)$$

Whereby

$$Error Rate = \frac{|Measured\ value - Reference\ value|}{Reference\ Value} \times 100\% \quad (3.6)$$

To improve the overall performance and functionality of the GWSN, it is recommended for the system to be recalibrated at least once a year. Also, for the future development, it is recommended to utilise wireless function of the GWSN to add over the air calibration feature. This feature will increase the GWSN flexibility especially when performing long term measurements and the system is not available for the in-house sensor calibration.

3.3 Conclusion

In this chapter, the step-by-step design, and implementation of Generic wireless sensor nodes and the Gateway of the wireless sensor network have been explained. The development of firmware for data extraction, data processing, and data storage have also been explored. The chapter has also explained the different types of sensors, sensor modules, and sensor interfaces selected for the application and the reasons for selecting them. The next chapter explains design of all the proposed experiments, and details of what has been done and why. This includes the descriptions of where, how, and when the experiments were performed.

Chapter Four

Design of the Experiments, Measurements, and Results Discussion

4 Introduction

This chapter explains the design of all the proposed experiments, and details of what has been done and why. This includes the descriptions of where, how, and when the experiments were performed. The experiments were designed to demonstrate, evaluate, and validate the effectiveness of the system. This was important for calibration, characterisation, and measurement, to see how the system behaved before deployment. The results from the measurements are also discussed in detail.

4.1 Building Material Thermal Performance

4.1.1 Sensing System Calibration

This part explains the calibration of the sensors and the sensing system. The sensors include HFP01 heat flux sensors, air temperature sensors, surface temperature and humidity sensors. A high precision milli-voltmeter was used to validate the heat flux sensors before the measurement campaign, and the temperature and humidity sensors were calibrated in a controlled laboratory environment since the heat flux sensors are initially calibrated by the manufacturer[3].

Air temperature, surface temperature, and humidity sensors were calibrated by the experiment conducted in the Kambic KK-190 CHLT climate chamber at Energy, Geoscience, Infrastructure and Society (EGIS). The chamber can be set according to the ranges in Table 4.1.

Table 4.1. Climatic chamber operating ranges.

Air temperature (°C)	-40 - +180
Surface temperature (°C)	-40 - +180
Relative humidity (%)	+10 – 98

A 1-week measurement was performed to provide the calibration of the system and estimate the accuracy. During calibration, the system was configured to take measurements after every 5 minutes. The GWSN system reading compared to the climatic chamber reading is presented in Figure 4.1 to Figure 4.3 and the final results are summarised in Table 4.2.

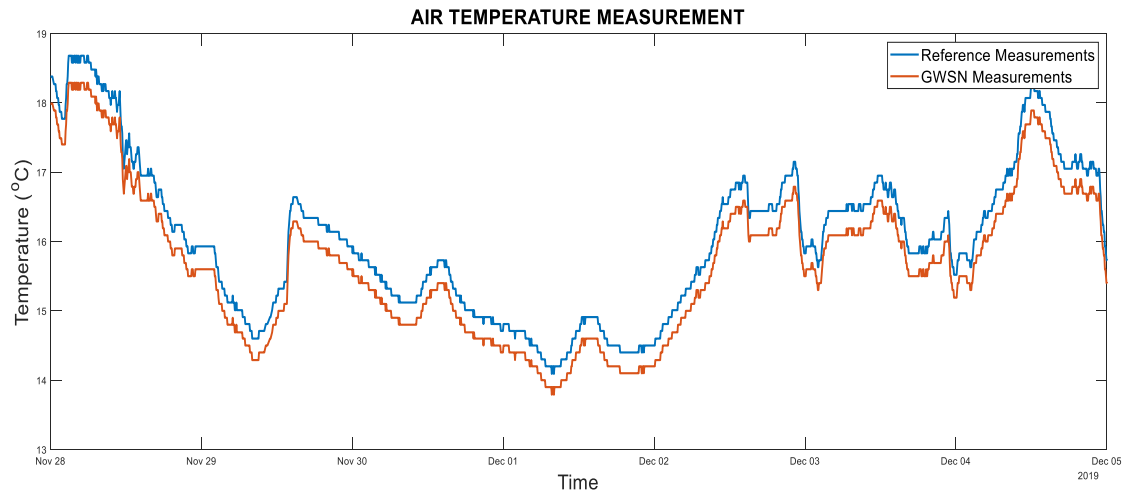


Figure 4.1. A plot showing air temperature measurements comparison between reference measurement by standard device and measurements by GWSN.

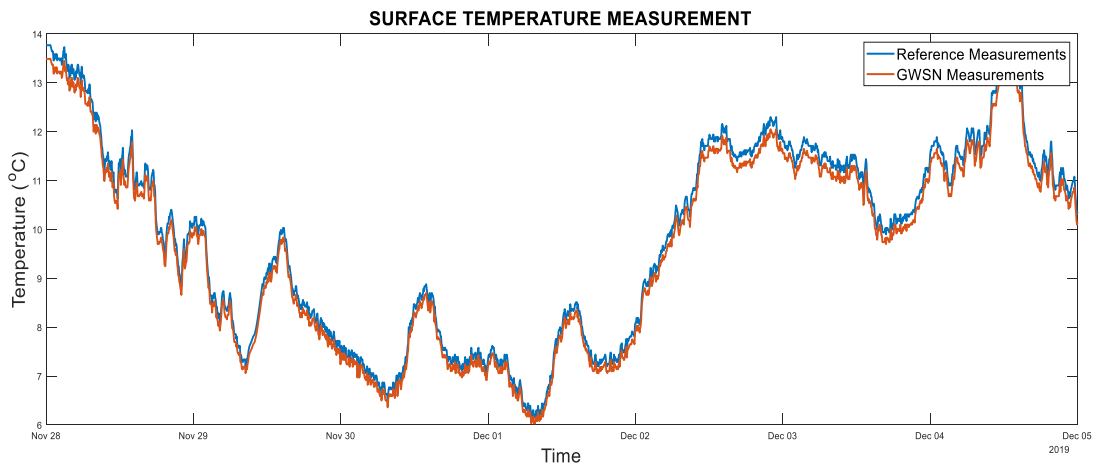


Figure 4.2. A plot showing a surface temperature measurements comparison between reference measurement and measurement taken using GWSN.

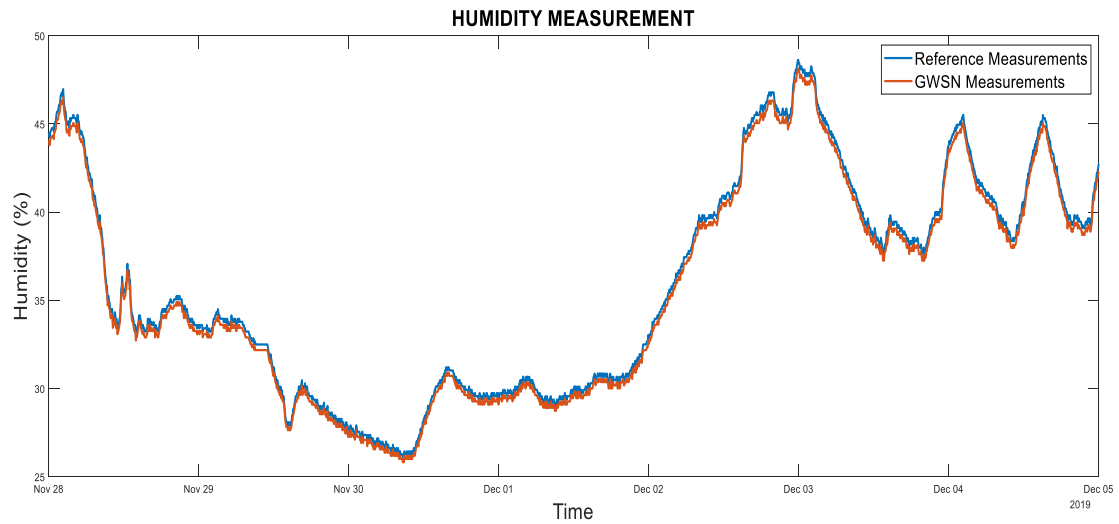


Figure 4.3. A plot showing humidity measurements comparison between reference measurement and measurement taken using GWSN.

Table 4.2. Summary of thermal performance measurement system response when compared to the reference or standard measurements.

Parameters	Air Temperature (°C)	Surface Temperature (°C)	Relative Humidity (%)
Accuracy	98 %	98 %	99 %

4.1.2 Theoretical U-value calculation

In order to verify the suitability of the measuring system, the u-values measured in situ must be compared with the calculated values. A commercial software BRE U-value Calculator[160], is normally used for comparison provided all the material properties are known or can be estimated or assumed. Though, from the study conducted by [161], it has been observed that, the u-value obtained from calculation method is always overestimated and in situ measurements gives better results than that from u-value calculation.

BRE U-value Calculator uses British standard ISO 6946:2007[76], for u-value calculation. From the standard, the thermal transmittance of the building material is the inverse of the thermal resistance. Theoretical total resistance (RT) of the building material comprised of the uniform layer perpendicular to the heat flux is calculated using Equation (4.1).

$$R_T = \left(\frac{m^2 \cdot K}{W} \right) = \frac{1}{U} = R_{si} + R_1 + R_2 \dots + R_N + R_{se} \quad (4.1)$$

Whereby.

R_T = Total thermal resistance in $m^2 \cdot K/W$

U = is the thermal transmittance, in $W/(m^2 \cdot K)$

$R_1 + R_2 + \dots + R_N$ = Thermal resistances of each layer (from 1 to N) in $m^2 \cdot K/W$

R_{si} and R_{se} = Interior and exterior surface resistances in $m^2 \cdot K/W$. The equivalent model to represent how heat moves from the side of high temperature to the side of low temperature is presented in in Figure 4.4.

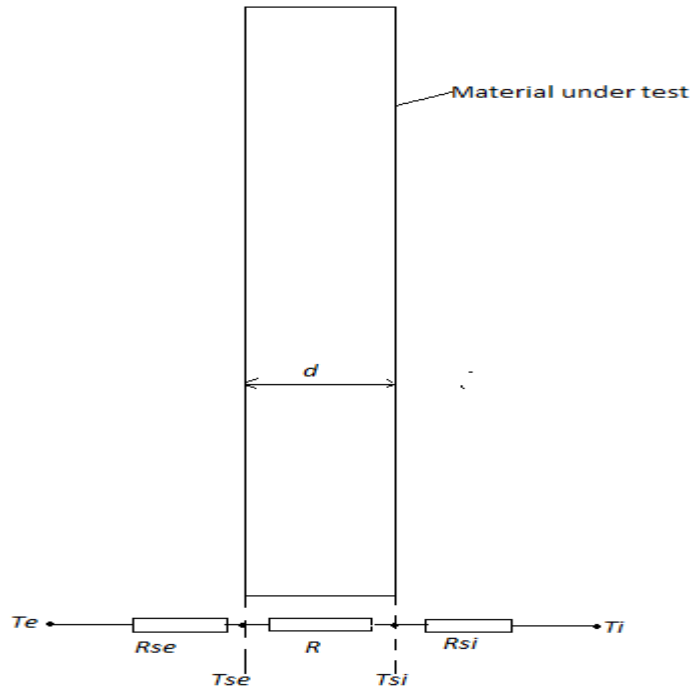


Figure 4.4. Diagram showing heat movement through the building material.

According to the British standard ISO 6946:2007[76], the values for exterior and interior surface resistances (R_{se} and R_{si}) of the bulky material for the horizontal heat flux is given as 0.04 and 0.14. By considering thickness of the material and thermal conductivity of the material under test, thermal resistance (R) can be determined using Equation (4.2).

$$R \left(\frac{m^2 \cdot K}{W} \right) = \frac{d}{\lambda} \quad (4.2)$$

Whereby.

R = Thermal resistance of the material $m^2 \cdot K/W$

d = is the thickness of the layer of the material in m

λ = is the design thermal conductivity of the material in $W/(m \cdot K)$.

Values of λ is calculated in accordance with ISO 10456[162] if based on measured data. In other cases, λ is obtained from tabulated values given in [162]. Provided all the material parameters are available, theoretical value will be determined and used to compare to the measured value. For this study, measured u-value was compared to the data provided in [1] and [2], since other required parameters like R_{se} and R_{si} were not given.

4.1.3 Thermal Performance Measurement

In order to meet the British Standard [73] with reduced power consumption, the heat flow method was customised, (see the proposed system architecture in Figure 4.5). A sensor node measures and transmits the following parameters via wireless communication to the gateway via the XBee communication module for further processing[3]:

- Ambient air temperature on both sides of the walls was noted as T_e and T_i with the unit of K (Kelvin).
- The surface temperature on both sides of the walls was noted as T_{se} and T_{si} with the unit of K (Kelvin).
- Heat flux through the walls (envelope), whose density is noted as Φ with the unit of W/m^2 .

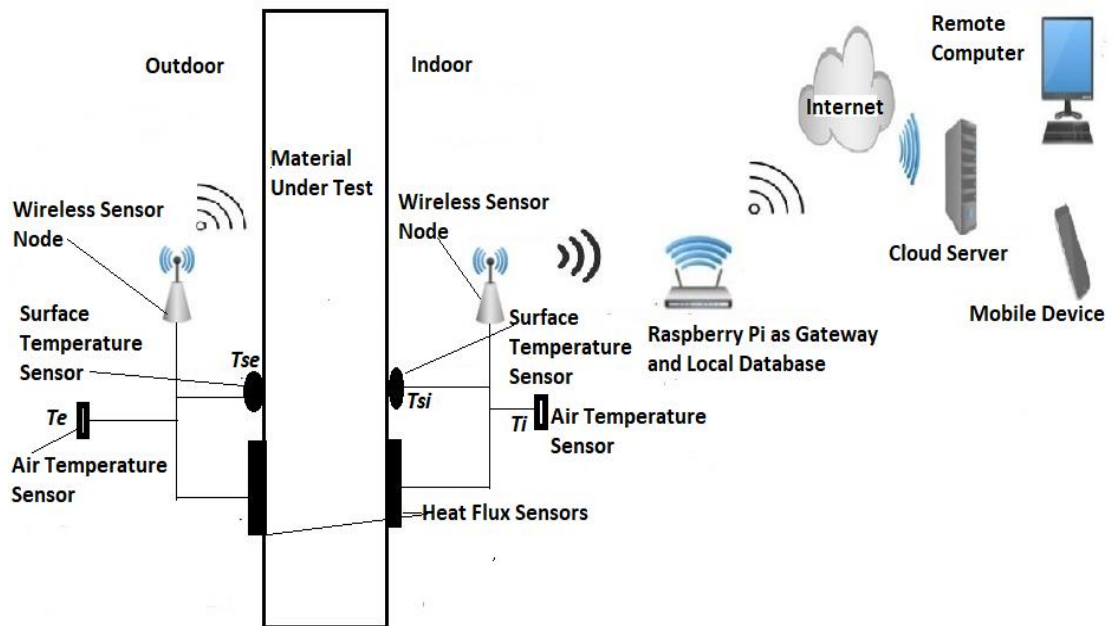


Figure 4.5. A diagram of a proposed measurement system architecture showing the position of the sensors, sensor nodes and flow of information from the sensor nodes, gateway node to the cloud [3].

This study employs direct computation to estimate thermal transmittance (U-Value in (1) with unit W/(m²K)), thermal resistance (R-Value in (2) with unit m²K/W), and thermal conductivity (Λ -Value in (3) with unit W/(m²K)), where j represents the jth measurement spot out of the number of measurement spots J. Heat is assumed to flow continuously throughout the material and the thermal mass can be safely neglected [73]. To obtain close approximate values, equations (4.1) to (4.3) have been treated in a standard manner [73] by taking the conventional method's factors and setup into account. The Matlab script used to implement average method for Equation (63) to (4.5) for the analysis is presented on Appendix 6.

$$U - Value = \frac{\sum_{j=1}^J \Phi_j}{\sum_{j=1}^J (T_{ij} - T_{ej})} \quad (4.3)$$

$$R - Value = \frac{\sum_{j=1}^J (T_{sij} - T_{sej})}{\sum_{j=1}^J \Phi_j} \quad (4.4)$$

$$\Lambda - Value = \frac{\sum_{j=1}^J \Phi_j}{\sum_{j=1}^J (T_{sij} - T_{sej})} \quad (4.5)$$

4.1.3.1 Experimental Setup

To validate the designed system, the sensors were installed to measure the thermal transmission value on one of the windows in the laboratory as shown in Figure 4.6. The heat flux, indoor and outdoor temperatures (surface and ambient) were continuously measured for seven days. BS Standard [73] recommends the Hukseflux HFP01-05 for heat flow measurement with a sensitivity of 62.2x10⁻⁶ V/(W/m²). The sensor was calibrated by the manufacturer after first being selected. Water- and moisture-resistant NTC thermistor B57020M2 sensors from EPCOS were used to measure surface temperatures. Air temperatures were measured from both sides of the structure under test using the HTM2500LF [133]. Despite being highly sensitive and stable, this sensor will not be harmed by immersion in water[3].

One wireless node was placed outside the window to measure outdoor air temperature and outdoor glass surface temperature. A second wireless node was placed indoors to measure the heat flow within the structure, the air temperature, and the surface temperature of the structure. The data was collected every five minutes and then sent to the gateway node for pre-processing, before being pushed into an SQL server[3]. All of

the measurements and sensor placements were performed as per BS ISO 9869 guidelines[73][3].

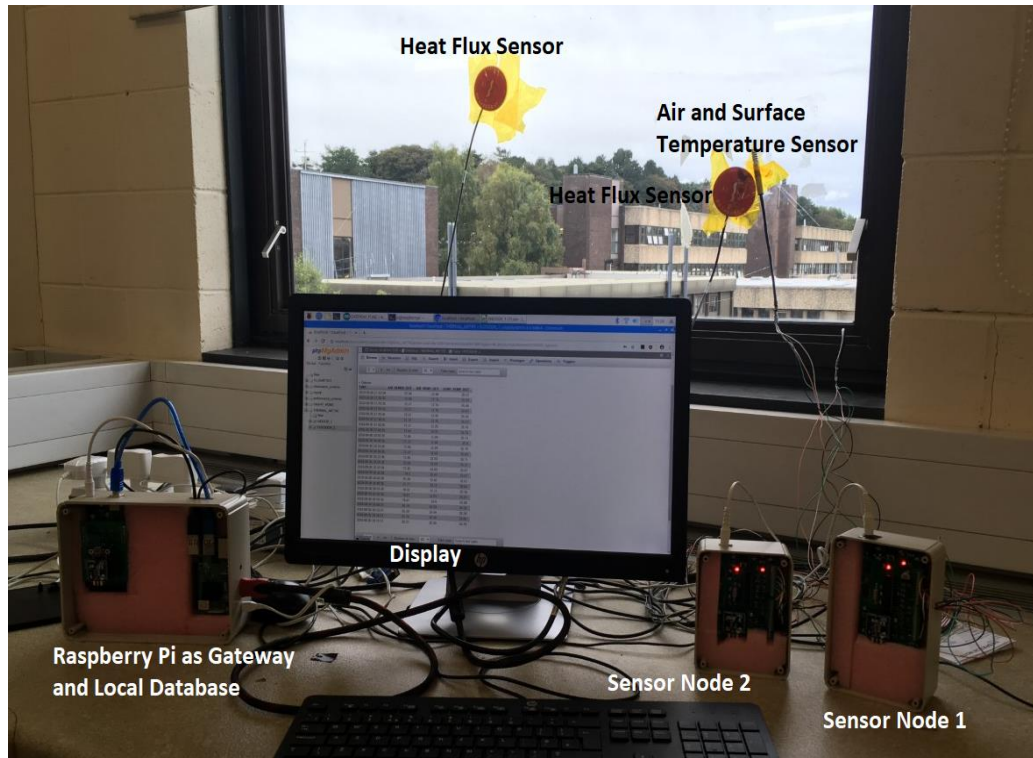


Figure 4.6. A picture of measurement setup for thermal performance of building material with heat flux and temperature sensors located on the MUT [3].

The seven-day measurement data is plotted in Figure 4.7. It can be observed that, for the entire duration of the measurement, the indoor and outdoor temperature difference was always greater than 10°C , the wind speed measured was less than 3m/s , and there was no direct solar radiation to the sensors (as the window faces North). To validate the designed system, thermal transmittance, thermal resistance, and thermal conductivity were calculated through (4.1) to (4.3) on three consecutive days, as advised in the British Standard [73]. The measurements and the range of typical U-values are shown in Figure 4.8 to 4.8 and summarised in Table 4.3[3]. The thermal performance value of the window glass under test is taken from [1] and [2].

From the seven-day measurements summarised in Table 4.3, Day 1 to Day 3, and Day 5 to Day 7 were relatively steady. The average values of thermal resistance and thermal conductance were also calculated using steady-state values from the measurements taken on Days 1 through 3. Thermal resistance on average was $0.025\text{ W}/(\text{m}^2\text{K})$, as shown in Figure 4.13, whereas thermal conductivity on average was $40\text{ W}/(\text{m}^2\text{K})$ [3], as shown in Figure 4.14.

Table 4.3. Summary of thermal transmittance measurement [3].

Measurement period (Day)	Typical U-value (W/m ² K)[1][2]	U-value measurement (W/m ² K)	Average U-value measurement (W/m ² K)
1-3	4.8-5.8	4.56-4.86, see Figure 4.4	4.82
2-4		4.55 - 4.78, see Figure 4.5	4.75
3-5		4.55 - 4.65, see Figure 4.6	4.65
4-6		4.64 – 4.79, see Figure 4.7	4.75
5-7		4.55 - 5.11, see Figure 4.8	4.85

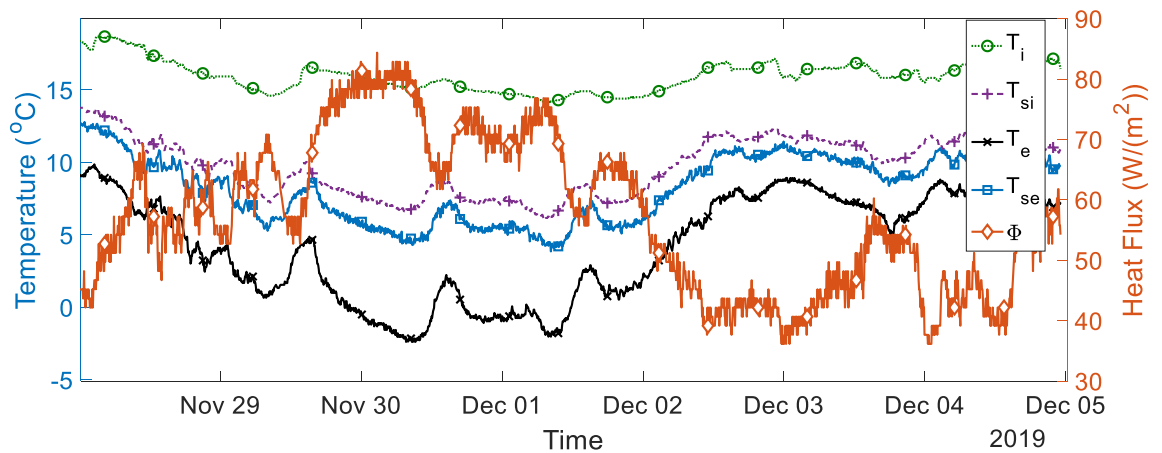


Figure 4.7. A plot for overall thermal transmission parameters measurement data for 7 days.

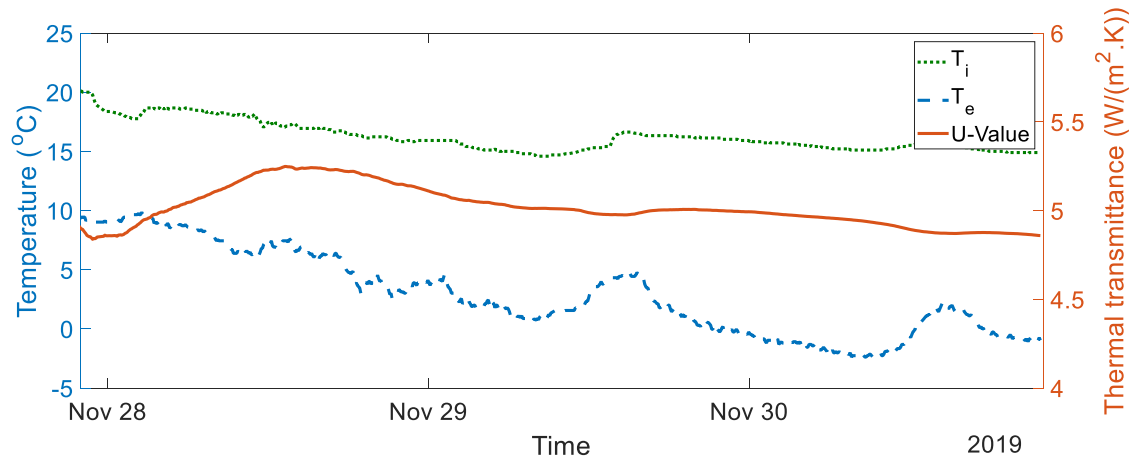


Figure 4.8. A plot for thermal transmittance measurement data from Day 1 to Day 3. ($\text{W}/(\text{m}^2\text{K})$).

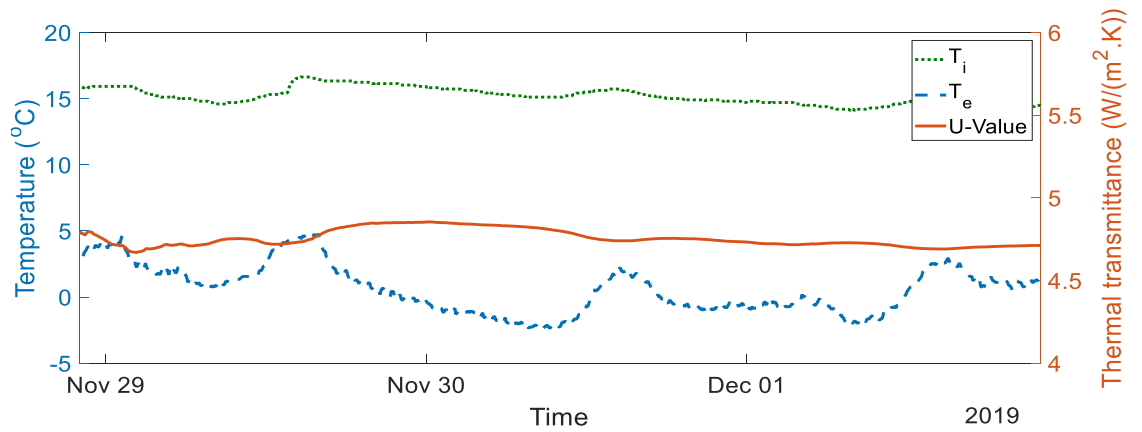


Figure 4.9. A plot for thermal transmittance measurement data between Day 2 and Day 4.

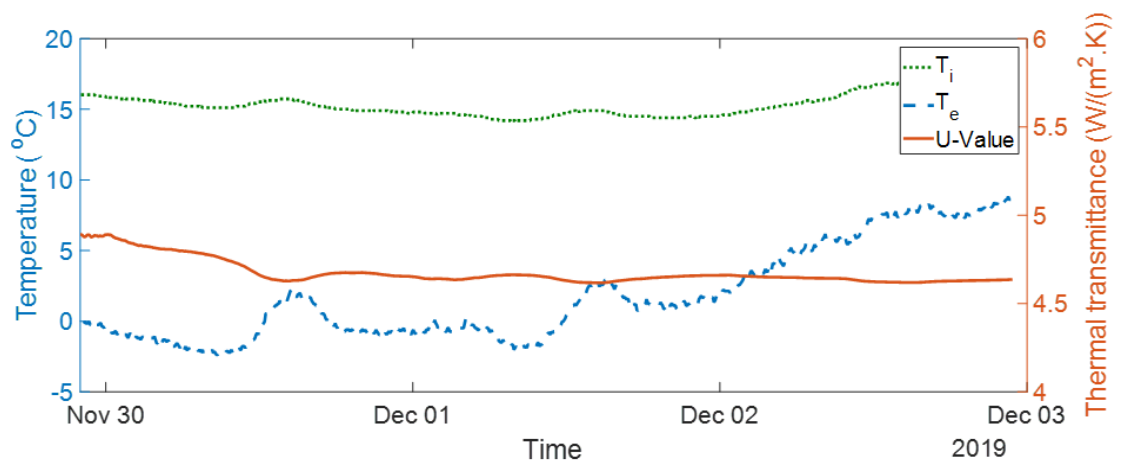


Figure 4.10. A plot for thermal transmittance measurement data between Day 3 and Day 5.

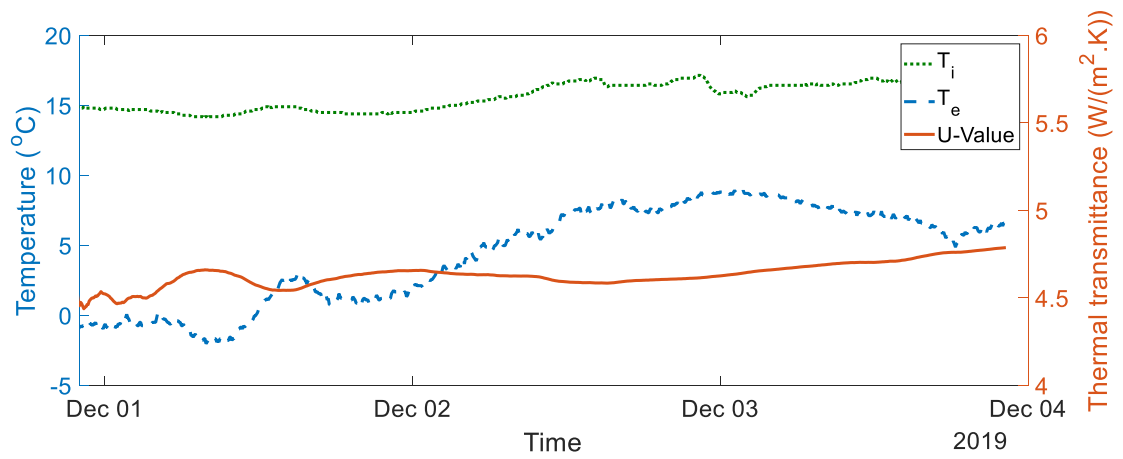


Figure 4.11. A plot for thermal transmittance measurement data between Day 4 and Day 6.

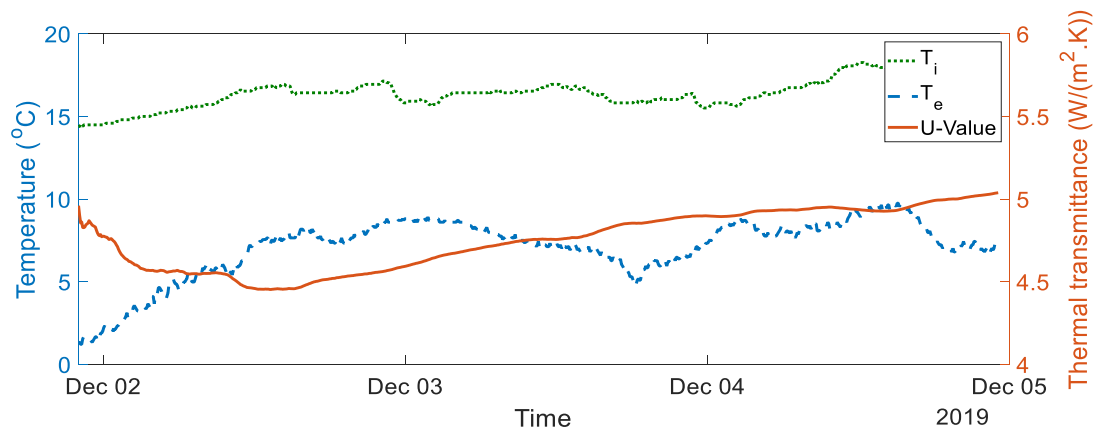


Figure 4.12. A plot for thermal transmittance measurement data between Day 5 and Day 7.

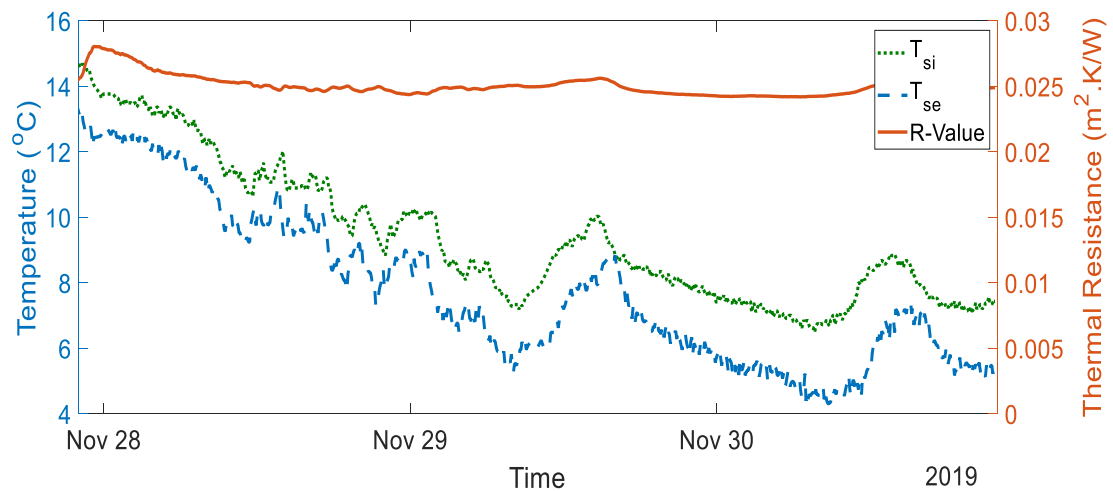


Figure 4.13. A plot for thermal resistance measurement data from Day 1 to Day 3.

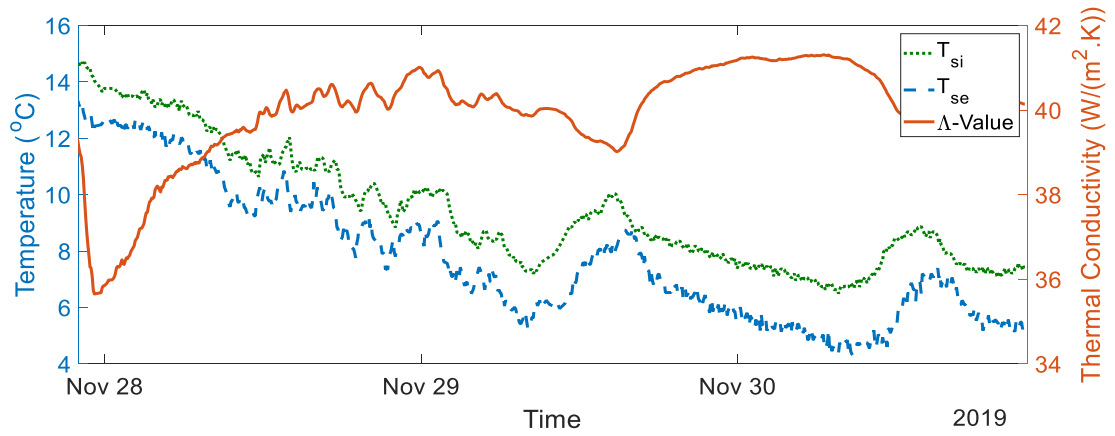


Figure 4.14. A plot fort thermal conductivity measurement data from Day 1 to Day 3.

According to estimates of the thermal performance data, the sample used in the experiment had a typical U-value between 4.8 and 5.8 W/m²K and a thermal resistance value of 0.025m²·K/W[1][2]. Thermal resistance values from the GWSN real-time measurement were between 0.025 and 0.03 m²K/W, with an average of 0.025 m²K/W, and thermal transmittance values varied between 4.55 and 5.11 W/m²K. Based on the data obtained, the results are within the range of typical values[3].

4.1.4 Summary of Thermal Performance Measurements

In this section, we have shown how the design of GWSN has eliminated the limitations of conventional heat flow meters. In principle, the GWSN works similar to a heat flow meter, but it has increased flexibility and greater performance. With its high resolution and low cost, the platform is an open platform. Additionally, it is compact, easy to customize, deployable, and maintainable[3].

4.1.5 Heat Loss in Real-Time

Using the measurement setup in Figure 4.6, real-time heat loss in materials was also recorded. This shows real-time temperature variations at different levels from outdoor air temperature to outdoor material surface temperature, then indoor material surface temperature to indoor air temperature. The observation for seven days is as shown in Figure 4.15.

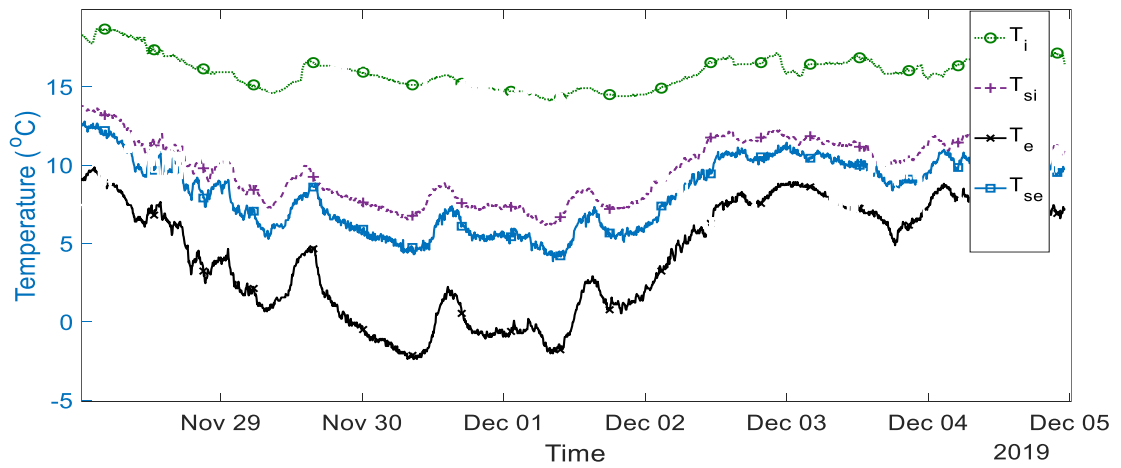


Figure 4.15. A plot showing a real-time temperature variations measurement data for external (surface and air) and internal (surface and air temperature) for 7 days.

Measured data were compared from time to time with the in-lab weather station to see the variations, and the results were the same. This tracking is used to analyse how building materials are responding to surrounding temperature variations.

4.1.6 Indoor Thermal Comfort Measurement

As suggested from the literature, thermal comfort can be predicted by simply measuring air temperature (T_i) and humidity (H_i) of the indoor environment. Using the setup in Figure 4.6, the value of indoor air humidity and the temperature were recorded for seven days. The observations are shown in Figure 4.16.

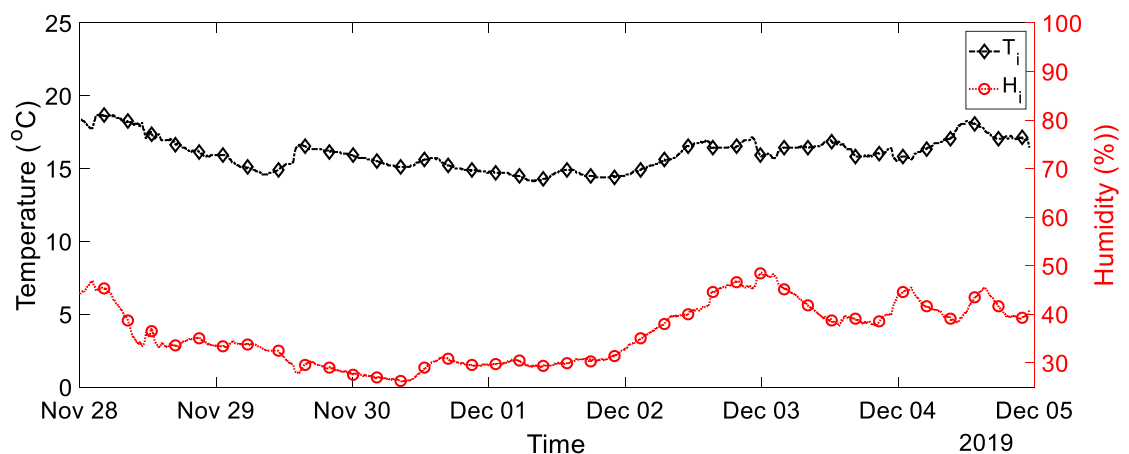


Figure 4.16. A plot showing thermal comfort variation for 7 days.

Measured data were compared from time to time with the in-lab weather station to see the variations, and the results were the same.

4.1.7 Hygrothermal Properties of the Building Environment

The proposed methodology measures the fluctuation of internal air moisture relative to, in-material air moisture, and external fluctuation. The parameters are compared to see how the material responds to the fluctuation in moisture levels.

In the proposed setup (see Figure 4.17), moisture is measured in different layers of the building envelope. Collected data is sent wirelessly to the gateway for processing. The gateway forwards data to the remote server for storage and allows real-time monitoring, visualisation, and analysis.

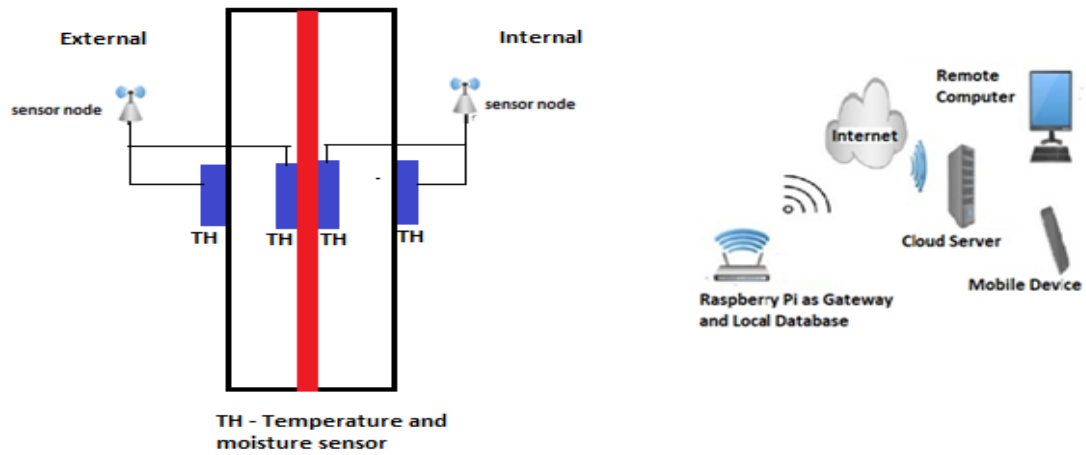


Figure 4.17. A diagram for moisture measurement setup showing location of sensors (with red line presenting inner layer of the material), sensor nodes and how data are communicated from the nodes to the cloud.

Using the setup in Figure 4.6, only the variations on both sides of the materials were measured. This is due to the nature of the MUT, which is a single glazed window. The summary of variation for seven days is shown in Figure 4.18.

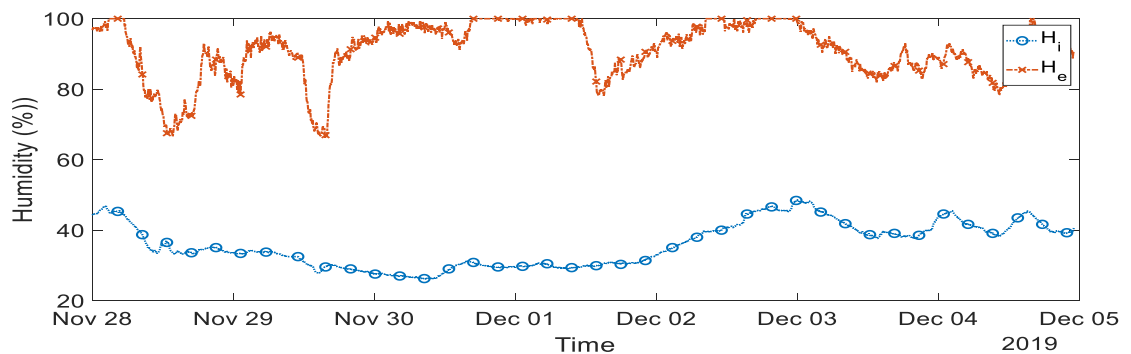


Figure 4.18. A plot showing humidity variations between indoor and outdoor for 7 days.

Measured humidity was compared from time to time with the standard measurements. Using this humidity variation along with the temperature variations measured in Figure 4.15, the hygrothermal properties of the building materials can be analysed.

4.1.8 Building Indoor Air Quality

4.1.8.1 Sensing System Calibration

This section presents how the GWSN is configured and used in IAQ applications. The sensors used include: the COZIR Ambient CO₂ sensor for carbon dioxide measurement, the Sharp Photoelectric Dust Sensor for PM_{2.5}, and the TGS2602 sensor for VOCs. Since the COZIR Ambient CO₂ sensor and Dust sensors are calibrated by the manufacturers, after the interface with the GWSN the measurements were taken and compared with the standard IAQ measurement system. The IAQ measurement system accuracy and operating ranges are summarised in Table 4.4.

Table 4.4. Reference IAQ measuring system range and accuracy

Parameters	Measuring Range	Accuracy
Carbon dioxide	0 to 5000ppm	± 10
Total Volatile Organic Compounds	0.001 to 9.999 mg/M ³	± 10
Particulate Matter (PM 2.5)	0 to 999 µg/M ³	± 10
Temperature	0 to 50 °C	± 1
Humidity	20 to 90 %RH	± 4

A 1-week measurement was performed to provide calibration of the system and estimate the accuracy. During calibration, the system was configured to take measurements after every minute. The GWSN system reading was compared to the standard IAQ measurement system reading, and the comparison between reference CO₂ is presented in Figure and summarised in Table 4.5. For the TGS2602 sensor, the calibration was done separately.

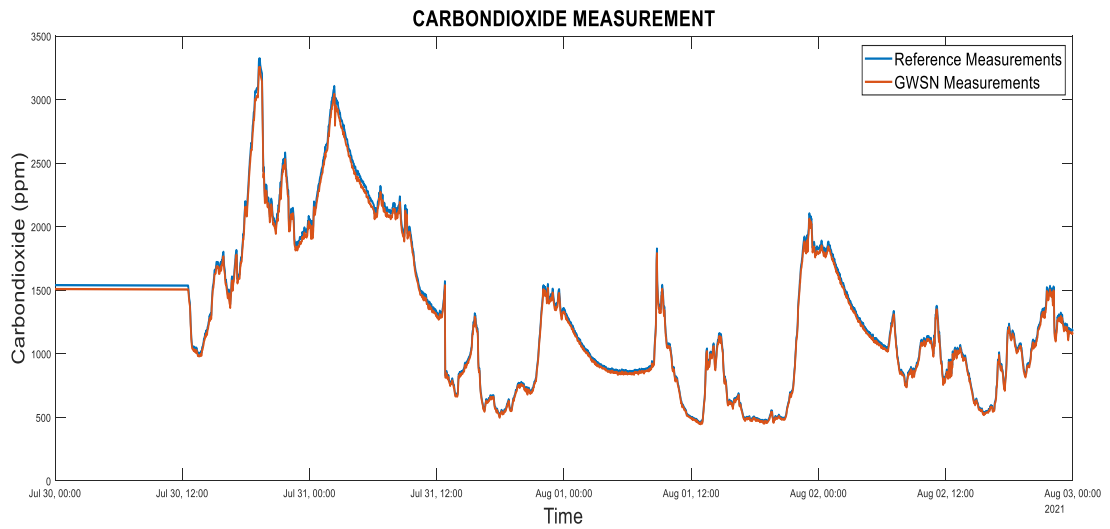


Figure 4.19. A plot showing CO₂ measurements comparison between reference measurements and the measurements taken by GWSN

Table 4.5. GWSN performance for CO₂ measurements.

Parameters	Carbon dioxide (ppm)
Accuracy	98 %

4.1.9 TGS2602 Sensor Calibration

The sensor used for measuring VOCs is the TGS2602 from Figaro[141]. The sensor requires calibration before usage. This requires the use of special chambers and standard reference equipment. Currently, the special chamber used for maintaining gas concentrations at a certain level, the gas generators, and the device for tracking gas concentrations are very expensive to acquire. In order to address these challenges, this study introduces a novel logarithmic calibration model that does not require calibration at any predefined levels, and therefore can eliminate the need for a special calibration chamber.

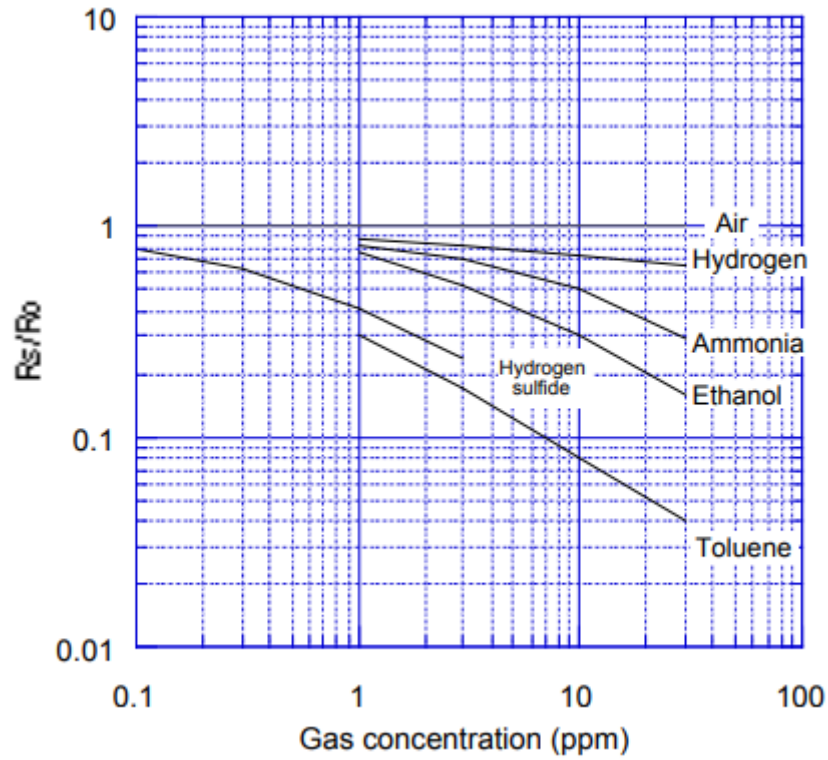


Figure 4.20. A plot showing sensitivity characteristics of TGS2602 for various organic compounds [141].

Using typical sensitivity characteristics (as shown in Figure 4.20), the value of ppm is evaluated. Once the ratio R_s/R_o (X-axis) is calculated, then the value of ppm (Y-axis) can be evaluated. From the graph, the value of ratio $R_s/R_o=1$ and is used as reference. From the datasheet, sensor resistance (R_s) is given by Equation (4.6).

$$R_s = \left(\frac{V_{cc}}{V_{RL}} - 1 \right) R_L \quad (4.6)$$

Whereby.

V_{cc} is the supply voltage

R_L is the load resistance

V_{RL} is Load voltage

The value of R_o is obtained by calculating the value of R_s in the fresh air. This is achieved by measuring the sensor value and converting the average value into voltage; then, by the use of the R_s formula in the Equation 4.4, R_o is evaluated. Step by step calibration of the sensor is presented in Appendix 7.

Using the written C program, the values of load voltage (V_{RL}) and sensor resistance can also be calculated. Since the value of R_o is varying, the sensor should be allowed to pre-

heat for 10 hrs to obtain the required value of Ro. The complete program to determine ppm using the TGS2602 sensor is provided as separate attachment.

The VOC sensor TGS2602's voltage output signal is modelled in Equation (4.7) using an approximate logarithmic conversion model as:

$$\log(y) = m * \log(x) + b \quad (4.7)$$

Whereby:

y = ratio (Rs/Ro)

x = ppm values

m = gradient of the line

b = point of intersection

From the typical sensitivity characteristics of TGS2602 sensor in Figure 4.20. A plot showing sensitivity characteristics of TGS2602 for various organic compounds [141], the calculated values of m and b are as summarised in Table 4.6.

Table 4.6. Logarithmic conversion model parameters are estimated from measurement data using the logarithmic estimation method.

Gas	The slope of the line (m)	Intersection point(b)
Hydrogen	-0.138362901	-0.003862722
Ammonia	-0.251929636	-0.045757491
Ethanol	-0.615822437	0.064498379
Hydrogen Sulphide	-0.376451093	-0.405100498
Toluene	-0.574031268	-0.511596672

Using the value of m and b obtained in Table 4.6, the value of ppm can be evaluated using Equation (4.8):

$$ppm = 10^{\frac{(\log(ratio)-b)}{m}} \quad (4.8)$$

Whereby:

ppm= gas value in parts per million

m = slope of the line

b = intersection point

$$ratio = R_s / R_o$$

Due to the unavailability of a professional chamber for measuring the individual gases, the TGS2602 sensor was calibrated by measuring the total volatile organic compounds (TVOCs), and the results were compared to the standard device. The summary of the response is shown in Table 4.7 and the comparison between the reference measurements and GWSN measurements is presented in Figure 4.21.

Table 4.7. GWSN measurement performance on VOC measurements

Parameters	TVOCs(ppm)
Accuracy	97 %

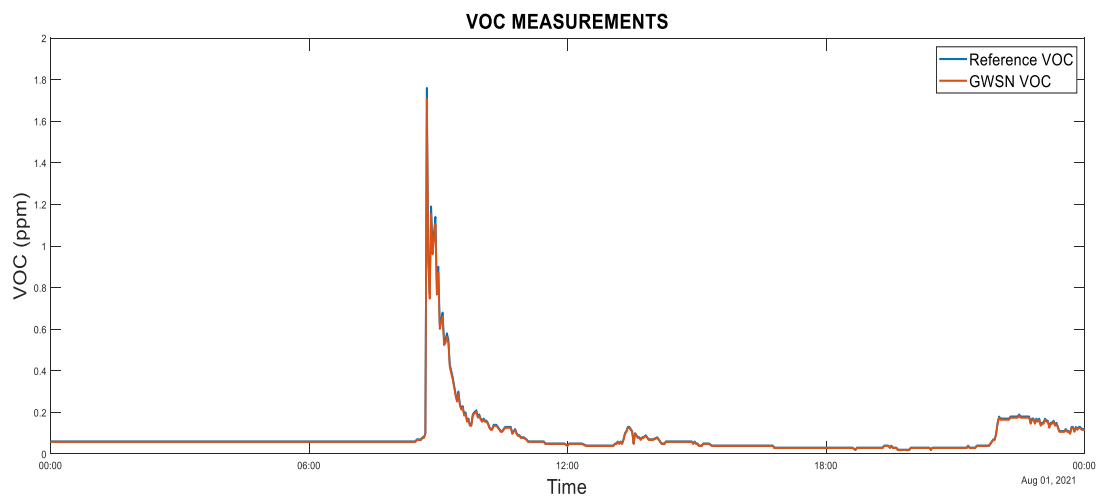


Figure 4.21. A plot for VOC measurements comparison between the reference measurements and measurement taken using GWSN.

4.1.10 Summary of Indoor Air Quality Measurements

This section presented how a GWSN) can be configured and used to measure IAQ). Selected sensors were interfaced with the node, and the system was configured based on the requirement of each sensor. Firmware was implemented for sensor data extraction, processing, and storage. The results from the Carbon dioxide sensor and Dust sensor were compared to a commercially available IAQ measurement system, and the accuracies were 98 % and 97 % respectively.

For the micro gas sensor (TGS2602), a novel logarithmic model for sensor calibration was introduced and implemented. This replaced expensive conventional calibration methods that require a special chamber with a reference tool for tracking reference gas concentration. After the characterisation, the measurements from TGS2602 were compared to those of a commercially available IAQ measurement system, and the accuracy was 97 %.

4.1.11 Building Material Acoustic Measurement

This section explains what has been done in calibrating the designed system and explores the proposed methodology for airborne sound insulation.

4.1.11.1 Acoustic Sensing System Calibration

Testing of the acoustic sensing nodes took place in a reverberant chamber. This removes the influence that positioning, or reverberation of the surface can have on sound pressure level readings by creating a diffused sound field. During laboratory measurement, the system under calibration and a Bruel & Kjaer Type 2250[163], sensor, (a standard sound level meter (SLM)) were placed on one side of the reverberant room, whilst the sound source Bruel & Kjaer Type 4224[164] [117] sensor was placed in the other corner of the reverberant room, as shown in Figure 4.22.

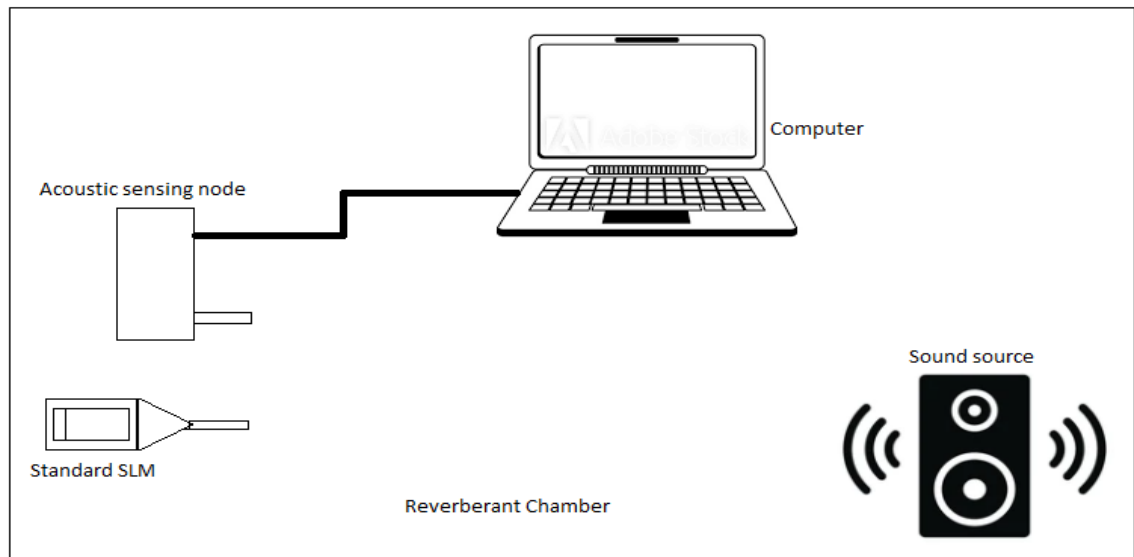


Figure 4.22. Setup for laboratory calibration of the acoustic sensing system. Bruel & Kjaer Type 2250 SLM and acoustic sensor microphones were placed in two different points in the reverberation chamber. The acoustic sensing system was connected to the computer for data visualisation and power supply to the GWSN.

The sound source was adjusted to produce different sound pressure levels. The sound level in dB was recorded using a standard SLM, whilst the ADC values were recorded from the device under test. The recorded values are as shown in the plot in Figure 4.23. Since the dB values are not linear to the ADC values, the linear model is implemented to predict the value of dB from measured values.

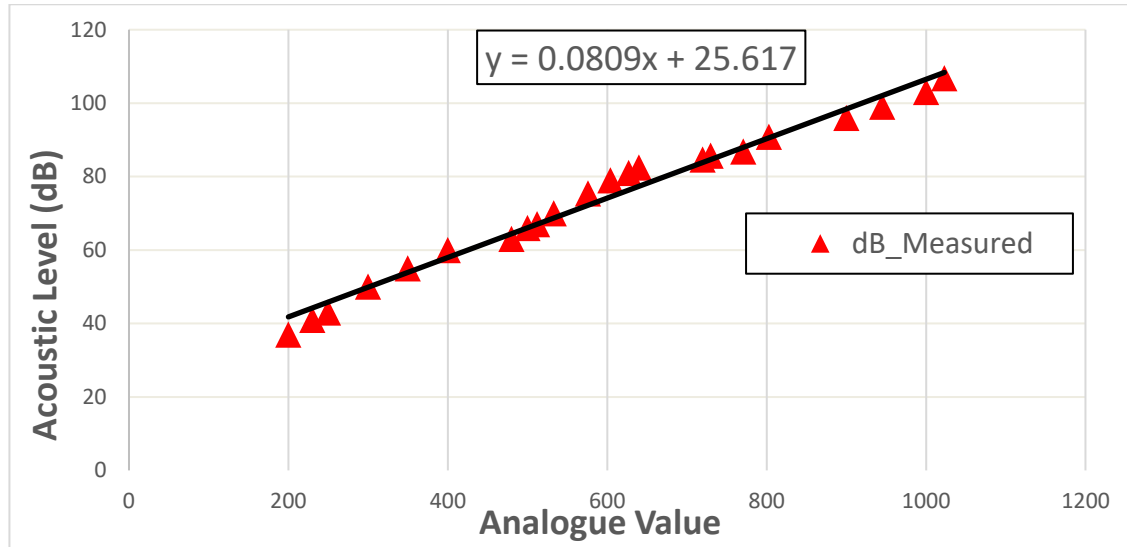


Figure 4.23. A plot of a linear fit created from measured acoustic data for acoustic sensor calibration.

From the graph, the values of dB from the standard SLM are not linear to the ADC values recorded from the designed acoustic sensing system. Since there is one input x and one output y , the basic linear regression model is applied and used to predict the values of dB from the measured ADC values. The basic linear model can be presented as in Equation (4.9) and the output of regression model is summarised in Table 4.8:

$$y[n] = b + mx[n] \quad (4.9)$$

Whereby:

y = output

x = input

b = line intercept

m = slope of the line

In Appendix 8, the measured value of acoustic and its corresponding dB values from standard acoustic meter is used with regression model to evaluate the measured value in

dB. The pictures showing the equipment used for acoustic measurements and their arrangements is shown in Figure 4.24.



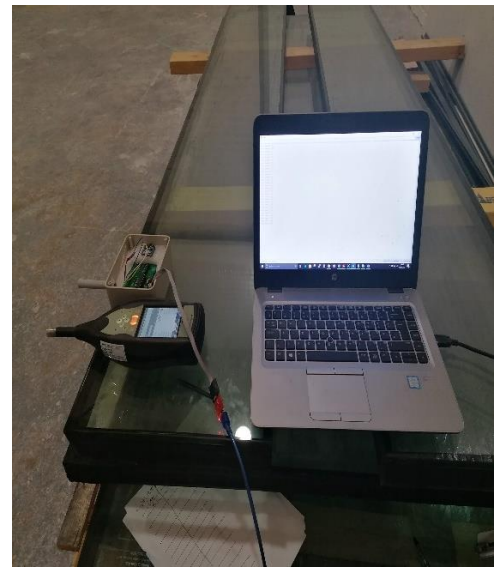
(a)



(b)



(c)



(d)

Figure 4.24. Acoustic measurements and calibration at EGIS reverberant chamber. (a)The reverberant chamber entrance, (b) Sound source (Brüel & Kjær Type 4224) used during measurements, (c) Sound source position during measurements, (d) GWSN and Standard SLM (Brüel & Kjær Type 2250) position during measurements

Table 4.8. Linear regression model output from the measured acoustic data

Parameter	Model	Intercept (b)	Slope (m)	Unit of y
Acoustic	Equation 4.7	25.617	0.081	Decibel (dB)

Using the values of intercept and slope in Table 4.8, the predicted dB is evaluated. Linear regression Equation (4.10) becomes:

$$dB_{predicted} = b + m * ADC_{measured} \quad (4.10)$$

Whereby:

$dB_{predicted}$ = Predicted sound level in dB

b = line intercept

m = Slope of the line

$ADC_{measured}$ = Measured analogue value

The complete program to evaluate the dB value is presented as a separate attachment. In this section, only two important lines are explained. To achieve continuous measurement and evaluation of dB values of the acoustic signal, ADC values are continuously read from the analogue pin of the sensing node. The comparison between the reference measurements and GWSN measurements is presented in Figure 4.25. A plot of sound level measurements comparison between Reference measurements and the measurements taken using GWSN. Summary of the observation is shown in Table 4.9.

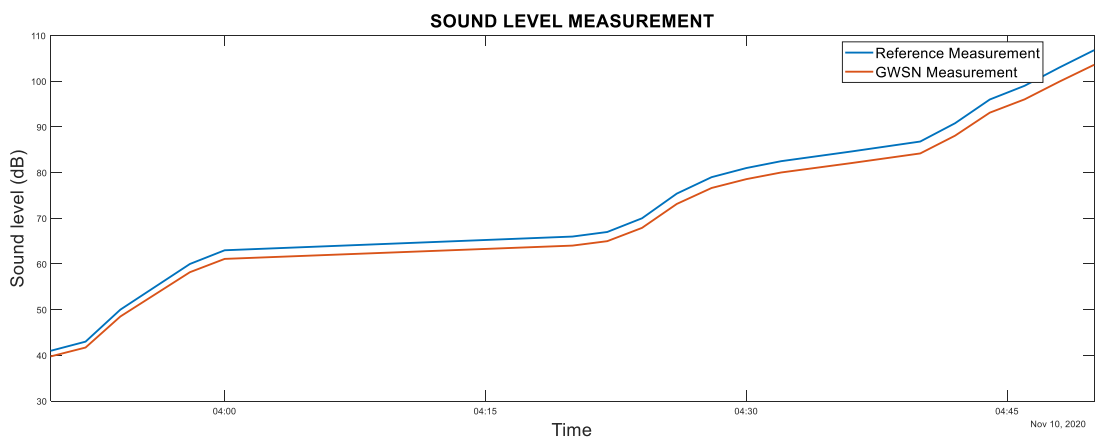


Figure 4.25. A plot of sound level measurements comparison between Reference measurements and the measurements taken using GWSN.

Table 4.9. GWSN sound/acoustic level measurements response

Parameters	Sound Level (ppm)
Accuracy	97 %

4.1.12 Airborne Sound Insulation Measurement

In the proposed methodology, a sound source is located on one side of the material/structure under test, and a constant sound level is applied. Using the sensor located on both sides of the material and two sensors located on the cavities (between bricks and insulating material), sound levels are measured and used to determine the absorption level of the material or structure. In the proposed setup of Figure 4.26, the sound level will be measured in different layers of the building envelope. Collected data will be sent wirelessly to the gateway for processing. The gateway will forward data to the remote server for storage and allow real-time monitoring, visualisation, and analysis.

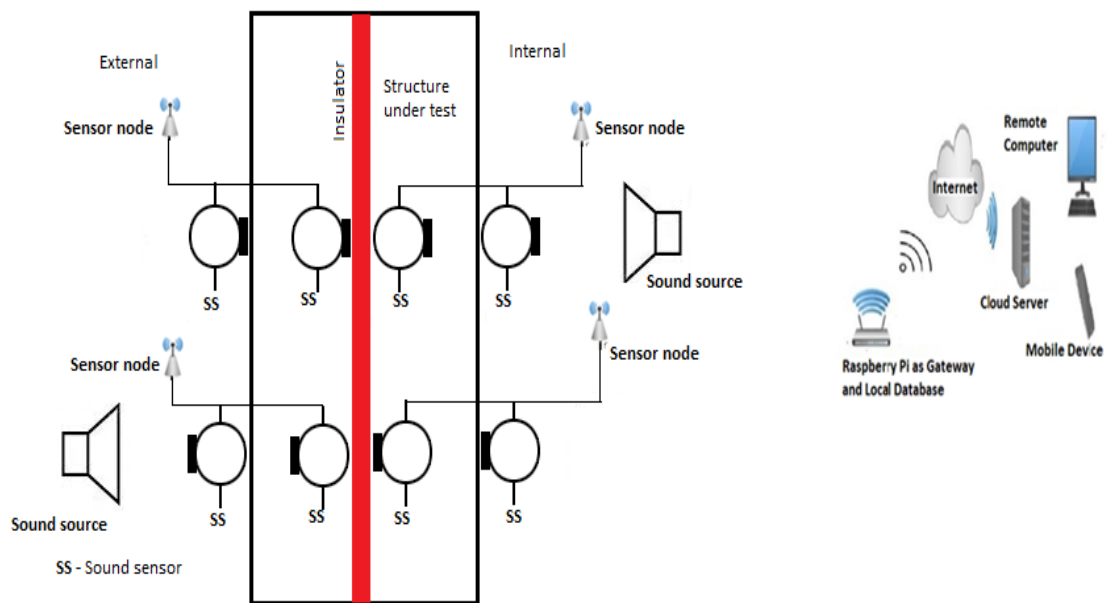


Figure 4.26. A diagram for acoustic measurement showing the location of sensor (with red line presenting inner layer of the material), sensor nodes, sound sources and the flow data from the nodes to the cloud through the gateway.

For the new structures, acoustic sensors can be embedded within the structure to increase the resolution of the measurements. It also helps to determine the reduction index in different layers especially in the structure that contains multiple layers. For the existing structures, sensors are positioned in two sides of the material under test and the acoustic levels are collected and compared to see how much signal has been attenuated as travelling from the side of acoustic source to other side of the material through the material. The incident signal and transmitted signal through the material is used to determine the sound reduction index (SRI) of the material.

4.1.13 Summary of Acoustic Measurement

This section presented how a GWSN can be configured and used to measure acoustic levels. Selected sensors were interfaced with the node and the system was configured based on the requirements of each sensor. Firmware was implemented for sensor data extraction, processing, and storage. To achieve dB conversion, a novel linear model for sensor calibration was introduced and implemented.

The designed system has been tested over the range of 55 dB to 106 dB at 97 % accuracy and compared to the Class one Bruel & Kjaer Type 2250 SLM. The custom-made acoustic sensing system is inexpensive, low-powered, and easily extended when more sensing nodes are needed. It can also be configured to be used in general-purpose noise measurement.

4.2 Conclusion

This chapter has provided detailed information on the facilities, testing methods, and equipment that was used, explaining how and where the work was carried out; it has also described the experiments which were conducted, essentially explaining what was done and why. As an alternative to conventional measurements methods, the GWSN proposed in this chapter combines the following features [3]:

- a) Data can be collected and processed by the GWSN in real time.
- b) In accordance with a user's specifications or the requirements of the measurements, GWSN can take any number of measurements at any time interval.
- c) Different measurements can be taken within 100 m indoors or 1.2 km outdoors by using the same gateway (the coordinator node).

- d) Internet access allows remote access to these measurements, and the gateway can be reconfigured remotely at any time from any location.
- e) Internet access can be easily accessed through WiFi or cable.
- f) The GWSN is accurate, cheap, and small in size.

GWSN also offers the capability of storing, processing, and allowing remote access to information via the gateway, which consists of an embedded system (the Raspberry Pi). With more sensors in different rooms or buildings, the star network can be converted into a mesh network[3]. In the next chapter, new sensing platforms using backscatter technology is introduced. The theory of modulation and the spread spectrum technique used in backscattering is explored. The trade-off between hardware complexity/power consumption and link performance is also investigated.

Chapter Five

Universal Backscatter tag

5 Introduction

As the number of applications that demand extended battery life and free maintenance increases, it becomes difficult to use COTS devices like BLE, XBee, LoRa, and WiFi (described in previous sections). In this chapter, backscatter communication is introduced.

Backscatter communication is concerned with shifting the power-consuming radio frequency (RF) carrier synthesis functions to carrier emitters (which can be dedicated or ambient)[165]. When compared to backscatter radio, conventional radio (as shown in Figure 5.1(a)) contains active devices like mixers, power amplifiers, low noise amplifiers etc., and all these devices demand dedicated power sources to make them operate, thus contributing to maximum power consumption. Backscatter passive radio (see Figure 5.1(b)) contains an antenna with terminations impedance toggled by switches to achieve either signal absorption or signal reflection[166].

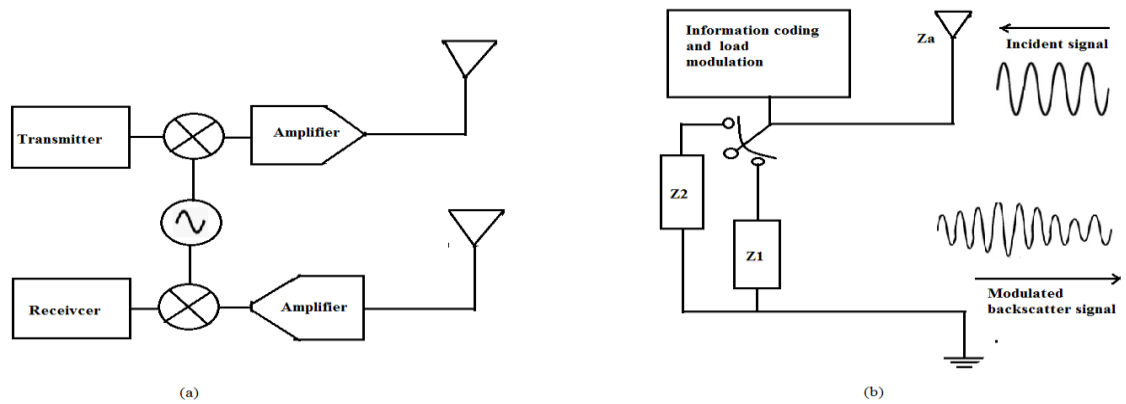


Figure 5.1. A diagram of communication systems (a) Conventional radio (b) Backscatter passive radio [166].

Backscatter communication technology removes the costly and power-hungry RF frontends (e.g. mixers and power amplifiers), and facilitates communication using lower power than that of conventional radios[167].

Despite this development in technology, some challenges still hinder the practicality of backscatter in some applications. Some limitations are: power consumption, bandwidth utilisation, cost, and maintenance (battery replacement)[167]. Also, most of the research

so far has focused on single-carrier backscattering, and the modulators used are specific for a certain type of modulation and are not transferable[165]. This part of the research will focus on the theory of modulation and spread spectrum techniques used in backscattering and investigate the trade-off between hardware complexity/power consumption and link performance. The implementation of the multicarrier backscattering technique and harmonic suppression in frequency-shifted backscatter systems to enhance bandwidth utilisation will be explained in Chapter Six.

5.1 State of the Art Literature Backscatter Modulations

5.1.1 Amplitude Shift Keying (ASK)

Conventional ASK is concerned with varying the amplitude of the high-frequency carrier by the information signal. In backscatter communication, a commercial radio frequency identification (RFID) Tag uses an ASK scheme, whereby variation is achieved by the ON-OFF keying (OOK) method. The OOK is performed by switching between the matched load impedance and a full reflection circuit for the tag antenna. This allows the electromagnetic waves received by an antenna to be either scattered or absorbed by the sequence controlled by the information from the respective tag[168]. The backscattered signal will be received by the use of a simple envelope detection circuit, before sampling and decoding to recover the information backscattered from the tag. Using single throw multi throw switches (as in Figure 5.2) or controllable impedance devices, a higher-order ASK modulation can be achieved[169].

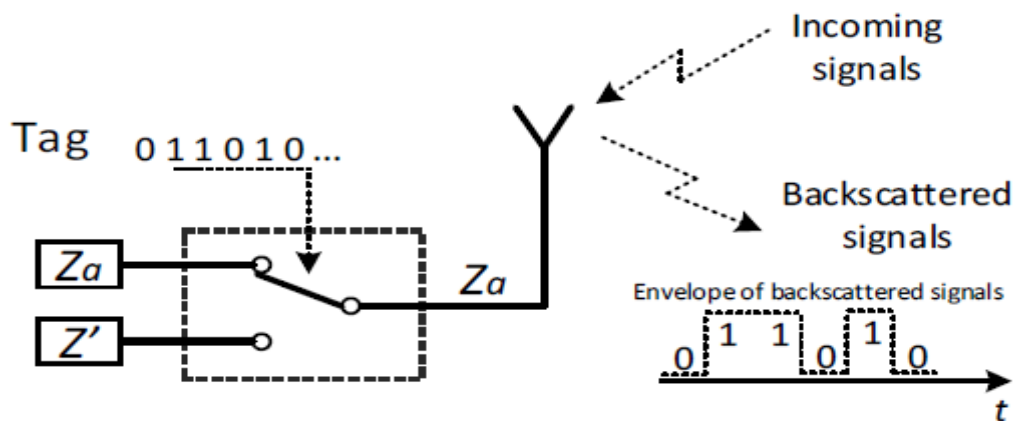


Figure 5.2. A schematics to illustrate a tag backscattering using OOK modulated signals with tag impedance Z_a an Z' and antenna impedance Z_a [165].

For a basic OOK, the antenna termination impedance should be designed with maximum separation between them, whilst for the higher order ASK termination, impedances should fall within the reflection coefficient circle separated by equal radius intervals, as in Figure 5.3. ASK is popular because of its simplicity in terms of transmission and reception, since no frequency or phase reference is required. The main problem with ASK is that it is highly susceptible to noise[165].

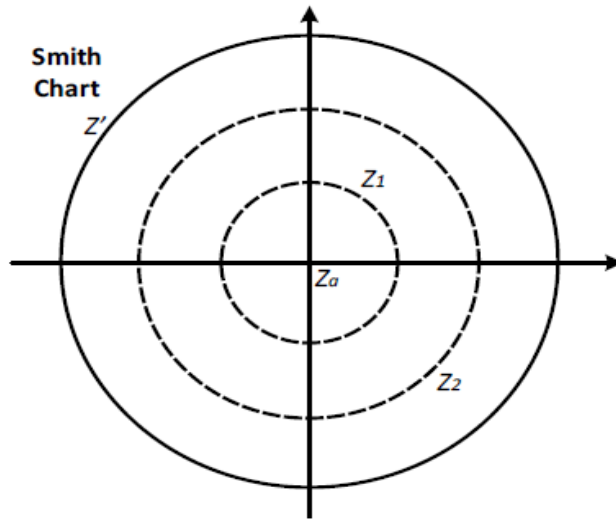


Figure 5.3. A smith chart plot showing design guidance on antenna termination impedance for ASK modulation with impedance allocation [165].

5.1.2 Frequency Shift Keying (FSK)

FSK modulation is a type of modulation that is concerned with varying the frequency of the high-frequency carrier with respect to the information signal. FSK is achieved by varying the termination impedances connected to the antenna according to the modulation frequency shift, and thus the backscattering communication [170][171]. High order FSK was also implemented in[172].

To achieve maximum power in FSK modulation in Figure 5.4, termination impedances Z_1 and Z_2 should be oppositely located in the outermost reflection coefficient circle on the Smith chart in Figure 5.5[165]. FSK backscattering differs from ASK, in that it offers more resilience to noise.

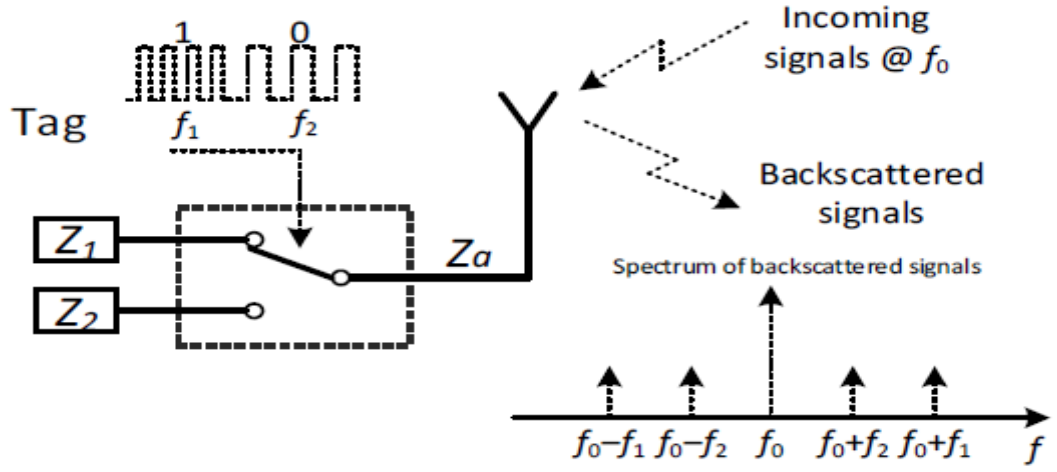


Figure 5.4. A schematic for illustration of a tag backscattering using 2FSK modulated signals with tag impedance Z_1 and Z_2 and antenna impedance Z_a [165].

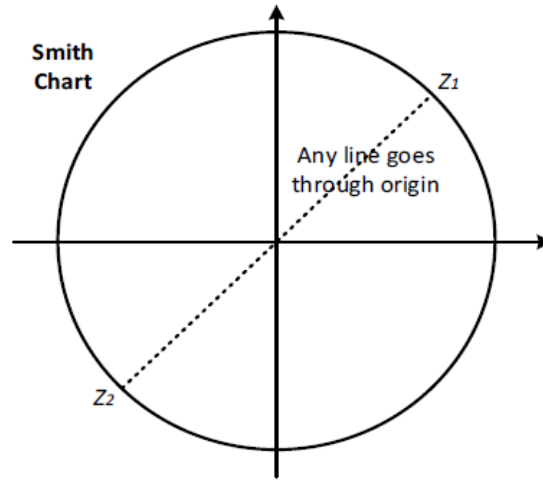


Figure 5.5. A Smith chart plot showing a design guidance on antenna termination impedance Z_1 and Z_2 for 2FSK modulation [165].

5.1.3 Phase Shift Keying (PSK)

PSK is the type of modulation whereby a phase of the carrier is varied in accordance with the information. In backscatter communication, when the incoming signal is a one-tone continuous wave, the phase of the backscatter signal is determined by the termination impedances. To achieve N-order PSK backscatter modulation, several uniformly separated loads in a reflection coefficient circle are required[165]. Also, several switching circuits controlled by the information signal are required[173]. The arrangement is as shown in Figure 5.6, and the load location on the Smith chart is shown in Figure 5.7.

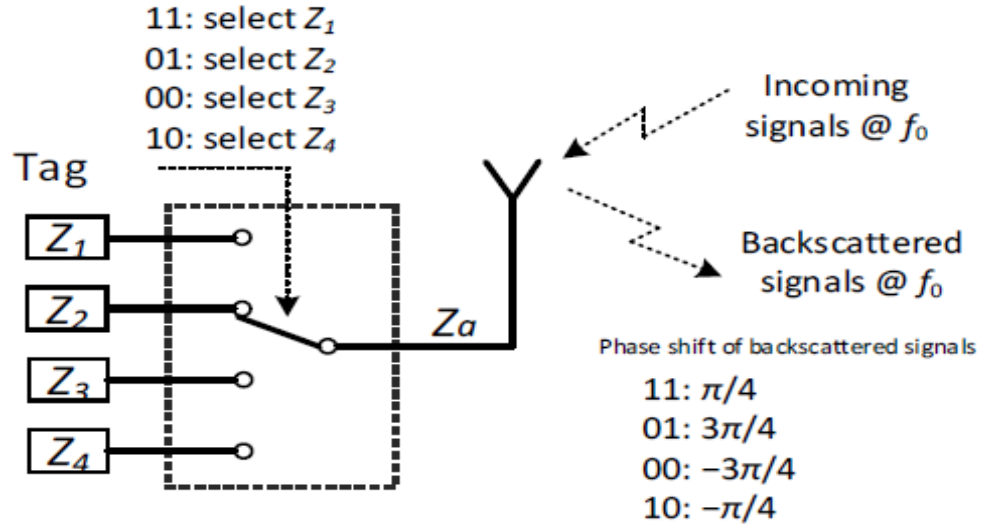


Figure 5.6. A schematic for illustration of a tag backscattering using QPSK modulated signal with tag impedance Z_1 , Z_2 , Z_3 and Z_4 and antenna impedance of Z_a [165].

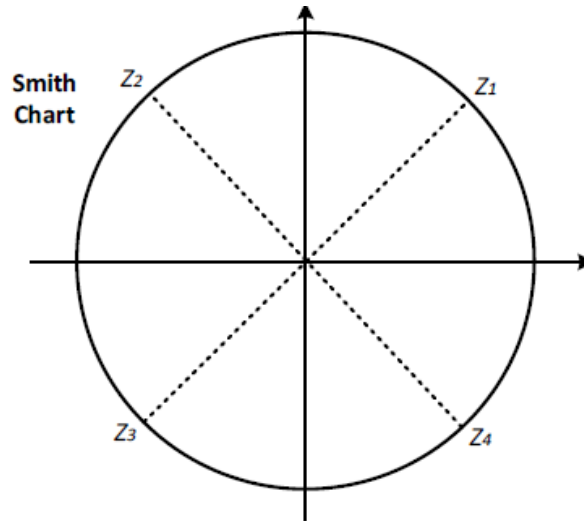


Figure 5.7. A smith chart plot of an ideal choice of antenna termination impedance Z_1 , Z_2 , Z_3 and Z_4 for the QPSK backscatter modulation [165].

5.1.4 Quadrature Amplitude Modulation (QAM)

In backscatter communication, an M-ary QAM scheme can be implemented with M termination impedances that toggle with respect to tag antenna[165]. In Figure 5.8, 16-QAM modulation is implemented with 5 switches with lumped termination as 16 to 1 multiplexer. The arrangement is hardware-consuming and increases power consumption up to a few mW[174]. To reduce the power consumption, a complementary metal oxide

semiconductor (CMOS) based design was proposed in [175] which uses a resistor and capacitor to achieve termination impedance.

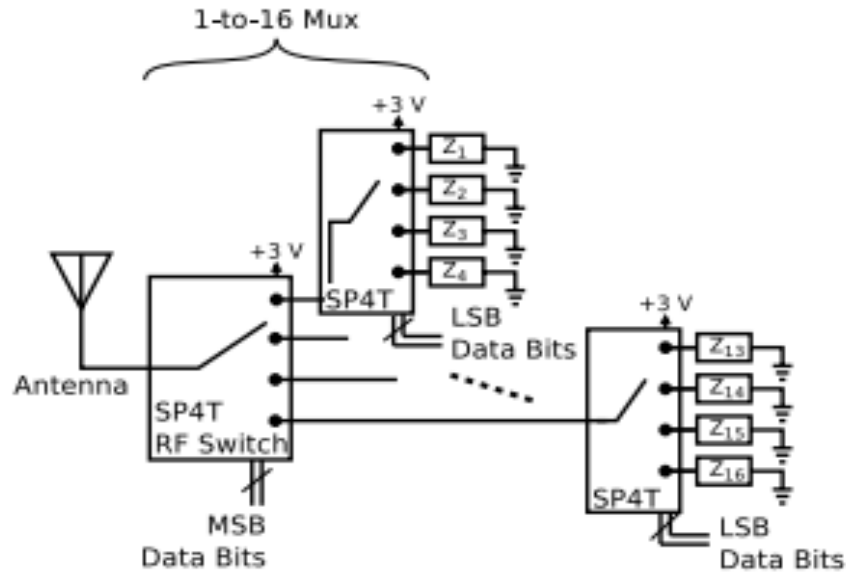


Figure 5.8. A schematic for 16-QAM backscatter modulator [174].

5.1.5 Chirp Spread Spectrum (CSS) Modulation

In digital communication, Chirp spread spectrum (CSS) is a spread spectrum technique that utilises linear frequency modulation to encode information. Time delay in the chirp signal translates into a frequency shift at the output, after correlating with an appropriate Chirp. CSS uses frequency shift to encode data as a cyclic time shift. This type of modulation achieves very high sensitivity at the cost of a low data rate, and by achieving sensitivity below -149 dBm, the system becomes reliable and suitable for long-range communication[165].

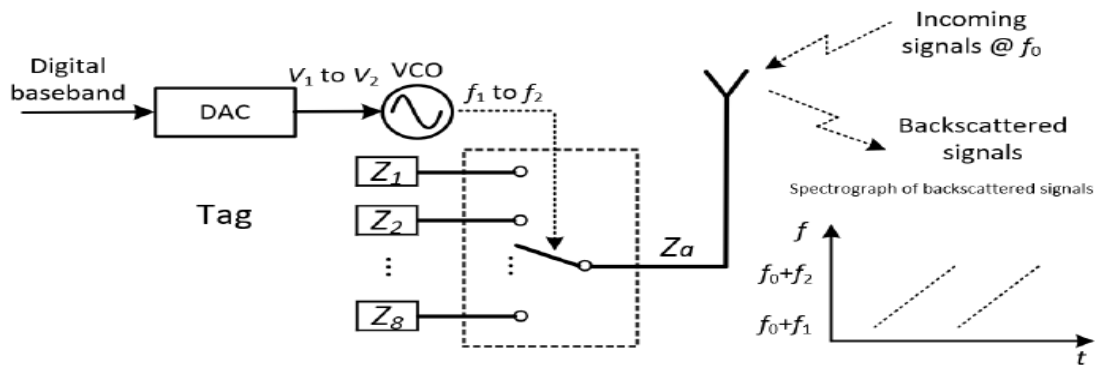


Figure 5.9. A schematic for CSS (LoRa-PHY compatible) backscatter tag [176].

In the CSS scatter tag in Figure 5.9, the frequency with which the tag and termination impedance is toggled is linearly increased or decreased to create Up-chirp or down-chirp. The linear variation is achieved by the use of a Digital to Analogue Converter (DAC) controlled Voltage-controlled Oscillator (VCO). To obtain the required resolution, the DAC bits must be equal to the spreading factor of the LoRa symbol. The number of termination impedances was increased from 2 to 8 to suppress mirror frequency and 3rd and 5th components. CSS is resilient to in-band and out-of-band interference[165]. Also, it does not require fine-grind frequency synchronisation at the receiver end[176]. Design guidance on antenna termination impedance and the spectrogram of backscattered signals is shown in Figure 5.10.

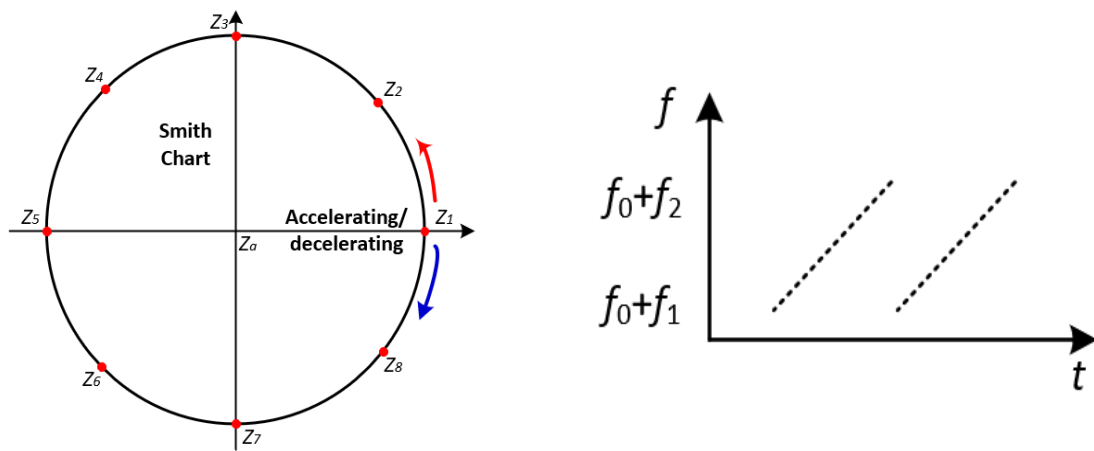


Figure 5.10. (a) A smith chart plot for the design guidance on antenna termination with the impedance accelerating/decelerating clockwise/anticlockwise of the unit circle (b) Spectrogram of backscattered signals [165].

5.1.6 Summary of SOTA Backscatter Modulation

From the SOTA backscatter modulation, the following can be observed[165]:

- a) ASK is simple, but susceptible to noise.
- b) FSK is resilient to noise.
- c) PSK has complex hardware.
- d) QAM has complex hardware, but a higher bit rate.
- e) CSS is resilient to interference.

All of these techniques use single carrier backscatter modulation, and each implementation is suitable for the specific modulation technique and not transferable to other modulation techniques.

To enhance efficiency, bandwidth utilisation, and increase range whilst reducing power consumption and cost, the IQ modulator proposed in [177] is adopted and used to bridge the gaps stated in previous implementations.

5.2 IQ Backscatter Modulator

The architecture of the inphase-quadrature (IQ) modulator in Figure 5.11 has been designed using a Wilkinson power divider (WPD). The incoming signal is 3-dB divided into two arms of WPD which are terminated by Metal oxide semiconductor field effect transistor (MOSFET). The two paths are characterised by a 45° phase difference, achieved by transmission line delay. The reflected signal at port A from path B and path C is characterised by a 90° phase difference, since the signal in the I path passes through the delay line twice. Because of this phase difference, the impedance generated will be orthogonal when presented in an IQ plane, as in Figure 5.12. A smith chart plot showing reflection coefficient observed at antenna port A when V_I and V_Q of two transistors (ATF-54143) on IQ backscatter tag are swept from 0 to 0.6 V[177].

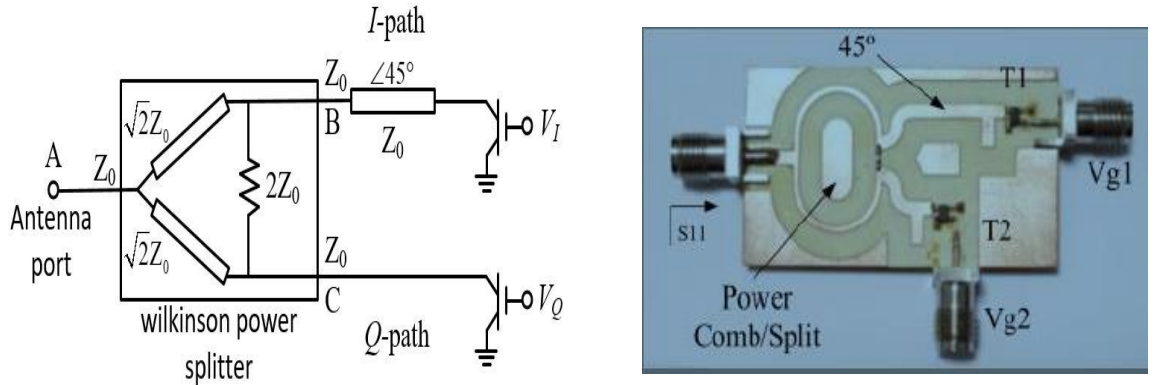


Figure 5.11. IQ backscatter modulator (a) Circuit diagram (b) Implementation on [177].

The transistor ATF-54143 from Broadcom has been selected and used because of its ultra-low current ($0.2 \mu\text{A}$) when Gate voltage is below 0.6 V. By varying the gate voltage from 0 to 0.6 V in steps of 1 mV, the reflection coefficients span in the orthogonal direction, as shown in Figure 5.12.

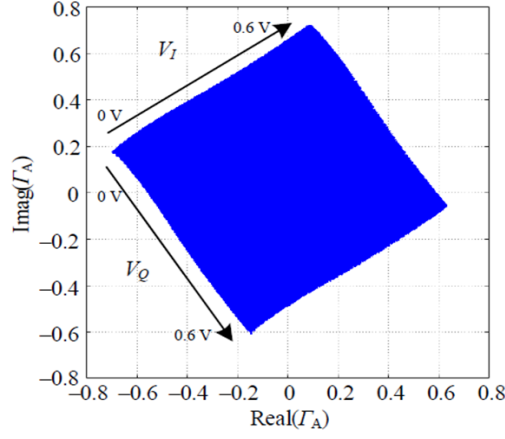


Figure 5.12. A smith chart plot showing reflection coefficient observed at antenna port A when V_I and V_Q of two transistors (ATF-54143) on IQ backscatter tag are swept from 0 to 0.6 V [167].

5.2.1 IQ Modulator Termination Impedances Analysis Using Phase Rotation

As shown in Figure 5.13, assume that a circle is fitted inside the shaded impedance area generated by the IQ backscatter modulator. When the modulation produces a constant envelope, the antenna termination resistance is located within the circumference of the circle [165]. Assuming the point in the reflection circle is the outer point, various impedances can be selected by changing Φ_n to achieve different types of modulation.

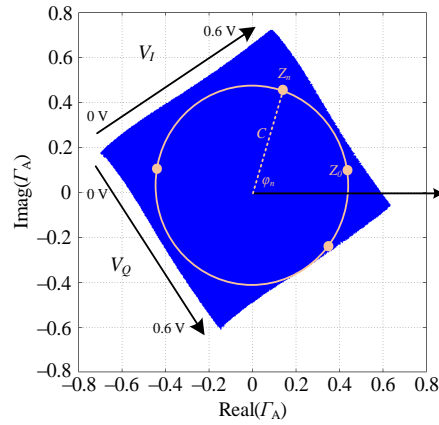


Figure 5.13. A smith chart plot of IQ modulator reflection coefficients with constant envelope reflection circle fitted inside [165].

Various load impedances can be selected on the fitted reflection coefficient circle of Figure 5.12, denoted as Z_n ($n = 1, 2 \dots M$). Thus, the reflection coefficient Γ_n , when the load Z_n is connected to the tag antenna, can be expressed as [165]:

$$\Gamma_n = \frac{Z_n - Z_a}{Z_n + Z_a} = C \cdot \exp(j\varphi_n) \quad (5.1)$$

Where the magnitude of the reflection coefficient circle and φ_n is the angular displacement between Z_n and Z_{n-1} , as labelled in Figure 5.13.

Backscatter signal is achieved by multiplying the incoming signal, i.e. $\exp(j2\pi f_0 t)$, with the modulating signal. Combining Equation (5.1) with the incoming signal, the expression becomes:

$$S_{bs}^{(n)}|_{t=\frac{n}{\Delta f}} = \exp(j2\pi f_0 t) \cdot C \exp(j\varphi_n) \quad (5.2)$$

When the frequency is varied, Equation (5.2) can be represented as:

$$S_{bs}^{(n)}|_{t=\frac{n}{\Delta f}} = C \cdot \exp j2\pi \left(f_0 t + \frac{\varphi_n \Delta f}{2\pi n} \right) \quad (5.3)$$

And when the phase of the incoming signal is varied, Equation (5.2) can be presented as:

$$S_{bs}^{(n)}|_{t=\frac{n}{\Delta f}} = C \cdot \exp j \left(2\pi f_0 t + \varphi_n \right) \quad (5.4)$$

The initial phase of the incoming signal is assumed to be zero.

5.2.1.1 Chirp Spread Spectrum

From Equation (5.3), it can be observed that, to achieve a chirp signal, the frequency term $\left(\frac{\varphi_n \Delta f}{2\pi n}\right)$ has to be a linear function with respect to time as from Equation (5.5). In other words, $\left(\frac{\varphi_n \Delta f}{2\pi n}\right)$ needs to be a linear function of n , namely[165]:

$$\varphi_n = \frac{2\pi A}{\Delta f} n^2 + \frac{2\pi B}{\Delta f} \cdot n \quad (5.5)$$

Where A is the starting frequency and B is bandwidth.

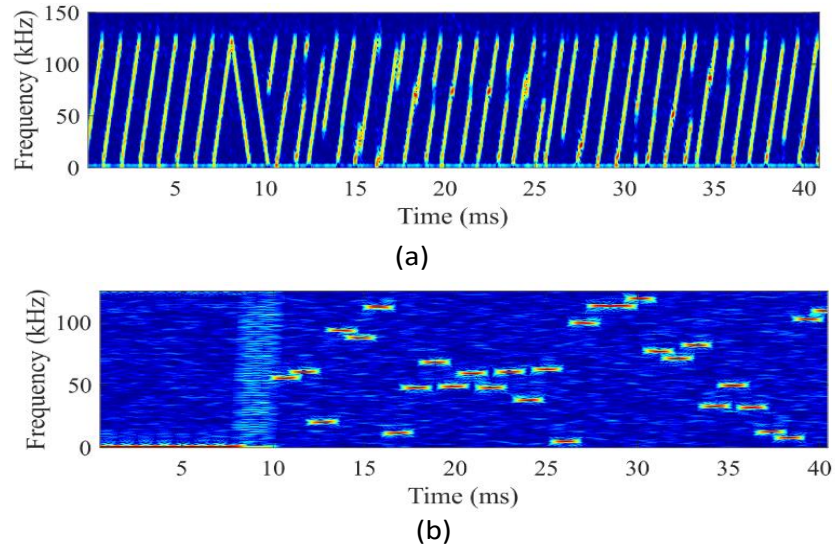


Figure 5.14. (a) A plot of a received LoRa packet spectrogram (measurement). (b) Spectrogram after LoRa decoding [177].

Assuming the value of C is known, solving equation (9) for φ_n ($n = 0, 1, 2, \dots, N$), then Γ_n and Z_n , can be obtained[165]. CSS backscatter using an IQ modulator was first demonstrated by [177], where by rotating the phase of the signal either clockwise or anticlockwise, The LoRa backscatter signal in Figure 5.14 was generated and transmitted.

5.2.1.2 Binary Phase Shift Keying (BPSK)

From Equation (5.4), it can be observed that, to achieve a BPSK signal, the phase term φ_n has to be varied in two equal steps (0° and 180°) to cover the reflection coefficient circle[165]. To achieve two distinct equally spaced impedances, the φ_n in equation (8) is being replaced $\frac{2\pi(n-1)}{M}$. So Equation (5.4) becomes[165]:

$$S_{bs}^{(n)}|_{t=\frac{n}{\Delta f}} = C \cdot \exp j \left(2\pi f_o t + \frac{2\pi(n-1)}{M} \right) \quad (5.6)$$

Where M is the total number of discrete steps.

From Equation (5.1), the impedance of the selected number loads can be calculated as:

$$\Gamma_n = \frac{Z_n - Z_a}{Z_n + Z_a} = C \cdot \exp j \frac{2\pi(n-1)}{M} \quad (5.7)$$

Provided the value of C is known, the values of Γ_n and Z_n can be obtained.

5.2.1.3 Quadrature Phase Shift Keying (QPSK)

From Equation (5.4), it can be observed that, to achieve a QPSK signal, the phase term φ_n has to be varied in four equal steps (45° , 135° , 225° , and 315°) to cover the reflection coefficient circle[165]. To achieve four distinct equally spaced impedances, the φ_n in Equation (5.4) is being replaced $\frac{\pi(n-1)}{M}$. So, Equation (5.4) becomes:

$$S_{bs}^{(n)}|_{t=\frac{n}{\Delta f}} = C. \exp j \left(2\pi f_o t + \frac{\pi(n-1)}{M} \right) \quad (5.8)$$

Where M is the total number of discrete steps.

From Equation (5.1), four distinct equally spaced impedances of the selected number of loads can be calculated as:

$$\Gamma_n = \frac{Z_n - Z_a}{Z_n + Z_a} = C. \exp j\pi \left(\frac{2(n-1)}{M} \right) \quad (5.9)$$

Provided the value of C is known, the values of Γ_n and Z_n can be obtained.

5.2.1.4 Quadrature Amplitude Modulation

One of the capabilities of the IQ modulator is to achieve any order QAM with only two transistors. To synthesise a QAM backscatter signal, a maximum square is fitted within the achieved impedance area as shown in Figure 5.12. By careful selection of reflection coefficients, QAM constellation symbols in Figure 5.15 will be obtained with a maximum magnitude that will result in maximum backscatter QAM energy. Each constellation symbol corresponds to transistor voltage pairs (V_I , V_Q). So, by using a different combination of voltage pairs (V_I , V_Q), different reflection coefficients will be achieved, and different QAM orders will be synthesised[165].

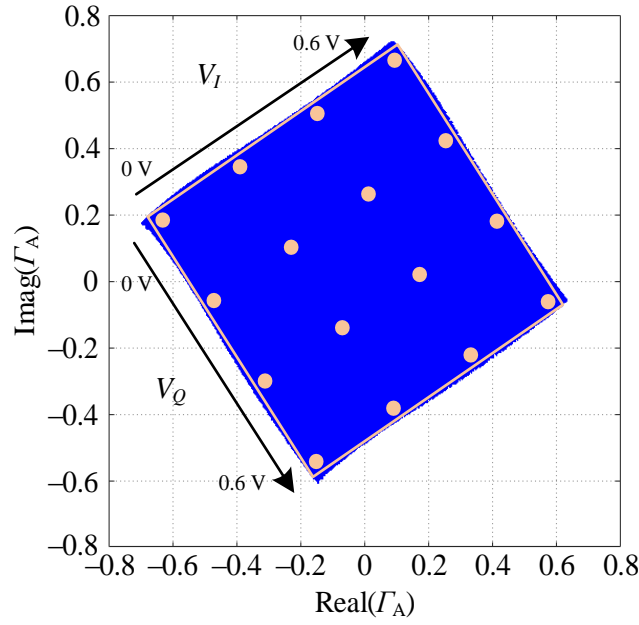


Figure 5.15. A smith chat plot of a 16-QAM backscatter modulation in IQ plane [165].

5.2.1.5 Frequency Shift Keying

In the IQ backscatter modulator, FSK, maximum power backscattered signals are achieved by rotating the phase of the signal to attain two distinct impedances oppositely located on the reflection coefficient circle fitted inside the shaded impedance area spanned by the IQ backscatter modulator of Figure 5.11[165]. To achieve this, Equation (5.6) can be used.

5.2.2 Performance of Modulation Technique and Spread Spectrum used in Backscattering

This part analyses the performance of various modulation techniques and spread spectrum used in backscattering. M-ary frequency shift keying (M-FSK), M-ary phase-shift keying (M-PSK), and M-ary quadrature amplitude modulation (M-QAM) are analysed over the additive white Gaussian noise (AWGN) and Rayleigh fading channel. Bit to error ratio (BER) performance of orthogonal frequency multiplexing (OFDM), direct sequence spread spectrum (DSSS) and CSS will be analysed. Finally, the trade-off between hardware complexity/power consumption of the modulation techniques and spread spectrum used in backscattering communication will be investigated.

5.2.2.1 Performance of Various Linear Digital Modulation Schemes Over AWGN Channel

Table 5.1 shows the summary of theoretical BER (P_b) for various linear modulations. Whereby, E_b is the average bit energy, N_o is the average noise energy, m is bit per symbol, and M is the modulation order.

Table 5.1. The Equations for the theoretical BER for various linear modulation [178].

Modulation	Bit Error Rate (P_b)
BPSK	$P_b = 0.5 \operatorname{erfc}(\sqrt{\frac{E_b}{N_o}})$ (5.10)
QPSK	$P_b = 0.5 \operatorname{erfc}(\sqrt{\frac{E_b}{N_o}})$ (5.11)
M-PSK	$P_b = \frac{1}{m} \operatorname{erfc}(\sqrt{\frac{ME_b}{N_o} \sin\left(\frac{\pi}{M}\right)})$ (5.12)
M-QAM	$P_b = \frac{2}{m} (1 - \frac{1}{\sqrt{M}}) \operatorname{erfc}(\sqrt{\frac{3ME_b}{2(M-1)N_o}})$ (5.13)
D-BPSK	$P_b = 0.5 e^{\frac{E_b}{N_o}}$ (5.14)
D-QPSK	$P_b = Q_1(a, b) - 0.5 I_0(ab) e^{-0.5(a^2+b^2)}$ (5.15) Where: $a = \sqrt{\frac{2E_b}{N_o}} (1 - \frac{1}{\sqrt{2}})$ (5.16) $b = \sqrt{\frac{2E_b}{N_o}} (1 + \frac{1}{\sqrt{2}})$ (5.17) $Q_1(a, b) = \text{Marcum } Q \text{ function}$ $I_0(ab) = \text{Modified Bessel function}$

Figure 5.16 shows that, using BPSK, the transmission can tolerate signal to noise ratio (SNR) greater than 12 dB. For BPSK, when SNR decreases from 12 dB then BER increases rapidly. QPSK can tolerate SNR up to 20 dB. For good reception, 4QAM can be used, while for high-speed data transmission, 16QAM or any other higher-level linear digital modulation can be used.

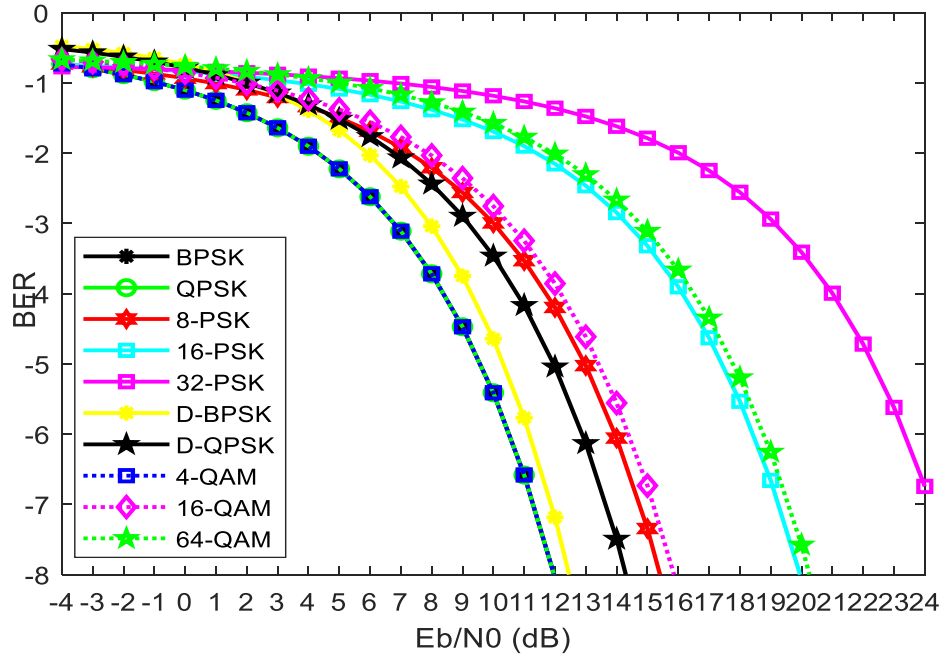


Figure 5.16. A Matlab plot showing the performance of various linear digital modulation schemes over AWGN channel [178].

For M-PSK

- Error rate degrades as the modulation level increases.
- Spectral efficiency increases as the modulation level increases.
- It has complex hardware.

For M-QAM

- Power efficiency decreases with an increase in modulation level, but not as early as M-PSK.
- Spectral efficiency increases as the modulation level increases.
- It has complex hardware but a higher bit rate.

5.2.2.2 Performance of M-PAM over AWGN Channel.

Using the Equation (5.18), symbol error rate (SER) is presented as P_s [179];

$$P_s = 2\left(1 - \frac{1}{M}\right)Q\left(\sqrt{\frac{6}{M^2-1}}\gamma_s\right) \quad (5.18)$$

Whereby.

M is the modulation order

γ_s symbol energy to noise ratio (E_s/N_0)

Figure 5.17 shows that, using 2-PAM, the transmission can tolerate SNR greater than 10 dB. For 2-PAM, when SNR decreases from 10 dB then BER increases rapidly. 4-PAM can tolerate SNR up to 13.5 dB, and for 8-PAM minimum tolerance SNR is 17 dB. 16-PAM extends to 18 dB, whilst 32-PAM tolerance is up to 23 dB. For good reception, 2-PAM can be used, while for high-speed data transmission, 4-PAM or any other higher-level M-PAM can be used.

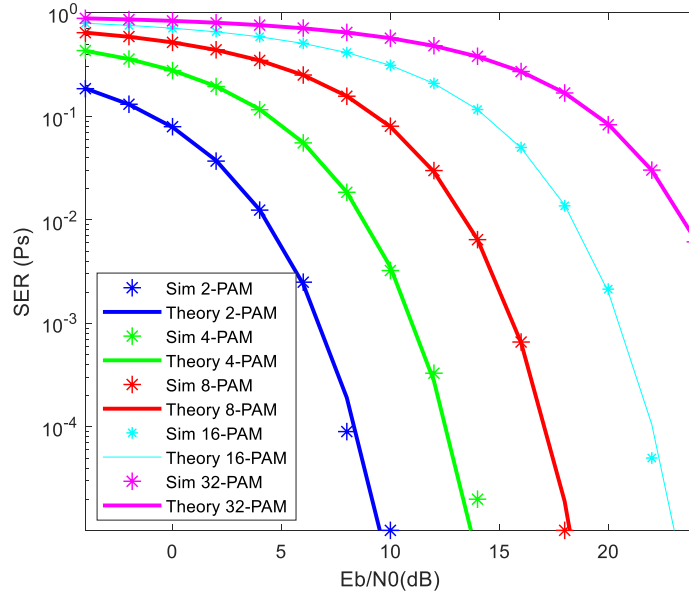


Figure 5.17. A Matlab plot showing the performance of M-PAM over AWGN channel.

5.2.2.3 Performance of M-PAM over Rayleigh Flat Fading Channel

Using the Equation (5.19), symbol error rate (SER) is presented as P_s [179];

$$P_s = \frac{4}{\pi} \left(1 - \frac{1}{\sqrt{M}}\right) \int_0^{\frac{\pi}{2}} \kappa \gamma_s \left(-\frac{g}{\sin^2 \phi}\right) d\phi - \frac{4}{\pi} \left(1 - \frac{1}{\sqrt{M}}\right)^2 \int_0^{\frac{\pi}{4}} \kappa \gamma_s \left(-\frac{g}{\sin^2 \phi}\right) d\phi \quad (5.19)$$

Whereby.

M is the modulation order

γ_s is the symbol energy to noise ratio (E_s/N_0) and

$$g = \frac{1.5}{(M-1)} \quad (5.20)$$

The performance in Figure 5.18 shows the BER plot for 2-PAM, 4-PAM, 8-PAM, 16-PAM, and 32-PAM over Rayleigh flat fading channel. If one value of BER is taken as a benchmark, it can be observed that 2-PAM will always have a minimum value of E_b/N_0 , followed by 4-PAM, 8-PAM, 16-PAM, and finally 32-PAM. As 2-PAM has a minimum

value compared to other M-PAM, is recommended to use 2-PAM for modulation and transmission in Rayleigh flat fading channel.

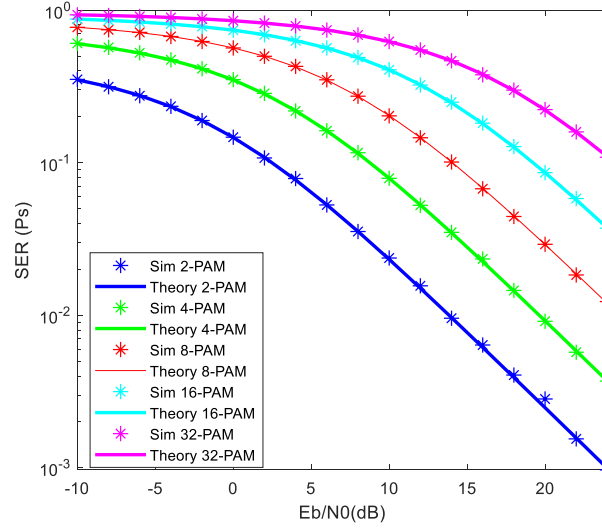


Figure 5.18. A Matlab plot showing the Performance of M-PAM over Rayleigh flat fading channel.

5.2.2.4 Performance of M-PSK over Rayleigh Flat Fading Channel

Using the Equation (5.21), symbol error rate (SER) is presented as P_s [179];

$$P_s = \frac{1}{\pi} \int_0^{\frac{(M-1)\pi}{M}} \kappa \gamma_s \left(1 - \frac{g}{\sin^2 \phi}\right) d\phi \quad (5.21)$$

Whereby.

M is the modulation order

γ_s is the symbol energy to noise ratio (E_s/N_0) and

$$g = \sin^2\left(\frac{\pi}{M}\right) \quad (5.22)$$

Figure 5.19, it shows the BER plot for 2-PSK, 4-PSK, 8-PSK, 16-PSK, and 32-PSK over the Rayleigh flat fading channel. If one value of BER is taken as a benchmark, it can be observed that 2-PSK will always have a minimum value of E_b/N_0 , followed by 4-PSK, 8-PSK, 16-PSK, and 32-PSK. As 2-PSK has a minimum value compared to other M-PSK, it is recommended to use 2-PSK for modulation and transmission in Rayleigh flat fading channel

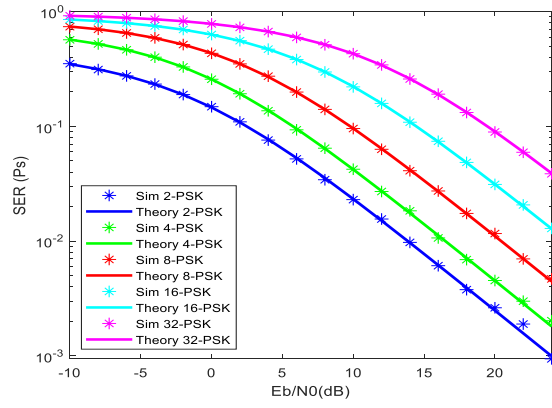


Figure 5.19. A Matlab plot showing the performance of M-PSK over Rayleigh flat fading channel.

5.2.2.5 Performance of M-PSK over AWGN Channel.

Using the Equation (5.23), symbol error rate (SER) is presented as P_s [179];

$$P_s = Q(\sqrt{2\gamma_b}) \quad (5.23)$$

Whereby.

γ_b is the is the bit energy to noise ratio (E_b/N_0)

Figure 5.20 shows that, using BPSK, the transmission can tolerate SNR greater than 9.5 dB. For BPSK, when SNR decreases from 9.5 dB then BER increases rapidly. QPSK can tolerate SNR up to 10 dB, and for 8PSK minimum tolerance SNR is 14 dB. 16PSK extends to 18 dB, whilst 32PSK tolerance is up to 23 dB. For good reception, BPSK can be used, while for high-speed data transmission, QPSK or any other higher-level MPSK can be used.

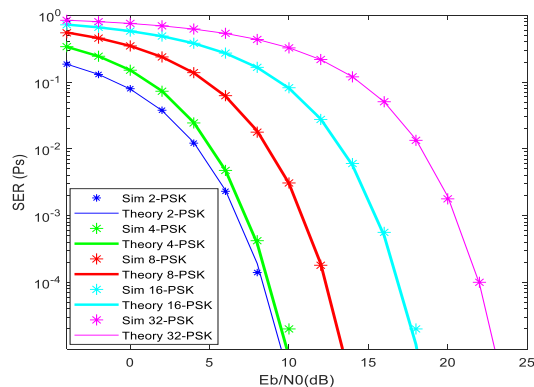


Figure 5.20. A Matlab plot showing the performance of M-PSK over AWGN channel.

For M-PSK:

- a) Error rate degrades as the modulation level increases.
- b) Spectral increases as the modulation level increases.
- c) It has complex hardware.

5.2.2.6 Performance of M-FSK over AWGN Channel.

Using the Equation (5.24), symbol error rate (SER) is presented as P_s ;

$$P_s = \sum_{i=1}^{M-1} \frac{(-1)^{i+1}}{i+1} \binom{M-1}{i} \exp\left(-\frac{i}{i+1} \gamma_s\right) \quad (5.24)$$

Whereby.

M is the modulation order

γ_s is the symbol energy to noise ratio (E_s/N_0)

Figure 5.21 shows that using 32FSK, the transmission can tolerate SNR greater than 6.5 dB. For 32FSK, when SNR decreases from 6.5 dB, then BER increases rapidly. 16FSK can tolerate SNR up to 7.5 dB, and for 8FSK minimum tolerance SNR is 8.5 dB. 4FSK extends to 10 dB, whilst 2FSK tolerance is up to 12.5 dB. For good reception, 32FSK can be used, while for high-speed data transmission, 2FSK can be used.

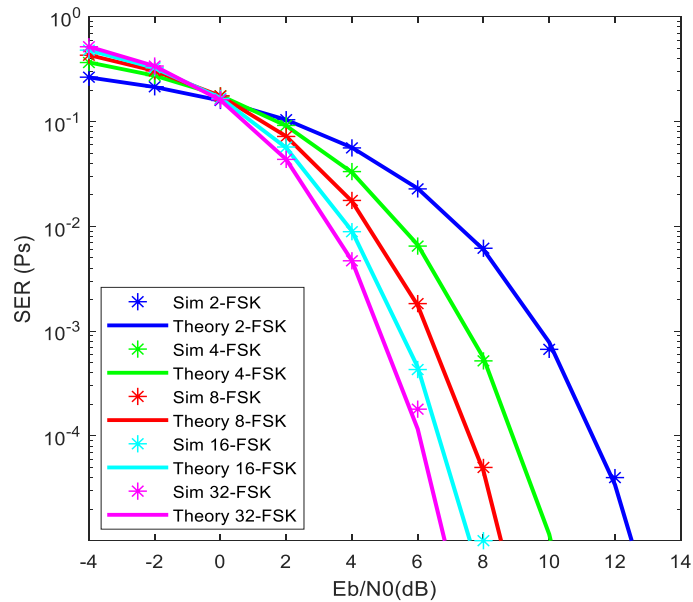


Figure 5.21. A Matlab plot showing the performance of M-FSK over AWGN channel.

For M-FSK:

- a) As the modulation level increases, power efficiency improves (fewer energy per bit is required).
- b) Spectral efficiency decreases as the modulation level increases, for example. BPSK is power efficient compared to BFSK.

5.2.2.7 Performance of M-QAM over Rayleigh Flat Fading Channel

Using the Equation () for symbol error rate (SER) as P_s [179];

$$P_s = 2\left(\frac{M-1}{M\pi}\right) \int_0^{\frac{\pi}{2}} \kappa \gamma_s \left(-\frac{g}{\sin^2 \phi}\right) d\phi \quad (5.25)$$

Whereby.

M is the modulation order

γ_s is the symbol energy to noise ratio (E_s/N_0) and

$$g = \frac{3}{(M^2-1)} \quad (5.26)$$

The performance in Figure 5.22 shows the BER plot for 4-QAM, 16-QAM, 64-QAM, and 256-QAM over Rayleigh flat fading channel. If one value of BER is taken as a benchmark, it can be observed that: 4-QAM will always have a minimum value of E_b/N_0 , followed by 16-QAM, 64-QAM, and finally 256-QAM. As 4-QAM has a minimum value compared to other M-QAM, it is recommended to use 4-QAM for modulation and transmission in Rayleigh flat fading channel.

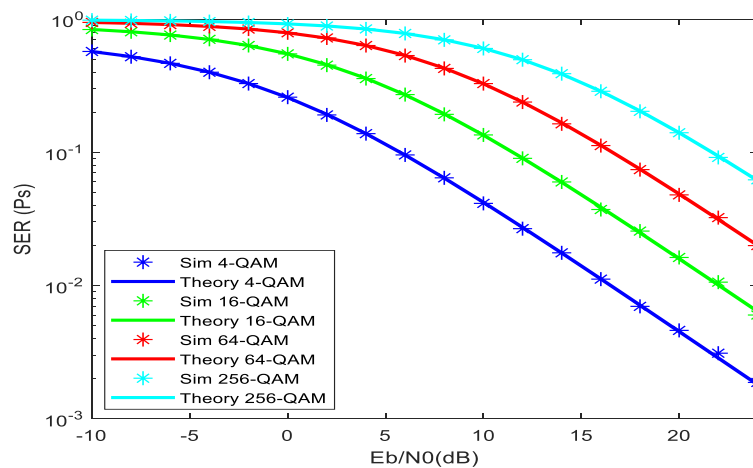


Figure 5.22. A plot showing performance of M-QAM over Rayleigh flat fading channel.

5.2.2.8 Performance of M-QAM over AWGN Channel.

Using the Equation (5.27), symbol error rate (SER) is presented as P_s [179];

$$P_s = 1 - [1 - 2(1 - \frac{1}{\sqrt{M}})Q(\sqrt{\frac{3\gamma_s}{(M-1)}})]^2 \quad (5.27)$$

Whereby

M is the modulation order

γ_s is the symbol energy to noise ratio (E_s/N_0)

Figure 5.23 shows that, using 4QAM, the transmission can tolerate SNR greater than 10 dB. For 4QAM-OFDM, when SNR decreases from 10 dB, then BER increases rapidly. 16QAM can tolerate SNR up to 14 dB, and for 64QAM minimum tolerance SNR is 18 dB. 256QAM extends to 23.5 dB. For good reception, 4QAM can be used, whilst for high-speed data transmission, 256QAM can be used.

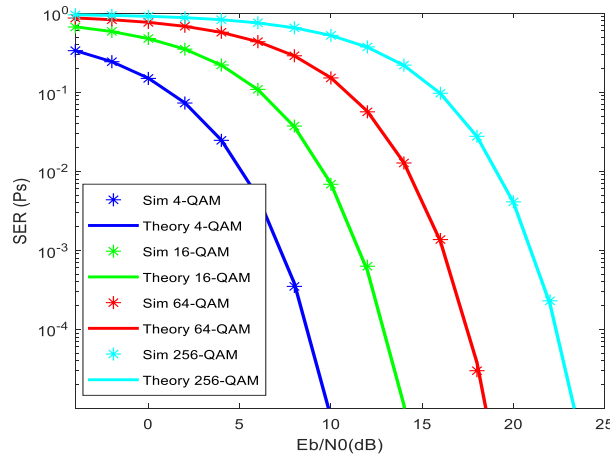


Figure 5.23. A plot showing performance of M-QAM over AWGN channel.

For M-QAM:

- Power efficiency decreases with an increase in modulation level, but not as early as M-PSK.
- Spectral efficiency increases as the modulation level increases.
- It has complex hardware but a higher bit rate.

5.2.3 Spread Spectrum Technology

Backscatter communication is one of the fast-emerging areas of communication today. The development of a new generation of sensor nodes depends on the appropriate wireless and access scheme. To accommodate many sensor nodes, the scheme must offer a high

data rate, low power consumption, and a certain level of robustness. However, some challenges hinder the practicality of the technology. The challenges include bandwidth limitation due to spectral availability, interference, and power consumption.

To solve some of these challenges, spread spectrum is the recommended technology. This section explains the theory of spread spectrum techniques used in backscattering and investigates their trade-off between hardware complexity/power consumption and link performance.

Spread spectrum is a technique used in backscattering whereby the backscatter signal with a particular bandwidth is intentionally spread in the frequency domain which results in the signal with a wider bandwidth. As this process uses low power, it makes the communication signal hard to be detected and intercepted, whilst higher spectra redundancy makes the signal more resistant to jamming.

5.2.4 Orthogonal Frequency-Division Multiplexing

OFDM is a technique in backscatter communication whereby a single backscatter carrier is split across several separate narrowband multiple carrier frequencies, to reduce interference and crosstalk. To describe OFDM, several sub-channels (N) need to be specified and are normally set to the power of 2. The sizes of Discrete Fourier transforms (DFT), as well as Inverse DFT need to be declared accordingly. Transmission is achieved by first converting the information stream into a parallel sub-channel, then the data symbol/subcarriers are modulated using a selected modulation scheme, either MQAM or MPSK. All the subcarriers are orthogonal to each other.

5.2.4.1 OFDM Performance

To investigate the efficiency of the OFDM system, it is important to justify the performance of the system with respect to different factors. Selected factors for this simulation are AWGN and Rayleigh's flat fading channel. The selected simulation parameters for the OFDM are shown in Table 5.2.

Table 5.2. Simulation Parameters for OFDM.

Number of OFDM Symbols to transmit	10000
Modulation type	M-QAM, M-PSK
Modulation order	4, 8, 16, 32, 64, 256
Total number of subcarriers	64
Number of symbols in the cyclic prefix	16

5.2.4.2 Performance of MPSK-CP-OFDM and MQAM-CP-OFDM on AWGN Channel

To study the performance of OFDM on AWGN channel, Equation (5.28)[179] is used,

$$P_s = 10 * \log_{10}(k * N / (N + N_{cp})) E_b N_0 dB \quad (5.28)$$

Whereby.

k = number of bits per modulated symbol.

N_{cp} = Number of symbols in cyclic prefix.

N = Total number of subcarriers.

E_bN₀ = Energy bit to noise ratio

Figure 5.24(a) shows that, using QPSK-OFDM, the transmission can tolerate SNR greater than 11 dB. For QPSK-OFDM, when SNR decreases from 11 dB, then BER increases rapidly. 8-PSK-OFDM can tolerate SNR up to 14 dB, and for 16PSK-OFDM minimum tolerance SNR is 18 dB. 32PSK-OFDM and 64PSK-OFDM extend to a very big value. For good reception, QPSK-OFDM can be used, whilst for high-speed data transmission, 64PSK-OFDM can be used.

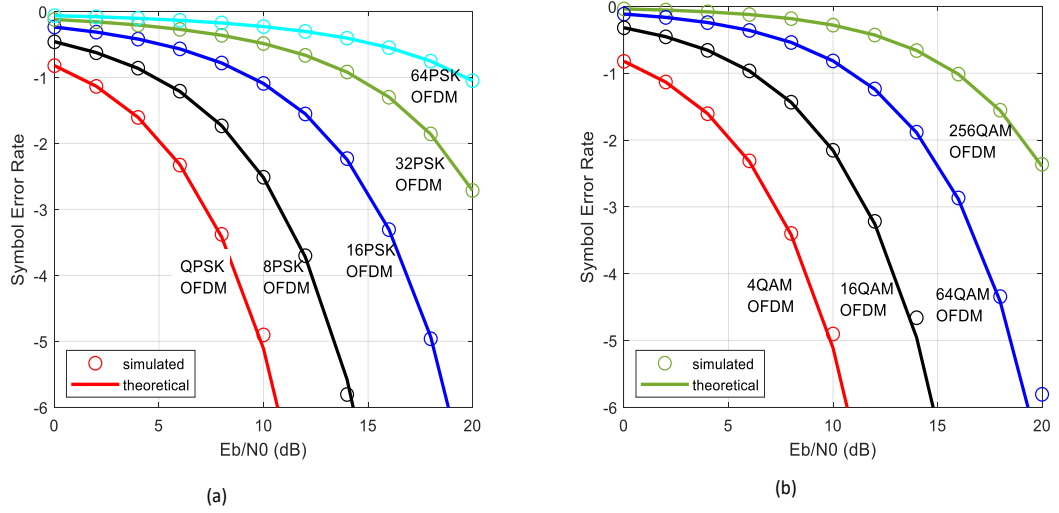


Figure 5.24. A Matlab plot showing the performance of CP-OFDM on AWGN channel (a) MPSK (b) MQAM

Figure 5.24(b) shows that, using 4QAM-OFDM, the transmission can tolerate SNR greater than 11 dB. For 4QAM-OFDM, when SNR decreases from 11 dB, then BER increases rapidly. 16QAM-OFDM can tolerate SNR up to 15 dB, and for 64QAM-OFDM minimum tolerance is SNR is 19 dB. 256QAM-OFDM extends to a very big value. For good reception, 4QAM-OFDM can be used, whilst for high-speed data transmission, 256QAM-OFDM can be used.

5.2.4.3 Performance of MPSK-CP-OFDM and MQAM-CP-OFDM on Frequency Selective Rayleigh Channel

To study the performance of OFDM over frequency selective channel, the block diagram of OFDM transmitter and receiver in Figure 5.25, is considered.

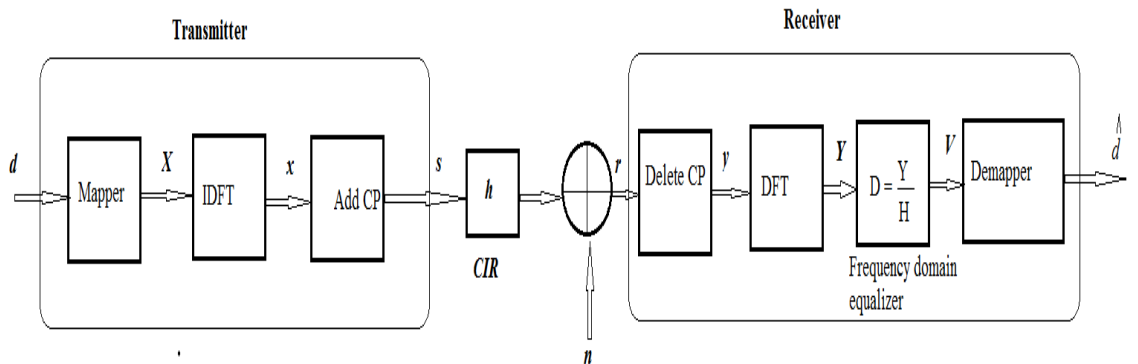


Figure 5.25. A diagram of OFDM transmitter and receiver model.

In this model \mathbf{h} represent frequency channel while \mathbf{H} represent frequency response and \mathbf{n} is additive white Gaussian[179].

Using the convolution, the transmission of OFDM can be presented in Equation (5.29) as

$$Y = DFT[IDFT(X) \otimes h + n]$$

$$Y = DFT[IDFT(X) \otimes h] + z \quad (5.29)$$

Where \mathbf{X} is the input to the IDFT

$$Y = X \cdot DFT[h] + z$$

$$Y = X \cdot H + z \quad (5.30)$$

When the frequency response of channel is known, the process of equalization is presented in Equation (5.31)

$$V = \frac{Y}{H} \quad (5.31)$$

The symbol error rate (P_s) is finally presented as

$$P_s = 10 * \log_{10}(k * N / (N + N_{cp})) E_b N_0 dB \quad (5.32)$$

Whereby.

k = number of bits per modulated symbol.

N_{cp} = Number of symbols in cyclic prefix.

N = Total number of subcarriers.

$E_b N_0$ = Bit to noise ratio

Figure 5.26(a) shows the BER plot for BPSK, QPSK, 8-PSK, 16-PSK, 32-PSK, and 64-PSK over Rayleigh's flat fading channel. If one value of BER is taken as a benchmark, it can be observed that BPSK will always have a minimum value of E_b/N_0 , followed by QPSK, 8-PSK, 16-PSK, 32-PSK, and 64-PSK. As BPSK has a minimum value compared to other M-PSK, is recommended to use BPSK for modulation and transmission in Rayleigh flat fading channel.

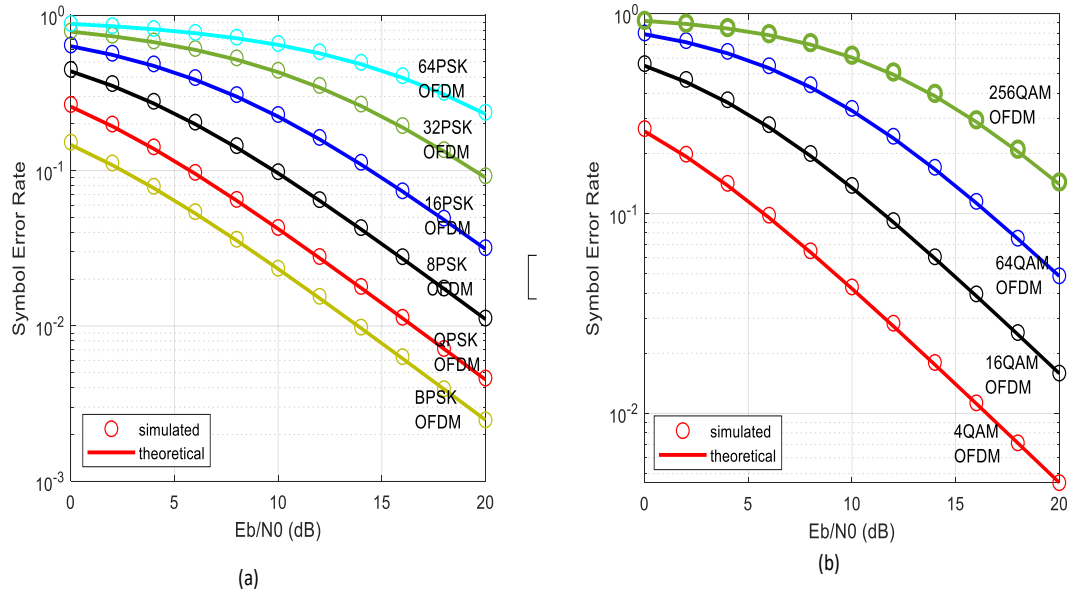


Figure 5.26. A Matlab plot showing the performance of CP-OFDM on frequency selective Rayleigh channel (a) MPSK (b) MQAM.

Figure 5.26(b) shows the BER plot for 4-QAM, 16-QAM, 64-QAM, and 256-QAM over Rayleigh flat fading channel. If one value of BER is taken as a benchmark, it can be observed that 4-QAM will always have a minimum value of E_b/N_0 , followed by 16-QAM, 64-QAM, and finally 256-QAM. As 4-QAM has a minimum value compared to other M-QAM, is recommended to use 4-QAM for modulation and transmission in Rayleigh flat fading channel.

5.2.5 Direct Sequence Spread Spectrum

DSSS is a spread spectrum technique in backscatter whereby each bit is represented by multiple bits by the use of spreading code. This makes the backscatter signal wider in bandwidth than the information signal.

5.2.5.1 DSSS Performance Analysis

To observe the performance of the DSSS techniques, the system simulated using selected digital modulations, such as BPSK, QPSK, 8PSK, 16PSK, and QAM with an additional AWGN. For a given data rate and channel condition, the results are presented in Figure 5.27. Modulation type and order are shown in Table 5.3.

Table 5.3. Simulation Parameters for DSSS

Modulation type	BPSK, QPSK, 8PSK, 16PSK, QAM
Modulation order	2, 4, 8, 16

Figure 5.27 shows that, using DSSS-BPSK, the transmission can tolerate SNR greater than 6 dB. For DSSS-BPSK, when SNR decreases from 6 dB, then BER increases rapidly. The DSSS-QPSK is almost the same as DSSS-BPSK provided the same channel properties have been used. For good reception, DSSS-BPSK/DSSS-QPSK can be used, whilst for high-speed data transmission, other higher-level modulation can be used.

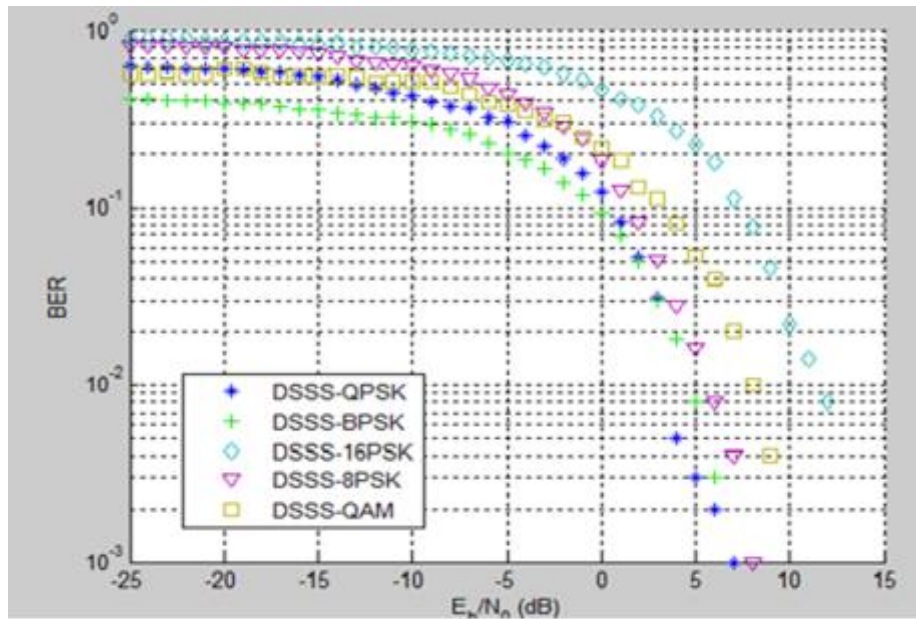


Figure 5.27. A Matlab plot for BER vs E_b/N_0 plot for DSSS used with various phase modulation [180].

This section investigates the performance of different phase modulation used with DSSS) in presence of an AWGN channel. The simulation results have shown that when Direct Sequence Spread Spectrum is used with DSSS-BPSK spread spectrum, a better error performance can be achieved in terms of BER as compared to other techniques.

5.2.6 Chirp Spread Spectrum

Chirp spread spectrum is one of the spread spectrum techniques used in digital communication. CSS uses a wideband linear frequency modulated chirp to encode the information. The chirp can be of increasing or decreasing frequency with respect to time. As CSS uses the entire located spectrum to transmit the signal, it becomes robust to

channel noise. It also offers high resistance to multipath fading, even when very low power is used. CSS offers good performance in conjunction with low time delay and low power consumption. LoRa is one of the spread spectrum modulations based on Chirp spectrum modulation.

5.2.6.1 CSS Performance with Different Spreading Factors (SF)

To observe the performance of the CSS techniques, the system was simulated using different spreading factors. Other simulation parameters are shown in Table 5.4.

Table 5.4. Simulation parameters for CSS

Spreading factor	7 to 12
Bandwidth (kHz)	125
Sampling frequency (kHz)	125
Preamble length	8
Sync length	2
Total bits to be transmitted	27720

From Figure 5.28, it can be observed that, for the given simulation parameters in Table 7, a lower value of SF) of 7 offers a high value of SNR compared to the high value of SF. By selecting the SF of the signal, the level of the SNR can be controlled.

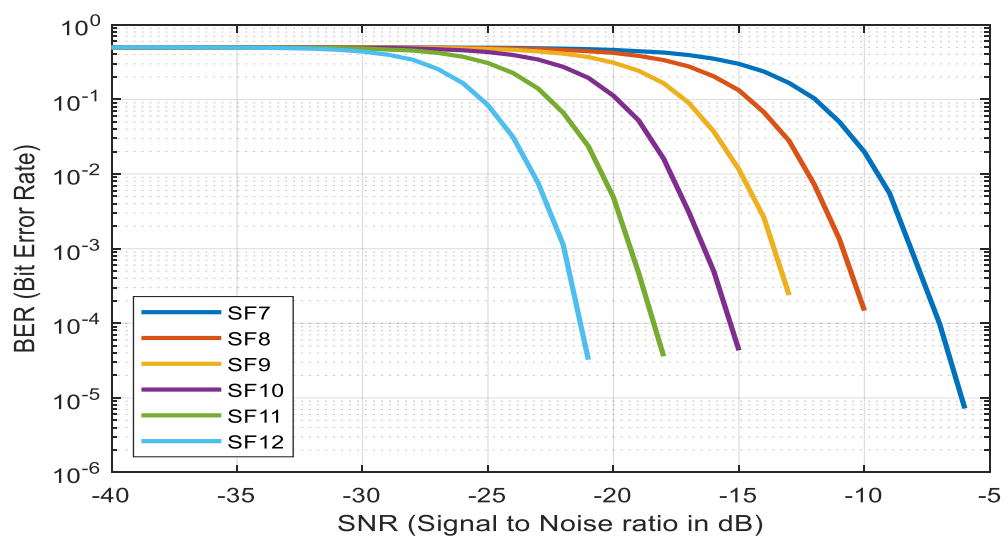


Figure 5.28. A Matlab plot for LoRa BER Performance at different Spreading Factors (SF).

5.2.7 Summary

As the modulation level increases,

- a) I and Q points on the constellation become closer to each other. This reduces the data errors, but the transmission is highly susceptible to noise.
- b) When BER decreases SNR increases, as the signal is stronger than noise.
- c) The excellent data rate is achieved at the cost of increasing bandwidth.
- d) Complex processing hardware is required during transmission as well as the reception.

Signals with higher spectral density require more transmitting power, whilst signals with lower spectral density have higher immunity against interference.

Example:

- a) DSSS has a very low power spectral density compared to FHSS, thus DSSS uses low transmit power.
- b) QAM and PSK have the same power spectral density, thus need the same amount of transmit power.
- c) OQPSK, $\pi/4$ -DQPSK has the same power spectral density as QPSK.

For M-PSK:

- a) Error rate degrades as the modulation level increases.
- b) Spectral power density increases as the modulation level increases.
- c) It has complex hardware.

For M-QAM:

- a) Power efficiency decreases with an increase in modulation level, but not as early as M-PSK.
- b) Spectral efficiency increases as the modulation level increases.
- c) It has complex hardware but a higher bit rate.

For M-FSK:

- a) As the modulation level increases, power efficiency improves (less E_b is required).

- b) Spectral efficiency decreases as the modulation level increases, for example. BPSK is power efficient compared to BFSK.

5.3 Conclusion

In this chapter, new sensing platforms using backscatter technology have been introduced. The theory of modulation and the spread spectrum technique used in backscattering have been explored. The trade-off between hardware complexity/power consumption and link performance has been investigated. The summary for each section has been presented in the specific sections. In the next chapter, a novel backscatter tag compatible with WiFi is proposed and implemented. A novel harmonic suppression approach suitable for a frequency-shifted backscatter system is proposed, implemented, and validated.

Chapter Six

Backscatter Systems Theoretical Analysis and Simulation Validation

6 Introduction

This chapter explains the theoretical analysis and simulation validation of the backscatter systems. A novel multicarrier backscatter system is proposed and implemented. The harmonic suppression approach suitable for frequency-shifted backscatter systems is also proposed and demonstrated.

6.1 Multicarrier Backscatter Transmission

6.1.1 Introduction

One of the biggest challenges with backscatter modulation, as mentioned earlier, is bandwidth utilisation, as most of the technique uses single carrier backscatter modulation resulting in single wave backscattering. To overcome this challenge and enhance bandwidth utilisation using IQ modulator, a multicarrier backscatter system is proposed and implemented. The system allows multiple carriers to be backscattered from a received single carrier[167].

6.1.2 Implementation of Multicarrier Backscatter

To illustrate how multicarrier backscattering is achieved using IQ modulator, the preamble of IEEE 802.11g (WiFi3), which has 64 OFDM subcarriers, is modulated[165].

The procedure for IEEE 802.11g (WiFi3) preamble generation is as follows:

- a) A short training symbol from IEEE 802.11g guidance is selected and used.

$$\begin{bmatrix} 0 & 0 & 1+j & 0 & 0 & 0 & -1-j & 0 & 0 & 0 & 1+j & 0 & 0 & 0 & -1-j & 0 & 0 & 0 & -1-j & 0 & 0 & 0 & 1+j & 0 & 0 & 0 & 0 & 0 & 0 & -1-j \\ 0 & 0 & 0 & -1-j & 0 & 0 & 0 & 1+j & 0 & 0 & 0 & 1+j & 0 & 0 & 0 & 1+j & 0 & 0 & 0 & 1+j & 0 & 0 & 0 & 1+j & 0 & 0 & 0 & 1+j & 0 & 0 \end{bmatrix}$$

- b) Using 64-point IFFT, short training symbols are converted from frequency to time domain.
- c) Then, the first 16 samples are selected and copied 10 times (in the time domain).
- d) Then, the long training symbol is selected and used.

$$\begin{bmatrix} 1 & 1 & -1 & -1 & 1 & 1 & -1 & 1 & -1 & 1 & 1 & 1 & 1 & 1 & -1 & -1 & 1 & 1 & -1 & 1 & -1 & 1 & 1 & 1 & 1 & -1 & -1 & 1 & 1 & -1 & 1 \\ -1 & 1 & 1 & -1 & -1 & -1 & -1 & 1 & 1 & -1 & -1 & 1 & 1 & -1 & 1 & -1 & 1 & 1 & -1 & 1 & -1 & 1 & 1 & 1 & 1 & -1 & -1 & 1 & 1 & 1 & 1 \end{bmatrix}$$

- e) Again, using 64-point IFFT, long training symbols are converted from frequency to time.

Finally, short training samples and long training samples are cascaded together with guard samples to form a total of 320 complex-valued samples in the time domain. The normalised output samples are presented in an IQ plane in Figure 6.1.

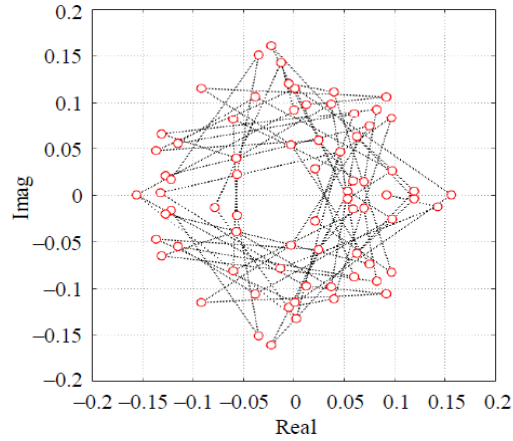


Figure 6.1. A smith chart plot showing 320 preamble samples in IQ plane in the IEEE 802.11g. (Some samples are overlapped) [167].

Since the output in Figure 6.1 is normalised to achieve maximum backscatter signal output, IFFT output is scaled up to fit into the reflection coefficient area, and the output is shown in Figure 6.2.

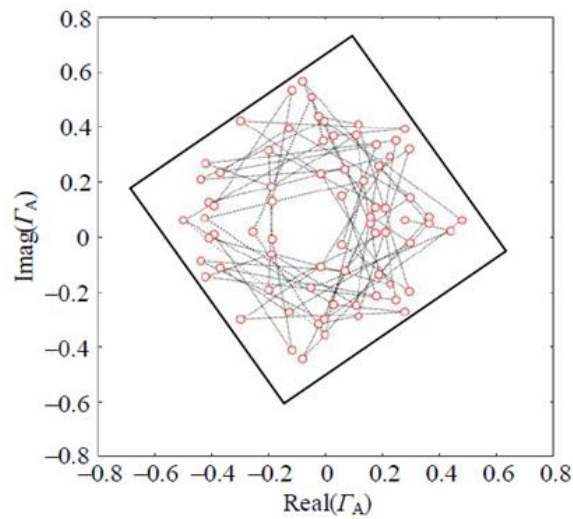


Figure 6.2. A smith chat plot for the scaled 320 samples to fit into the shaded area in Figure 5.12 [167].

Each sample in Figure 6.2 corresponds to a pair of transistor gate voltages (V_I , V_Q). For 320 samples, 320(V_I , V_Q) is applied at IQ modulator using the required sampling rate to achieve a backscatter signal from a single incoming carrier wave[165].

6.1.3 Summary of Multicarrier Backscatter Communication

From this section, it can be observed that multicarrier backscatter communication has been achieved for the first time. Using OFDM and BPSK, a preamble signal which is compatible with WiFi has been generated. As the generated signal is compatible with WiFi, no dedicated reader is required for receiving and encoding the backscattered signal. The existing WiFi infrastructure can be used directly as the receiver of the signal. Using the same approach, the OFDM payload can be generated and backscattered.

The next stage is an over the air test (OTA) to measure the performance of the system and investigate how the concept can be adopted and used in other multicarrier commercial wireless systems.

6.2 Harmonic Suppression in Frequency Shifted Backscatter Communications

In recent years, there has been great improvement in the performance of backscatter systems. This includes the link budget as well as data rates. As the number of deployed backscatter sensors increases, the necessity of managing channel bandwidth also increases. When a large number of backscatter tags is integrated, inter-user interference must be taken into account and managed[181]. Most of the previous research has focused on dealing with in-band signals only, whilst ignoring the harmonics. Leaving harmonics untreated can jeopardise the link performance of other channels[182].

Different methods have been proposed to solve this challenge, where in[[182]], a series of four discrete complex impedances was used to cancel the first mirror harmonic. The approach was extended in[183], where 8 discrete complex impedances were used to suppress the 3rd and 5th harmonics[23]. Though this method shows promising results, it is hardware-based and cannot be adjusted as per the requirement of the network. This brings the need for a scalable method to utilise and optimise the available spectrum resources[23].

In a conventional frequency-shifted backscatter system, the link budget is improved by reducing the interference caused by the RF carrier. This is achieved by shifting the

backscatter signal away from the ambient signal in the frequency domain[23][184]. But shifting the signal away leads to the generation of unwanted harmonics, thus compromising the spectrum usage. This section focuses on scalable harmonic suppression/cancellation in frequency backscatter systems.

6.2.1 Mathematical Representation of Frequency Shifted Backscattering

The basic operation of the frequency shifting backscatter system is illustrated in Figure 5.4 of Section 5.2.2. Assume the incoming electromagnetic wave is a single tone signal with a frequency f_0 as shown in Equation (6.1)[23].

$$s_{in} = \cos(2\pi f_0 t) = \text{Re}(e^{j2\pi f_0 t}) \quad (6.1)$$

Whereby the magnitude is assumed to be unity and the initial phase is zero.

As presented in Figure 5.4, when the switch is toggled between open and short at constant frequency f_{bs} , the resulted reflection coefficient between the load and the tag antenna is represented as a square wave as shown in Figure 6.3[23].

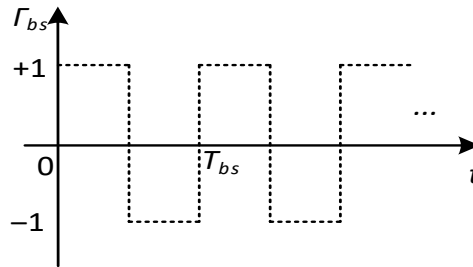


Figure 6.3. The diagram for the reflection coefficient Γ_{bs} in time when the switch is toggling between open and short at a frequency of $f_{bs} = 1/T_{bs}$. [23].

The reflection coefficient presented in Figure 6.3 can be further expanded using Fourier transform, as shown in Equation (6.2).

$$\Gamma_{bs}(t) = \frac{4}{\pi} \sum_{n=1,3,5}^{\infty} \frac{1}{n} \sin(2n\pi f_{bs} t) \quad (6.2)$$

The reflection coefficient in Equation (6.2), combined with the incoming electromagnetic wave in Equation (6.1), results in the backscatter signal S_{bs} in Equation (6.3).

$$S_{bs} = S_{in} \Gamma_{bs}(t) = \frac{4}{\pi} \sum_{n=1,3,5}^{\infty} \frac{1}{n} \cos(2n\pi f_0 t) \cdot \sin(2n\pi f_{bs} t) \quad (6.3)$$

From Equation (6.3), assuming $f_0 + f_{bs}$ is the desired frequency component, the signal will contain the first-order harmonic frequency of $f_0 - f_{bs}$ and higher harmonics at $f_0 \pm nf_{bs}$ ($n=3, 5$)

Another observation in Equation (6.3) is frequency conversion loss when translating the incoming electromagnetic wave at f_0 to the desired signal ($f_0 + f_{bs}$) is $-20\log_{10}(4/\pi \times 0.5)$ (3.9 dB). The mirror harmonic contains a similar power level. The higher-order harmonics contains $-20\log_{10}(1/n)$ dB lower compared to the first harmonic (9.5 dB for 3rd harmonic and 14 dB for 5th harmonic)[23].

6.2.2 Harmonic Suppression with Load Impedance of Complex Value

If we consider the ideal backscatter tag, the magnitude of reflection on the Smith chart is assumed to be unity. As the load impedance varies counter-clockwise along the circle with a constant speed ω_1 , the backscatter signal S_{bsl} becomes[23]:

$$S_{bs} = \cos(2\pi f_0 t + \omega_1 t) = \cos [2\pi(f_0 + f_1)t] \quad (6.3)$$

Where $f_1 = \omega_1/(2\pi)$ and incoming signal S_{in} in Equation (6.1) is assumed.

The process can be presented in Equation (6.5) as:

$$S_{bs1} = \text{Re}(e^{j\pi f_0 t} \cdot \Gamma_{bs1}) \quad (6.4)$$

Whereby

$$\Gamma_{bs1} = e^{j2\pi f_1 t} \quad (6.5)$$

From Equation (6.4) it can be observed that no harmonic is generated when the reflection coefficient at speed ω_1 , a pure backscatter tone $f_0 - f_1$, is created. Because this is an ideal case and it cannot be achieved in reality, the recommended practical approach is to use either an IQ modulator circuit or a single N-Throw with variable reactance. As the recommended practical solutions are far from ideal, a significant loss will be experienced by the proposed solution.[23]

When Equation (6.6) is discretised with M equal spaced in a smith chart complex impedance, the Equation becomes[23]:

$$\Gamma_{bs2} = \begin{cases} e^{j0} & t \in [k/f_1, (kM+1)/Mf_1) \\ e^{j\frac{2\pi}{M}} & t \in [(kM+1)/Mf_1, (kM+2)/Mf_1) \\ e^{j\frac{(M-1)\pi}{M}} & t \in [(kM+M-1)/Mf_1, (k+1)/f_1) \end{cases} \quad (6.6)$$

Where $k = (0, 1, \dots)$ and $M \geq 2$.

By applying the complex Fourier expansion, $\Gamma_{bs2}(t)$ can be written as:

$$\Gamma_{bs2}(t) = f_1 \sum_{p=-\infty}^{\infty} X_p \cdot e^{j2\pi p f_1 t} \quad (6.7)$$

Where the X_p ($p = -\infty, \dots, +\infty$) of the P^{th} term of the expansion in Equation (6.8) can be evaluated as:

$$X_p = \int_0^{1/f_1} \Gamma_{bs2}(t) \cdot e^{-j2\pi p f_1 t} dt \quad (6.8)$$

By substituting Equation (6.7) into (6.9) we get:

$$X_0 = 0 \quad (6.9)$$

$$X_p|_{p \neq 0} = \frac{j}{2pf_1\pi} \sum_{m=0}^{M-1} e^{j\frac{2\pi[m-p(m-1)]}{M}} - e^{j\frac{2\pi m(1-p)}{M}} \quad (6.10)$$

The magnitude of backscatter P^{th} in Equation (6.8) is:

$$A_p = f_1 |X_p| \quad (6.11)$$

Table 6.1. Normalised Power (A_p In dB) Of Backscatter Harmonics (Up To ± 5) For Different Numbers Of Discrete Impedances [23].

P	M							
	2	3	4	5	6	7	8	9
-5	-17.9	-15.6	$-\infty$	$-\infty$	-14.4	$-\infty$	$-\infty$	$-\infty$
-4	$-\infty$	$-\infty$	$-\infty$	-12.6	$-\infty$	$-\infty$	$-\infty$	$-\infty$
-3	-13.4	$-\infty$	-10.5	$-\infty$	$-\infty$	$-\infty$	$-\infty$	$-\infty$
-2	$-\infty$	-7.7	$-\infty$	$-\infty$	$-\infty$	$-\infty$	$-\infty$	$-\infty$
-1	-3.9	$-\infty$	$-\infty$	$-\infty$	$-\infty$	$-\infty$	$-\infty$	$-\infty$
1	-3.9	-1.65	-0.91	-0.58	-0.40	-0.29	-0.22	-0.18
2	$-\infty$	$-\infty$	$-\infty$	$-\infty$	$-\infty$	$-\infty$	$-\infty$	$-\infty$
3	-13.4	$-\infty$	$-\infty$	$-\infty$	$-\infty$	$-\infty$	$-\infty$	$-\infty$
4	$-\infty$	-13.7	$-\infty$	$-\infty$	$-\infty$	$-\infty$	$-\infty$	$-\infty$
5	-17.9	$-\infty$	-14.9	$-\infty$	$-\infty$	$-\infty$	$-\infty$	$-\infty$

From Table 6.1 it can be observed that the first upper band harmonics converge to 0 dB when M is increased to infinity. The table can be used as the benchmark when selecting f_I and M for harmonic cancellation.

6.2.3 Mirror Harmonic Suppression with Orthogonal Loads

From Table 6.1 it can be observed that, when $M > 2$, there will be no 1st order mirror harmonic, but harmonics of $(I-M)$ and $(I+M)$ are still present. This part will explore the approach and proposed hardware for cancelling all the higher harmonics[23].

From trigonometric identities in Equations (6.13) and (6.14), it can be seen that, by shifting the incoming electromagnetic signal by 90° , a copy of all terms in Equation (6.2) can be created, namely $(\cos 2\pi f_0 + \pi/2)$ and $(\sin 2\pi n f_{bs} + \pi/2)$, and all the mirror harmonics can be suppressed[23].

$$\cos x \cdot \sin y = 0.5[\sin(x + y) - \sin(x - y)] \quad (6.12)$$

$$\sin x \cdot \cos y = 0.5[\sin(x + y) + \sin(x - y)] \quad (6.13)$$

The 90° phase shift can be achieved in the hardware by adding a $\frac{1}{4}\lambda$ on the transmission line. 90° phase shift in Equation (6.2) is achieved by moving the square waveform in Figure 6.3 leftward by $T_{bs}/4$. This is achieved by using the IQ modulator circuit of Figure 5.11.

From the circuit of Figure 5.11, the incoming signal S_{in} is equally divided, before being delayed by 45° in one branch. As the incoming signal passes through the 45° delay twice (First during incoming and the second after backscattering), the phase shift of $0.707 \times S_{in}$ in the top branch of the IQ modulator circuit becomes 90° [23]. The backscatter signal, in this case, can be expressed as in Equation (6.15):

$$S_{bs5} = 0.5\Gamma_Q \cos(2\pi f_0 t) - 0.5\Gamma_I \cdot \sin(2\pi f_0 t) \quad (6.14)$$

Where Γ_I and Γ_Q are reflection coefficients of the two transistors used in the IQ modulator circuit and are controlled by transistor gate voltages V_I and V_Q .

As Γ_I is shifted quarterly compared to Γ_Q , using the Fourier expansion this can be written as:

$$\Gamma_I(t) = \frac{4}{\pi} \sum_{n=1,3,5}^{\infty} \frac{1}{n} \cos(2n\pi f_{bs}t) \quad (6.15)$$

$$\Gamma_Q(t) = \frac{4}{\pi} \sum_{n=1,3,5}^{\infty} \frac{1}{n} \sin(2n\pi f_{bs}t) \quad (6.16)$$

When Equations (6.16) and (6.17) are substituted in Equation (6.15) it becomes:

$$S_{bs5} = \frac{2}{\pi} \sum_{n=1,3,5}^{\infty} \frac{1}{n} \cos(2\pi f_0 t) \cdot \sin(2n\pi f_{bs}t) + \frac{2}{\pi} \sum_{n=1,3,5}^{\infty} \frac{1}{n} \sin(2\pi f_0 t) \cdot \cos(2n\pi f_{bs}t)$$

$$S_{bs5} = \frac{2}{\pi} \sum_{n=1,3,5}^{\infty} \frac{1}{n} \sin[2\pi(f_0 + n f_{bs})t] \quad (6.17)$$

From Equation (6.18), it can be seen that all the lower band harmonics have been removed. Using the same approach, the higher harmonics can also be cancelled/suppressed[23].

6.2.4 Summary of Harmonic Suppression in Frequency Shifted Backscatter Systems

In this section, harmonic suppression for a frequency-shifted backscatter system has been explored. The proposed approach is scalable and can be used to independently manipulate the lower and higher harmonics as per the requirements of the network. The laboratory and field measurements will be conducted to validate the proposed methodology[23].

6.3 Proposed Implementation of WiFi Backscatter Tags in the GWSN

The Tag receives the incoming single carrier electromagnetic wave from a commodity WiFi router, convert into OFDM modulated IEEE 802.11g preamble, then backscatter it to a commodity WiFi device (WiFi router).

In a proposed architecture in Figure 6.4, power consuming sensor nodes and Gateway of GWSN is replaced by WiFi backscatter tags and WiFi router. A tag measures and transmits the required parameters via wireless communication to the cloud via the WiFi router for further processing.

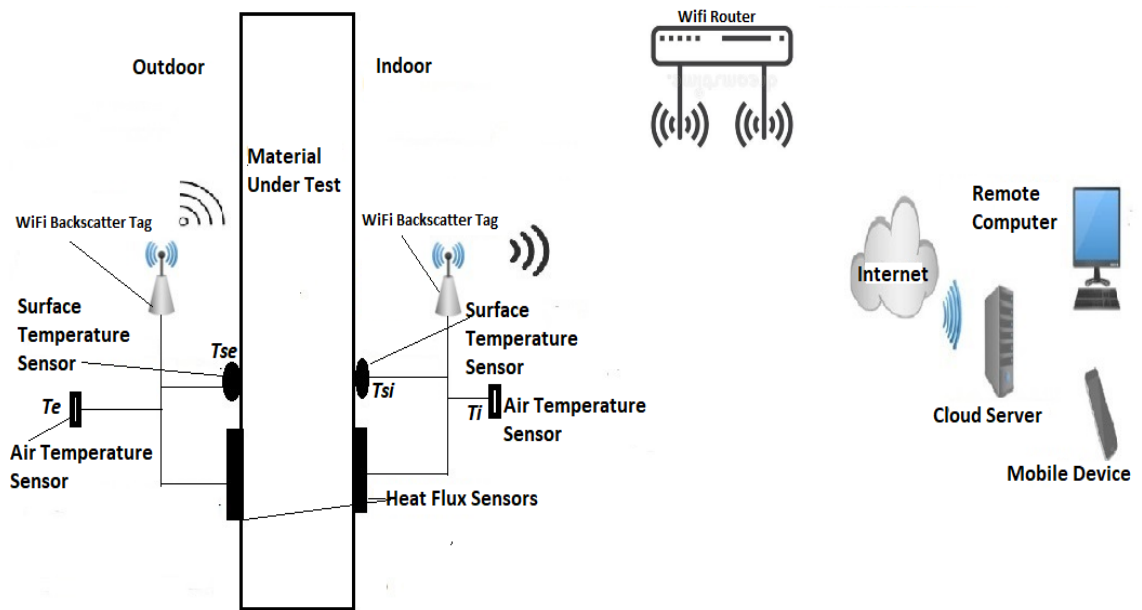


Figure 6.4. Proposed Implementation of Wi-Fi Backscatter on GWSN showing how the backscatter tag will replace the sensor node in GWSN and the flow of signal from the tag to the cloud.

For this architecture, all the processing will be performed on the remote computer. GWSN Gateway node can be included on the proposed architecture if the local processing and storage of data is required

6.4 Conclusion

In this chapter, a novel backscatter tag compatible with WiFi has been proposed and implemented. No dedicated reader is required as the receiver of the backscatter signal, as the existing WiFi infrastructure is used directly. A novel harmonic suppression approach suitable for a frequency-shifted backscatter system has also been proposed, implemented, and validated. An over the air test (OTA) to measure the performance of the system, laboratory and field measurements will be conducted to validate the proposed methodology. In the next chapter, conclusions from the results are discussed, the contributions presented, and recommendations for future work are made.

Chapter Seven

Conclusion and Future Work

7 Introduction

In this chapter, conclusions from the results are discussed, and the contributions and recommendations for future work are presented.

7.1 Summary of the Research

The project aimed to develop a generic wireless sensing system that will assess how building materials interact with the environment and the impact of a building on indoor environment quality. The research aims and objectives were formulated based on findings from the literature review and the requirements of the project. The work was carried out in several stages to meet the stated objectives.

Objective (a) - To study the state-of-the-art systems as benchmarks to understand the interactions between buildings, environment, and occupants' wellbeing.

To meet this objective, background information on building materials measurements and how variations in building materials affect indoor environment quality have been explored. From the review, it has been concluded that, the material used for the construction of the building envelope has an impact on how quickly changes in weather conditions are felt. As external weather changes, the indoor weather will also change. Building material thermal insulation has a direct effect on the indoor environment weather. As the outdoor air temperature varies, the indoor air temperature will also vary. The time taken for the temperature change to be noticed depends on the quality and properties of the material used for construction.

When the outdoor humidity/temperature varies, the indoor humidity/temperature will also vary. The time taken for the changes to be felt depends on the quality and properties of the building materials used. By proper selection of building materials, the quality of the indoor environment can be controlled by regulating the influence of outdoor humidity and temperature on the indoor variations. Most bacteria and viruses that cause respiratory infections survive in high and low humidity. Dust mites, mould spores, and other

allergens also survive in a high humidity environment. High humidity increases the levels of noxious gases such as ozone and formaldehyde

The physical properties of the material determine the amount of sound which can be reflected and absorbed. As the sound/noise hits the surface of the building materials, a portion of sound will be reflected, and some will be absorbed. Acoustic or sound insulation is one of the important parameters when designing building materials. This is because of the importance of controlling and limiting the amount of noise, for the benefit and wellbeing of people in homes, offices, and schools.

Objective (b) - To design and implement a generic wireless sensing system that collects data from multiple sensors.

Objective (c) - To conduct laboratory experiments on measurements of building material properties and indoor environment quality.

Objective (d) - To develop an application platform for visualising, monitoring, and assessing the impact of the environment on buildings, and the impact of the building on indoor environment quality.

To meet objectives (b-d), this thesis takes the initiative of designing and implementing a low-powered, open-source, flexible, and small-sized Generic wireless sensor network (GWSN) that can continuously monitor the building materials and building environment, The designed system is comprised of two custom-made sensor nodes and a gateway, as well as purpose designed firmware for data collection and processing. For the proof of concept and experimental studies, several measurement strategies were designed, to demonstrate, evaluate, and validate the effectiveness of the system. The data was collected from selected case study areas in the School of Energy, Geoscience, Infrastructure and Society (EGIS) laboratories by measuring and monitoring building structures and indoor environment quality parameters using the designed GWSN. The measured data includes heat flux through the material, surface and air temperatures on both sides of the material/structure, moisture variation, ambient temperature, relative humidity, carbon dioxide, volatile organic compounds, particulate matter, and sound/acoustic levels. Based on the estimates of the thermal performance data, the sample used in the experiment had a typical U-value between 4.8 and 5.8 W/m²K and a thermal resistance value of 0.025m²·K/W[1][2]. Thermal resistance values from the GWSN real-time measurement were between 0.025 and 0.03 m²K/W, with an average of 0.025

$\text{m}^2\text{K/W}$, and thermal transmission values varied between 4.55 and 5.11 $\text{W/m}^2\text{K}$. Based on the data obtained, the results are within the range of typical values[3].

For thermal comfort measurements, the results of humidity and temperature from GWSN were compared to values in the Kambic climatic chamber in the EGIS laboratory, and the accuracies were 99 % and 98 % respectively. For the IAQ measurements, the values of CO₂ and TVOCs were compared to the commercial off-the-shelf measuring system, and the accuracies were 98 %, and 97 %. Finally, the GWSN was tested for acoustic measurements in the range of 55 dB to 106 dB. The results were compared to class one Bruel & Kjaer SLM. The accuracy of GWSN was 97 %. The summary of GWSN performance is presented in Table 7.1.

Table 7.1. Summary of the GWSN operating performance

Measured Parameter	Accuracy (%)
Humidity (%)	99
Temperature (°C)	98
CO ₂ (ppm)	98
TVOC (ppm)	97
Acoustic (dB)	97

7.2 Key Research Contributions

The aims and objectives set for this dissertation were completed, and the following are the contributions:

For part one of the research:

- a) Design and build a novel, low-powered, open-source, flexible, and small-sized GWSN that can continuously monitor building materials and building environment to address the limitations of the conventional measurement methods and the technological gap stated in the previous studies. The GWSN can be used for in-lab and in-situ applications to measure and analyse the thermal physical properties of building materials/building structures. The system can also measure IAQ thermal comfort and airborne sound insulation of the building envelope. In summary, the designed GWSN used customised hardware and firmware that performs the following:

- f) Measuring heat flux through the material, air temperature, and surface temperature on both sides of the building material. They are used to evaluate the thermal transmittance (U-value), thermal conductivity, and thermal resistance of the material.
 - g) Measuring air temperature and humidity. They are used to analyse the thermal comfort of the building envelope.
 - h) Measuring VOCs dust, and carbon dioxide. They are used to analyse the IAQ of the building envelope.
 - i) Measuring sounds/acoustic. They are used to analyse airborne sound insulation.

b) Creation of:

- New firmware to collect the data, process it and store it in the local database.
- A novel logarithmic model that uses the sensitivity characteristics curve of the TGS2602 sensor to estimate the values of various VOCs
- A novel linear regression model that uses raw acoustic data to predict the decibel level.

A key contribution of part one of the research was the design of a wireless system that solves the challenges of existing measurement methods and links the study of the variation of building materials with the environment and its impact on indoor air quality.

For part two of the research, the contributions are:

- a) New sensing platforms using backscatter technology have been introduced. The theory of modulation and spread spectrum technique used in backscattering has been explored. The trade-off between hardware complexity/power consumption and link performance has been investigated.
- b) A novel multicarrier backscatter tag compatible with WiFi has been implemented. No dedicated reader is required for intercepting the incoming backscattered signal; the existing WiFi infrastructure can be used directly.
- c) The harmonics generated by a frequency-shifted backscatter communication system were studied, and a novel harmonic suppression method was developed.

7.3 GWSN on Complex structures

GWSN system measures thermal performance based on heat flow method in BS 9869[73]. All the measurements procedures and setup for different types of structures follows the standard[73]. According to [73], sensors (heat flux and temperature sensors) shall be mounted according to the purpose of the measurements. Other important consideration to be taken are:

- a) The proper sensor mapping must be investigated by using infra-red thermography in accordance with ISO 6781:1983[185].
- b) Sensors shall be mounted in such a way to ensure a result which is representative of the whole element.
- c) Several should be heat flux sensors installed to obtain a representative average.
- d) Sensors shall not be installed in the vicinity of thermal bridges, cracks or similar sources of error.
- e) Sensors shall not be under the direct influence of either a heating, cooling devices and the external surface of the element under test should be protected from rain, snow and direct solar radiation.

Measurements on this research focuses on glass structure, which is considered as less complex structure with low value of thermal resistance. For structures of high R-value and high thermal mass, internal and external thermal mass factors (F_i and F_e) must be calculated for the structure concerned and an adjustment, involving these factors, to the measured flux at each data point must be performed.

For a structure consisting of N plane parallel layers, numbered from 1 to N with layer 1 at the indoor surface, for heat flux measured at the indoor surface, as follows; For each layer k, estimate its thermal resistance R_k in square metres kelvin per watt ($m^2 \cdot K/W$) (thickness divided by thermal conductivity or thermal resistance of airspace) and its thermal capacity C_k in joules per square metre kelvin [$J/(m^2 \cdot K)$].

Let R be the estimated total thermal resistance of the wall, i.e. the sum of all R_{ks} . Then for each layer k, the inner (R_{ik}) and outer (R_{ek}) is determined as;

$$R_{ik} = \sum_{j=1}^{k-1} R_j \quad R_{ek} = \sum_{j=k+1}^N R_j \quad (7.1)$$

And thermal mass factors.

$$F_{ek} = C_k \left[\frac{R_k}{R} \left\{ \frac{1}{6} + \frac{R_{ik} + R_{ek}}{3R} \right\} + \frac{R_{ik} R_{ek}}{R^2} \right] \quad (7.2)$$

$$F_{ik} = C_k \left[\frac{R_{ek}}{R} + \frac{R_k^2}{3R^2} + \frac{R_{ik} R_{ek}}{R^2} \right] \quad (7.3)$$

Note:

- a) For the interior layer ($j = k = 1$), $R_{ik} = 0$; for the exterior layer ($j = k = N$), $R_{ek} = 0$.
- b) When thermal transmittance is being measured, surface resistance should be included so that the measured temperatures are environmental (ambient) temperatures rather than surface temperatures
 - Add R_{si} to each value of R_{ik}
 - Add R_{se} to each value of R_{ek}
 - Add $R_{si} + R_{se}$ to R .

The thermal mass factors for the structure are then given by

$$F_1 = \sum_{k=1}^N F_{ik} \quad (7.4)$$

and

$$F_e = \sum_{k=1}^N F_{ek} \quad (7.5)$$

7.4 Future Work

A list of suggestions for further research, following on from this dissertation, is as follows.

For part one of the research:

- a) The research was focused on in-laboratory measurements only. The application and analysis should be widened by deploying the designed system on-site.
- b) The scripts used for thermal performance measurements worked as expected, and all results were compared to those found in reference documents. The U-value was calculated using an average method, with sensor values collected for seven days. For more analysis, the dynamic method for U-value measurements could be used, and the results compared with the results obtained using the average method.
- c) As per the scope of this research, data analysis has been performed using manual input to the Matlab software. To make the system more flexible and reliable, it is recommended to have an interface that will receive the sensor data directly from various nodes, load to the Matlab software, and perform the required analysis directly, without the need for any physical intervention.
- d) The gateway as the centre of all the operations of the sensor network has to be reliable in operation. To achieve this, Python script needs to include the script to handle internet connection status that can detect connection failure and store the data on the local database when there is no internet.

- e) Further reduction in power consumption per node could be achieved by adding high side switching or using a microcontroller in duty circle mode. Provided the measurement is not compromised, any other power-saving strategy can be used.

For part two of the research:

As the sensing platform using backscattering in this report covers only theoretical analysis and simulation validation, future work could focus on experimental validation of the backscattering communication system by performing the following:

- a) Implement the hardware of a universal backscatter tag using an IQ modulator.
- b) OTA to measure the performance of the system and investigate how the concept can be adopted and used in other multicarrier commercial wireless systems.
- c) Universal backscatter tags integration with GWSN.

7.5 Research Conclusion

The new GWSN was a sufficient tool for assessing how building materials interact with the environment, and the impact of a building on indoor environment quality. The output system is simple, and easily understood by building material experts. This was made possible by the use of the input parameters to a GWSN. The experimental setup could assist in the material development cycle by observing and analysing the quality of building materials in each stage of design and manufacturing.

8 References

- [1] C. Wood, “Thermal Performance of Historic Windows,” *The Building Conservation Directory*, 2012. [Online]. Available: <https://www.buildingconservation.com/articles/thermal/thermal.htm>. [Accessed: 04-Jan-2020].
- [2] Designing Buildings Ltd, “U-values,” *Designing buildings Wiki*, 2019. [Online]. Available: <https://www.designingbuildings.co.uk/wiki/U-values>. [Accessed: 04-Jan-2020].
- [3] R. Lihakanga, Y. Ding, G. M. Medero, S. Chapman, and G. Goussetis, “A high-resolution open source platform for building envelope thermal performance assessment using a wireless sensor network,” *Sensors (Switzerland)*, vol. 20, no. 6, 2020.
- [4] CSIC, “The K-Briq: The Sustainable Brick,” *online*, 2021. [Online]. Available: <https://www.cs-ic.org/library/the-k-briq/>. [Accessed: 02-Dec-2021].
- [5] Rima Sabina, “Kenoteq launches brick made almost entirely of construction waste,” *online*, 2020. [Online]. Available: <https://www.dezeen.com/2020/03/02/kenoteq-k-briq-brick-construction-waste/>. [Accessed: 02-Dec-2021].
- [6] Forbes, “Scottish Startup Creates Breakthrough Brick Made From Construction Waste,” *online*, 2020. [Online]. Available: <https://www.forbes.com/sites/scottsnowden/2020/05/07/scottish-startup-creates-breakthrough-brick-made-from-construction-waste/?sh=3003ab212cc7>. [Accessed: 02-Dec-2021].
- [7] V. Echarri, A. Espinosa, and C. Rizo, “Thermal transmission through existing building enclosures: Destructive monitoring in intermediate layers versus non-destructive monitoring with sensors on surfaces,” *Sensors (Switzerland)*, vol. 17, no. 12, 2017.
- [8] G. Ficco, F. Iannetta, E. Ianniello, F. R. D’Ambrosio Alfano, and M. Dell’Isola, “U-value in situ measurement for energy diagnosis of existing buildings,” *Energy Build.*, vol. 104, pp. 108–121, 2015.
- [9] H. Awad, M. Gül, H. Zaman, H. Yu, and M. Al-Hussein, “Evaluation of the thermal and structural performance of potential energy efficient wall systems for mid-rise wood-frame buildings,” *Energy Build.*, vol. 82, pp. 416–427, 2014.
- [10] A. Ahmad, M. Maslehuddin, and L. M. Al-Hadhrani, “In situ measurement of thermal transmittance and thermal resistance of hollow reinforced precast concrete

- walls,” *Energy Build.*, vol. 84, pp. 132–141, 2014.
- [11] E. Sassine, Z. Younsi, Y. Cherif, A. Chauchois, and E. Antczak, “Experimental determination of thermal properties of brick wall for existing construction in the north of France,” *J. Build. Eng.*, vol. 14, no. September, pp. 15–23, 2017.
 - [12] L. Pitt, P. R. Green, and B. Lennox, “A sensor network for predicting and maintaining occupant comfort,” *2013 IEEE Work. Environ. Energy Struct. Monit. Syst. EESMS 2013 - Proc.*, 2013.
 - [13] W. Torresani, N. Battisti, A. Maglione, D. Brunelli, and D. Macii, “A multi-sensor wireless solution for indoor thermal comfort monitoring,” *2013 IEEE Work. Environ. Energy Struct. Monit. Syst. EESMS 2013 - Proc.*, 2013.
 - [14] I. M. Tolentino, R. S. Juson, B. U. Tan, and M. R. Talampas, “Design, development, and evaluation of a simple wireless sensor network for indoor microclimate monitoring,” *TENCON 2010 - 2010 IEEE Reg. 10 Conf.*, pp. 2018–2023, 2010.
 - [15] P. Changhai, Q. Kun, and W. Chenyang, “Design and Application of a VOC-Monitoring System Based on a ZigBee Wireless Sensor Network,” *Sensors Journal, IEEE*, vol. 15, no. 4, pp. 2255–2268, 2015.
 - [16] X. Yang, L. Yang, and J. Zhang, “A WiFi-enabled Indoor Air Quality Monitoring and Control System : the Design and Control Experiments,” pp. 3–8, 2017.
 - [17] S. C. Folea and G. Mois, “A low-power wireless sensor for online ambient monitoring,” *IEEE Sens. J.*, vol. 15, no. 2, pp. 742–749, 2015.
 - [18] R. Plessis, A. Kumar, G. P. Hancke, and B. J. Silva, “A wireless system for indoor air quality monitoring,” pp. 0–5, 2016.
 - [19] “BSI Standards Publication Acoustics — Field measurement of sound insulation in buildings and of building elements Part 1 : Airborne sound insulation (ISO,” 2014.
 - [20] NTI audio, “Building Acoustic Measurements,” *online*, 2021. [Online]. Available: <https://www.nti-audio.com/en/applications/room-building-acoustics/building-acoustics>.
 - [21] Lumen, “Build a logarithmic model from data,” 2013. [Online]. Available: <https://courses.lumenlearning.com/ivytech-collegealgebra/chapter/build-a-logarithmic-model-from-data/>. [Accessed: 02-Dec-2021].
 - [22] STATOLOGY, “Logarithmic Regression in Excel (Step-by-Step),” 2021. [Online]. Available: <https://www.statology.org/logarithmic-regression-excel/>.

[Accessed: 02-Dec-2021].

- [23] Y. Ding, R. Lihakanga, R. Correia, G. Goussetis, and N. B. Carvalho, “Harmonic Suppression in Frequency Shifted Backscatter Communications,” *IEEE Open J. Commun. Soc.*, vol. 1, no. July, pp. 990–999, 2020.
- [24] T. Constructor, “Properties of Building Materials and their Importance in Construction,” 2021. [Online]. Available: <https://theconstructor.org/building/properties-of-building-materials-construction/14891/>. [Accessed: 08-Oct-2021].
- [25] S. Kang, D. Ou, and C. M. Mak, “The impact of indoor environmental quality on work productivity in university open-plan research offices,” *Build. Environ.*, vol. 124, pp. 78–89, 2017.
- [26] Y. Al horr, M. Arif, M. Katafygiotou, A. Mazroei, A. Kaushik, and E. Elsarrag, “Impact of indoor environmental quality on occupant well-being and comfort: A review of the literature,” *Int. J. Sustain. Built Environ.*, vol. 5, no. 1, pp. 1–11, 2016.
- [27] M. C. Lee, K. W. Mui, L. T. Wong, W. Y. Chan, E. W. M. Lee, and C. T. Cheung, “Student learning performance and indoor environmental quality (IEQ) in air-conditioned university teaching rooms,” *Build. Environ.*, vol. 49, no. 1, pp. 238–244, 2012.
- [28] M. Frontczak and P. Wargocki, “Literature survey on how different factors influence human comfort in indoor environments,” *Build. Environ.*, vol. 46, no. 4, pp. 922–937, 2011.
- [29] P. U. Europe, “‘ Breathability ’ of building elements,” 2013.
- [30] UCAR, “How Weather Affects Air Quality,” 2021. [Online]. Available: <https://scied.ucar.edu/learning-zone/air-quality/how-weather-affects-air-quality>. [Accessed: 08-Oct-2021].
- [31] L. Fang, “Impact of temperature and humidity on the perception of indoor air quality,” *Indoor Air*, vol. 8, no. 2, pp. 80–90, 1998.
- [32] REHVA, “Effects of indoor air humidity,” 2021. [Online]. Available: <https://www.rehva.eu/rehva-journal/chapter/effects-of-indoor-air-humidity>. [Accessed: 08-Oct-2021].
- [33] K. Loupos and A. Amditis, “Fiber Optic Sensors,” vol. 21, no. especially civil, 2017.
- [34] M. Sun, W. J. Staszewski, and R. N. Swamy, “Smart sensing technologies for

- structural health monitoring of civil engineering structures,” *Adv. Civ. Eng.*, vol. 2010, 2010.
- [35] J. P. Newhook, B. Bakht, A. Mufti, and G. Tadros, “Monitoring of Hall ’ s Harbour wharf,” vol. 4337, pp. 234–244, 2001.
 - [36] P. L. Fuhr, D. R. Huston, P. J. Kajenski, and T. P. Ambrose, “Performance and health monitoring of the Stafford Medical Building using embedded sensors,” *Smart Mater. Struct.*, vol. 1, no. 1, pp. 63–68, 1992.
 - [37] I. B. Kwon, C. Y. Kim, and M. Y. Choi, “Continuous measurement of temperature distributed on a building construction,” *Proc. SPIE - Int. Soc. Opt. Eng.*, vol. 4696, no. June, pp. 273–283, 2002.
 - [38] P. L. Fuhr and D. R. Huston, “Corrosion detection in reinforced concrete roadways and bridges via embedded fiber optic sensors,” *Smart Mater. Struct.*, vol. 7, no. 2, pp. 217–228, 1998.
 - [39] B. P. Cosentino, B. Grossman, C. Shieh, S. Doi, H. Xi, and P. Erbland, “Fiber-optic chloride sensor development,” *J. Geotech. Eng.*, vol. 121, no. 8, pp. 610–617, 1995.
 - [40] C. K. Soh, K. K.-H. Tseng, S. Bhalla, and A. Gupta, “Performance of smart piezoceramic transducers in health monitoring of RC bridge,” *Smart Mater. Struct.*, vol. 9, pp. 553–542, 2000.
 - [41] Y. Y. Lim, S. Bhalla, and C. K. Soh, “Structural identification and damage diagnosis using self-sensing piezo-impedance transducers,” *Smart Mater. Struct.*, vol. 15, no. 4, pp. 987–995, 2006.
 - [42] G. Song, H. Gu, and Y. L. Mo, “Smart aggregates: Multi-functional sensors for concrete structures - A tutorial and a review,” *Smart Mater. Struct.*, vol. 17, no. 3, 2008.
 - [43] X. Zhao, H. Li, D. Du, and J. Wang, “Concrete structure monitoring based on built-in piezoelectric ceramic transducers,” vol. 6932, p. 693208, 2008.
 - [44] X. Yi, C. Cho, J. Cooper, Y. Wang, M. M. Tentzeris, and R. T. Leon, “Passive wireless antenna sensor for strain and crack sensing - Electromagnetic modeling, simulation, and testing,” *Smart Mater. Struct.*, vol. 22, no. 8, 2013.
 - [45] C. Cho, X. Yi, D. Li, Y. Wang, and M. M. Tentzeris, “Passive Wireless Frequency Doubling Antenna Sensor for Strain and Crack Sensing,” *IEEE Sens. J.*, vol. 16, no. 14, pp. 5725–5733, 2016.
 - [46] R. Khalifeh *et al.*, “Development of wireless and passive corrosion sensors for

- material degradation monitoring in coastal zones and immersed environment,” *IEEE J. Ocean. Eng.*, vol. 41, no. 4, pp. 776–782, 2016.
- [47] Z. Meng and Z. Li, “RFID Tag as a Sensor - A Review on the Innovative Designs and Applications,” *Meas. Sci. Rev.*, vol. 16, no. 6, pp. 305–315, 2016.
 - [48] P. Kalansuriya, R. Bhattacharyya, and S. Sarma, “RFID tag antenna-based sensing for pervasive surface crack detection,” *IEEE Sens. J.*, vol. 13, no. 5, pp. 1564–1570, 2013.
 - [49] S. Caizzzone and E. DiGiampaolo, “Wireless Passive RFID Crack Width Sensor for Structural Health Monitoring,” *IEEE Sens. J.*, vol. 15, no. 12, pp. 6767–6774, 2015.
 - [50] A. M. J. Marindra and G. Y. Tian, “Chipless RFID Sensor Tag for Metal Crack Detection and Characterization,” *IEEE Trans. Microw. Theory Tech.*, vol. 66, no. 5, pp. 2452–2462, 2018.
 - [51] A. Siddiqui, R. Mahboob, and T. Islam, “A Passive Wireless Tag with Digital Readout Unit for Wide Range Humidity Measurement,” *IEEE Trans. Instrum. Meas.*, vol. 66, no. 5, pp. 1013–1020, 2017.
 - [52] E. M. Amin, M. S. Bhuiyan, N. C. Karmakar, and B. Winther-Jensen, “Development of a low cost printable chipless RFID humidity sensor,” *IEEE Sens. J.*, vol. 14, no. 1, pp. 140–149, 2014.
 - [53] X. Yi, T. Wu, Y. Wang, and M. M. Tentzeris, “Sensitivity modeling of an RFID-based strain-sensing antenna with dielectric constant change,” *IEEE Sens. J.*, vol. 15, no. 11, pp. 6147–6155, 2015.
 - [54] G. Chakaravarthi, K. P. Logakannan, J. Philip, and J. Rengaswamy, “Reusable Passive Wireless RFID Sensor for Strain Measurement on Metals,” vol. 18, no. 12, pp. 5143–5150, 2018.
 - [55] C. Occhiuzzi, C. Paggi, and G. Marrocco, “Passive RFID strain-sensor based on meander-line antennas,” *IEEE Trans. Antennas Propag.*, vol. 59, no. 12, pp. 4836–4840, 2011.
 - [56] E. DiGiampaolo, A. DiCarlofelice, and A. Gregori, “An RFID-enabled wireless strain gauge sensor for static and dynamic structural monitoring,” *IEEE Sens. J.*, vol. 17, no. 2, pp. 286–294, 2017.
 - [57] A. A. Babar, S. Manzari, L. Sydanheimo, A. Z. Elsherbeni, and L. Ukkonen, “Passive UHF RFID tag for heat sensing applications,” *IEEE Trans. Antennas Propag.*, vol. 60, no. 9, pp. 4056–4064, 2012.

- [58] J. J. Martinez-Martinez, F. Javier Herraiz-Martinez, and G. Galindo-Romera, "Design and Characterization of a Passive Temperature Sensor Based on a Printed MIW Delay Line," *IEEE Sens. J.*, vol. 16, no. 22, pp. 7884–7891, 2016.
- [59] M. Krüger, C. U. Grosse, and P. J. Marrón, "Wireless Structural Health Monitoring Using MEMS," *Key Eng. Mater.*, vol. 293–294, pp. 625–634, 2005.
- [60] A. Sabato, "Pedestrian bridge vibration monitoring using a wireless MEMS accelerometer board," *Proc. 2015 IEEE 19th Int. Conf. Comput. Support. Coop. Work Des. CSCWD 2015*, pp. 437–442, 2015.
- [61] T. D. Tan, N. T. Anh, and G. Q. Anh, "Lowcost structural health monitoring scheme using MEMS-based accelerometers," *Proc. - 2011 2nd Int. Conf. Intell. Syst. Model. Simulation, ISMS 2011*, vol. 0, pp. 217–220, 2011.
- [62] T. Torfs *et al.*, "Low Power Wireless Sensor Network for Building Monitoring," *IEEE Sens. J.*, vol. 13, no. 3, pp. 1–1, 2012.
- [63] M. Ahmed, M. M. Chitteboyina, D. P. Butler, and Z. Celik-Butler, "MEMS Force sensor in a flexible substrate using nichrome piezoresistors," *IEEE Sens. J.*, vol. 13, no. 10, pp. 4081–4089, 2013.
- [64] F. Caimmi, S. Mariani, M. De Fazio, and P. Bendiscioli, "Investigation of the effectiveness and robustness of a MEMS-based structural health monitoring system for composite laminates," *IEEE Sens. J.*, vol. 14, no. 7, pp. 2208–2215, 2014.
- [65] S. Azeem, P. Sharan, and S. Talabattula, "MOEMS Based Photonic Crystal Sensor for Structural Health Monitoring System," no. 978, pp. 31–34, 2014.
- [66] S. Sindhuja and J. Siluvai, "MEMS-based wireless sensors network system for post- seismic tremor harm evaluation and building monitoring.," pp. 1–4, 2015.
- [67] B. Buttarazzi, G. Troiani, W. Liguori, and M. Basili, "Smart Sensor Box: A Real Implementation of Devices Network for Structural Health Monitoring," *Proc. - 11th Int. Conf. Signal-Image Technol. Internet-Based Syst. SITIS 2015*, pp. 816–823, 2016.
- [68] A. Sabato, C. Niezrecki, G. Fortino, and S. M. Ieee, "Wireless MEMS - Based Accelerometer Sensor Boards for Structural Vibration Monitoring : A Review," vol. 17, no. c, pp. 226–235, 2016.
- [69] A. Al-Radaideh, A. R. Al-Ali, S. Bheiry, and S. Alawnah, "A wireless sensor network monitoring system for highway bridges," *1st Int. Conf. Electr. Inf. Technol.*, pp. 119–124, 2015.

- [70] W. Sujatmiko, F. Suhedi, and A. Rumiawati, "Thermal resistance measurements of building envelope components of the minang traditional house using the heat flow method," *Proceeding - 2016 Int. Semin. Sensors, Instrumentation, Meas. Metrol. ISSIMM 2016*, pp. 88–92, 2017.
- [71] E. Sassine, "A practical method for in-situ thermal characterization of walls," *Case Stud. Therm. Eng.*, vol. 8, pp. 84–93, 2016.
- [72] A. Rasooli, L. Itard, and C. I. Ferreira, "A response factor-based method for the rapid in-situ determination of wall's thermal resistance in existing buildings," *Energy Build.*, vol. 119, pp. 51–61, 2016.
- [73] "BSI Standards Publication Thermal insulation — Building elements — In- situ measurement of thermal resistance and thermal transmittance Part 1 : Heat flow meter method," 2014.
- [74] G. Desogus, S. Mura, and R. Ricciu, "Comparing different approaches to in situ measurement of building components thermal resistance," *Energy Build.*, vol. 43, no. 10, pp. 2613–2620, 2011.
- [75] E. Lucchi, "Applications of the infrared thermography in the energy audit of buildings: A review," *Renew. Sustain. Energy Rev.*, vol. 82, no. November 2017, pp. 3077–3090, 2018.
- [76] "BS EN ISO 6946 : 2017 BSI Standards Publication Building components and building elements - Thermal resistance and thermal transmittance - Calculation methods," 2017.
- [77] Hukseflux, "TRSYS01 thermal measuring system," 2022. [Online]. Available: <https://www.hukseflux.com/products/thermal-conductivity-sensors/thermal-conductivity-measuring-systems/trsys01-thermal>. [Accessed: 23-Oct-2022].
- [78] J. M. A. Márquez, M. Á. M. Bohórquez, and S. G. Melgar, "A new metre for cheap, quick, reliable and simple thermal transmittance (U-Value) measurements in buildings," *Sensors (Switzerland)*, vol. 17, no. 9, 2017.
- [79] M. Frei, J. Hofer, A. Schlüter, and Z. Nagy, "An easily-deployable wireless sensor network for building energy performance assessment," *Energy Procedia*, vol. 122, pp. 523–528, 2017.
- [80] A. Kylili, P. A. Fokaides, P. Christou, and S. A. Kalogirou, "Infrared thermography (IRT) applications for building diagnostics: A review," *Appl. Energy*, vol. 134, pp. 531–549, 2014.
- [81] M. Fox, S. Goodhew, and P. De Wilde, "Building defect detection: External versus internal thermography," *Build. Environ.*, vol. 105, pp. 317–331, 2016.

- [82] E. W. Nick Gromicko, "IR Cameras: An Overview for Inspectors," 2022. [Online]. Available: <https://www.nachi.org/ir-camera-overview-inspectors.htm>. [Accessed: 23-Oct-2022].
- [83] C. Evangelides, G. Arampatzis, A. A. Tsambali, E. Tzanetaki, and C. Tzimopoulos, "Moisture estimation in building materials with a simple procedure," *Constr. Build. Mater.*, vol. 164, pp. 830–836, 2018.
- [84] Z. Karaca, "Water absorption and dehydration of natural stones versus time," *Constr. Build. Mater.*, vol. 24, no. 5, pp. 786–790, 2010.
- [85] K. Fukui, C. Iba, and S. Hokoi, "Moisture behavior inside building materials treated with silane water repellent," *Energy Procedia*, vol. 132, pp. 735–740, 2017.
- [86] M. Al-Naddaf, "A new automatic method for continuous measurement of the capillary water absorption of building materials," *Constr. Build. Mater.*, vol. 160, pp. 639–643, 2018.
- [87] D. Vandevorde, M. Pamplona, O. Schalm, Y. Vanhellemont, V. Cnudde, and E. Verhaeven, "Contact sponge method: Performance of a promising tool for measuring the initial water absorption," *J. Cult. Herit.*, vol. 10, no. 1, pp. 41–47, 2009.
- [88] E. Litavcova *et al.*, "Diffusion of moisture into building materials: A model for moisture transport," *Energy Build.*, vol. 68, no. PARTA, pp. 558–561, 2014.
- [89] A. Sardella, P. De Nuntiis, and A. Bonazza, "Efficiency evaluation of treatments against rising damp by scale models and test in situ," *J. Cult. Herit.*, vol. 31, pp. S30–S37, 2018.
- [90] T. FLIR, "Infrared Camera with Extended Temperature Range FLIR E5-XT," *online*, 2022. [Online]. Available: <https://www.flir.co.uk/products/e5-xt/?vertical=condition+monitoring&segment=solutions>. [Accessed: 22-Nov-2022].
- [91] F. Sandrolini and E. Franzoni, "An operative protocol for reliable measurements of moisture in porous materials of ancient buildings," *Build. Environ.*, vol. 41, no. 10, pp. 1372–1380, 2006.
- [92] E. Franzoni, F. Sandrolini, and S. Bandini, "An experimental fixture for continuous monitoring of electrical effects in moist masonry walls," *Constr. Build. Mater.*, vol. 25, no. 4, pp. 2023–2029, 2011.
- [93] W. John McCarter, G. Starrs, S. Kandasami, R. Jones, and M. Chrisp, "Electrode configurations for resistivity measurements on concrete," *ACI Mater. J.*, vol. 106, no. 3, pp. 258–264, 2009.

- [94] BS EN 772-11, "Methods of Test for Masonry Units Part 11 : Determination of Water Absorption of Aggregate Concrete , Manufactured Stone and Natural Action and the Initial Rate of Water Absorption of Clay Masonry Units," *BSI Stand. Publ.*, pp. 1–12, 2011.
- [95] British Standards Institution, *BSI Standards Publication Hygrothermal performance of building materials and products — Determination of hygroscopic sorption properties*. 2013.
- [96] ISO 12572, *ISO12572: Hygrothermal performance of building materials and products -- Determination of water vapour transmission properties -- Cup method*, vol. 2016. 2016, p. 28.
- [97] K. R. Gowers and S. G. Millard, "Measurement of concrete resistivity for assessment of corrosion severity of steel using wenner technique," *ACI Mater. J.*, vol. 96, no. 5, pp. 536–541, 1999.
- [98] A. A. Ramezani pour, A. Pilvar, M. Mahdikhani, and F. Moodi, "Practical evaluation of relationship between concrete resistivity, water penetration, rapid chloride penetration and compressive strength," *Constr. Build. Mater.*, vol. 25, no. 5, pp. 2472–2479, 2011.
- [99] A. J. Garzon, J. Sanchez, C. Andrade, N. Rebolledo, E. Menéndez, and J. Fullea, "Modification of four point method to measure the concrete electrical resistivity in presence of reinforcing bars," *Cem. Concr. Compos.*, vol. 53, pp. 249–257, 2014.
- [100] C. Lee and S. Wang, "Application of Four-electrode Method to Analysis Resistance Characteristics of Conductive Concrete," vol. 4, no. 12, pp. 11–15, 2010.
- [101] Y. L. Tan and C. E. Chong, "Resistivity measurement of a small-volume sample using two planar disc electrodes and a new geometric factor," *IEEE Sens. J.*, vol. 8, no. 5, pp. 516–521, 2008.
- [102] R. B. Polder and W. H. A. Peelen, "Characterisation of chloride transport and reinforcement corrosion in concrete under cyclic wetting and drying by electrical resistivity," *Cem. Concr. Compos.*, vol. 24, no. 5, pp. 427–435, 2002.
- [103] W. J. Mccarter, T. M. Chrisp, G. Starrs, A. Adamson, E. Owens, and P. A. M. Basheer, "Developments in Performance Monitoring of Concrete Exposed to Extreme Environments," vol. 18, no. September, pp. 167–175, 2012.
- [104] R. Du Plooy, S. Palma Lopes, G. Villain, and X. Dérobert, "Development of a multi-ring resistivity cell and multi-electrode resistivity probe for investigation of cover concrete condition," *NDT E Int.*, vol. 54, pp. 27–36, 2013.

- [105] G. S. Duffó and S. B. Farina, “Development of an embeddable sensor to monitor the corrosion process of new and existing reinforced concrete structures,” *Constr. Build. Mater.*, vol. 23, no. 8, pp. 2746–2751, 2009.
- [106] T. S. Larsen and P. Heiselberg, “Single-sided natural ventilation driven by wind pressure and temperature difference,” *Energy Build.*, vol. 40, no. 6, pp. 1031–1040, 2008.
- [107] R. F. Rupp, N. G. Vásquez, and R. Lamberts, “A review of human thermal comfort in the built environment,” *Energy Build.*, vol. 105, pp. 178–205, 2015.
- [108] L. Fang, G. Clausen, and P. O. Fanger, “Temperature and humidity: important factors for perception of air quality and for ventilation requirements,” *ASHRAE Trans.*, vol. 106, 2000.
- [109] ISO, “ISO 7730: Ergonomics of the thermal environment Analytical determination and interpretation of thermal comfort using calculation of the PMV and PPD indices and local thermal comfort criteria,” *Management*, vol. 3, pp. 605–615, 2005.
- [110] L. Yang, H. Yan, and J. C. Lam, “Thermal comfort and building energy consumption implications - A review,” *Appl. Energy*, vol. 115, pp. 164–173, 2014.
- [111] R. V. Andersen, J. Toftum, K. K. Andersen, and B. W. Olesen, “Survey of occupant behaviour and control of indoor environment in Danish dwellings,” *Energy Build.*, vol. 41, no. 1, pp. 11–16, 2009.
- [112] Z. Xu, G. Hu, C. J. Spanos, and S. Schiavon, “PMV-based event-triggered mechanism for building energy management under uncertainties,” *Energy Build.*, vol. 152, pp. 73–85, 2017.
- [113] ISO 7726, “Ergonomics of the thermal environment — Instruments for measuring physical quantities,” *Int. Organ. Stand.*, no. 1, 1998.
- [114] S. M. Saad, A. R. Mohd Saad, A. M. Y. Kamarudin, A. Zakaria, and A. Y. M. Shakaff, “Indoor air quality monitoring system using wireless sensor network (WSN) with web interface,” *2013 Int. Conf. Electr. Electron. Syst. Eng.*, pp. 60–64, 2013.
- [115] D. Lohani and D. Acharya, “SmartVent: A Context Aware IoT System to Measure Indoor Air Quality and Ventilation Rate,” *2016 17th IEEE Int. Conf. Mob. Data Manag.*, pp. 64–69, 2016.
- [116] I.-H. Peng, Y.-Y. Chu, C.-Y. Kong, and Y.-S. Su, “Implementation of Indoor VOC Air Pollution Monitoring System with Sensor Network,” *2013 Seventh Int. Conf. Complex, Intelligent, Softw. Intensive Syst.*, pp. 639–643, 2013.

- [117] Y. Xiang, R. Piedrahita, R. P. Dick, M. Hannigan, Q. Lv, and L. Shang, "A Hybrid Sensor System for Indoor Air Quality Monitoring," *2013 IEEE Int. Conf. Distrib. Comput. Sens. Syst.*, pp. 96–104, 2013.
- [118] CEN, "EN 15251:2007 Indoor environmental input parameters for design and assessment of energy performance of buildings addressing indoor air quality, thermal environment, lighting and acoustics," vol. 3, 2008.
- [119] En 13779, "Ventilation for buildings — Performance requirements for ventilation and," vol. 3, p. 72, 2007.
- [120] Bruel & Kjaer, "Measurements in building acoustics," *Bruel & Kjaer*, pp. 1–44, 1988.
- [121] J. P. Lynch, A. Sundararajan, K. H. Law, A. S. Kiremidjian, T. Kenny, and E. Carryer, "Embedment of structural monitoring algorithms in a wireless sensing unit," *Struct. Eng. Mech.*, vol. 15, no. 3, pp. 285–297, 2003.
- [122] R. Balaji and M. Sasikumar, "Structural health monitoring (SHM) system for polymer composites: A review," *Indian J. Sci. Technol.*, vol. 9, no. 41, 2016.
- [123] H. Murayama, K. Kageyama, H. Naruse, A. Shimada, and K. Uzawa, "Journal of Intelligent Material Systems and Structures Application of Fiber-Optic Distributed Sensors to Health Monitoring for Full-Scale Composite Structures," 2013.
- [124] X. Wang, "Study of sensor network applications in building construction," 2013.
- [125] V. S. Gunge and P. S. Yalagi, "Smart Home Automation: A Literature Review," *Int. J. Comput. Appl. Natl. Semin. Recent Trends Data Min.*, no. Rtdm, pp. 975–8887, 2016.
- [126] S. D. T. Kelly, N. K. Suryadevara, and S. C. Mukhopadhyay, "Towards the implementation of IoT for environmental condition monitoring in homes," *IEEE Sens. J.*, vol. 13, no. 10, pp. 3846–3853, 2013.
- [127] M. Shakeri, A. Sadeghi-Niaraki, S. M. Choi, and S. M. Riazul Islam, "Performance analysis of iot-based health and environment wsn deployment," *Sensors (Switzerland)*, vol. 20, no. 20, pp. 1–22, 2020.
- [128] P. P. Ray, "A survey on Internet of Things architectures," *J. King Saud Univ. - Comput. Inf. Sci.*, vol. 30, no. 3, pp. 291–319, 2018.
- [129] RF Wireless World, "RF & Wireless Vendors and Resources," 2012. [Online]. Available: <https://www.rfwireless-world.com/>. [Accessed: 24-Apr-2020].
- [130] DIGI, "XBee/XBee-PRO S2C Zigbee," *Digikey*, 2018.
- [131] U. Guide, "XBee®/XBee-PRO S2C Zigbee®." 2018.

- [132] Yole Study, “Sensor for Smart homes and Buildings,” 2017.
- [133] Measurement Specialities, “HTM2500LF – Temperature and Relative Humidity Module,” no. October, p. 9, 2012.
- [134] T. Sensors, “Hukseflux.” Hukseflux, pp. 1–43, 2016.
- [135] CyberBlogSpot, “Using ADS1115 Module with Arduino,” *online*, 2021. [Online]. Available: <https://cyberblogspot.com/using-ads1115-module-with-arduino/>. [Accessed: 19-Nov-2021].
- [136] T. Instruments, “Texas Instruments ADS1115 Series Analog to Digital Converters.” 2018.
- [137] E. Ag, “NTC thermistors for temperature measurement,” no. March, pp. 1–22, 2013.
- [138] P. M. Utc, “DHT Sensors,” p. 15, 2018.
- [139] P. Data, “CozIR ® - A Flexible Low Power CO 2 Sensor CozIR ® - A Flexible Low Power CO 2 Sensor,” no. June, pp. 1–32, 2020.
- [140] S. Corporation, “Gp2Y1010Au0F,” *Compact Opt. Dust Sens.*, vol. Date Dec., pp. 1–9, 2006.
- [141] Figaro, “TGS 2602-for the detection of Air Contaminants * Air cleaners * Ventilation control * Air quality monitors * VOC monitors * Odor monitors.”
- [142] Sharp, “Specifications for dust sensor GP2Y1010AU0F,” *RS Components*, 2017.
- [143] Sharp, “Application note of Sharp dust sensor GP2Y1010AU0F,” 2021.
- [144] “Adafruit Electret Microphone Amplifier - MAX4466 with Adjustable Gain.” [Online]. Available: <https://thepihut.com/products/adafruit-electret-microphone-amplifier-max4466-with-adjustable-gain>. [Accessed: 20-Apr-2021].
- [145] C. INC, “Electret condenser microphone,” 2008.
- [146] Maxim Integrated Products, “Maxim Intergrated LM4466 Microphone Preamplifiers with Complete Shutdown,” pp. 1–15, 2001.
- [147] F. Wu, C. W. Tan, M. Sarvi, C. Rudiger, and M. R. Yuce, “Design and Implementation of a Low-Power Wireless Sensor Network Platform Based on XBee,” *2017 IEEE 85th Veh. Technol. Conf. (VTC Spring)*, pp. 1–5, 2017.
- [148] Z. Bouthaina, “Supervision and detection of faults in electrical machines using a network of XBee-based sensors,” Mohamed Khider Biskra University, 2020.
- [149] Nexperia, “2N7002 N-channel Trench MOSFET,” *Datasheet*, vol. 23, no. September, 2011.
- [150] Electro Schematics, “Bidirectional Logic Level Converter Circuit,” *online*, 2021.

- [Online]. Available: <https://www.electroschematics.com/bidirectional-logic-level-shifter/>. [Accessed: 26-Oct-2021].
- [151] Components101, “XBee S2C – RF Module,” *online*, 2021. [Online]. Available: <https://components101.com/wireless/xbee-s2c-module-pinout-datasheet>. [Accessed: 18-Oct-2021].
- [152] T. Atmel, H. Performance, L. Power, A. Avr, and M. Family, “Atmega328P Datasheet Summary,” 2016.
- [153] S. Theme, “Blog about electronics and utilities in general,” *online*, 2016. [Online]. Available: <http://eletronicautilidades.blogspot.com/2016/05/como-programar-o-arduino-fora-da-placa.html>. [Accessed: 26-Oct-2021].
- [154] M. Quirion and G. Ballivy, “Laboratory investigation on Fabry-Pérot sensor and conventional extensometers for strain measurement in high performance concrete,” *Can. J. Civ. Eng.*, vol. 27, no. 5, pp. 1088–1093, 2000.
- [155] R. Components, “Arduino, Uno Rev 3,” *online*, 2021. [Online]. Available: <https://docs.rs-online.com/ab83/0900766b80e8ba21.pdf>. [Accessed: 26-Oct-2021].
- [156] E. Upton, “Raspberry Pi 3 Model B, url:<https://www.raspberrypi.org/blog/raspberry-pi-3-model-bplus-sale-now-35/>,” p. 2837, 2018.
- [157] ST, “LD1117 Adjustable and Fixed Low-Dropout Voltage Regulator,” no. April. pp. 1–44, 2013.
- [158] Semiconductor Components Industries, “Voltage Regulators - Positive.” ON Semiconductor, 2019.
- [159] Texas Instrument, “ADS111x Ultra-Small, Low-Power, I 2C-Compatible, 860-SPS, 16-Bit ADCs With Internal Reference, Oscillator, and Programmable Comparator,” *Texas Instrum.*, 2018.
- [160] BRE, “BRE U-value Calculator software by Building Research Establishment Ltd,” *online*, 2016. [Online]. Available: <https://projects.bre.co.uk/uvalues/>. [Accessed: 21-Nov-2022].
- [161] P. Baker, “Technical Paper 10 U - values and traditional buildings,” no. January. 2011.
- [162] “BS EN ISO 10456:2007-2022 Building materials and products —Hygrothermal properties - Tabulated design values and procedures for determining declared and design thermal values.” .

- [163] Brüel & Kjær, “Hand-held Analyzer Types 2250,” vol. 1983, 2006.
- [164] B. & Kjær, “Sound Source Type 4224,” pp. 145–180, 2016.
- [165] Y. Ding, G. Goussetis, R. Correia, N. B. Carvalho, R. Lihakanga, and C. Song, “Signal Modulation Schemes in Backscatter Communications,” in *Backscattering and RF Sensing for Future Wireless Communication*, M. A. I. Q. H. Abbasi, H. T. Abbas, A. Alomainy, Ed. Wiley, 2021, pp. 19–40.
- [166] K. Maurya, Rajiv, Chandan, “Ambient Backscatter: Power And Communication To Battery-Free Devices,” *online*, 2019. [Online]. Available: <https://www.electronicsforu.com/electronics-projects/electronics-design-guides/telecom-ambient-backscatter>. [Accessed: 17-Jan-2022].
- [167] Y. Ding, G. Goussetis, R. Correia, R. Lihakanga, N. B. Carvalho, and P. Petridis, “Enabling Multicarrier Backscattering Communications,” in *2020 IEEE MTT-S International Wireless Symposium, IWS 2020 - Proceedings*, 2020, pp. 11–13.
- [168] J. Kimionis, A. Bletsas, and J. N. Sahalos, “Increased range bistatic scatter radio,” *IEEE Trans. Commun.*, vol. 62, no. 3, pp. 1091–1104, 2014.
- [169] S. N. Daskalakis, R. Correia, G. Goussetis, M. M. Tentzeris, N. B. Carvalho, and A. Georgiadis, “Four-PAM Modulation of Ambient FM Backscattering for Spectrally Efficient Low-Power Applications,” *IEEE Trans. Microw. Theory Tech.*, vol. 66, no. 12, pp. 5909–5921, 2018.
- [170] G. Vougioukas, S. N. Daskalakis, and A. Bletsas, “Could battery-less scatter radio tags achieve 270-meter range?,” *2016 IEEE Wirel. Power Transf. Conf. WPTC 2016*, no. May 2016, 2016.
- [171] A. Varshney, O. Harms, C. Pérez-Penichet, C. Rohner, F. Hermans, and T. Voigt, “LoRea: A Backscatter Architecture that Achieves a Long Communication Range,” *SenSys 2017 - Proc. 15th ACM Conf. Embed. Networked Sens. Syst.*, vol. 2017-Janua, pp. 15–16, 2017.
- [172] V. Liu, A. Parks, V. Talla, S. Gollakota, D. Wetherall, and J. R. Smith, “Ambient backscatter: Wireless communication out of thin air,” *Comput. Commun. Rev.*, vol. 43, no. 4, pp. 39–50, 2013.
- [173] R. Correia and N. B. Carvalho, “Design of high order modulation backscatter wireless sensor for passive IoT solutions,” *2016 IEEE Wirel. Power Transf. Conf. WPTC 2016*, pp. 22–24, 2016.
- [174] S. J. Thomas and M. S. Reynolds, “A 96 Mbit/sec, 15.5 pJ/bit 16-QAM modulator for UHF backscatter communication,” *2012 IEEE Int. Conf. RFID, RFID 2012*, pp. 185–190, 2012.

- [175] S. J. Thomas, E. Wheeler, J. Teizer, and M. S. Reynolds, "Quadrature amplitude modulated backscatter in passive and semipassive UHF RFID systems," *IEEE Trans. Microw. Theory Tech.*, vol. 60, no. 4, pp. 1175–1182, 2012.
- [176] V. Talla, M. Hessar, B. Kellogg, A. Najafi, J. R. Smith, and S. Gollakota, "LoRa Backscatter: Enabling The Vision of Ubiquitous Connectivity," vol. 1, no. 3, 2017.
- [177] D. Belo *et al.*, "IQ Impedance Modulator Front-End for Low-Power LoRa Backscattering Devices," *IEEE Trans. Microw. Theory Tech.*, vol. 67, no. 12, pp. 5307–5314, 2019.
- [178] M. Viswanathan, *SIMULATION OF DIGITAL COMMUNICATION SYSTEMS USING MATLAB*, Second edi. Mathuranathan Viswanathan, 2013.
- [179] M. Viswanathan and S. Edition, *Wireless Communication Systems in Matlab*, Second Edi. Mathuranathan Viswanathan, 2020.
- [180] S. Deshmukh and U. Bhosle, "Performance Evaluation of Spread Spectrum System Using Different Modulation Schemes," *Procedia Comput. Sci.*, vol. 85, no. Cms, pp. 176–182, 2016.
- [181] J. Kimionis and M. M. Tentzeris, "Pulse shaping: The missing piece of backscatter radio and RFID," *IEEE Trans. Microw. Theory Tech.*, vol. 64, no. 12, pp. 4774–4788, 2016.
- [182] V. Iyer, V. Talla, B. Kellogg, S. Gollakota, and J. R. Smith, "Inter-technology backscatter: Towards internet connectivity for implanted devices," *SIGCOMM 2016 - Proc. 2016 ACM Conf. Spec. Interes. Gr. Data Commun.*, pp. 356–369, 2016.
- [183] R. Correia *et al.*, "Chirp Based Backscatter Modulation," *IEEE MTT-S Int. Microw. Symp. Dig.*, vol. 2019-June, pp. 279–282, 2019.
- [184] C. Song, Y. Huang, J. Zhou, J. Zhang, S. Yuan, and P. Carter, "A high-efficiency broadband rectenna for ambient wireless energy harvesting," *IEEE Trans. Antennas Propag.*, vol. 63, no. 8, pp. 3486–3495, 2015.
- [185] "BSI Standards Publication Performance of buildings — Detection of heat , air and moisture irregularities in buildings by infrared methods Part 3 : Qualifications of equipment operators , data analysts and report writers." 2015.

Appendix

Appendix 1: XBee S2C 3mW module Configurations

Hardware requirements

- 2 x ZigBee S2C
- 2 x XBee adaptor
- 2 x USB cable

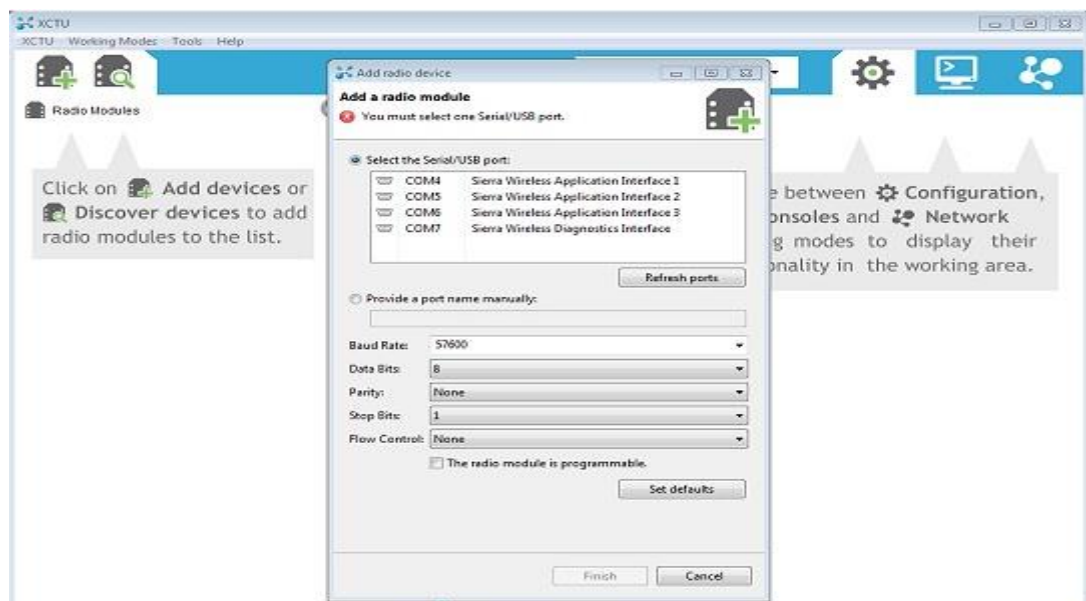
Software requirements

ZigBee module can be configured using XCTU configuration software. This free software and can be downloaded from the Digi website.

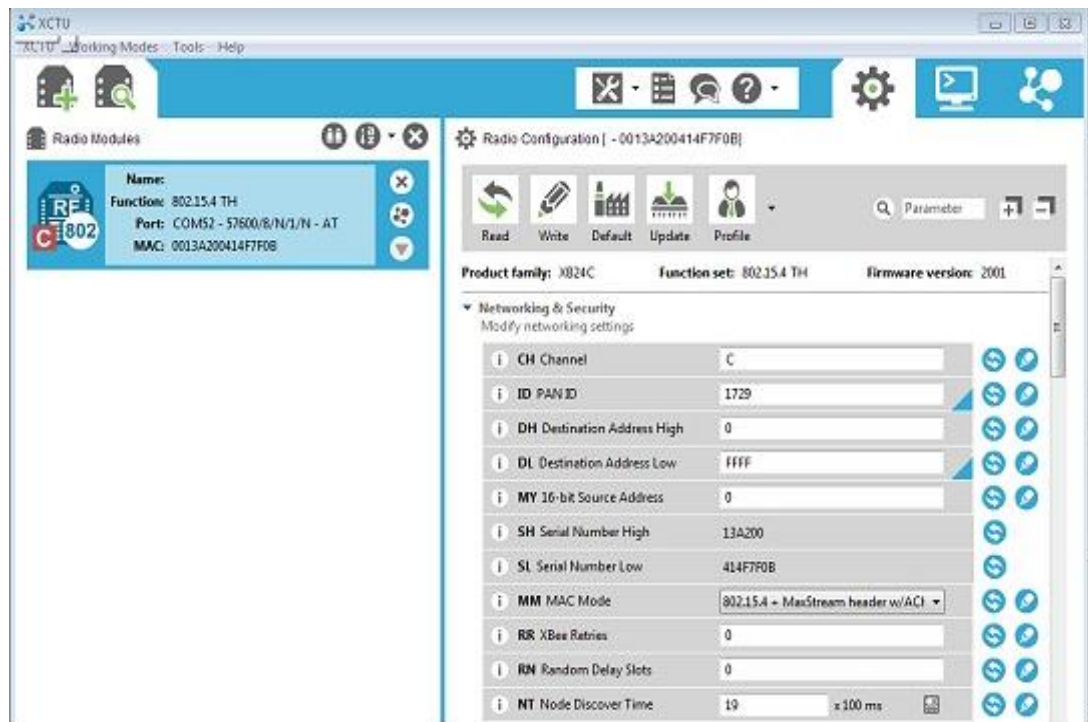
Procedure

Download and install XCTU configuration software from Digi

Connect the module and check Firmware. This will open the list of serial ports. Select the one that your XBee is connected to and set the Baud Rate if required. The default baud rate for XBee radios is 9600.

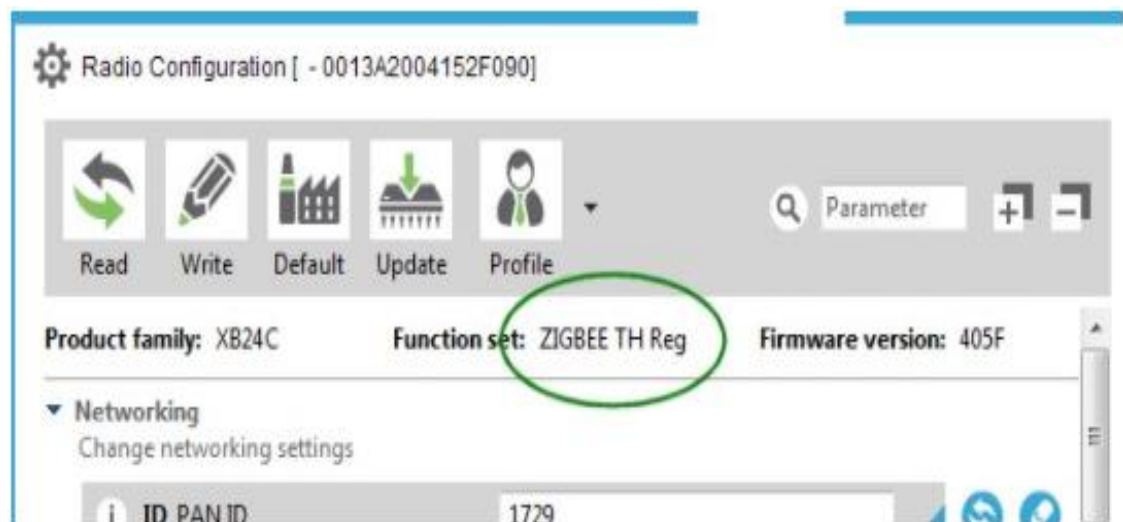


- Once the connection between software and XBee radio is established, XCTU will download the current settings for the module



Setup using the new ZIGBEE TH REG firmware

In the configuration panel, the current setup will be displayed as ZIGBEE TH REG.




By the use of the Update icon, the function set can be adjusted. Select ZIGBEE TH REG and click the Update button to load the new firmware

Update firmware

Update the radio module firmware

Configure the firmware that will be flashed to the radio module.

Select the product family of your device, the new function set and the firmware version to flash:

 Product family	Function set	Firmware version
XB24C	802.15.4 TH	405F (Newest)
	DigiMesh 2.4 TH	405E
	ZIGBEE TH Reg	4059
		4055

[View Release Notes](#)

☒ Force the module to maintain its current configuration. [Select current](#)

[Update](#) [Cancel](#)

Coordinator Setup

To work as coordinator /gateway the following steps need to be followed

ID PAN ID

This is a unique number to your network setup and needs to set the same on all the XBee modules operating on the same network. A hexadecimal number between 0 and FFFF can be used to avoid potential conflict with other XBee radios. CE Coordinator Enable must be set to “enabled” for the module to work as coordinator.

The screenshot shows the 'Radio Configuration' window for a device with ID '- 0013A2004152F090'. The interface includes a toolbar with 'Read', 'Write', 'Default', 'Update', and 'Profile' buttons, along with a search bar and zoom controls. Below the toolbar, the 'Product family' is 'XB24C', 'Function set' is 'ZIGBEE TH Reg', and 'Firmware version' is '405F'. The 'Networking' section is expanded, showing a list of parameters to configure. The 'ID PAN ID' is set to '1729' (circled in red). The 'CE Coordinator Enable' is set to 'Enabled [1]' (circled in blue). Other parameters include 'SC Scan Channels' (1FFE), 'SD Scan Duration' (4), 'ZS ZigBee Stack Profile' (0), 'NJ Node Join Time' (FF), 'NW Network Watchdog Timeout' (0), 'JV Channel Verification' (Disabled [0]), 'JN Join Notification' (Disabled [0]), 'OP Operating PAN ID' (1729), 'OI Operating 16-bit PAN ID' (4F0F), 'CH Operating Channel' (13), and 'NC Number of Remaining Children' (14).

Parameter	Value	Unit/Type
ID PAN ID	1729	
SC Scan Channels	1FFE	Bitfield
SD Scan Duration	4	exponent
ZS ZigBee Stack Profile	0	
NJ Node Join Time	FF	x 1 sec
NW Network Watchdog Timeout	0	x 1 minute
JV Channel Verification	Disabled [0]	
JN Join Notification	Disabled [0]	
OP Operating PAN ID	1729	
OI Operating 16-bit PAN ID	4F0F	
CH Operating Channel	13	
NC Number of Remaining Children	14	
CE Coordinator Enable	Enabled [1]	

Destination Address Low (DL)

For the Coordinator to communicate with other modules, DL Destination Address is set to FFFF which is the broadcast address. When done click saves to store the settings.

▼ Addressing
Change addressing settings

i	SH Serial Number High	13A200	↺
i	SL Serial Number Low	4152F090	↺
i	MY 16-bit Network Address	C982	↺
i	MP 16-bit Parent Address	FFFE	↺
i	DH Destination Address High	0	↺
i	DL Destination Address Low	FFFF	↺
i	NI Node Identifier		↺
i	NH Maximum Hops	1E	↺
i	BH Broadcast Radius	0	↺
i	AB Master-Ons Broadcast Time	CE	↺

End Device Setup

CH Channel

Defaults are set to C but should match the Coordinator setup.

ID PAN ID

Set the same as in Coordinator

Destination Address High (DH)

Set to 0

Destination Address Low (DL)

Set to 0

MY 16-bit source address

Set to 1

CE Coordinator Enable

Set to End Device

Read

Write

Default

Update

Profile

Parameter

+

-

Product family: XB24C

Function set: 802.15.4 TH

Firmware version: 2001

Networking & Security

Modify networking settings

i	CH Channel	C			
i	ID PAN ID	1729			
i	DH Destination Address High	0			
i	DL Destination Address Low	0			
i	MY 16-bit Source Address	1			
i	SH Serial Number High	13A200			
i	SL Serial Number Low	4152F090			
i	MM MAC Mode	802.15.4 + MaxStream header w/ACI			
i	RR XBee Retries	0			
i	RN Random Delay Slots	0			
i	NT Node Discover Time	19	x 100 ms		
i	NO Node Discover Options	0	Bitfield		
i	TO Transmit Options	0	Bitfield		
i	CB 802.15.4 Compatibility	0	Bitfield		
i	CE Coordinator Enable	End Device [0]			
i	SC Scan Channels	1FFE	Bitfield		

Appendix 2: Datasheet of a Generic Wireless sensor Network

Product Overview

A Generic wireless sensor network incorporates two custom-made Sensor nodes and one Gateway. Sensor nodes contain everything to support varieties of analogue and digital sensors with 10-bits and added features of 16-bits high-resolution ADC. The nodes contain inbuilt circuits to interface with some of the commonly used analogue and digital sensors.

Area of measurement and measured parameters

Table 1. Building structure monitoring

Area of analysis	Related parameters
Thermal properties d) Thermal transmittance e) Thermal resistance f) Thermal conductance	g) Heat flux through the material. h) The surface temperature of both sides of the material i) An air temperature of both sides of the material
Hygrothermal properties	• Humidity/air moisture

Table 2. Indoor Environment Quality monitoring

Area of analysis	Related parameters
Human comfort (Indoor thermal comfort)	c) Ambient temperature d) Relative humidity
Human health (Indoor air quality)	d) Carbon dioxide e) Volatile organic compound f) PM 2.5
Airborne sound Insulation	g) Sound/acoustic

Table 3. Sensor node version_1 Technical specification

Microcontroller	ATmega328P
Communication module	XBee S2C
Power supply	5 to 12V
RF data rate	250kbps
Transmission Frequency	2.4GHz to 2.5GHz
Indoor/Urban Range	200ft
Outdoor RF line-of-sight Range	up to 4000ft

Transmit Power Output	6.3mW (8dBm) in Boost mode, 2mW (3dBm) in Normal mode
Receiver Sensitivity	-102dBm in Boost mode, -100dBm in Normal mode
Operating Temperature	-40°C to 85° C
Operating frequency	16MHz
Operating mode	Continuous mode/sleeping mode
High resolution analogue inputs	16 bits ADC, 4 single ended input/ 2 differential inputs
10 bits analogue inputs	4 pins
Digital input	2 pins

Description of the sensor node version_1.

The sensor node in Fig. 1 is a bespoke design for low-power purposes, consisting of a power supply unit, a high-resolution ADS1115 16-bits, an Atmeg328P-PU microcontroller, and an S2C Xbee wireless communication module based on the IEEE 802.15.4/ZigBee Standard. The node is designed to measure temperature, heat flux, humidity, and moisture.

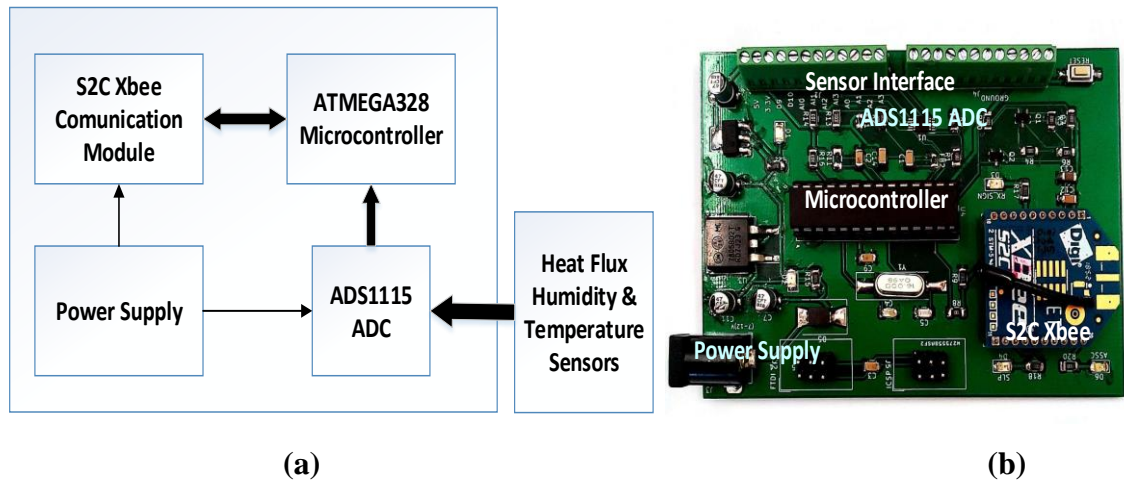


Figure 1. Sensor node version_1 (a) Block diagram, (b) Prototype

Table 4. Sensor node version_1 Technical specification

Microcontroller	ATmega328P
Communication module	XBee S2C
Power supply	5 to 12V
RF data rate	250kbps

Transmission Frequency	2.4GHz to 2.5GHz
Indoor/Urban Range	200ft
Outdoor RF line-of-sight Range	up to 4000ft
Transmit Power Output	6.3mW (8dBm) in Boost mode, 2mW (3dBm) in Normal mode
Receiver Sensitivity	-102dBm in Boost mode, -100dBm in Normal mode
Operating Temperature	-40°C to 85° C
Operating frequency	16MHz
Operating mode	Continuous mode/sleeping mode
VOC interface sensor	1 10-bits ADC
Dust sensor interface	1 pin
Thermistor interface	2 10-bits ADC
10-bits analogue inputs	3 pins
Digital input	5 pins
16-bits analogue inputs	4 pins

Sensor node version_1 Elements and Pin interface

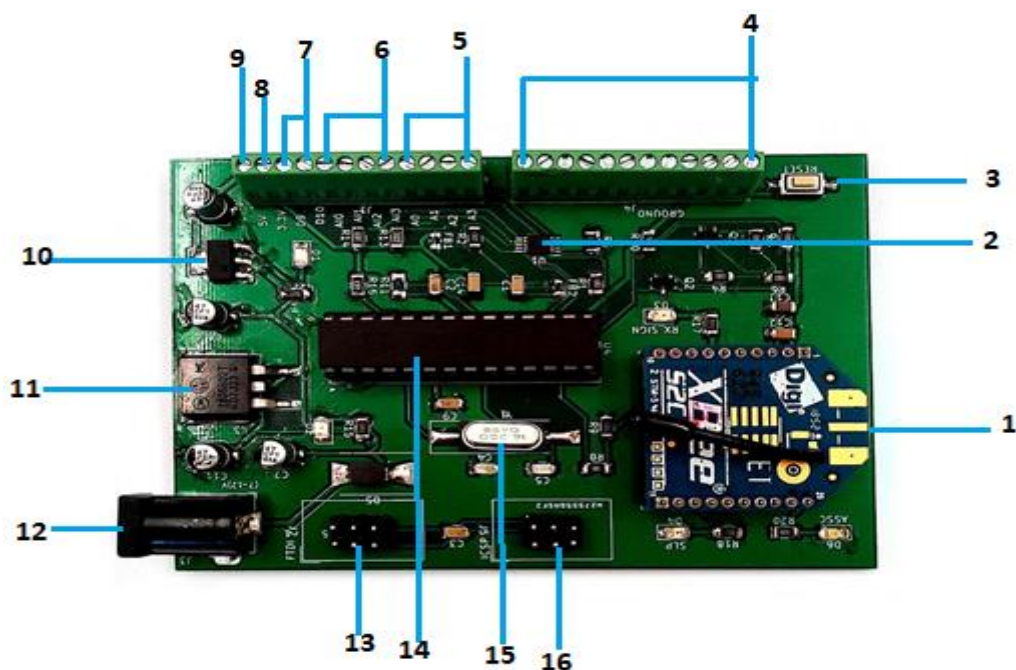


Figure 2. Sensor node version_1 Elements and pin interface

Table 5. Sensor node version_1 elements and pin interface description

1	XBee socket -The 10-pin socket with a 2mm pitch that mate with the popular XBee radios. It used to avoid soldering the XBee radio direct to the PCB board
2	ADS1115 -Precision analogue-to-digital converters (ADCs) with 16-bits of resolution
3	Reset button – Use to reset the entire board by restarting the program
4	Ground - Provide the common ground between the node and external circuits
5	Analogue pins- 10-bits ADC to Interface the analogue sensor directly to the node
6	Analogue pins - 16-bits ADC to interface a high-resolution sensor.
7	Digital pins – Interface digital sensor directly to the node
8	Power Pin 3V3 – Provide 3.3V supply voltage to the external circuit
9	Power Pin 5V – Provide 5V supply voltage to the external circuits
10	3.3V Voltage Regulator – Provides regulated 3.3V supply voltage to the node
11	5V Voltage Regulator – Provides regulated 5V supply voltage to the node
12	DC Voltage jack- Use to connect the external supply of 7-12 VDC to the node
13	FTDI header- Allow to connect and load bootloader on Atmel 328P
14	Atmel 328P Microcontroller - 8-bit AVR Microcontroller with 32K Bytes In-System Programmable Flash Used as Central processing unit of the entire node
15	16 MHz Crystal oscillator – Used to provide the timing and control signal to Atmel328P
16	ICSP (In-Circuit Serial Programming) Header – Use to program firmware to Atmel 328P

Description of sensor node version_2

sensor node in Fig. 2, is also a bespoke design for low-power purposes, consisting of a power supply unit, Atmeg328P-PU microcontroller, and an S2C XBee wireless communication module based on the IEEE 802.15.4/ZigBee Standard. The node also contains a built-in interface for the Co2 sensor, VOC sensor and dust sensor, temperature sensors, and humidity (air moisture) sensors.

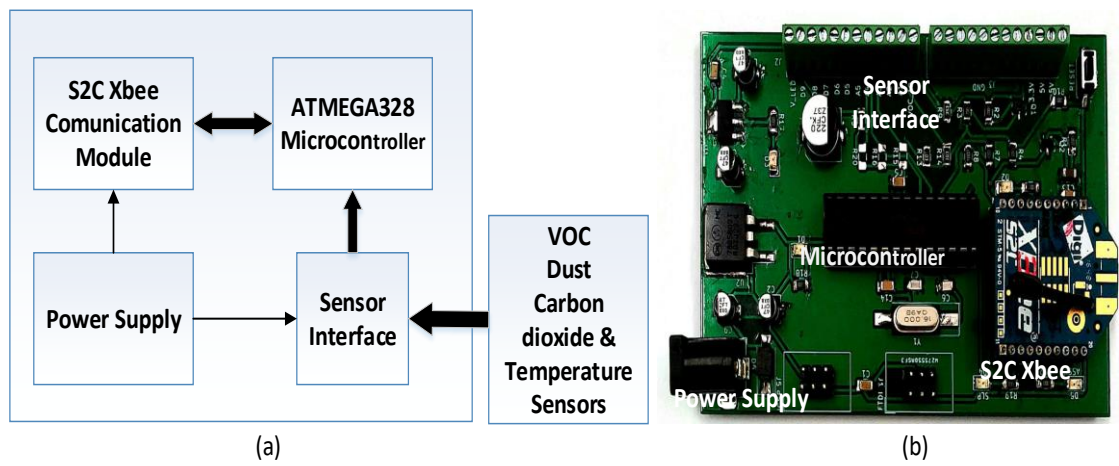


Figure 3: Sensor node version_2. (a) Block diagram (b) Prototype

Sensor node version_2 Elements and Pin interface

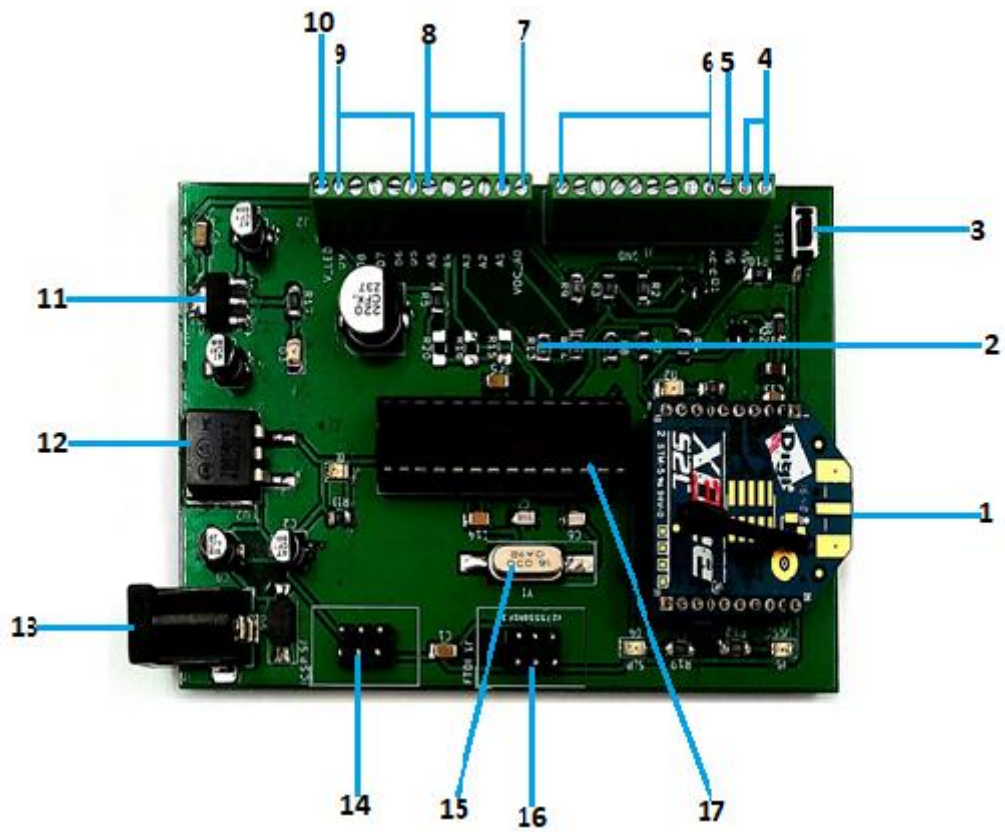


Figure 4. Sensor node version_2 Elements and pin interface

Table 6. Sensor node version_2 elements and pin interface description

1	XBee socket -The 10-pin socket with 2mm pitch that mate with the popular XBee radios. It used to avoid soldering the XBee radio direct to the PCB board
2	Sensor interface - Components added to allow direct connection of sensors to the node
3	Reset button – Use to reset the entire board by restarting the program
4	Power Pin 5V – Provide 5V supply voltage to the external circuits
5	Power Pin 3V3 – Provide 3.3V supply voltage to the external circuit
6	Ground - Provide the common ground between the node and external circuits
7	VOC pin- Use to interface TGS 2602 VOC direct to the node.
8	Analogue pins- Interface the analogue sensor directly to the node
9	Digital pins – Interface digital sensor directly to the node
10	VLED-pin – Provide the drive voltage for GP2Y1010AU0F
11	3.3V Voltage Regulator – Provides regulated 3.3V supply voltage to the node
12	5V Voltage Regulator – Provides regulated 5V supply voltage to the node
13	DC Voltage jack- Use to connect the external supply of 7-12 VDC to the node
14	ICSP (In-Circuit Serial Programming) Header – Use to program firmware to Atmel 328P
15	16 MHz Crystal oscillator – Used to provide the timing and control signal to Atmel328P
16	FTDI header- Allow to connect and load bootloader on Atmel 328P
17	Atmel 328P Microcontroller - 8-bit AVR Microcontroller with 32K Bytes In-System Programmable Flash Used as Central processing unit of the entire node

Description of Gateway node.

For data collection and data storage, a gateway or coordinator node has been designed. The gateway setup in Fig. 4 consists of an S2C XBee module, an Arduino board, and Raspberry Pi 3B+. To interface the communication module with the gateway, the XBee shield in Fig 5 has also been designed.

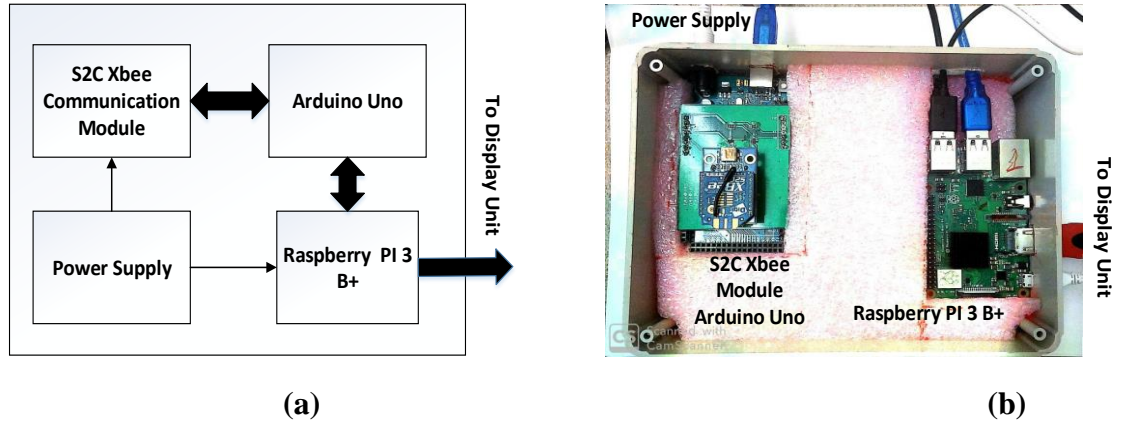


Figure 5. Gateway node. (a) Block diagram, (b) Prototype

Table 7. Gateway node technical specifications

Power supply	5V/2.5A DC power input
Slave processor	Arduino Mega
Master processor	Raspberry Pi 3 Model B+
Connectivity	2.4GHz and 5GHz IEEE 802.11.b/g/n/ac wireless LAN, Bluetooth 4.2, BLE
Arduino Mega Program/Debug Interface	ISP Header USB Type-B
Raspberry Pi interface	USB 2.0 Extended 40-pin GPIO header Full-size HDMI 4 USB 2.0 ports

XBee Gateway Communication Board

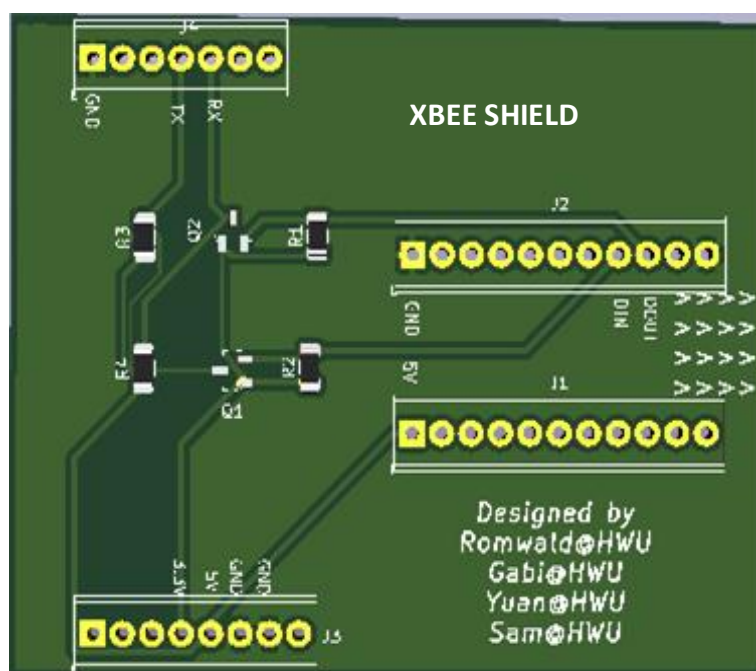


Figure 6. XBee Communication PCB

Gateway node Interface

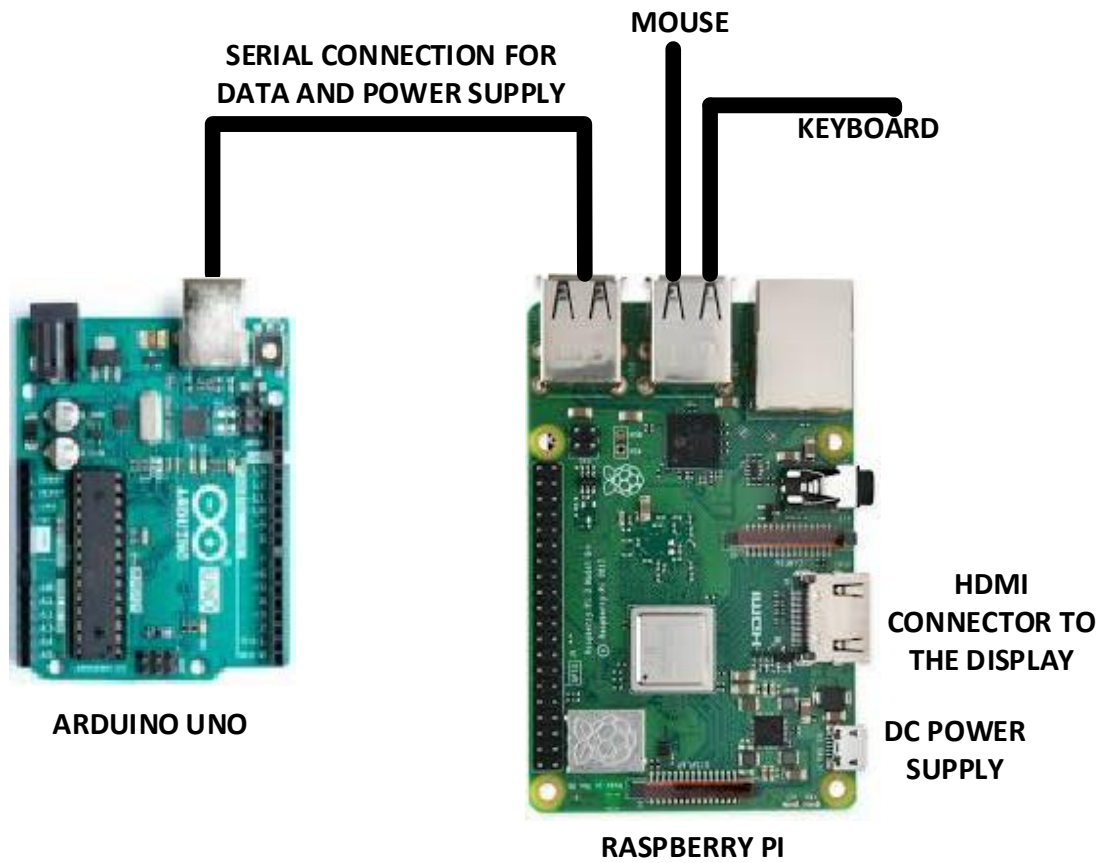


Figure 7. Gateway node interface

Table 8. Sensors and Sensing Technical specifications

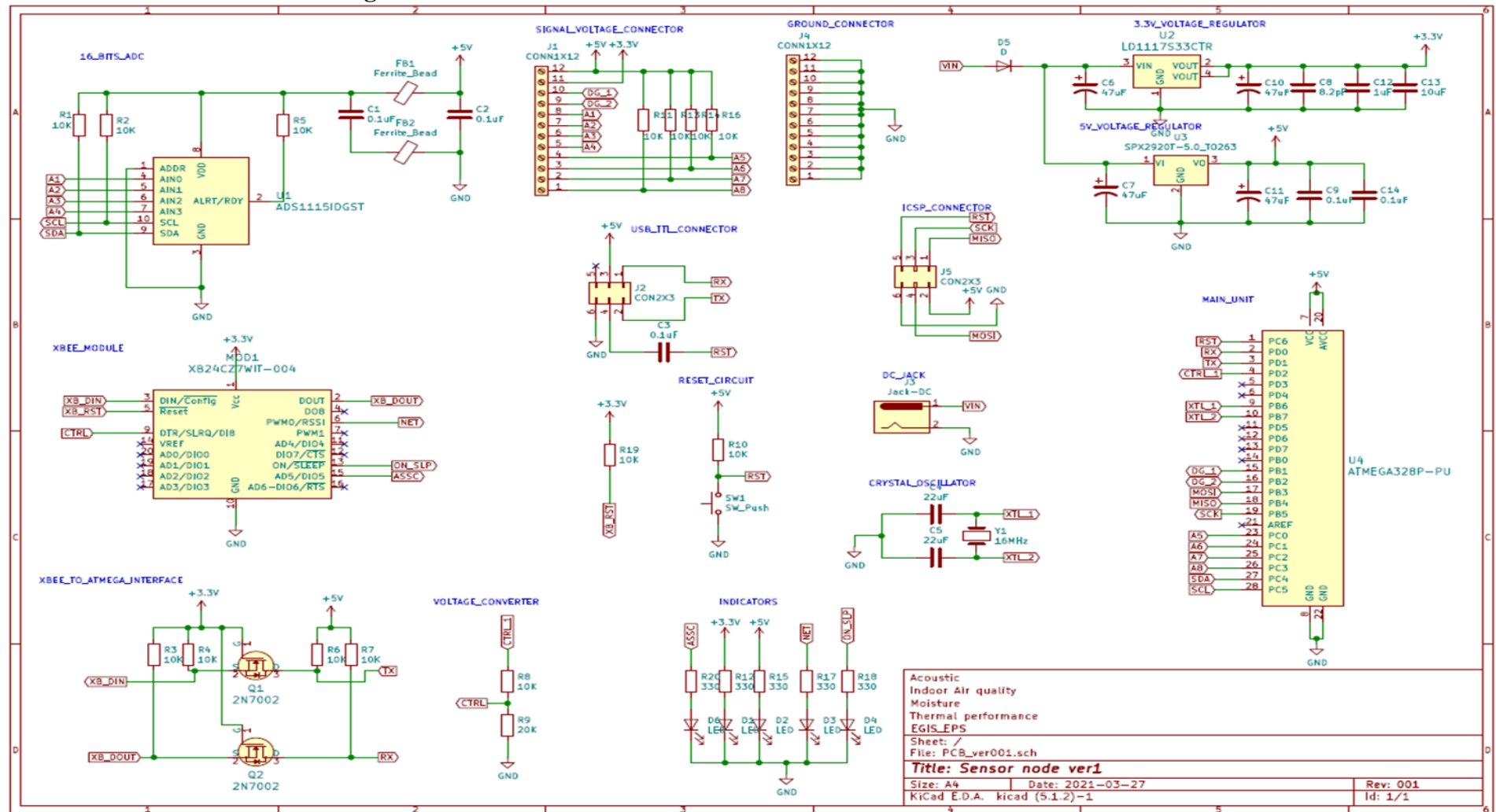
Parameter	Sensor type	Sensor specifications	
Heat flux through the material	HFP01-05 Heat flux sensor	Measurement range	-2000 to 2000 W/m ²
		Sensitivity range	50 to 70 x 10 ⁻⁶ V/(W/m ²)
		Sensitivity (nominal)	60 x 10 ⁻⁶ V/(W/m ²)
		Rated operating temperature range	-30 to +70 ° C
		Power supply	zero (passive sensor)
		Response time (95 %)	180 s
		Sensor resistance range	1 to 4 Ω
		Output type	Analogue
		Standards governing the use of the instrument	ISO 9869 ASTM C 1155-95 ASTM 1046-95
		Sensing area	8 x 10 ⁻⁴ m ²
Humidity and temperature	DHT22 Temperature and humidity sensor	Humidity Range	0 ~ 100% RH
		Operating Temperature	-40°C ~ 80°C
		Output Type	Digital
		Supply voltage	3.3 to 6 Vdc
		Response Time	2s
Air moisture and temperature	HTM2500LF	Humidity Measuring Range	1 to 99%

		Temperature Measuring Range	-40 to 85 °C
		Supply voltage	3 to 10 V DC (Typical 5 V)
		Temperature measurement	NTC 10kOhms +/- 1% direct output
		Output type	Analogue
		Humidity measurement	Typical 1 to 4 Volt DC output for 0 to 100%RH at 5Vdc
Volatile organic compound	VOC sensor TGS2602	Target gases	Air contaminants (VOCs, ammonia, H2S, etc.)
		Typical detection range	1 ~ 30ppm
		Heater voltage	5.0±0.2V AC/DC
		Load resistance	Variable (0.45kΩ min)
		Circuit voltage	5.0±0.2V DC
		Output type	Analogue
Dust	GP2Y1010AU0F Dust sensor	Supply voltage	-0.3 to 7 V (Typical 5 ±0.5 V)
		Output type	Pulse
Carbon dioxide	Cozir ambient Carbon dioxide sensor	Supply voltage	-0.3 to 6 V (Typical 3.3V)
		CO ₂ measurement range	0 to 10,000 ppm
		Response Time	30 s
		Humidity measurement range	0 to 100%

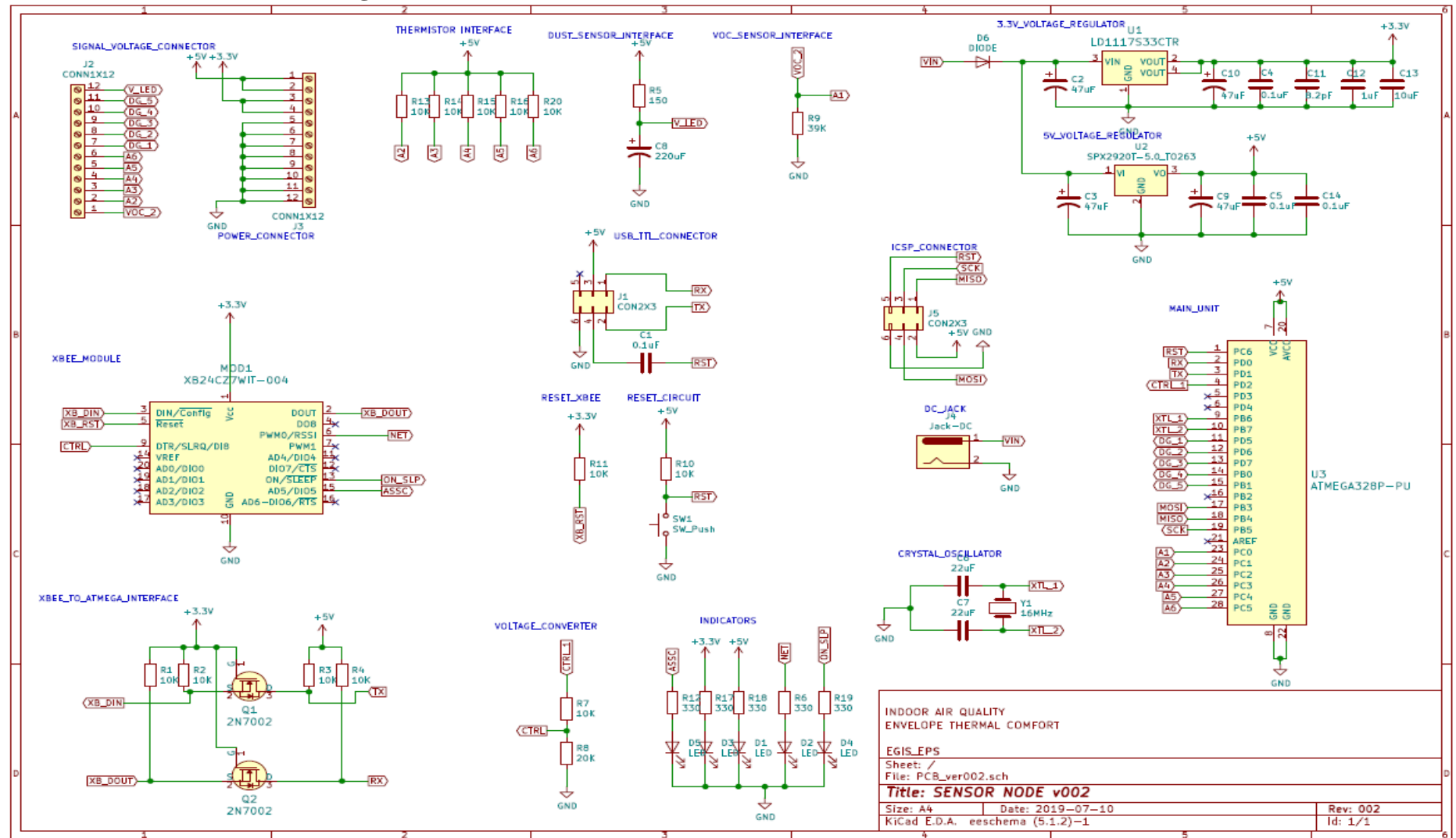
		Output type	Analogue/Digital
		Temperature measurement range	-25 to 55 °C
Surface and in-material temperature	B57020M2 and B57703M0103A019	Resistance in OHMS @ 25°C	10K
		Operating range	-55°C ~ 300°C
Acoustic sensor	GY-MAX4466 electret microphone amplifier	Operating frequency	20 – 20kHz
		Supply voltage	2.4 – 5Vdc
		Gain	25x to 125x

***All sensor has been selected to satisfy the requirement on each measurement.**

Sensor node version_1 circuit diagram



Sensor node version_2 circuit diagram



Appendix 3: Packets formats

NODE 1 (Heat flux indoor module 1)

1 Transmitter

Humidity	A_Temperature	S_Temperature	S_Temperature	Healflux_1	Heatflux_2
----------	---------------	---------------	---------------	------------	------------

1

1 Gateway Database

ID_1	Humidity	A_Temperature	Avg_S_Temperature	Avg_Healflux_1
------	----------	---------------	-------------------	----------------

1

1 NODE 2 (Heat flux outdoor module 1)

1 Transmitter

A_Temperature	Humidity	S_Temperature	S_Temperature
---------------	----------	---------------	---------------

1 Gateway Database

ID_2	Humidity	A_Temperature	Avg_S_Temperature	ID_2
------	----------	---------------	-------------------	------

1

1 NODE 3 (IAQ)

1 Transmitter

Humidity	Temperature	Carbon dioxide	VOC	Dust
----------	-------------	----------------	-----	------

1

1 Gateway Database

ID_3	Humidity	Temperature	Carbon dioxide	VOC	Dust
------	----------	-------------	----------------	-----	------

1

1 NODE 4 (Heat flux indoor module 2)

1 Transmitter

Humidity	A_Temperature	S_Temperature	S_Temperature	Healflux_1	Heatflux_2
----------	---------------	---------------	---------------	------------	------------

1 Gateway Database

ID_4	Humidity	A_Temperature	Avg_S_Temperature	Avg_Healflux_1
------	----------	---------------	-------------------	----------------

1

1 NODE 5 (Heat flux outdoor module 2)

1 Transmitter

A_Temperature	Humidity	S_Temperature	S_Temperature	A_Temperature
---------------	----------	---------------	---------------	---------------

1 Gateway Database

ID_5	Humidity	A_Temperature	Avg_S_Temperature	ID_5
------	----------	---------------	-------------------	------

Appendix 4: Gateway Configuration

Connect Raspberry Pi and Arduino board as shown in the figure

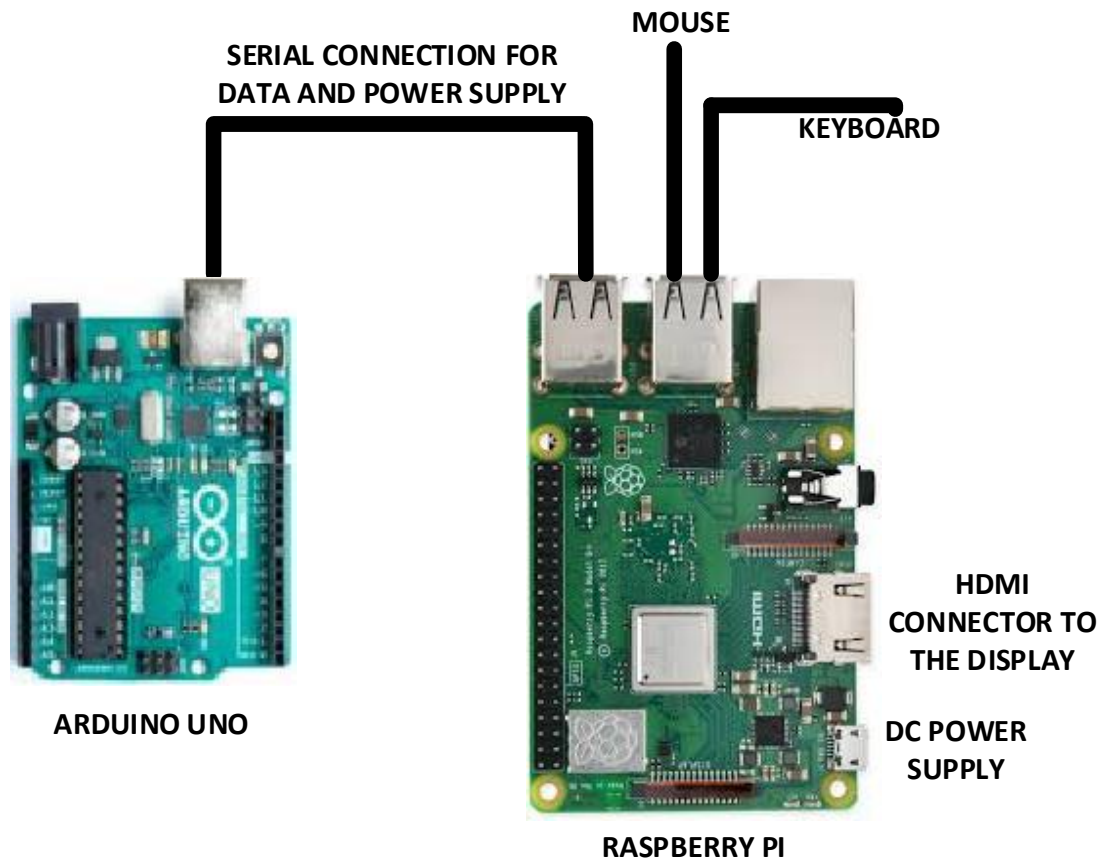


Figure 8: Gateway Connection

Set Up a Raspberry Pi Web Server

- By the use of the command prompt/terminal.
You can get there by pressing CTRL+ALT+T from the Raspbian desktop or remotely via SSH.
- Update the packages **to** get the latest versions of every file using the command:
 - `sudo apt-get update`
- Install apache2 using the command:
 - `sudo apt-get install apache2 -y`
- Install PHP for the server by using the command:
 - `sudo apt-get install php libapache2-mod-php -y`
- Install MariaDB so MySQL database can be used with your website. Using command:
 - `sudo apt-get install mariadb-server`
- When the download is finished. Set secure installation by command:
 - `sudo mysql_secure_installation`

- You will be asked for a root password. You can fill or leave it.
- Install the PHP-mysql connector for php pages to access the DB using command:
 - `sudo apt install php-mysql`
- Restart apache2 so all the setup can be activated using the command:
 - `sudo service apache2 restart`
- Test your server.
 - On the Raspberry Pi itself, you should be able to go to `http://localhost` a test page will be displayed. On the same network, you should be able to get there by visiting `http://raspberrypi.local` or `http://raspberrypi`, provided that your Raspberry Pi's hostname is `raspberrypi`.

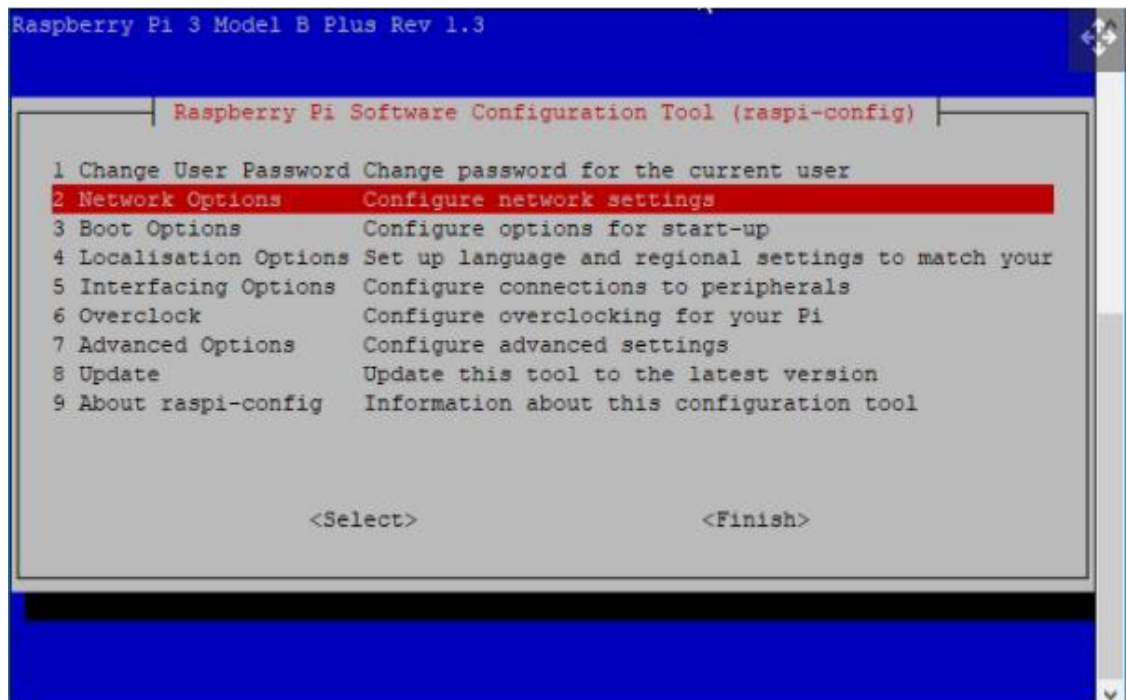


Changing Your Server's Host Name

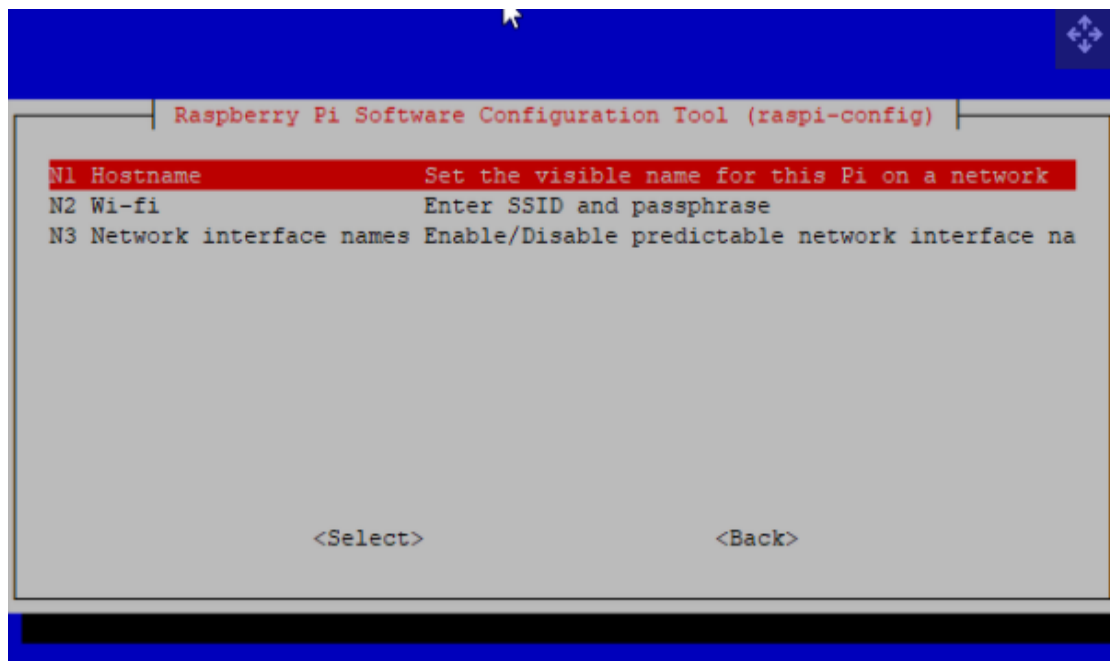
Enter the Raspberry Pi Configuration tool by using the command.

`sudo raspi-config`

Select Network Options to perform the rest of the settings



Then select the hostname, edit, save and reboot to accept changes



Install Arduino IDE on Raspberry Pi

Start the raspberry pi.

On Arduino's official website, navigate to the software page and download “Linux ARM 32 bits”. The file downloaded will be on format “Arduino-####-linuxarm.tar.xz” where #### is the version number.

On the Raspberry Pi, Open the terminal window and make sure you in-home directory.

On terminal window change directory and navigate to download folder,

Type `cd~` then `cd Downloads`

On the downloads folder, list the files using the command `ls`.

Locate the file with format `arduino-####-linuxarm.tar.xz`

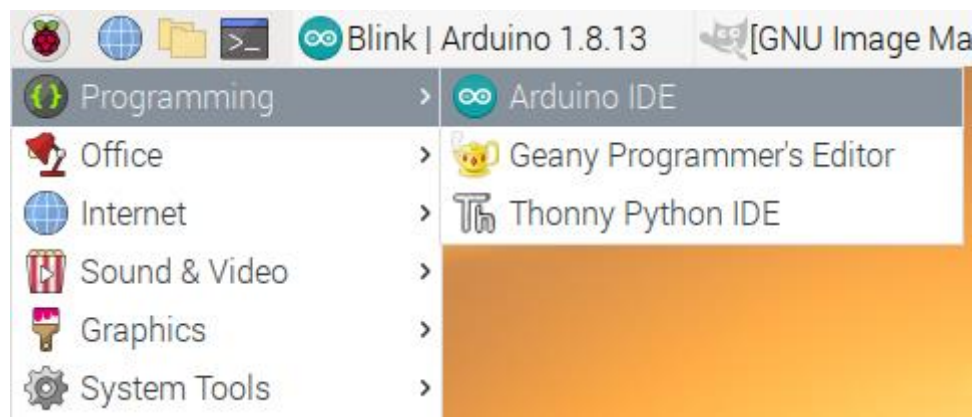
Extract files using the command `tar -xf arduino-####-linuxarm.tar.xz`. The folder with format “arduino-####” will be created.

Move the files to opt folder using command `sudo mv arduino-#### /opt`

Finalise the Installation of the Arduino IDE using command

`sudo /opt/arduino-####/install.sh`.

To run Arduino IDE, On the Raspberry Pi OS menu, open the programming menu and click on Arduino IDE to run the program



Appendix 5: Graphical User Interfaces

Graphical User Interface - Acoustic Measurements

The screenshot shows the phpMyAdmin interface with the 'ACOUSTIC_1' table selected. The table contains two columns: 'TIME' and 'ACOUSTIC'. The data is displayed in a grid with 13 rows visible. The left sidebar shows the database structure, including 'THERMAL_ANALYZER' and its sub-tables.

TIME	ACOUSTIC
2021-09-02 00:26:26	93.26
2021-09-02 00:26:27	93.26
2021-09-02 00:28:27	93.26
2021-09-02 00:28:28	93.26
2021-09-02 00:30:28	93.26
2021-09-02 00:30:29	93.26
2021-09-02 00:35:59	54.57
2021-09-02 00:38:00	55.32
2021-09-02 00:40:01	57.62
2021-09-02 00:42:02	53.83
2021-09-02 00:49:55	51.23
2021-09-02 00:51:56	52.87
2021-09-02 00:53:57	56.06

Graphical User Interface - Indoor Air Quality

The screenshot shows the phpMyAdmin interface with the 'AIQ_1' table selected. The table contains five columns: 'TIME', 'HUMIDITY', 'TEMPERATURE', 'CARBONDIOXIDE', and 'VOC'. The data is displayed in a grid with 184 rows visible. A warning message indicates that the current selection does not contain a unique column. The left sidebar shows the database structure, including 'THERMAL_ANALYZER' and its sub-tables.

Current selection does not contain a unique column. Grid edit, checkbox, Edit, Copy and Paste are disabled.

Showing rows 4575 - 4590 (4591 total, Query took 0.0173 seconds.)

TIME	HUMIDITY	TEMPERATURE	CARBONDIOXIDE	VOC
2021-09-15 12:08:14	74.2	23.4	1901	0.01
2021-09-15 12:10:14	74.3	23.4	1931	0.01
2021-09-15 12:12:16	74.3	23.4	1956	0.01
2021-09-15 12:14:16	74.2	23.4	1948	0.01
2021-09-15 12:16:18	74.7	23.4	1985	0.01
2021-09-15 12:18:19	74.7	23.4	2010	0.02
2021-09-15 12:20:20	74.8	23.5	2030	0.02
2021-09-15 12:22:21	75.2	23.6	2100	0.02
2021-09-15 12:36:28	75.7	24	1958	0.02
2021-09-15 12:38:29	75.6	24	1966	0.02
2021-09-15 12:42:31	75.4	24.1	1952	0.02
2021-09-15 12:44:32	75.3	24.2	1954	0.02
2021-09-15 12:46:33	75.1	24.2	1965	0.02
2021-09-15 12:48:34	75.1	24.2	1983	0.02
Console 12:58:40	74.9	24.4	2078	0.02

Graphical User Interface – Thermal Comfort Measurements

The screenshot shows the phpMyAdmin interface. On the left, the database structure is displayed, with the **THERMAL_ANALYZER** database selected. The **COMFORT_1** table is highlighted. The main panel shows the table structure and a query result for the **COMFORT_1** table. The query is `SELECT * FROM `COMFORT_1``. The result shows 517 rows, with the first 25 rows displayed. The columns are **TIME**, **HUMIDITY**, and **TEMPERATURE**.

TIME	HUMIDITY	TEMPERATURE
2020-11-10 04:07:40	81.4	18.6
2020-11-10 04:07:41	81.4	18.6
2020-11-10 04:09:41	81.1	18.6
2020-11-10 04:09:42	81.1	18.6
2020-11-10 04:13:14	80.5	18.9
2020-11-10 04:21:01	82.2	18.5
2020-11-10 04:23:02	81.6	18.7
2020-11-10 04:25:03	81.1	18.9
2020-11-10 04:27:04	80.69	18.9
2020-11-10 04:29:05	80.4	19
2020-11-10 04:31:06	80	19
2020-11-10 04:33:07	79.8	19.1
2020-11-10 04:35:08	79.69	19.1
2020-11-10 04:37:09	79.6	19.1
2020-11-10 04:39:10	79.4	19.2

Graphical User Interface - Thermal Performance Measurements (Outdoor)

The screenshot shows the phpMyAdmin interface. On the left, the database structure is displayed, with the **THERMAL_ANALYZER** database selected. The **OUTDOOR_1** table is highlighted. The main panel shows the table structure and a query result for the **OUTDOOR_1** table. The query is `SELECT * FROM `OUTDOOR_1``. The result shows 28242 rows, with the first 25 rows displayed. The columns are **TIME**, **AIR_HUMID_OUT**, **AIR_TEMP_OUT**, and **SURF_TEMP_OUT**.

TIME	AIR_HUMID_OUT	AIR_TEMP_OUT	SURF_TEMP_OUT
2019-11-27 19:12:06	98.11	9.34	13.37
2019-11-27 19:17:07	97.75	9.24	13.37
2019-11-27 19:27:09	97.93	9.45	13.68
2019-11-27 19:37:11	97.2	9.45	13.55
2019-11-27 19:47:13	98.48	9.45	13.59
2019-11-27 19:52:14	97.75	9.34	13.37
2019-11-27 19:57:15	98.66	9.34	13.33
2019-11-27 20:02:16	98.85	9.34	13.19
2019-11-27 20:07:17	97.56	9.45	13.28
2019-11-27 20:12:18	97.75	9.45	13.37
2019-11-27 20:17:19	97.01	9.45	13.33
2019-11-27 20:22:20	97.01	9.45	13.33
2019-11-27 20:27:21	97.01	9.34	13.06
2019-11-27 20:32:22	96.65	9.24	12.97
2019-11-27 20:37:23	96.83	9.34	13.01

Graphical User Interface – Thermal Performance Measurements (Indoor)

1

The screenshot displays the phpMyAdmin web interface. On the left, the database structure tree shows the 'THERMAL_ANALYZER' database selected, with tables including 'ACOUSTIC_1', 'ACOUSTIC_2', 'AIQ_1', 'COMFORT_1', 'INDOOR_1', 'INDOOR_2', 'OUTDOOR_1', 'OUTDOOR_2', and 'THERMAL_METRE'. The 'INDOOR_1' table is highlighted.

The main panel shows the 'INDOOR_1' table structure. A message indicates: 'Current selection does not contain a unique column. Grid edit, checkbox, Edit, Copy and Delete'. Below this, a status bar shows 'Showing rows 0 - 24 (28090 total, Query took 0.0005 seconds.)'. The SQL query 'SELECT * FROM `INDOOR_1`' is displayed. The table has 5 columns: 'TIME', 'AIR_HUMID_IN', 'AIR_TEMP_IN', 'SURF_TEMP_IN', and 'HEATFLUX'. The table contains 25 rows of data, showing measurements from 2019-11-27 19:11:40 to 20:21:54.

TIME	AIR_HUMID_IN	AIR_TEMP_IN	SURF_TEMP_IN	HEATFLUX
2019-11-27 19:11:40	42.95	20.31	14.7	54.243
2019-11-27 19:16:41	42.03	20.31	14.79	52.7363
2019-11-27 19:21:42	42.21	20.31	14.75	52.7363
2019-11-27 19:26:43	42.4	20.31	14.88	51.2295
2019-11-27 19:31:44	42.03	20.31	14.88	51.2295
2019-11-27 19:36:45	41.85	20.31	14.83	49.7228
2019-11-27 19:41:46	41.66	20.21	14.83	54.243
2019-11-27 19:46:47	42.03	20.11	14.7	54.243
2019-11-27 19:51:48	42.03	20.11	14.66	55.7498
2019-11-27 19:56:49	42.21	20.01	14.57	52.7363
2019-11-27 20:01:50	42.03	20.11	14.66	54.243
2019-11-27 20:06:51	42.21	20.11	14.61	52.7363
2019-11-27 20:11:52	41.85	20.01	14.61	51.2295
2019-11-27 20:16:53	41.85	20.11	14.57	52.7363
2020-11-27 20:21:54	41.66	20.01	14.48	52.7363

Appendix 6: Thermal Performance Measurement Matlab Scripts

```
%*****
%This Matlab script evaluate the the value of thermal transmittance (u-value)
%Thermal conductivity and and thermal resistance of the building materials
%based on the standard BS 9869(2014)
%*****

%matlab function to determine Thermal transmittance
% Average Method u-value
function uvalue = uvalue_avg( avHeatflux,Temp1,Temp2)
for i=1:length(avHeatflux) % The value of heatflux
if isnan(avHeatflux(i))
avHeatflux(i)=0; %Average heatflux value
Temp1(i)= 0; %The value of Indoor Air Temperature
Temp2(i)= 0; %The value of Outdoor Air Temperature
end
end
%U-value calculation using average method
uvalue=abs(cumsum(avHeatflux)./cumsum(Temp1-Temp2));
end
%*****

% Matlab function to calculate thermal conductivity of the material
function Thermal_Cond = ThermalCond( avHeatflux,SurfTemp1,SurfTemp2)
for i=1:length(avHeatflux)%The value of heatflux
if isnan(avHeatflux(i))
avHeatflux(i)=0;
SurfTemp1(i)= 0; %Indoor surface temperature
SurfTemp2(i)= 0; %Outdoor surface temperature
end
end
%Thermal conductivity calculation using average method
Thermal_Cond=abs(cumsum(avHeatflux)./cumsum(SurfTemp1-SurfTemp2));
end
%*****

%Matlab function to calculate thermal resistance
function Thermal_Res = ThermalRes( avHeatflux,SurfTemp1,SurfTemp2)
for i=1:length(avHeatflux) %The value of heatflux
if isnan(avHeatflux(i))
avHeatflux(i)=0;
SurfTemp1(i)= 0; %Indoor surface temperature
SurfTemp2(i)= 0; %Outdoor surface temperature
end
end
%Thermal resistance calculation using average method
Thermal_Res=abs(cumsum(SurfTemp1-SurfTemp2)./cumsum(avHeatflux));
end
```

Appendix 7: TGS 2602 Sensor calibration Code

```
/******  
This code used to calibrate TGS2602 Gas sensor from Figaro. Sensor need to be  
Conditioned at room temperature before calibrated and used for the first time  
*****/  
#define RL 47 //The value of resistor RL is selected as 47K  
void setup()  
{  
  Serial.begin(9600); //Initialise serial COM for displaying the value  
}  
  
void loop()  
{  
  float analog_value=0;//Store analogue value from the sensor  
  float VRL;// Load voltage  
  float Rs; //  
  float Ro; //  
  //Read the analog output of the sensor for 500 times for good average  
  for(int test_cycle = 1 ; test_cycle <= 500 ; test_cycle++)  
  {  
    analog_value = analog_value + analogRead(A0);  
  }  
  analog_value = analog_value/500.0; // calculate sample average  
  VRL = analog_value*(5.0/1023.0); //Convert analog value to voltage  
  //RS = ((Vc/VRL)-1)*RL is the formulae we obtained from datasheet  
  Rs = ((5.0/VRL)-1) * RL;//Evaluate the value of resistance at presence of measured gas  
  //RS/RO is 1 as we obtained from graph of datasheet  
  Ro = Rs/1;//Resistance ratio from TGS2602 datasheet  
  Serial.println();  
  Serial.print("Ro at fresh air = ");//Resistance of sensor at fresh air  
  Serial.println(Ro); //Display calculated Ro  
  delay(1000); //delay of 1sec  
}
```

Appendix 8: Linear Regression Model Output for Acoustic Sensing System Calibration

ADC	dB										
200	37										
230	41										
250	43	r	0.990614								
300	50										
350	55										
400	60	SUMMARY OUTPUT									
480	63										
500	66	Regression Statistics									
512	67	Multiple R	0.990614								
533	70	R Square	0.981316								
576	75.4	Adjusted R Square	0.980381								
604	79	Standard Error	2.846008								
627	81	Observations	22								
640	82.5										
720	84.6	ANOVA									
730	85.7		df	SS	MS	F	Significance F				
771	86.8	Regression	1	8508.059	8508.059	1050.408901	9.21557E-19				
803	90.8	Residual	20	161.9952	8.099759						
900	96	Total	21	8670.055							
945	99										
1000	103	Coefficient: Standard Error		t Stat	P-value	Lower 95%	Upper 95%	Lower 95.0%	Upper 95.0%		
1023	107	Intercept	25.61687	1.604432	15.96631	7.56922E-13	22.2700794	28.96365	22.2700794	28.96365407	
		ADC	0.080879	0.002495	32.41001	9.21557E-19	0.075673441	0.086084	0.075673441	0.086084453	